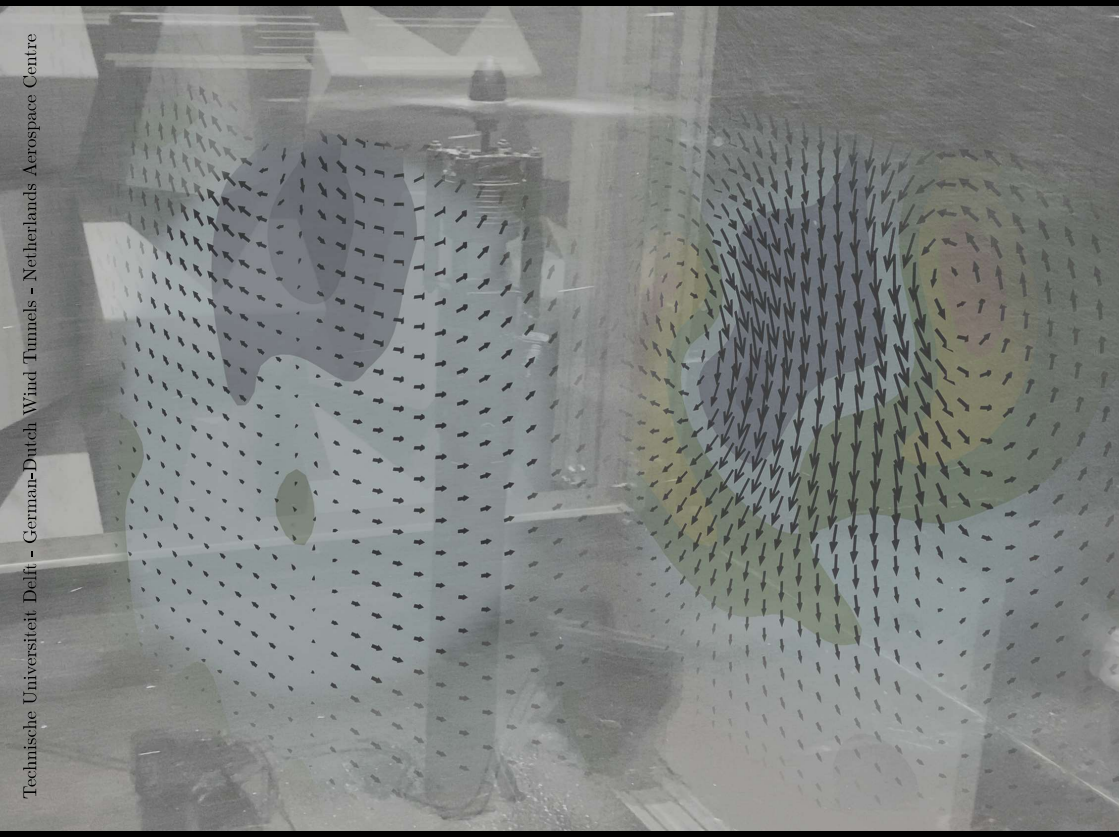
Wall Interference Assessment of Isolated Fixed-Pitch Propeller Tests

Filotas Tziaros



Technische Universiteit Delft - German-Dutch Wind Tunnels - Netherlands Aerospace Centre

TU Delft

nlr

DNW German-Dutch Wind Tunnels

Wall Interference Assessment of Isolated Fixed-Pitch Propeller Tests

by

Filotas Tziaros

Student Name	Filotas Tziaros
Student Number	5387752

University Supervisor:	Dr.ir. G.E. Elsinga
Faculty:	Mechanical Engineering (3mE), TU Delft
Company Supervisor:	S. Hegen
Company:	German-Dutch Wind Tunnels, DNW
Project Duration:	September, 2022 - July, 2023

TU Delft

nlr

DNW German-Dutch Wind Tunnels

Summary

The need to reduce greenhouse gas emissions is emergent throughout every industrial sector worldwide. For aviation, this has opened a market gap for small scale electric aircraft configurations (e-V/STOL). These configurations are very diverse and they are classified based on how lift is obtained. However, their flight envelope consists of the same operational regimes which in turn, are very diverse compared with the ones of a traditional aircraft. This challenges the way wind tunnel testing was developed and urges the need for new testing techniques and wall correction methods.

It is known for over a century that the flow inside a wind tunnel is not exactly the same as a free-air flow. This has to do with the existence of the wind tunnel test section boundaries which affect the flow over the model. Thus, the measured wind tunnel data deviate from the desired free-air performance measurements, except if the model is extremely small relative to the test section size. This is almost never satisfied due to physical scaling and structural considerations. Wall or boundary interference, is the quantification of those effects with the aim of correcting the wind tunnel performance measurements to their actual free-flight values. This is achieved by wall correction methods. These methods were developed in absence of high computing power and their purpose is to perform real-time adjustments to wind tunnel data. Consequently, they depend on simplified modeling assumptions, such as the linearized potential flow. As a result, these corrections might prove ineffective in generating reliable outcomes when dealing with non-linear boundary interference fields characterized by significant variations. For a given model, it is generally known that there is a limit at which wind tunnel test data are able to represent free-air conditions. This limit is called wind tunnel flow breakdown and it occurs when the model wake impinges on the boundaries of the wind tunnel test section, causing flow phenomena which would never occur in a free-flight situation. This phenomenon succeeds the non-linearities of boundary interference described above and is the worst case scenario for wind tunnel tests. The wall corrections completely fail to produce any valid outcome and the wind tunnel data are considered useless. This happens at low-speed/high-thrust conditions which are typical for a V/STOL aircraft during transition from hover to forward flight. Thus, powered wind tunnel testing at such conditions poses challenges in terms of data representation to an interference-free, free-air situation. Such conditions may also be encountered when the aircraft is operating in-ground vicinity and thus, the interference field for those cases is of interest. In the latter case, it is expected that the magnitude of the corrections and the wind tunnel flow breakdown limits would be significantly lower.

This Thesis aims to investigate wall interference effects between the rotor and the wind tunnel test section boundaries at low-speed/high-thrust conditions, establish the flow breakdown limits for a given propeller and test section and to gain insight into the effect that the bottom wall of the test section exhibits to the boundary interference field. This is realized by conducting wind tunnel tests on two different fixed-pitch propellers with varying incidence angles in both a closed-wall and a 3/4 open-jet test section of the NLR Aeroacoustic Wind Tunnel. Static wall pressure measurements are acquired and the flow-field in the vicinity of the propeller is quantified using large-scale, Tomographic Particle Tracking Velocimetry (PTV) with the use of helium filled soap bubbles (HFSB) as tracers. Finally, the interference-free performance data for these propellers are obtained from the second test campaign performed in the industrial Low-Speed-Wind Tunnel (LST) of the DNW.

The global flow topology of the wall-bounded tests in the AWT-closed test section is presented by means of wall pressure measurements and PTV. It was found that a distinct rise of the pressure coefficient leading to a maximum peak, corresponds to wake impingement. This firstly occurs on the advancing side of the rotor due to the larger vortex which is deflected further downward than the one on retreating

side.

A flow breakdown criterion which makes use of the static pressure distribution on the bottom wall of the test section is introduced. It aligns well with existing benchmarks available in literature for closed-wall test sections. This criterion can be applied to any test section consisting of a solid lower wall, as long as the distribution of static pressure is monitored. On the other hand, the comparison between the LST and AWT-closed test section data do not show any signs of flow breakdown. This could prompt additional questions regarding the necessity of an even larger test section for obtaining the interference free propeller performance data.

Various wall correction methods are utilized in order to evaluate their applicability for powered wind tunnel testing and to assess the impact of wall interference. It is shown that the developed Two-Variable-Method (TVM) does not provide satisfying results with respect to lift interference, when compared with the Heyson method. Nevertheless, blockage predictions follow the expected trends even for lifting cases, at least for the higher advance ratios where no flow impingement is present. For a simple non-lifting case, this method is deemed more reliable since its underlying assumptions are satisfied to a greater extend and its blockage predictions are also in good agreement with the Glauert's method.

For the purely lifting angle of attack, the comparison between the two test campaigns is not satisfactory both for in-ground and out-of-ground effect. This discrepancy arises from the fact that the predictions of all wall correction methods applied do not abide by the trend that is discernible based on the deviations of the bounded (AWT) to the unbounded (LST) data. That is mainly attributed to the load measurement system and to the possibly stalling conditions at the higher wind tunnel speeds. For the 0° incidence angle, there was a very good agreement between the AWT-closed test section and the LST data for both flight conditions (OGE, IGE). This was validated by both applied correction procedures (Glauert's method for off-center propellers & Two-Variable-Method). Even in that case, the AWT-3/4 open-jet results were not in good agreement implying effects which may not only be attributed to boundary interference.

Samenvatting

De noodzaak om de uitstoot van broeikasgassen te verminderen doet zich wereldwijd in elke industriële sector gevoelen. Voor de luchtvaart heeft dit een gat in de markt geopend voor kleinschalige elektrische vliegtuigconfiguraties (e-V/STOL). Deze configuraties zijn zeer divers en worden ingedeeld op basis van de manier waarop lift wordt verkregen. Hun vluchtomhullende bestaat echter uit dezelfde operationele regimes die op hun beurt zeer divers zijn in vergelijking met die van een traditioneel vliegtuig. Dit stelt de manier waarop windtunneltesten zijn ontwikkeld op de proef en vraagt om nieuwe testtechnieken en methoden voor wandcorrectie.

Het is al meer dan een eeuw bekend dat de stroming in een windtunnel niet precies hetzelfde is als een stroming in de vrije lucht. Dit heeft te maken met de grenzen van de windtunneltestsectie die de stroming over het model beïnvloeden. De gemeten windtunnelgegevens wijken dus af van de gewenste metingen van de prestaties in de vrije lucht, behalve als het model extreem klein is ten opzichte van de grootte van de testsectie. Dit is bijna nooit het geval vanwege fysieke schaling en structurele overwegingen. Muur- of grensinterferentie is de kwantificering van deze effecten met als doel de metingen van de windtunnelprestaties te corrigeren naar hun werkelijke waarden in de vrije lucht. Dit wordt bereikt door wandcorrectiemethoden. Deze methoden zijn ontwikkeld bij gebrek aan veel rekenkracht en hun doel is om real-time aanpassingen uit te voeren op windtunnelgegevens. Bijgevolg zijn ze afhankelijk van vereenvoudigde modelaannames, zoals de gelineariseerde potentiële stroming. Als gevolg hiervan kunnen deze correcties ineffectief blijken te zijn bij het genereren van betrouwbare uitkomsten bij het omgaan met niet-lineaire grensinterferentievelden die gekenmerkt worden door aanzienlijke variaties. Voor een bepaald model is het algemeen bekend dat er een limiet is waarboven windtunneltestgegevens de omstandigheden in de vrije lucht kunnen weergeven. Deze limiet wordt windtunnelstromingsdefect genoemd en treedt op wanneer het zog van het model de grenzen van de windtunneltestsectie raakt, waardoor stromingsverschijnselen ontstaan die nooit zouden optreden in een situatie met vrije vlucht. Dit fenomeen volgt de hierboven beschreven niet-lineariteit van grensinterferentie op en is het slechtste scenario voor windtunneltests. De wandcorrecties leveren geen enkel geldig resultaat op en de windtunnelgegevens worden als nutteloos beschouwd. Dit gebeurt bij lage snelheid/hoge stuwkracht condities die typisch zijn voor een V/STOL vliegtuig tijdens de overgang van zweven naar voorwaarts vliegen. Het testen van aangedreven windtunnels onder dergelijke omstandigheden levert dus uitdagingen op wat betreft de weergave van gegevens in een interferentievrije situatie in de vrije lucht. Dergelijke omstandigheden kunnen zich ook voordoen wanneer het vliegtuig in de nabijheid van de grond vliegt en in die gevallen is het storingsveld dus van belang. In het laatste geval wordt verwacht dat de grootte van de correcties en de doorslaglimieten van de windtunnel aanzienlijk lager zouden zij

Het doel van dit proefschrift is het onderzoeken van interferentie-effecten tussen de wand van de rotor en de grenzen van de windtunneltestsectie bij lage snelheid/hoge stuwkracht, het vaststellen van de stromingsafwijkingslimieten voor een bepaalde propeller en testsectie en het verkrijgen van inzicht in het effect dat de onderwand van de testsectie heeft op het interferentieveld. Dit wordt gerealiseerd door windtunneltests uit te voeren met twee verschillende vaste spoed propellers met verschillende invalshoeken in zowel een gesloten wand als een 3/4 open straal testsectie van de NLR Aeroakoestische Windtunnel. Statische wanddrukmetingen worden verkregen en het stromingsveld in de omgeving van de propeller wordt gekwantificeerd met behulp van grootschalige, tomografische Particle Tracking Velocimetry (PTV) met helium gevulde zeepbellen (HFSB) als tracers. Tot slot worden de storingsvrije prestatiegegevens voor deze propellers verkregen uit de tweede testcampagne die is uitgevoerd in de industriële Low-Speed-Wind Tunnel (LST) van DNW.

De globale stromingstopologie van de wand-gebonden testen in de AWT-gesloten testsectie wordt gepresenteerd door middel van wanddrukmetingen en PTV. Het bleek dat een duidelijke stijging van de drukcoëfficiënt die leidt tot een maximale piek, overeenkomt met zogaanstroming. Dit gebeurt eerst aan de oprukkende kant van de rotor door de grotere werveling die verder naar beneden wordt afgebogen dan de werveling aan de terugtrekkende kant.

Er wordt een stromingsafbraakcriterium geïntroduceerd dat gebruik maakt van de statische drukverdeling op de onderwand van de testsectie. Het komt goed overeen met bestaande benchmarks die in de literatuur beschikbaar zijn voor testsecties met een gesloten wand. Dit criterium kan worden toegepast op elke testsectie die bestaat uit een massieve onderwand, zolang de verdeling van de statische druk wordt gecontroleerd. Aan de andere kant laat de vergelijking tussen de LST- en AWT-data van gesloten testsecties geen tekenen van stromingsafbraak zien. Dit kan verdere vragen oproepen over de noodzaak van een nog groter testgedeelte voor het verkrijgen van gegevens over de prestaties van de propeller zonder interferentie.

Er worden verschillende wandcorrectiemethoden gebruikt om hun toepasbaarheid voor aangedreven windtunneltesten te evalueren en om de invloed van wandinterferentie te beoordelen. Er wordt aangetoond dat de ontwikkelde Twee-Variabele-Methode (TVM) geen bevredigende resultaten geeft met betrekking tot liftinterferentie, in vergelijking met de Heyson-methode. Desondanks volgen de verstoppingsvoorspellingen de verwachte trends, zelfs voor liftgevallen, tenminste voor de hogere vervroegingsratio's waarbij geen sprake is van stromingsinvloeden. Voor een eenvoudig nietheffend geval wordt deze methode betrouwbaarder geacht omdat aan de onderliggende aannames meer wordt voldaan en de voorspellingen voor verstopping ook goed overeenkomen met de methode van Glauert.

Voor de zuivere stijghoek is de vergelijking tussen de twee testcampagnes niet bevredigend, zowel voor het ingegraven effect als voor het effect buiten de grond. Deze discrepantie komt voort uit het feit dat de voorspellingen van alle toegepaste wandcorrectiemethoden zich niet houden aan de trend die zichtbaar is op basis van de afwijkingen tussen de begrensde (AWT) en de onbegrensde (LST) gegevens. Dit wordt voornamelijk toegeschreven aan het belastingsmeetsysteem en aan de mogelijke overtrekcondities bij de hogere windsnelheden. Voor de invalshoek van 0 graden was er een zeer goede overeenkomst tussen de AWT-gesloten testsectie en de LST-data voor beide vluchtcondities (OGE, IGE). Dit werd gevalideerd door beide toegepaste correctieprocedures (de methode van Glauert voor off-center propellers en de methode met twee variabelen). Zelfs in dat geval kwamen de AWT-3/4 open straal resultaten niet goed overeen, wat duidt op effecten die niet alleen kunnen worden toegeschreven aan grensinterferentie.

Acknowledgements

Over the past academic year, I had the privilege of conducting my thesis research at the DNW Large Low-speed Facility (LLF) Business Unit located in Marknesse, the Netherlands. The opportunity to dive into the realm of aerodynamics and wind tunnel testing at DNW was made possible by the abundant support and generosity of numerous individuals.

First of all, I would like to thank my supervisors Dr.ir. Gerrit Elsinga and Sinus Hegen on behalf of TU Delft and DNW, for granting me the remarkable chance to get involved in such a fascinating research project as well as for our engaging discussions on the research topic. Additionally, I would like to thank Frenk Wubben, Iwan Philipsen, Roy Gebbink and Mia Jovetić from the DNW Project Aerodynamics Department for always being available to answer my numerous questions with respect to every stage of the research. Their valuable input and assistance have been instrumental in the successful completion of this study. Additionally, i would like to thank Prof.dr.ing. G. Eitelberg for always finding time to discuss about several aspects of propeller aerodynamics and boundary interference. His enthusiasm and interest over these topics is really admirable.

I would also like to express my strong gratitude towards the NLR colleagues from the Vertical Flight and Aeroacoustics department (AVVA) for warmly welcoming me into their Aeroacoustic Wind Tunnel (NLR-AWT) and providing me with not only a workspace but also access to the necessary software tools I required for my research. In specific, I would like to thank Mark-Jan van der Meulen and Paul Admiraal for their collaboration in the data acquisition systems set-up and the tests implementation and Marthijn Tuinstra and Hasse Dekker for their assistance in PTV related matters. Finally, a special thanks to the NLR-AWT operators, Tim Deleij and Laurens de Haan for conducting all the hard practical work and for transforming the wind tunnel. Without your help the establishment of a functional test apparatus would not have been possible. Finally, a special thanks to Pieter van Zelst and Lars Ottenhof for their effective collaboration during the LST campaign.

Besides the academic and technical assistance, I would also like to thank all the colleagues with whom I carpooled and specifically Sandra Witkamp who graciously provided me with transportation all this time. Last but not least, I would also like to thank my family and my friends both in Greece and in the Netherlands for their endless encouragement and support and a special thanks to my friend Soulitsa for designing the cover of this report.

Filotas Tziaros
LLF - Business Unit, Marknesse, October 2023

Contents

Summary i

Samenvatting iii

Preface v

Nomenclature xvii

1 Introduction 1

1.1 Sociotechnological & Environmental Aspects . . . 1

1.2 Low Speed Wind Tunnel Technology . . . 2

1.3 Wind Tunnel Wall Interference & Corrections . . . 4

1.3.1 Wall Correction Methods . . . 6

1.3.2 Flow Breakdown . . . 9

1.4 Rotor Wall Interference Investigations . . . 17

1.4.1 Lifting Rotors . . . 18

1.4.2 Propellers . . . 19

1.4.3 PIV Investigations . . . 21

1.5 Tomographic PTV . . . 22

1.6 Thesis Aim & Objectives . . . 23

1.7 Thesis Outline . . . 24

2 Wall Correction Methods 25

2.1 Introduction . . . 25

2.2 The Classical Correction Method . . . 25

2.2.1 Lifting Rotors . . . 27

2.2.2 Blockage Corrections for Propellers . . . 27

2.3 The Heyson Method . . . 33

2.3.1 Correction Procedure . . . 36
2.4 Boundary Measurement Methods . . . 37
2.4.1 The 2D Two-Variable-Method . . . 37
2.4.2 The 3D Two-Variable-Method . . . 41

3 Experimental Methods 43

3.1 The NLR-AWT Campaign . . . 43
3.1.1 The NLR-AWT Facility . . . 43
3.1.2 General Test Setup . . . 45
3.1.3 Simulation & Test Conditions . . . 54
3.2 The DNW-LST Campaign . . . 55
3.2.1 The DNW-LST Facility . . . 55
3.2.2 General Test Setup . . . 56

4 Results 58

4.1 Global Flow Topology . . . 58
4.1.1 Wall Static Pressure Signatures . . . 58
4.1.2 Time-Averaged PTV Results . . . 70
4.1.3 Summary & Discussion . . . 83
4.2 Wall Corrections . . . 84
4.2.1 OGE Corrections . . . 85
4.2.2 Summary & Discussion . . . 92
4.2.3 IGE Corrections . . . 93
4.2.4 Summary & Discussion . . . 97
4.3 Flow Breakdown Limits . . . 99
4.3.1 Established Criteria . . . 99
4.3.2 Criterion Based on Wall Pressures . . . 100
4.3.3 Summary & Discussion . . . 101
4.4 Interference-Free Results . . . 102
4.4.1 OGE Comparison . . . 102
4.4.2 IGE Comparison . . . 104

4.4.3 Summary & Discussion . . . 106

5 Conclusions & Recommendations **108**

5.1 Conclusions . . . 108

5.2 Recommendations . . . 110

References **112**

A Theoretical Background **118**

A.1 Velocity Potential Equation for Incompressible Flows (Laplace Equation) . . . 118

A.2 Linearization of the Bernoulli Equation . . . 119

A.3 Velocity Potential Equation for Compressible Flows . . . 119

A.4 Linearized Velocity Potential Equation for Compressible Flows . . . 120

A.5 Prandtl-Glauert Transformation . . . 121

A.6 Greens Theorem for Incompressible Potential Flows . . . 121

A.6.1 The General Solution of the Laplace equation . . . 121

B Boundary Measurement Methods **124**

B.1 Overview . . . 124

C Test Plans **129**

C.1 NLR-AWT Test Campaign . . . 129

C.1.1 NLR-AWT Test Matrices . . . 129

C.1.2 NLR-AWT RAD Assignment . . . 130

C.2 DNW-LST Test Campaign . . . 137

C.2.1 DNW-LST Test Matrices . . . 137

D Uncertainty Assessment **138**

D.1 Load & Power Measurements . . . 138

D.1.1 Advance Ratio Estimation . . . 138

D.1.2 Thrust & Power Coefficients Estimation . . . 139

D.2 Wall Pressure Measurements . . . 142

D.3 PTV Measurements . . . 143

D.4 Conclusions . . . 149

List of Figures

1.1 Energy density comparison for different types of fuels used in aviation [21]. 2

1.2 Open (top) and closed (bottom) circuit wind tunnels (Daimler-Benz Aerospace Airbus, Bremen, Germany) (Defense Establishment Research Agency (DERA), Bedford, England) [6]. 3

1.3 Possible combinations of wind tunnel configurations [20]. 4

1.4 Free-air and wind tunnel bounded flow [26]. 5

1.5 Potential Flow Modelling Techniques. 7

1.6 Method of images for an airfoil wind tunnel test [84]. 8

1.7 Variation of rotor's lift for different wind tunnel test sections [67]. 10

1.8 Flow breakdown limits defined by [67]. 10

1.9 Jet impingement at tunnel wall during flow breakdown and at higher velocity increments respectively (from left to right) [88]. 11

1.10 Normal thrust force coefficient during the incipient stagnation region [88]. 11

1.11 Flow breakdown limits defined by [81]. 12

1.12 Flow breakdown limits defined by [69]. 12

1.13 Flow breakdown limits based on the three criteria defined by [88]. 13

1.14 Flow breakdown criteria comparison between [38] (dashed lines) and [85] (solid line). Taken from [38]. 14

1.15 V/STOL testing limits as a function of the wake impingement distance and the tunnel's geometry [40]. 14

1.16 Minimum allowable wind speed at flow breakdown onset [79]. 15

1.17 Average angle of attack correction for flow breakdown onset conditions [79]. 16

1.18 Comparison of flow breakdown limits between Biava et al. [8] (red) and Harris [31] (dashed). 16

1.19 Wind tunnel constraint flow along a closed wall test section. 20

1.20 Comparisons of different blockage estimations. 21

1.21 Scheme of the IPR algorithm [96]. 22

1.22 Iterative particle tracking for TP-STB with and without predictor (discarded particles are shown in gray) [61]. 23

2.1 Flow-field formulation for a centrally positioned propeller inside a wind tunnel. 28

2.2 Flow-field formulation for an unbounded flow over a propeller. 29

2.3 Flow-field formulation and control volume for an off-centered propeller wind tunnel test IGE. 31

2.4 Velocity correction ratio versus thrust coefficient for propellers with different blockage ratios. 32

2.5 Comparison between the M&S and the Glauert methods. 32

2.6 Propeller forces and their associated velocities [91]. 33

2.7 Induced velocities U_0, W_0 and skew angle definition [46]. 34

2.8 Heyson's theory for momentum, skew and effective skew angles [37]. 34

2.9 Modelling of the wake of the rotor in a wind tunnel [9]. 35

2.10 Angle of attack correction [46]. 36

2.11 Average lift interference parameter for different sized rotors, a comparison between HWC and R-302 [39]. 36

2.12 Flow domains for the wind tunnel and free-air flow [50]. 37

2.13 Domain for Green's Theorem application [50]. 38

2.14 Typical pressure measurements on the wind tunnel boundaries (upstream/front view) [49]. 40

3.1 The AWT closed wall test section. 44

3.2 The AWT 3/4 open-jet test section with automotive floor. 44

3.3 3D drawing of the automotive setup in NLR-AWT [32]. 45

3.4 Propellers used in the tests (propeller 2 left and propeller 1 right). 45

3.5 Electric motors used for the propeller tests (e-motor 2 left and e-motor 1 right). 46

3.6 Angle of attack definition, test stand and load cell. 46

3.7 Top view of the static pressure measurements inside the collector (4th pressure tap corresponds to both top and bottom wall) [62]. 47

3.8 View inside the transition for the closed test section. 48

3.9 Wind tunnel setup for the closed test section (propeller 2). 48

3.10 The AWT orifice-type helium-filled soap bubbles (HFSB) seeding rake. 49

3.11 Optical setup and double illumination strategy. 50

3.12 Imaging Setup. 50

3.13 Raw images of the measurement volume, PTV coordinate system and illumination directions. 51

3.14 Pre-processed images of the measurement volume (intensity scale is same for all three figures). 52

3.15 Normalized plate position based on estimated wind tunnel speed. 54

3.16 The DNW Low-Speed-Wind Tunnel (DNW-LST). 56

3.17 LST tunnel test setup during the test section calibration. 57

3.18 LST tunnel calibration factor for the tested free-stream velocities. 57

4.1 Pressure coefficient distributions of the advancing side on the bottom wall (top figures) and on the top wall (bottom figures) for different advance ratios (pressure bar numbering system in accordance with Figure 2.14). 60

4.2 Pressure coefficient distributions of the lower side on the left wall (top figures) and on the right wall (bottom figures) for different testing conditions (pressure bar numbering system in accordance with Figure 2.14, right and left wall correspond to $-y_{PTV}$ and $+y_{PTV}$ respectively). 61

4.3 Pressure coefficient distributions of the advancing side on the bottom wall (top figures) and on the top wall (bottom figures) for different advance ratios (pressure bar numbering system in accordance with Figure 2.14). 62

4.4 Pressure coefficient distributions of the lower side on the left wall (top figures) and on the right wall (bottom figures) for different testing conditions (pressure bar numbering system in accordance with Figure 2.14, right and left wall correspond to $-y_{PTV}$ and $+y_{PTV}$ respectively). 63

4.5 Pressure coefficient distributions of the advancing side on the ATF of the 3/4 open-jet test section for propeller 1 (top figures) and propeller 2 (bottom figures) at 90° incidence for different advance ratios. 65

4.6 Possible slipstream stagnation evolution based on the local maximum in pressure coefficient for the 90° incidence angle. 66

4.7 Pressure coefficient distributions of the advancing side on the bottom wall of the closed-wall test section for propeller 1 (left figures) and propeller 2 (right figures) for different advance ratios. 67

4.8 Pressure coefficient distributions of the advancing side on the ATF of the 3/4 open-jet test section for propeller 1 (top figures) and propeller 2 (bottom figures) at 60° incidence, for different advance ratios. 68

4.9 Possible slipstream stagnation evolution based on the local maximum in pressure coefficient for the 60° incidence angle. 69

4.10 Pressure coefficient distributions of the downward moving blade side on the bottom (top figures) and top (bottom figures) wall of the closed-wall test section for propeller 1 (left figures) and propeller 2 (right figures) for different advance ratios. 70

4.11 Axial and tangential velocity distribution within the measurement volume (x-slices) in the vicinity of the blades (a, b) and further downstream (c, d), for $\mu = 0.1$ (velocity vectors are flooded with the vertical velocity component). 72

4.12 Axial and tangential velocity distribution within the measurement volume (x-slices) in the vicinity of the rotor blades (a, c, d) and further downstream (b, e, f), for two different thrust conditions at zero incidence angle (velocity vectors are magnified for $\mu = 0.31$, for $\mu = 0.062$ all scalings are the same with Figure 4.11), (areas with insufficient seeding are covered in black). 73

4.13 Non-dimensional vorticity magnitude 2D contours on the retreating (a) and advancing (b) side of the rotor blades along with the isosurface of the Q-criterion for $\mu = 0.062$ (velocity vectors are shown for even spacing and are coloured for visualization purposes). 74

4.14 Non-dimensional vorticity magnitude 2D contours on the retreating (a) and advancing (b) side of the rotor blades along with the isosurfaces of the Q-criterion for $\mu = 0.1$ (velocity vectors are coloured for visualization purposes). 75

4.15 Local flow skew angle (direction) comparison with skew (solid white line) and effective (dashed white line) skew angles predicted by the HWC for the rotor wake modelling. . . 77

4.16 Flow angle (upwash/downwash) $x - y$ contour at a height of 8.6 cm below the rotor disk for the 3 tested conditions (LHS figures full angle range / RHS figures limited range. Velocity vectors are same for the 2 lower advance ratios and magnified for the higher) and comparison with the HWC averaged upwash over the disk $\Delta\alpha$. 78

4.17 Axial and tangential velocity distribution within the measurement volume (x-slices) at the propeller inflow (a, d, g), after the strut (b, e, h) and further downstream (c, f, i), for three different thrust conditions at 60° incidence angle (velocity vectors scaling is the same for $\mu = 0.3$ and $\mu = 0.2$), (areas with insufficient seeding are covered in black). . . 80

4.18 Axial and tangential velocity distribution within the measurement volume (x-slices) at the propeller inflow (a, d, g), after the strut (b, e, h) and further downstream (c, f, i), for three different thrust conditions at zero incidence angle (velocity vectors are magnified for $\mu = 0.198$, while the two lower advance ratios have the same scaling), (areas with insufficient seeding are covered in black). 82

4.19 Normalized out-of-plane vorticity distribution within the measurement volume at three different heights (z-planes) corresponding to half radius above the hub, at the hub location and close to the bottom boundary, for the three configurations examined (velocity vectors are magnified for $= 0.198$, while the two lower advance ratios have the same scaling). . 83

4.20 Glauert's incidence angle corrections for both propellers and test sections at 90° (top) and 60° (bottom). 86

4.21 HWC versus Glauert's flow angularity corrections for the propeller 1 at the closed test section at 90° incidence. 87

4.22 HWC versus Rubin et al. [73] modelling approaches for the flow deflection angle (closed-wall test section). 87

4.23 HWC flow angularity corrections for both propellers at 90° incidence and test sections. . 87

4.24 HWC flow angularity corrections for both propeller tests in the closed (left y-axis) and the 3/4 open-jet test (right y-axis) section, at 60° incidence angle. 88

4.25 Flow angularity corrections for both propeller tests in the closed test section, at 90° incidence angle. 89

4.26 Flow angularity corrections for both propeller tests in the closed test section, at 60° incidence angle. 89

4.27 Comparison between HWC (lift) and 2D-TVM (overall) blockage predictions. 90

4.28 Comparison between HWC (lift) and 2D-TVM (overall) blockage predictions. 91

4.29 Glauert's blockage corrections for propeller 2 in the closed test section, at 0° incidence angle. 91

4.30 HWC flow angularity and lift blockage corrections for both propellers and test sections at 90° incidence angle. 94

4.31 HWC flow angularity and lift blockage corrections for both propellers and test sections at 60° incidence angle. 95

4.32 Percentage reduction in flow angularity due to ground effect for the lifting angles of both propellers in the closed-wall test section 95

4.33 Glauert's method slipstream blockage versus total blockage predicted by the 2D-TVM for both propellers in the closed-wall test section (blockage is evaluated at three different vertical positions by the 2D-TVM). 96

4.34 Glauert's method slipstream blockage versus total blockage predicted by the 3D-TVM for both propellers in the closed-wall test section (blockage is evaluated at three different vertical positions by the 3D-TVM). 97

4.35 Flow breakdown limits proposed by Harris [31] and the thrust coefficient curves for both propellers. 99

4.36 Thrust coefficient as a function of advance ratio and incidence angle for propeller 2 out-of-ground-effect. 102

4.37 Comparison of the measured thrust coefficient for different wind tunnels and test sections for propeller 2 (uncorrected data). 103

4.38 Thrust coefficient as a function of advance ratio obtained for different wind tunnels and test sections (corrected and uncorrected data). 104

4.39 Comparison of the thrust coefficient measured in the LST and AWT-closed test section for propeller 2 in-ground-effect. 105

4.40 Thrust coefficient as a function of advance ratio obtained for different wind tunnels and test sections (corrected and uncorrected data). 105

A.1 Integration domain [47]. 122

B.1 Wind tunnel test section and model [3]. 124

B.2 Matrix of the wall pressure signature method [16]. 128

D.1 Bottom wall pressure measurements and uncertainty bands at the advancing side of propeller 1 during an rpm sweep. 143

D.2 Bottom wall pressure measurements and uncertainty bands at the advancing side of propeller 1 during a velocity sweep. 143

D.3 Normalized velocity uncertainty for a propeller 2 test at $\mu = 0.1$, 0° incidence angle (unprocessed data, colour bar same for all sub-figures). 146

D.4 Normalized velocity uncertainty for a propeller 2 test at $\mu = 0.1$, 0° incidence angle (post-processed data, colour bar same for all sub-figures). 147

D.5 Normalized velocity uncertainty for a propeller 2 test at $\mu = 0.197$, 0° incidence angle (post-processed data, colour bar same for all sub-figures). 148

D.6 Normalized velocity uncertainty for a propeller 2 test at $\mu = 0.063$, 0° incidence angle (post-processed data, colour bar same for all sub-figures). 149

List of Tables

1.1 Flow breakdown criteria and empirical observations available in literature. 17

3.1 Propeller general characteristics. 45

3.2 E-motor general characteristics. 46

3.3 Pressure taps distribution of a single bar (zero axial coordinate indicates the start of the test section). 47

3.4 Relevant parameters regarding the PTV setup and measurements. 53

3.5 Wind tunnel velocity sweep. 54

3.6 Range of the relevant dimensionless numbers based on the wind tunnel parameters. . . . 54

3.7 Range of the relevant dimensionless numbers based on the propeller parameters. 55

3.8 Relevant PTV recording and data processing parameters based on the wind tunnel free-stream velocity. 55

4.1 Relevant non-dimensional parameters for the boundary correction factors for the closed test section (δ_w is obtained from [6]). 85

4.2 Relevant non-dimensional parameters for the boundary correction factors for the 3/4 open-jet test section (δ_w is obtained from [86]). 85

4.3 Advance ratio and skew angle corresponding to flow breakdown for the closed-wall test section according to Harris [31]. 99

4.4 Advance ratio and skew angle corresponding to flow breakdown for the closed-wall test section according to Rae Jr. [67]. 99

4.5 Advance ratio and skew angle corresponding to flow breakdown for the 3/4 open-jet test section according to Harris [31]. 100

4.6 Advance ratio and skew angle corresponding to flow breakdown for the 3/4 open-jet test section according to Rae Jr. [67]. 100

4.7 Advance ratios for flow breakdown initiation based on bottom wall pressures ($AoA = 90°$).101

4.8 Advance ratios for flow breakdown initiation based on bottom wall pressures ($AoA = 60°$).101

C.1 Wind tunnel velocity sweep (for the 3/4 open-jet test section the sweep was from 40 to 6.5 m/s). 129

C.2 Pressure measurements for propeller 1, for both test sections, for a given AoA, corresponding to a height above the ground $(h/H)_{closed}$ (3 AoA's, or 3 different runs per test section). 130

C.3 Pressure measurements for propeller 2, for the closed-wall test section, for a given AoA, corresponding to a height above the ground $(h/H)_{closed}$ (3 AoA's, or 3 different runs). . 130

C.4 PTV measurements for propeller 2, for the closed-wall test section, for a given AoA, corresponding to a heights above the ground $(h/H)_{closed}$ (3 AoA's, or 3 different runs and 2 additional for a spinner height of 0.27, at 90° and 60°). 130

C.5 Pressure measurements for propeller 2, for the 3/4 open-jet test section, for a given $AoA_{3/4}$, on the tunnel centerline and at $((h/H)_{AoA=0^\circ} = 0.285$ (5 AoA's, or 5 different runs (centerline) and 3 additional, for h/H =0.285, at 0°). 130

C.6 RAD assignment for the closed test section wall pressure measurements. 131

C.7 RAD assignment for the closed test section wall pressure measurements. 134

C.8 Simulation conditions for the performance measurements of propeller 2 at 90° (5 runs (AoA's) for OGE and 3 (AoA's) for IGE) and at 0° (1 run for OGE and 1 for IGE). . . 137

C.9 Simulation conditions for the performance measurements of propeller 1 at 90° (1 run for IGE) and at 0° (1 run for OGE and 1 for IGE). 137

D.1 Random uncertainty assessment for the advance ratio estimation. 139

D.2 Random uncertainty assessment for the measured thrust. 140

D.3 Random uncertainty assessment for the thrust coefficient based on the wind tunnel speed. 140

D.4 Random uncertainty assessment for the thrust coefficient based on the blade tip speed. . 141

D.5 Random uncertainty assessment for the electric power estimation. 141

D.6 Random uncertainty assessment for the electric power coefficient estimation. 142

Nomenclature

Abbreviations

Abbreviation	Definition
AoA	Angle of Attack
ATF	Automotive Floor
AVVA	Vertical Flight and Aeroacoustics Department
AWT	Aeroacoustic Wind Tunnel
CFD	Computational Fluid Dynamics
DLR	German Aerospace Center
DSR	Dynamic Spatial Range
DNW	German Dutch Wind Tunnels
FRS	Flow Reference System
HFSB	Helium-Filled Soap Bubbles
HWC	Heyson Wall-Correction-Method Code
IGE	In-Ground Effect
IPR	Iterative Particle Reconstruction
LH_2	Cryogenic Liquid Hydrogen
LHS	Left-Hand-Side
LLF	Large Low-Speed Facility
LPT	Lagrangian Particle Tracking
LST	Low-Speed-Wind Tunnel
M&S	Mikkelsen and Sørrensen
MP	Multi-Pulse
NASA	National Aeronautics and Space Administration
NFAC	National Full-Scale Aerodynamics Complex
NLR	Royal Netherlands Aerospace Centre
OGE	Out-of-Ground Effect
OJ	Open-Jet
OTF	Optical Transfer Function
PIV	Particle Image Velocimetry
PSC	Particle Space Correlation
PTV	Particle Tracking Velocimetry
RHS	Right-Hand-Side
rpm	Revolutions per Minute
STB	Shake-The-Box
CMOS	Complementary MetalOxideSemiconductor
TP	Two-Pulse
TS	Test-Section
V/STOL	Vertical &/or Short Take-off and Landing
WaSiMe	Wall-Signature-Method Code
WT	Wind Tunnel or Wind Turbine

Symbols

Symbol	Definition	Unit
A	Surface Area or Current	m^2 or A
C	Coefficient	-
c	Coefficient or chord length	- or m
$c_D = \frac{D}{qA}$	Drag Coefficient	-
$c_L = \frac{L}{qA}$	Lift Coefficient	-
$C_P = \frac{P - P_{ref}}{q}$	Pressure Coefficient	-
$c_T = \frac{T}{\frac{1}{2}\rho u_{tip}^2 A}$	Thrust Coefficient Based on Tip Speed	-
$C_T = \frac{T}{qA}$	Thrust Coefficient Based on WT speed	-
$c_P = \frac{P}{\frac{1}{2}\rho u_{tip}^3 A}$	Power Coefficient Based on Tip Speed	-
D	Drag or Diameter	N or m
$D.L.$	Disk Loading	N/m^2
d	Pump Valve Diameter	
f	function	Variable Units
G	Green's Function	1/m
H	Wind Tunnel Height	m
h	Model Height Above WT floor	m
$\bar{K}$	Factor in the HWC Derived by Method of Images	-
L	Lift or Length	N or m
Ma	Mach Number	-
N	Normal Force	N
n	Unit Vector Normal to Surface or RPM	- or rpm
P	Point or Power or Pressure	m or W or Pa
$q = \frac{1}{2}\rho u_\infty^2$	Dynamic Pressure	Pa
R	Radius	m
Re	Reynolds Number	-
r	Distance Between 2 Points	-
S	Domain or Slipstream Surface	m^2
s	Tangential Unit Vector	-
T	Thrust	[N]
U	Horizontal Velocity	m/s
u	Velocity	m/s
V	Domain Volume or Voltage	m^3 or V
W	WT Width or Vertical Velocity	m or m/s
x	Axial Distance	m
α	AoA, Flow Angle or Solid Blockage Ratio	$^\circ$ or -
β	Prandtl-Glauert parameter	-
γ	WT-Semi-Width-to-Semi-Height Ratio	-
$\Delta\alpha$	Upwash Interference Velocity or AoA Correction	-
ϵ	Streamwise or Blockage Interference Velocity	-
ζ	WT-Semi-Height-to-Model-Semi-Height Ratio or Vertical Coordinate	- or m
θ	Momentum or Downwash Angle	$^\circ$

Symbol	Definition	Unit
λ	Velocity Ratio of Bounded to Unbounded Flow	-
$\mu = \frac{u_\infty}{u_{tip}}$	Advance Ratio	-
ξ	Axial Coordinate	m
ρ	Density	kg/m^3
σ	Slipstream Area Ratio or Solidity or Standard Deviation	- or - or Variable Units
Φ	Total Velocity Potential	m^2/s
ϕ	Velocity Potential	m^2/s
χ	Wake Skew Angle or Flow angle	$^\circ$
Ω	Arbitrary Constant	-
ω	Vorticity	s^-1
$\overline{\omega} = \frac{\omega}{(2*\pi*n/60)}$	Non-Dimensional Vorticity	-

Subscripts

Subscripts	Definition
b	Blades
cor	Corrected
crit	Critical
D	Drag
e	Electric
eff	Effective
F	Free-Air
f	Final
fbd	Flow Breakdown
hb	Below and within the wing span
I	Wall Interference
i	Component or Node Number
inv	Inversion
j	Component Number
L	Lift
M, m	Model or Measured
max	Maximum
min	Minimum
n	Downwash, Momentum
o	Fully Open
P	Pressure or Propeller
PTV	Obtained from PTV Velocity-Field
p	Poles
ref	Reference
T	Thrust or Tunnel
TT	Total Tunnel Flow
TF	Total Free Flow
tot	Total
u,D	Horizontal Velocity Due to Induced Drag
u,L	Horizontal Velocity Due to Induced Lift
WT	Wind Tunnel
w	Wall-Induced
w,D	Vertical Velocity Due to Induced Drag
w,L	Vertical Velocity Due to Induced Lift

Subscripts	Definition
0	Induced or Initial
1	Variable in the Prandtl-Glauert Coordinate Space
∞	Uniform-Flow, Far-Field, Free-Stream

1

Introduction

The most fundamental ways to determine the aerodynamics of any aircraft are real condition testing (flight tests), wind tunnel testing and CFD. All of those go side by side during the design process of the aircraft. The tested object in all cases could be either scaled or full scale. These ways have their advantages and disadvantages from a practical and a theoretical point of view. CFD is mostly used in the preliminary design stage due to its digital nature which enhances the flexibility of the design space, followed by wind tunnel and flight tests respectively. Compared to CFD, wind tunnel testing has the advantage of more reliable data generation since the fluid flow is not modelled, while it prevails over the flight tests for safety and economic reasons. On the other hand, wind tunnel testing has its own disadvantages in terms of geometric scale effects (Froude, Reynolds), Mach number effects and wall and support interference effects. This Thesis focuses on wall interference effects for low-speed wind tunnel testing of powered configurations. The goal is to evaluate the aerodynamic performance of the most basic component of such configurations, namely the rotor. For this reason, low speed wind tunnel tests are going to be performed for two isolated fixed-pitch propellers in both a closed and a (3/4) open-jet test section of the NLR Aeroacoustic Wind Tunnel (NLR-AWT). Despite the differences that they may exhibit, the terms propeller and rotor will interchangeably be used in the remaining of this report. This chapter presents the motivational drivers behind this research which are split into three parts. Those are the sociotechnological and environmental aspects, the development of wind tunnel testing and wall interference. Particle tracking Velocimetry (PTV) is also introduced as the applied measurement technique. In the end, the aim and objectives of this research are presented.

1.1. Sociotechnological & Environmental Aspects

Nowadays, the need to turn away from fossil fuels is emergent for the whole world due to the surging temperature levels induced by the emitted greenhouse gases and for energy security reasons. According to Ballesteros et al. [5], even if all the goals of the European Green Deal regarding the decarbonization of aviation will be met, similar efforts to reduce emissions in other transport modes will see aviation's share of total transport emissions rising from 12% in 2015 to about 60% by 2050. Over the last years, electric propulsion as well as hydrogen as an energy carrier for both combustion and fuel cells have been penetrating in the energy mix worldwide. Inevitably, this would also affect the aviation industry. Considering electric propulsion, small, short range aircraft types would be an option since modern batteries do not meet the energy requirements for long range flights. With respect to fuel properties, one of the most important criteria is the energy density of the fuel, as reducing weight and volume is of vital importance for aviation. Figure 1.1 presents several fuels as a function of their energy density (energy per unit mass) and volumetric energy density (energy per unit volume). As it can be seen,

cryogenic hydrogen (LH_2) has a volumetric energy density about four times higher than jet-A/kerosene, while its specific energy density is about 1/3 less. This means that an aircraft flying on LH_2 would need approximately 4 times larger storage tank volume (not accounting for insulation), in which the fuel would in turn, weight three times less compared to kerosene [21].

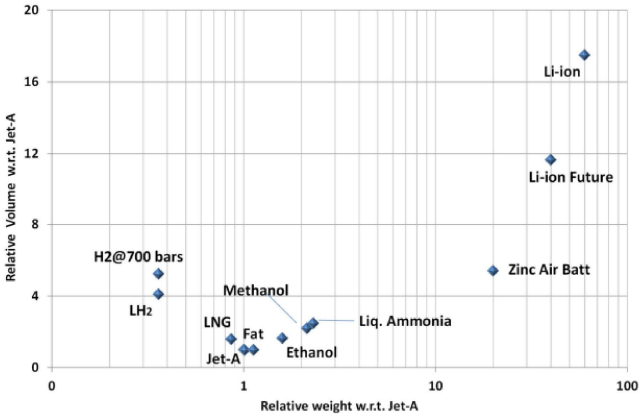


Figure 1.1: Energy density comparison for different types of fuels used in aviation [21].

For the reasons explained above, airplane travel will most likely split into two separate categories based on the passenger-km distance. Regarding short distance travels, this realization has boosted the need for small scale electric aircraft configurations, namely e-V/STOL. Such configurations are diverse and vary from VTOL types including helicopters, tilt-propellers/rotors and/or lifting jets to STOL types with highly deflected flaps or jet flaps. V/STOL systems are characterized by diverse powered lifting configurations whose behavior in cruise mode is completely different by that in take-off or landing. The latter is characterized by low speed regimes in which wind tunnel testing is very challenging [16]. In other words, during low speed wind tunnel testing of a V/STOL vehicle, complex flow structures may emerge due to the interaction of its wake with the wind tunnel walls and (free-stream) velocity. This topic is analyzed more in depth in the coming chapters. The isolated rotor configuration performed in the current study can serve as a baseline for more complex (V/STOL) configurations that might be tested in the future.

1.2. Low Speed Wind Tunnel Technology

The most fundamental characterization of wind tunnels is based on the flow regime that they operate:

- Subsonic (Low Speed) (Ma ≤ 0.3)
- Transonic (Ma ≈ 1)
- Supersonic (Ma > 1)
- Hypersonic (Ma > 5)

Since the rotor tests are going to be performed in the low speed regime, for the rest of this Thesis low speed wind tunnels will be plainly referred as wind tunnels. Strictly speaking, there are two types of

wind tunnel configurations, further characterized by two basic test section types. In reality, the situation is slightly different, since wind tunnels are big and complicated structures which cannot be characterized that easily. For that reason, it is considered that every wind tunnel is unique. According to Barlow et al. [6], "virtually every wind tunnel with a test section larger than 2 ft^2 is one of a kind", confirming the former statement. However, for the purpose of this study, the initial simplified classification is going to be given. For a more descriptive characterization of low speed wind tunnels the reader is referred to [6] and [20]. The two basic types of low speed wind tunnels are closed and open circuit, both of which can be further characterized depending on their test section (closed, open). Figure 1.2 shows an open (top) and a closed circuit wind tunnel (bottom). This distinction is more definite than the one depending on the test section type, since a combination of different wall types (e.g. conventional, slotted, adaptive, streamlined walls, etc.) and/or different test sections (e.g. closed, open, 3/4 open (bottom-only) test section, etc.) is possible. Figure 1.3 shows a table with some possible combinations of different wind tunnel types.

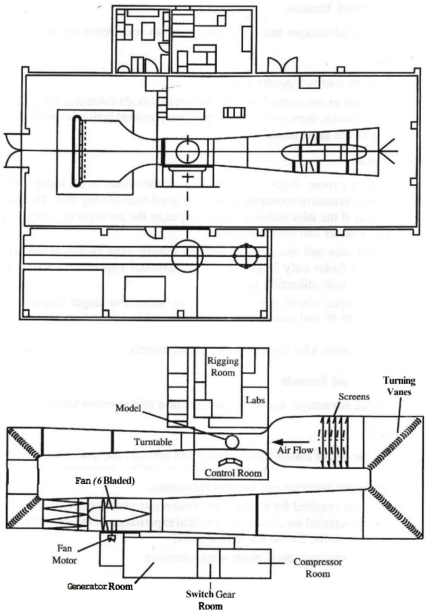


Figure 1.2: Open (top) and closed (bottom) circuit wind tunnels (Daimler-Benz Aerospace Airbus, Bremen, Germany) (Defense Establishment Research Agency (DERA), Bedford, England) [6].

From the above figures, it is evident that each wind tunnel is unique and each specific configuration has certain advantages and disadvantages which depend on the application. Regarding the circuit type distinction, the situation is clearer since an open circuit type has worst quality inflow, unstable pressure distribution, higher energy requirements and more noise than a closed return type [20]. Thus, most of the wind tunnels operating today are closed circuit. Since this Thesis focuses on boundary interference, the test section configuration is of importance. When comparing in terms of test sections, things become more complicated or better, application dependent. For example, closed wind tunnels with conventional walls are more mature than most of the other types, since it is the most common configuration used throughout many years now. Most of the wall correction methods were initially

Wind tunnel configurations			
Circuit	**Test section configuration**	**Plenum**	**Design name**
Closed	Open	ventilated	"Göttingen-type"
		not ventilated	
	Closed	no plenum	
	slotted walls	ventilated	
		not ventilated	
	streamlined walls	no plenum	
	adaptive walls	no plenum	
Open	Open	not ventilated	"Eiffel type"
	Closed	no plenum	"NPL"
	slotted walls	not ventilated	
	streamlined walls	no plenum	
	adaptive walls	no plenum	

Figure 1.3: Possible combinations of wind tunnel configurations [20].

developed for this configuration and the boundaries along with the prescribed boundary conditions are easily determined. On the other hand, testing a model such as a wind turbine in a closed test section is not preferred since the model usually needs to be scaled down extensively. This is due to the fact that closed test sections require relatively low blockage ratios (ratio of the model's area to the wind tunnel cross section). Moreover, most of the time it is not feasible to reduce the scale of such models significantly, because the rotor cannot maintain its actual mechanical properties. Additionally, most similarity parameters cannot be (easily) satisfied simultaneously. Another reason is that the flow is heavily influenced by the presence of the walls and big corrections are needed in order to eliminate wall interference. Therefore, for such tests, open or 3/4 open (floor only) test sections are mainly used, due to the higher acceptable blockage ratios and since they almost accurately resemble the actual working conditions of the model with the least possible interference. Such arguments usually apply for ground mobility vehicles such as cars, or trucks and for civil construction aerodynamic simulations. Several types of open test sections are preferred, with the 3/4 open-jet being the most dominant at least by the automotive industry. In the case of a high lifted configuration, during take-off or landing conditions, the open or 3/4 open test sections might be more suitable for wind tunnel tests since they include less wall interference than the closed wall. Furthermore, open-jet test sections offer the advantage of high quality aeroacoustic testing due to the positioning of the microphones outside the flow, the absence of walls and the use of anechoic plenum chambers. This notion, as perceived here, is not verified with available literature where most powered lift tests are performed in closed wall test sections. To the author's knowledge, up until today, only a limited number of power lifted configurations have been aerodynamically tested in open jet facilities and reported in academia. Most of forementioned tests were performed for aeroacoustic measurements and not focused on aerodynamic characterization, or wall interference. This can be explained by the fact that wall interference corrections in such types of test sections are limited and not sufficiently realized. More information regarding wall correction methods will be given in the following sections.

1.3. Wind Tunnel Wall Interference & Corrections

As mentioned before, interference effects are a significant factor which affects the quality of wind tunnel measurement data. Interference effects in low speed wind tunnels could arise from the influence of the tunnel's and model's wall boundary layers, disturbances from intrusive measuring equipment, model supports, and irregularities of the air-stream itself due to non-uniformity, unsteadiness or small-scale turbulence [22]. In different applications these can all be equally important, but the scope of the present Thesis is the aerodynamic interference of the wind tunnel boundaries on the model. Since the initial existence of aerodynamics, it is known that free-air flow is not the same as the flow in a wind tunnel.

This is attributed due to the presence of the walls (boundaries) and a schematic representation is shown in Figure 1.4. For the determination of the free-flight aerodynamic performance of any configuration, wind tunnel boundary (wall) induced interference needs to be eliminated. This is accomplished with the use of wall correction methods. One of the first who established the background theory related to wind tunnel wall interference was L. Prandtl, with the development of lifting-line theory. Prandtl analysed the problem of the wall interference at a lifting line for both an open and a closed test section while involving two dimensions only [65]. After that, H. Glauert [29] carried on Prandtl's research path and set the theoretical and practical framework to wall induced interference and wind tunnel wall correction methods. According to [16], there are four factors that govern this aerodynamic interference on the model:

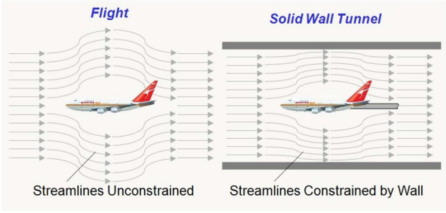


Figure 1.4: Free-air and wind tunnel bounded flow [26].

1. The nature of the aerodynamic forces generated by the model (lift, drag, pitching moment), but also the constitution of the total drag (sum of the induced drag[1], the skin friction drag[2] and the pressure drag[3] [1]) and the contributions of simulated power units (e.g. rotors, propellers, fans and jets).
2. The free stream velocity u_∞ (or Mach number or dynamic pressure).
3. The ratio of the model's size with respect to the test section size.
4. The type of the test section walls.

According to the above interference factors, a global classification for any subsonic wall interference correction is:

(a) Blockage Corrections : Corrections due to the reduction of the effective cross sectional area of the wind tunnel's test section (mostly concern the free-stream velocity).
(b) Lift Interference Corrections: Corrections due to the flow angularity induced by a lifting object because of the interaction of its circulation with the walls of the wind tunnel (mostly concern the angle of attack).

A further distinction of the wall corrections is between primary and residual corrections. This has to do with the sequence that these corrections are applied and as it is inferred, the primary corrections are applied beforehand, usually during the calibration procedure, while the secondary or residual ones are usually applied with the model positioned in the tunnel. Regarding blockage, the most common approach is to correct the free-stream velocity as measured in the empty wind tunnel to the free-flight value and hence obtain the equivalent static and dynamic pressures. Secondary or residual corrections are referred to as residual variations in the wall-interference velocities and can be interpreted as wall-induced distortions of the model and its wake. Those corrections are dependent on the tested configurations. Most common residual corrections are [43]:

[1]Drag due to lift generation (upwash)
[2]Viscous drag due to wall shear stress
[3]Viscous drag due to flow separation

1. Blockage corrections: Corrections on the wind tunnel free-stream velocity due to the space occupied by the model (blockage), its wakes and possible engine slipstreams. For example, the presence of the model induces a local increase in dynamic pressure in the remaining unblocked area (mass continuity). Thus, the model encounters a dynamic pressure higher than the actual free-stream value used to calculate the force coefficients. Same applies for the wake which occupies a velocity deficit area resulting in a higher dynamic pressure in the remaining unblocked area according to mass continuity. In cases of thrust generating devices (e.g. engine, propeller, rotor, etc.), the presence of locally higher velocities in the slipstream leads to a lower value of the dynamic pressure outside the slipstream (mass conservation). This has exactly the opposite effect than the model and its wake induced blockages mentioned previously.
2. Lift Interference:
    - Lift interference to correct for different streamline curvature due to the presence of the walls.
    - Lift blockage or lift interference on the direction of the effective wind speed. When lift is generated from a wing there is an amount of drag associated with the lift called induced drag. Due to this, an additional amount of induced velocity is generated in the direction of the effective wind speed. This affects the amount of upwash (circulation) generated because of the presence of the walls. Thus, a correction is required. Lift blockage is strongly depended on the amount of lift generated by the wing.
3. Drag Interference:
    - Drag is also affected by the same wall interference on the direction of the effective wind speed due to the rotational movement of the upwash. This results to another residual correction due to the lift redirection mentioned above.
    - A slight buoyancy force will affect the model due to a wake blockage gradient in the longitudinal direction. This could necessitate an additional correction.

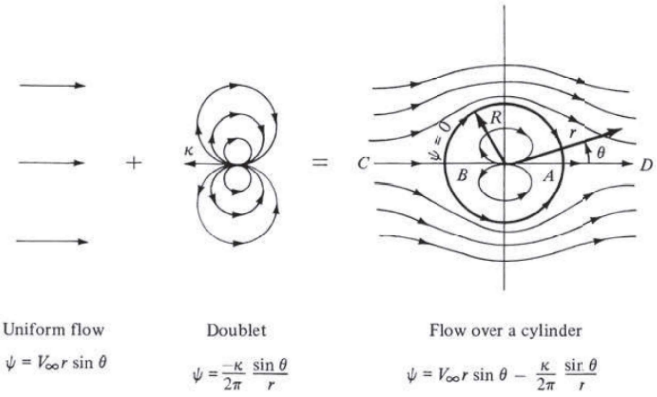
The significance of each correction depends on the tested configuration, the blockage ratio of the model with respect to the wind tunnel cross-section and on the type of the test section. For rotor testing, accurate lift interference corrections are essential for obtaining high quality accurate results, while solid and wake blockage are less important. However, the latter has a higher influence in closed wind tunnels than in open-jet test sections where the flow is free to expand [6]. It also depends on the type of the rotor or wake, so for a given blockage ratio, for a wind turbine, where the wake expands, this effect is stronger than for a propeller-type rotor, where the wake contracts. This will be discussed later in more detail.

1.3.1. Wall Correction Methods

There are several methods to determine wall interference whose accuracy depends on the assumptions and approximations made during the derivations. There are computational methods where viscous CFD models or panel methods are employed, but those are beyond of the scope of this Thesis due to their computational expense. This Thesis is restrained to simpler methods which are based on rougher approximations, but they are readily available to provide corrections either on-line, or within a very short amount of time. Such corrections are still mostly used by wind tunnel test engineers worldwide due to their fast computational nature accompanied with relatively good accuracy compared to the forementioned computational methods. The basic assumption of such methods is the linearized potential flow approximation. Under the assumptions of slender bodies, at small angles of attack and small perturbations an approximate solution for an inviscid, compressible subsonic or supersonic flow can be obtained by linearizing the velocity potential equation and solving the Laplace equation for compressible flows. This is the backbone of all the methods that will be discussed further in this Thesis and for that reason it is explained in depth in Appendix A. The most general classification of such correction methods which apply for both open and closed test sections are:

A. Conventional Wall Correction Methods

This group of methods uses the method of images to model the constraint flow inside the wind tunnel and are one of the oldest methods to assess wall interference. In general, the flow pattern around an airfoil can be modelled mathematically by replacing it with a vortex system composed of a lifting line vortex and a pair of trailing vortices. Similarly, a solid body may be represented by a source-sink doublet system and a wake may be represented by a source, as shown in Figures 1.5a and 1.5b respectively. The respective strengths of those systems are a function of the circulation around the object and can be related with the drag and lift or with the induced velocities [1], [29]. Therefore, an entire configuration or component may be simulated by those means to almost any degree of accuracy desired, depending on the complexity of calculations that can be tolerated. Potential flow analysis assumes flow of infinite extent (far-field analysis), so in order to appropriately resemble the walls of the wind tunnel the addition of an image system that produces a zero streamline matching between the solid boundaries is employed. This is presented in Figure 1.6a, where the image systems are established in order to match for the top and the bottom wall of a closed test section of the wind tunnel. For an open (free) surface, the circulation of the corresponding image imposed is of the opposite direction than in closed walls in order to obtain a zero pressure gradient at that boundary as shown in Figure 1.6b. After the image system is established, its effect on the model is the same as that of the boundary it represents and the far-field analysis is satisfied as long as the image pairs are added up to infinity in both directions. In practice, a finite number of image pairs is added which introduces a certain error but makes the calculation faster. This error can vary from significant values ($O(1)\%$), to infinitesimally small ones. In this Thesis, the technique of the method of images is applied by more than one correction approaches, further highlighting its importance.

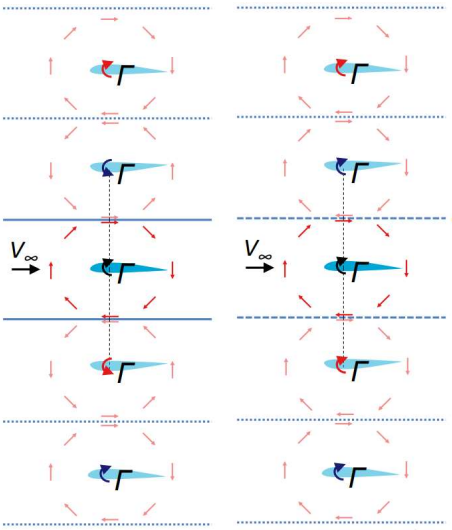


(a) Representation of a flow over a cylinder [1].



(b) Modelling the wake behind a body by a source [16].

Figure 1.5: Potential Flow Modelling Techniques.



(a) Closed wall test section. **(b)** Open-jet test section.

Figure 1.6: Method of images for an airfoil wind tunnel test [84].

Another wall correction method which also uses the method of images to determine wall interference is the Heyson method. This method was developed by H. Heyson during the 1960's for the NASA and it is dedicated in calculating lift interference. It was originally developed for single-rotor helicopter testing but was later extended for more general V/STOL configurations by incorporating lift interference corrections for the modelling of wings, propellers and rotors. DNW has made significant steps in developing an in-house HWC (Heysons Wall Correction) code based on the work of Heyson as reported mainly in [33]. This started by the early work of Philipsen [63], while it was later modified for on-line use and to handle cases of negative lift (wake directed upwards) Broersma [9]. Further work was made by Voorst [91] in order to appropriately quantify lift interference effects due to the propeller's normal force, while Jovetic [46] expanded the HWC code in order to include the effects of wing dihedral on lift interference. The code was verified with results from the original code given in [39] and for all the extensions described above. For more information regarding the capabilities of the HWC code, its restructuring and adaptations the reader is referred to [64]. In a general overview, the HWC code requires as an input the incidence angle and the measured lift and drag of every component. In case forces for some components are not measured, an estimation for the lift and drag is needed. The forces are then utilized in order to adapt the strengths of the vertical and horizontal doublets which represent the model's slipstream. Finally, the image mirroring technique is employed in order to satisfy the flow's boundary conditions resulting to the determination of lift interference. In section 2.3, the basic theory of the Heyson Method is presented for propellers and rotors.

B. Boundary Measurement Methods

Measuring the flow conditions at the boundaries has a valuable effect for wind tunnel testing. This is particularly efficient in the case of solid wall test sections. Boundary measurement methods make use of those measurements and deduct the wall interference induced by the presence of the boundaries. There are several different methods depending on the number of parameters that need to be determined (measured) and whether or not a model representation is needed. The boundary conditions in the measurement volume inside the test section also play a significant role and one can imagine that closed

wall test sections are more suited for the application of such methods since, measurements are performed relatively easy and the location of the boundaries is distinct. Irrespective to the method chosen, they all rely on the same theoretical background, which is the representation of the flow inside the wind tunnel and/or the free-air flow as a perturbation velocity potential. General overview regarding these methods and their application can be found in Ashill [3], Ewald [16], and Mokry et al. [58]. Appendix B gives a brief overview regarding those methods, while section 2.4 presents a more in-depth analysis of the ones used in the current research.

1.3.2. Flow Breakdown

As mentioned in the beginning of this Chapter, the testing of V/STOL models in wind tunnels can bring up several problems different from those encountered in conventional aircraft testing, where the testing techniques are more mature. This dissimilarity originates from the different ways that lift is obtained. Conventional aircrafts usually obtain moderate lift coefficients from their wings that slightly deflect the flow downwards. Their operating conditions are characterized by high translational speeds, at which this small downwash is sufficient to provide them lift and sustain flight. This nature makes them incapable of achieving vertical take-off or landing. On the other hand, V/STOL models like helicopters, are able of achieving vertical short take-off and landing due to their high values of lift coefficients. This happens because they are designed to deflect the flow at high downwash angles (e.g. hover mode). In vertical flight mode, the rotor must be able to supply a thrust force to support the helicopter weight. Additionally, the helicopter or other V/STOL vehicle, must also be capable of translational flight, which means that it must be able to produce a propulsive force to oppose the fuselage drag and rotor drag in forward flight, resulting in smaller downwash angles. For low speeds at least, this propulsive force is obtained from the rotor, by tilting the thrust vector forward. In a fixed-wing aircraft, the lift, propulsion, and control forces are provided by largely separate aerodynamic surfaces. In the helicopter, all three are provided by the rotor [45]. This downwash angle variation is what makes such configurations unique but is also the cause for the differences observed in wind tunnel testing. For a long time, it is known that for a given rotor in a certain wind tunnel, there is a maximum limit of deflection of the flow downwards. That is because for relatively high deflections, the rotor's induced flow may disrupt the continuous wind tunnel flow resulting in situations which do not resemble actual flight, but rather represent a flow similar to recirculation [66]. This phenomenon is called flow breakdown, it is mostly encountered in low speed regimes and when it occurs, the measured coefficients cannot be further corrected to represent actual flight conditions. It is important to note that flow breakdown can occur for low speed wind tunnel testing of conventional configurations such as wings at high angles of attack, but it is less possible due to the relatively small lift coefficients and unpowered nature of such models. According to Ewald [16], there are several ways to delay flow breakdown in order to extend the effective measurement range. Ground blowing seems to be the most effective way, while a moving ground can also contribute in removing the ground vortex, or at least controlling it.

Closed Test Section Investigations

There are several parameters which might affect flow breakdown such as the size of the rotor, the position of the rotor inside the test section, the size of the wind tunnel test section, the type of the test section, the angle at which the wake is deflected (downwash angle or wake skew angle), the amount of lift obtained (or thrust), etc. From the mid 1960's until the early 1980's there was a high interest in defining the parameters which affect flow breakdown and also defining the limits for a given wind tunnel and rotor. It is no coincidence that, this interest in flow breakdown research coincided with frequent rotor and V/STOL testing during that period. Some of the earliest investigations were made by Rae and others in University of Washington who investigated the limiting conditions for rotor testing in a wind tunnel with different closed test sections. During this test campaign Rae Jr. [66], [67], tested two different rotors at three different rectangular closed test sections $[(3 \times 4.5), (4 \times 6), (8 \times 12)]\text{ft}^2$ and different thrust values. For a given thrust, the angle of attack was varied by varying the rotor's shaft

angle and the advance ratio was also varied by changing the tunnel speed while holding a constant rotor rpm. The initial realization of flow breakdown was identified as the point of low advance ratio, at which the measured lift was the same irrespective of the wind tunnel geometry as shown in Figure 1.7. This observation was later verified by tuft studies and static pressure measurements on the wall under the rotor. The reduction of the advance ratio caused a region of reversed flow near the tunnel's bottom wall, which was moving forward on the advancing side of the rotor disk up to 1.5 or 2 times the rotor's diameter. According to that identification procedure, he identified flow breakdown for different solid blockage ratios (A_M/A_{WT}) and different test section width to height ratio (W/H) as a function of the momentum downwash angle which is the complementary angle of the wake skew angle as defined in equation (35). The forementioned limits can be seen in Figure 1.8. Furthermore, he indicated that for a given rotor, at three different thrust conditions, the flow breakdown occurred at different tip speed ratios, but at the same wake skew angle. Therefore, according to the author's view the wake skew angle was sufficient to determine the flow breakdown for those tests. He also referred that another investigation in Langley Research Center in a 3/4 open-jet test section had a similar response but at slightly larger downwash angles (or smaller skew angles), indicating that the latter test section is more tolerant to flow breakdown. Finally, the author concluded that there are two distinct types of flow breakdown, which both result into a rapid decrease of lift.

1. The first type occurs when the rotor's wake moves across the floor laterally and then, it also impinges on the upper wall of the wind tunnel, implying a high rotor diameter with respect to the width of the tunnel ($D/W \to 1$).
2. The second type occurs when the wake impinges on the tunnel floor and moves upstream under the model creating a ground vortex propagating and interfering with the rotor induced flow-field.

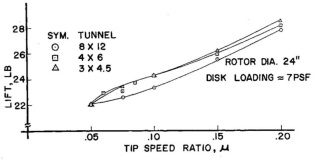
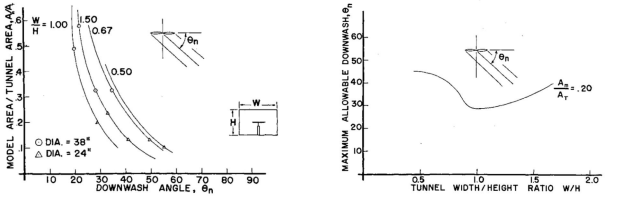


Figure 1.7: Variation of rotor's lift for different wind tunnel test sections [67].



(a) Flow breakdown limits as a function of the blockage ratio, the downwash angle and tunnel's width to height ratio, for two different rotors.

(b) Flow breakdown limits as a function of the downwash angle and tunnel's width to height ratio, for a given rotor.

Figure 1.8: Flow breakdown limits defined by [67].

Approximately, at the same period of time, Tyler et al. [88] performed experimental investigations in order to define the flow breakdown limits of inclined jets. By using tufts and pressure taps, they introduced a new term which describes the situation when the model's wake has penetrated the boundary

layer of the bottom wall of the wind tunnel in order to weakly stagnate on the floor. This region is characterized by unsteadiness and intermittent periods of horseshoe vortices formation upstream the stagnation. This region was named the incipient stagnation, at which flow breakdown would occur with a further decrease in wind tunnel speed. A typical flow breakdown along with two stable stagnation points is depicted in Figure 1.9a. The incipient stagnation as defined by the authors is seen in Figure 1.9c and it is determined such that the distance between the two stagnation points x_F, x_B tends to zero. They also showed that over a jet inclination ranging from $-5°$ to $20°$, at incipient stagnation conditions, the normal thrust coefficient (or lift coefficient) is maintained at a constant value irrespective of the number of jets and their configuration. This situation is shown in Figure 1.10.

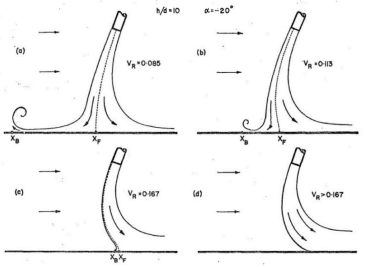


Figure 1.9: Jet impingement at tunnel wall during flow breakdown and at higher velocity increments respectively (from left to right) [88].

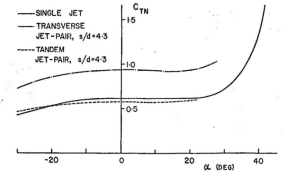
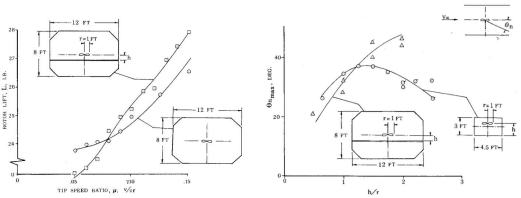


Figure 1.10: Normal thrust force coefficient during the incipient stagnation region [88].

Flow breakdown investigations continued during the late 1970's by Shindo et al. [81], who investigated the effect of a vertically off-centered model. They introduced a new criterion for flow breakdown that identifies the critical advance ratio (μ_{crit}), under which data are not correctable anymore. This was identified, as the point where the lift curve diverges from the expected behavior with decreasing advance ratio, as compared to a baseline measurement which resembles the free-air case in the larger test section ($(8 \times 12)\text{ft}^2$) as shown in Figure 1.11a. The maximum allowable momentum downwash angle $\theta_{n,max}$ was calculated for every critical advance ratio with varying the vertical position of the rotor h, by adjusting the ground floor position in order to obtain the testing limits as a function of its distance. They concluded that the optimum vertical position is located on the centerline, a reasonable realization, since in any other position the flow is impaired by the presence of either the bottom or top wall. The latter observation is justified for $(3 \times 4.5)\text{ft}^2$ wind tunnel tests, where the $\theta_{n,max}$ curve has a maximum at around the half-height of the wind tunnel, but it is not verified by the $(8 \times 12)\text{ft}^2$ tests since the maximum height range achieved in those was lower than the tunnel's half-height which resulted in an increasing trend for the positions tested. The above observations are presented in Figure 1.11b.

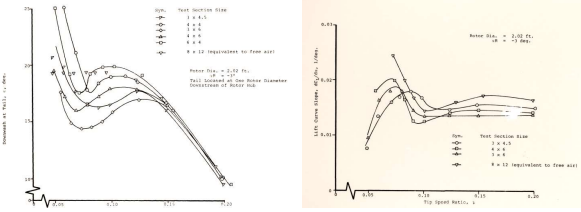


(a) Critical advance ratio estimation ($\mu_{crit} \approx 0.1$) from the lift advance ratio curve.

(b) Flow breakdown limits as a function of the downwash angle $\theta_{n,max}$ and the model's vertically off-center position h.

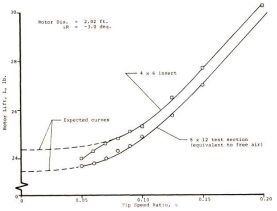
Figure 1.11: Flow breakdown limits defined by [81].

The same researchers in Rae Jr. et al. [69], highlighted the importance of the rotor diameter to the wind tunnel width ratio (D/W) rather than the tunnel's width-to-height ratio (W/H) mostly discussed during their previous investigations described earlier. During low speed testing of a rotor-tail wing configuration, they introduced another criterion which is based on the uncorrected downwash angle at the tail wing, which states that flow breakdown is defined from the point at which this angle starts to surge at extremely high values as shown in Figure 1.12a. They also defined an additional criterion based on the rotor's lift curve slope ($dc_L/d\alpha$) as shown in Figure 1.12b and they compared it with the criterion based on the expected behavior of the rotor's lift with respect to the "free" conditions (or the large test section reference conditions approximating free air) which was discussed previously and it is shown in Figure 1.12c.



(a) Criterion based on the uncorrected downwash angle at the tail wing.

(b) Criterion based on the rotor's lift curve slope ($dc_L/d\alpha$).



(c) Criterion based on the expected behavior of the rotor's lift with respect to the large test section reference conditions.

Figure 1.12: Flow breakdown limits defined by [69].

The above results are summarized in Figure 1.13, from which is clear that when assessing flow breakdown with respect to the momentum downwash angle at the tail, the limits are more restrictive compared to the criteria based on the rotor measurements. In other words, the tail's aerodynamic coefficients will

be affected earlier than the rotor's respective coefficients due to flow breakdown. This effect is also a function of the tail's vertical distance from the rotor [68]. Furthermore, the criterion based on the rotor's lift curve slope ($dc_L/d\alpha$) is more restrictive compared to the criterion based on the rotor's lift behavior with respect to a large wind tunnel test section measurements.

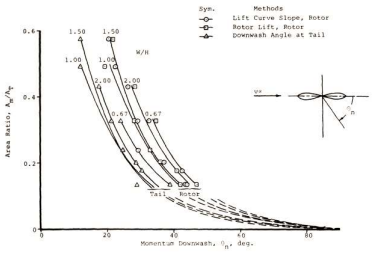


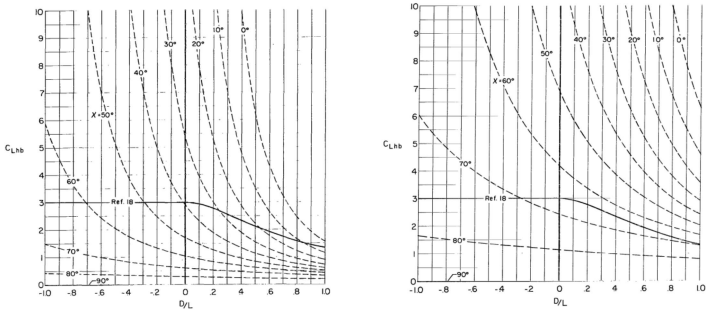
Figure 1.13: Flow breakdown limits based on the three criteria defined by [88].

Other researchers like South [85] have tried to incorporate the limits of V/STOL wind tunnel testing by means of a lift coefficient c_{Lhb} based on the the tunnel cross-sectional area below and within the wing span as a function of total lift and drag measured forces. This is shown in equation (1). This criterion was based on experimental observations of flow reversal on the floor of a closed wind tunnel for jet-flap models. It does not describe the limits where the results become "uncorrectable" to actual flight conditions, but rather the coming onset of possible flow breakdown in case of more severe conditions. H. Heyson [38], in a rather extensive report compares his theoretical model with the limits obtained by South [85]. He concludes that, the effect of the wake skew angle as introduced by him, has a rather important effect in defining the wind tunnel limits for a given lifting system and it cannot be ignored. Therefore, he classifies South's limits to skew angles representing axial flight or propeller mode ($\chi_{eff} \rightarrow 90°$), as the nature of the experiments he performed. This is shown in Figure 1.14, where those limiting conditions according to Heyson's model are compared with that of the South's criterion. In all cases, the limit is the indicated line above which flow breakdown, in case of [38], or impingement on the floor in the case of [85], occurs. Indeed, the effect of the wake skew angle, or else the direction at which the wake is distorted for a given wind tunnel and rotor speed has a significant effect and it cannot be ignored. The relation derived in [38], which is used for the comparison in Figure 1.14 is given by equation (2).

$$c_{Lhb} = \begin{cases} 3 & -1 \leq D_D/L \leq 0 \\ \frac{3}{\sqrt{1+4(D_D/L)^2}} & 0 < D_D/L \leq 0.6 \end{cases} \tag{1}$$

$$c_{Lhb} = \frac{\pi(D/h)}{(tan(\chi) + (D_D/L))^2 cos(\chi)} \tag{2}$$

In a further attempt to correlate wind tunnel limits with respect to flow breakdown Heyson [40], correlated the data of Rae Jr. [67], together with a few point measurements from references Grunwald [28] and Heyson et al. [41], in a form that could be used to provide an indication of the upper limit of V/STOL testing. This correlation is presented in Figure 1.15, where the vertical axis is the distance behind the model at which the theoretically straight wake impinges on the floor non-dimensionalized by the total span of the lifting system and the abscissa is either the ratio of height-to-width of the wind tunnel or the opposite (whichever is greater than 1). The effect of the width-to-height ratio of the wind tunnel is directly captured and the observations that the square wind tunnel, particularly when it has corner fillets, is the least desirable. Since the forementioned data obtained for this graph, defined flow breakdown as the point of lateral recirculation inside a closed test section, from that point of view, the



(a) Rotor diameter-to-height above the floor ratio $D/h = 0.5$.

(b) Rotor diameter-to-height above the floor ratio $D/h = 2$.

Figure 1.14: Flow breakdown criteria comparison between [38] (dashed lines) and [85] (solid line). Taken from [38].

most desirable geometry would be one with "rectangularities" on the order of 1.25 to 1.5. The above correlation was made possible by computing the impingement distance directly from the geometric momentum skew angle as shown in Figure 2.8b, which leads to the following equation. Unfortunately, the above results correspond to a short range of incidence angles, therefore the applicability range of equation (3) needs to be considered, in case a direct comparison is made.

$$(\frac{\chi_f}{D}) = \frac{h}{D} tan(\chi) = \frac{tan(\chi)}{2\sigma\gamma\zeta} \tag{3}$$

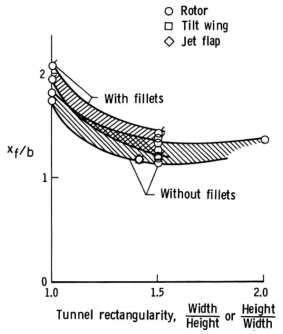
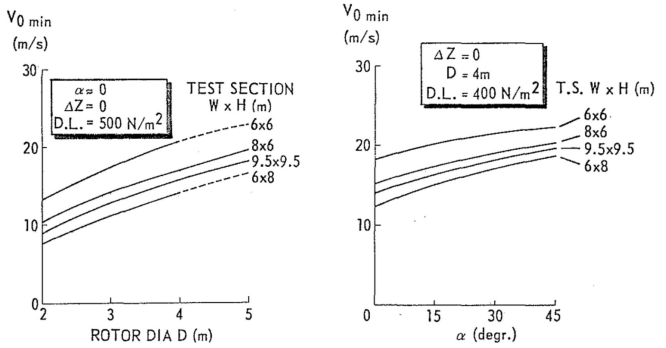


Figure 1.15: V/STOL testing limits as a function of the wake impingement distance and the tunnel's geometry [40].

Preliminary research with respect to flow breakdown has also been made by DNW Seidel et al. [79], where the Heyson's empirical breakdown limits are evaluated for the DNW tunnel dimensions. HWC code was then used in order to investigate the minimum allowable free-stream speed above which the data can be corrected. This is shown in Figure 1.16, for a fixed incidence angle and for a fixed rotor diameter, respectively. It can be observed that the limits become more restrictive with the increase of

both forementioned parameters. However, since equation (3) is applicable for small angles of attack $[-7°, 7°]$, the increasing trend of the free-stream speed with the angle of attack shown in Figure 1.16b is subject of doubt for large angles of attack. Moreover, Figure 1.16 points out something remarkable which is also discussed by Rae Jr. [67]. The test section which has a larger height-to-width ratio seems more suitable than the larger square test section of $9.5 \times 9.5\text{m}^2$. This is of course a limitation of the current assessment procedure, which may lead to misinterpretations, since the smaller test section of $\gamma = 0.75$ is indeed more tolerant to flow impingement on the walls leading to recirculation, but on the other side the corrections that would be needed in order to eliminate wall interference would be very high, leading to large errors, or in the end uncorrectable data. This is presented in Figure 1.17, where average corrections for lift interference at flow breakdown onset are presented. It is clear that the forementioned test section leads to large and non-uniform corrections whose reliability is questionable. Thus, it is not only the onset of flow breakdown which could lead to unreliable data, but the magnitude and non-uniformity of the corrections as well. It is known that, the larger the magnitude of the corrections, the larger is the error in the estimation of the aerodynamic characteristics and that in general the corrections should be as low as possible. This is another aspect which should be considered even before the onset of flow breakdown.



(a) Variation with rotor diameter.

(b) Variation with incidence angle.

Figure 1.16: Minimum allowable wind speed at flow breakdown onset [79].

In an effort to investigate the testing limits of the Ames 80×120 Foot Wind Tunnel, Shinoda [83] measured the pressure distribution on all four walls of the wind tunnel. It was concluded that the side and floor pressures were affected by the presence of the rotor only in the low speed regime and the authors were able to identify flow breakdown, for the tested rotor (four-bladed S-76), by the strong pressure signature on the floor and dynamic rotor loads and blade flapping motion at or below $\mu = 0.04$. Finally, Biava et al. [8], proposed a method based on a Reynolds-averaged NavierStokes solver, coupled with an actuator disk representation for the rotor, in which they indicated the limiting range of Politecnico di Milano large wind tunnel for a given rotor tested and compared them with data available in literature. A perfect agreement was not achieved, but the results indicated by Harris [31] were close enough to the forementioned limiting conditions as shown in Figure 1.18.

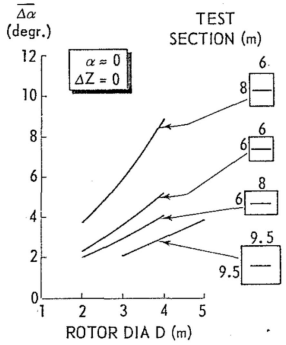


Figure 1.17: Average angle of attack correction for flow breakdown onset conditions [79].

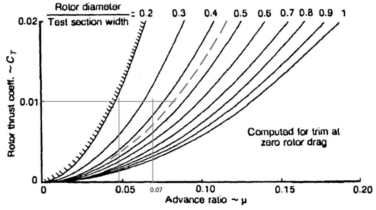


Figure 1.18: Comparison of flow breakdown limits between Biava et al. [8] (red) and Harris [31] (dashed).

Different Test Section Configurations

According to the above observations, it is clear that both flow breakdown and the magnitude of the corrections could possibly lead to useless wind tunnel data. The use of mixed boundary test sections can aid in alleviating wall interference effects. This is particularly discussed by Seidel et al. [79] and Heyson et al. [41], but unfortunately, hardly any effort has been made in order to quantify those effects for open jet or slotted test section configurations. As previously discussed, Biava et al. [7] proposed a trim-to-torque method, based on CFD results instead of flight tests. They identified the limiting conditions for the open jet (4×3.8) test section of Politecnico di Milano which corresponded to conditions where the rotor wake either escapes almost completely the wind tunnel return circuit or strongly impacts on the lower deflector inducing a strong wall effect. As with flow breakdown identification, the limits corresponding to the open and the closed test sections are not directly comparable, as presented by the authors and therefore, it still remains unclear whether the open test section is more or less prone to the flow breakdown phenomenon.

In-Ground-Effect

All of the breakdown limits discussed above are for OGE wind tunnel testing. This is expected since, correcting wind tunnel data for free (OGE) flight is the most common practice. However, when simulating a flow in-ground-effect, the corrections on the aerodynamic coefficients are not that severe since the floor of the wind tunnel is considered as a natural border and therefore, no corrections are needed for it. Moreover, one would expect that flow breakdown, if any, for IGE testing is achieved with far

more severe conditions corresponding to minimal advance ratios, or very high thrust conditions. That is discussed by Heyson [40], but no further investigations have been made at least according to the author's knowledge.

Overview

Table 1.1, presents the most relevant criteria and observations discussed above, regarding flow breakdown identification. It is evident that efforts to understand and relate flow breakdown are limited and mostly relied upon old research, which mainly occurred during the 1960's and 1970's. This by any sense does not mean that wind tunnel testing limits are not important, or that this phenomenon is fully understood. It is profound that, most studies relied upon rotor testing in closed test sections, but hardly any progress has been made to understand and quantify those limits in different test sections, for different testing conditions like (IGE), or for complete V/STOL configurations. With respect to the review presented here, it is wise to point out that the limiting conditions may be altered significantly if the lift is concentrated in several discrete and separate distributed points.

Table 1.1: Flow breakdown criteria and empirical observations available in literature.

Flow Breakdown Criteria (Low Advance Ratio)	**Closed TS**	**Open-Jet TS**	**OGE**	**IGE**
Collapsing of measured quantities (L, T, P) irrespective of the TS size or type	✓	-	✓	-
Rapid decrease of lift (lift curve diverges when compared with a larger TS or free-flight result)	✓	-	✓	-
Rapid increase of momentum angle, after a local minimum	✓	-	✓	-
Rapid decrease of the lift curve slope $(c_L/d\alpha)$, after a local maximum	✓	-	✓	-
South's Criterion (equation (1))	✓	-	✓	-
Heyson's Criterion (equation (3), Figure 1.14)	✓	-	✓	-
Harris' Criterion (Figure 1.18)	✓	-	✓	-
Empirical Observations (Low Advance Ratio)	**Closed TS**	**Open-Jet TS**	**OGE**	**IGE**
Strong pressure signature on the bottom wall	✓	-	✓	-
Strong pressure signature on the collector "lip"	-	✓	✓	-
Wake moving upstream $(1.5 \sim 2)D$ on the advancing side of the rotor blade (tuft study)	✓	-	✓	-
Non-linearity & high magnitude of the corrections	✓	-	✓	-

1.4. Rotor Wall Interference Investigations

In this subsection, an overview of rotor and propeller wind tunnel tests, with emphasis on wall correction methods and data comparison with different wind tunnel test sections is presented. Wall correction methods necessity is also going to be investigated by means of the results available in the literature. To begin with, it is important to understand the two different operating conditions of a rotor. The operating conditions of a rotor can vary a lot depending on the angle of attack. Close to 0 degrees incidence angles (axial propeller mode), the thrust generally decreases with airspeed, or else, with increasing advance ratio, whereas the opposite trend is observed at angles close to 90 degrees (hover mode). This is known for almost a century, while in the latter condition the rotor is usually treated like a wing. In the current thesis, the words rotor and propeller are used interchangeably based on the operating condition. Researchers Rubin et al. [72], presented that transition from propeller mode to hover mode and were able to distinguish that there is a specific angle at which the rotor's thrust is insensitive to the changes with respect to air speed (advance ratio), or more specifically, $\frac{\partial c_T}{\partial \mu} \approx 0$. That angle was named by the authors angle of thrust behavioral inversion AoA_{inv} and signals the transition from axial-dominance to wing-like behavior for the rotor. According to them, the AoA_{inv} is occurring at lower angles for higher pitch propellers, but also that fixed pitch propellers with low blade pitch angles mostly inverse from propeller to wing-like behavior at angles mostly higher or equal to 60°. This aspect is important when assessing wall interference on a rotor at different angles of attack. Above the thrust behavioral inversion AoA_{inv}, lift interference is expected to be dominant, while for smaller

incidence angles, blockage is expected to dominate. In the following part a distinction is made based on the operating condition of the rotor, namely, lifting rotor (wing-like behavior) or propeller.

1.4.1. Lifting Rotors

An interesting investigation of wall interference effects has already been discussed and was made by Shinoda et.al [82] at the Ames Research Center. A full-scale four-bladed S-76 helicopter rotor was tested in the NASA Ames 80×120-Foot Wind Tunnel. The resulting performance data were compared with the calculations from a comprehensive rotorcraft analytical solver, CAMRADIJ/A and with results already obtained for the same rotor in the 40×80 test section. Comparisons with the solver exhibited good correlations, since there was a consistent overestimation of the solver's predicted power coefficients. However, according to the authors, for advance ratios lower than 0.1 the solver's predictions strongly diverged from the measured ones. Regarding the rotor tests, the dataset for the 40×80 test section was limited and no sufficient comparison could be made. There are some parts of the uncorrected dataset which are in agreement with the uncorrected results for the 80×120 test section, although a few are not and their agreement turns better when corrected. Moreover, the Glauert classical correction was used which is not suitable for capturing the large wake deflections occurred close to hovering conditions. This effect could also have added some minor data discrepancy. Overall, the data of the smaller test section did not cover the lower speed range ($\mu > 0.1$) and their limited database is insufficient for reaching the conclusion that wall corrections are not necessary even in the case of the small wind tunnel ($\alpha = 0.47, W/D = 0.55$), as the authors originally imply through the data comparison between both test sections.

A further investigation in the same facility (40×80 test section) was made by Goulding et al. [27], where the above rotor (S-76) was tested again, along with a 28-foot diameter four-bladed experimental test-purpose-built rotor ($\alpha = 0.2, W/D = 0.35$). The wind tunnel free-stream velocity ranged approximately from 30 to 50 m/s. A careful assessment of both flow angularity corrections and blockage corrections is made. Regarding the former, a comparison is made between the Heyson method and the classical (Glauert) corrections for both rotors. The trend presented in the angle correction - lift graph follows a linear relation, in accordance with the linear dependence exhibited for the wake skew angle. Heyson method angularity corrections are greater than the classical for both rotors which is not in accordance with observations of Rae Jr. et al. [69] and Langer et al. [51], although reported for much lower advance ratios. An interesting point is the regime at which those corrections exhibit this linear relation. This combined with the fact that the corrections in the angle of attack are relatively small ($0°$- $2°$) led to the realization that the current tests are not performed in the low speed-high thrust regime. This can be also observed by the relatively high values of the skew angle reported by the authors for both rotors. Assuming the following relation to be valid for the presented data (in Goulding et al. [27]) and an almost zero incidence angle, the regime in terms of the advance ratio can be estimated for both rotor tests. Given the above assumption, a conservative estimate about the minimum advance ratio corresponds to $\mu_{min} \approx 0.42$ for the S-76 and $\mu_{min} \approx 0.38$ for the smaller rotor. This explains the observations made above, regarding the linearity and the magnitude of the corrections, because the inertia of the main flow is still comparable to that of the induced wake.

$$(\frac{L}{q}) = c_L A \sim \frac{c_T}{\mu^2} A \tag{4}$$

The authors comment on the fact that, despite the smaller rotor induces more downwash (smaller skew angle) for a given lift, the flow angularity corrections lie in between those for the S-76 rotor, following an almost parallel slope. Since the wake skew angle is adequately connected with lift interference, they reported that trend as problematic. Blockage correction is also investigated by means of the Heyson method and a wall signature method developed by the NFAC. The latter is able to estimate the overall net-blockage effect of the wind tunnel, since it is based on boundary measurements. The predicted

blockage corrections are also small for both methods (rotor and net-blockage) and the trend between the two rotors is properly captured. However, it is observed that for the rotor the dynamic pressure corrections exhibit a non-linear absolute increase as the lift-to-dynamic pressure ratio increases (advance ratio decreases). The same trend is observed for the test rig solid and wake blockage, represented as the difference between the wall signature method and the Heyson's method estimated blockages. Therefore, it is expected that in the low speed - high thrust regime, blockage corrections for both the rotor and the test stand, would also become significant as is commented by the authors of [27].

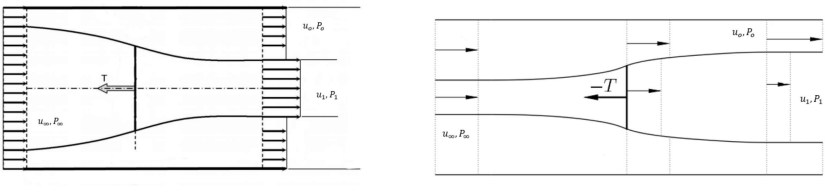
Another rotor test performed by Kolaei et al. [48] at the University of Toronto, created an extensive database of thrust and power measurements at various inflow angles ranging from 0° to 90°. The main rotor tested had a diameter of 0.4 meters leading to a blockage area ratio of 0.16 and a diameter-to-width ratio of 0.45. The data lie on the low-speed - high-thrust regime, corresponding to advance ratios of $(0.03 - 0.3)$. This was made possible by varying the tunnel speed and the rpm of the motor. In order to achieve such conditions the wind tunnel speed was set to very low values, ranging from (2-5) m/s. They detected that thrust had a slight dependency on the Reynolds number, while power was mostly unaffected. This was determined for both static and transitional conditions by varying the rpm of the motor, while keeping the advance ratio constant. Classical wall interference corrections were applied for solid blockage, but also corrections for the measured torque, thrust and roll moment for the effect of the base loads registered by the load cells of the test stand without the rotor. Furthermore Heyson's method was used for flow angularity corrections. Those were insignificant for incidence angles corresponding to propeller mode ($AoA \rightarrow 0°$) at any advance ratio, but also at any incidence angle for moderate to high advance ratios in general. The authors reported that for very low advance ratios ($\mu_{min} \leq 0.1$) both thrust and power measurements collapsed with each other and were independent of the incidence angle. They implied that only by correcting the angle of attack it is possible to properly correlate those measurements. By observing the flow angularity corrections at that range, they are between 5 and 15 degrees. The uncertainties associated with such large corrections are of the order of the angle of attack. Therefore, such data may not be able to get corrected in order to represent free-air results. Additionally, when all the measurements collapse with each other, irrespective of the angle of attack, then flow breakdown most likely takes place. It is hypothesized by the current author that, flow breakdown had already occurred, which then led to such large angle corrections.

In a further investigation of wall interference effects on lifting bodies of revolution, Langer et al. [51] correlated thrust and power data obtained from different tests namely, a 40% scale model Bo105 tested in five different wind tunnel test sections: 1) 6×6m closed, 2)8×6m closed, 3) 8×6m 12% open slots, 4) 9.5×9.5m closed and 5) the 8×6m open jet, in the DNW LLF, a full-scale test in the NASA Ames 40 × 80-Foot Wind Tunnel and a DLR flight test program. They identified flow breakdown in the low-speed - high-thrust regime, as the collapsing of the power measurements irrespective to the test section configuration. At advance ratios close to 0.1 the power coefficients deviated with respect to each test section, as expected. Lift interference corrections were assesed by the use of the classical (Glauert) method and Brook's code, a method similar to Heyson's method with the difference that it is based on vortical rather than dipole wake distribution modeling. By comparing the two correction methods they concluded that the classical corrections predict larger angle corrections than the Brooks method. These differences seemed to magnify at higher thrust levels. Moreover, at low advance ratios the flow angularity corrections had their biggest deviation with respect to each other, while their predictions were becoming identical at higher advance ratios. Overall, a good correlation of the data from the different test sections was achieved.

1.4.2. Propellers

When the rotor is operating in axial dominance conditions, flow angularity corrections are negligible, whereas blockage corrections may become significant. As it has already been discussed, blockage mainly occurs due to the space occupied by the model (solid blockage) and due to its wake or slipstream (wake blockage). For such configurations, the solid blockage is usually neglected because the propeller is

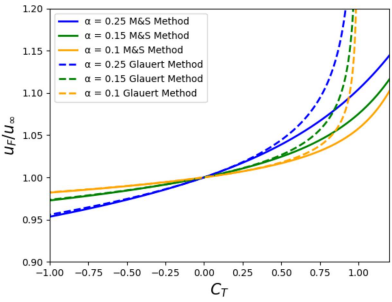
not acting as a bluff-body and thus, slipstream/wake blockage is expected to be dominant. There are two different treatments for propellers and wind turbines. The difference lies in the fact that, in the propeller state, power is added to the flow, thus u_∞ and C_T act in the same direction, whereas the opposite happens in wind turbines. This effect can be seen in Figure 1.19, where the forementioned difference in thrust direction can be interpreted as wake contraction or expansion.



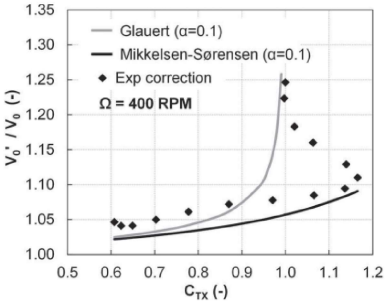
(a) Propeller. **(b)** Wind turbine [57].

Figure 1.19: Wind tunnel constraint flow along a closed wall test section.

Glauert [29] was the first to demonstrate the effects of blockage on a closed wall wind tunnel with the use of the actuator disk theory to model the propeller and one dimensional axial momentum theory. His representation had a singularity at $C_T = 1$. Then, other researchers like Mikkelsen et al. [57], based on similar assumptions derived analytical expressions in which, they managed to get rid of the singularity problem. The differences between the two approaches for a closed test section, can be seen in Figure 1.20a, by means of the ratio of equivalent free air-to-tunnel velocity u_F/u_∞ and the thrust coefficient C_T. The same researchers extended their investigations in order to determine blockage in open-jet configurations [80]. Their research was mostly based in wind turbine blockage, but since the governing equations are the same, their results can also be extended to propeller blockage. In the case of the open test section and by the use of CFD, they proposed a formula to model the specific axial momentum flux exiting the control volume through the free boundaries and showed that for propellers this amount is negligible and not influenced by the blockage ratio, while for wind turbines it can rapidly increase. Dossena et al. [13], compared both methods described above with a proposed experimental correction which for a given thrust, represented the ratio of the velocities corresponding to the open and the closed test section respectively. This is shown in Figure 1.20b. The differences between the different approaches are significant, even for small blockage area ratios and especially for higher thrust values. Furthermore, it is not justified that this experimental blockage correction proposed by [13] is in analogy with the unbounded to bounded flow ratio, since strictly speaking, the open jet wind tunnel cannot be fully considered as a free-air condition due to the presence of the shear layers interfering with the flow field structure, but it still may provide a reasonable estimation. In a similar manner, Werle [93] and [92] proposed blockage corrections for wind turbines and propellers respectively. According to his observations, there seems to be a power law dependency between blockage corrections and blockage area ratio for the case of a wind turbine while the same corrections seem to be negligible and insensitive to the blockage area ratio occupied by a propeller. All of the above observations were mainly derived for blockage area ratios up to 25%.



(a) Theoretical comparison between Glauert's and Sørensen-Mikkelsen blockage corrections at different area blockage ratios.



(b) Comparison between Glauert's, Sørensen-Mikkelsen and experimental blockage corrections [13].

Figure 1.20: Comparisons of different blockage estimations.

1.4.3. PIV Investigations

In recent years, PIV measurements have become more popular due to their rapid development and non-intrusive nature. There is an extensive literature with respect to PIV investigations of wind tunnel flows along rotors operating at different conditions. Those investigations mainly concern the aerodynamic characterization of the flow structures around the rotor (e.g. tip-vortex, ground-vortex), or the interaction between different model components (e.g.rotor-fuselage-tail-wing interactions). Up to the authors knowledge, only limited research has made use of the PIV capabilities to deduct conclusions regarding wall interference in subsonic wind tunnels. The most relevant will be presented in the following part.

Researchers Dossena et al. [13], performed 2D PIV measurements on the wake of a wind turbine in closed and open test sections for three conditions corresponding to advance ratios of 0.66, 0.4 and 0.28 respectively. They used their proposed experimental blockage correction discussed earlier to adjust the velocity in the closed test section and achieve comparable conditions between the two test sections. According to their observations the time averaged and instantaneous wake properties like velocity and turbulent intensity were weakly affected by the presence of the walls, further justifying the correction method. Moreover, they observed that at the highest advance ratio, the wake was strongly asymmetric, especially in the tip region compared to lower wind tunnel speeds. This was attributed due to the unsteady nature of the tip vortices appearing on the advancing side (upwind part of revolutions) of the rotor blades.

Another investigation with respect to 2D lift interference corrections in an open jet wind tunnel, was done by Faleiros et al. [17]. They performed 2D PIV measurements in the wake of a 2D airfoil and by the use of the integral momentum conservation and mass balance principles they were able to determine the effective angle of attack, lift and drag of the airfoil. Their results exhibited bigger deviations with respect to closed test section measurements, for cases with high angles of attack. That was attributed as a limitation of the open jet wind tunnels, as high incidence angles correspond to higher deflections of the jet, which then results to situations where part of the jet is directed outside the collector, as also discussed by Biava et al. [7]. Another reason could be that such big corrections (in this case 6.68 degrees) introduce large errors in the estimation of the aerodynamic coefficients. The forementioned test was performed on a 2D model airfoil, but since lifting rotors resemble wing behavior, it is presented due to the limited investigations available in the field of rotor wall interference in open jet wind tunnels.

1.5. Tomographic PTV

PTV has been successfully applied for many decades (Maas et al. [54], Malik et al. [55]) by using epipolar geometry in order to detect particle pairs and find its location by solving the triangulation problem. Its application was restricted to low seeding densities due to the occurrence of ghost particles (Elsinga et al. [15]) and the under-determined nature of the triangulation problem. The Iterative Particle Reconstruction (IPR) method (Wieneke [96]), successively managed to increase the particle image density due to its highly efficient procedure of solving the triangulation problem iteratively. This method takes advantage of the gradient information by slightly shaking the position of each particle in the volume and finally, predicting its position based on the local residual minimization. The IPR algorithm is shown in Figure 1.21. However, at high seeding densities, the presence of ghost particles becomes dominant, and may heavily influence the velocity estimation and its gradients (Elsinga et al. [15]). The Shake-The-Box (STB) method introduced by Schanz et al. [77] was designed such that it includes as much temporal and spatial information as possible resulting in a 4D PTV, or, Time-Resolved (Lagrangian) Particle Tracking (LPT). It incorporates useful methods from different fields such as the volume self-calibration (Wieneke [97]) and Optical Transfer Function (OTF) calibration (Schanz et al. [76]), of Tomographic PIV (Elsinga et al. [14]), along with the IPR and the use of a predictor (extrapolation) of the particle positions similar to classical 3D PTV. This method successfully reconstructs the flow's temporal particle tracks leading to the suppression of ghost particles [75]. That is mainly due to the inclusion of the temporal and spatial information (usually 4 time steps) of the particle trajectory and to the shaking procedure in which any particle with intensity below a certain threshold (usually 5%) is deleted, while the intensity is updated after each iteration to discard ghost particles and noise. The advantages of Time-Resolved STB unfortunately, cannot be applied to high speed flows due to the limitations of the acquisition frequency of high speed systems. Therefore, a new approach exploiting use of multiple double-systems (Multi-Pulse STB, MP-STB)(illumination and image setup) was introduced by Novara et al. [60]. In order to compensate for the loss in temporal and spatial information (2 pulses (timesteps)), this approach makes use of the successive application of the IPR method along with a predictor scheme based on cross-correlation (Particle Space Correlation, PSC, Novara et al. [59]). The number of double-pulses is usually decided based on the available amount of high speed equipment (laser, cameras).

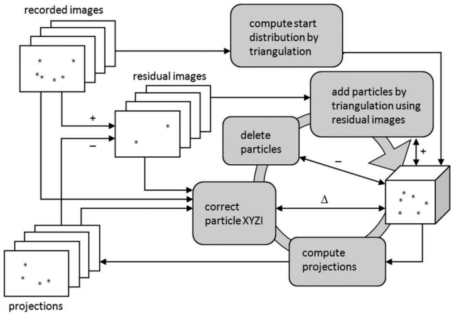


Figure 1.21: Scheme of the IPR algorithm [96].

Given the amount of high speed systems available and that the average flow is of interest at this research study, the double-pulse Shake-The-Box (TP-STB) (Novara et al. [61]) technique is chosen. The image matching process and the IPR method are similar to the one described above for the MP-STB and they are shown in Figure 1.22, for the cases of no predictor (top right) and with predictor based on PSC (bottom right). The output of the TP-STB method are single two particle pair tracks shown in black.

The multi-pulse STB technique has been successively applied for flows up to Mach 0.84 [56].

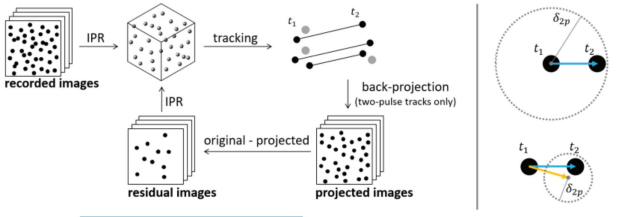


Figure 1.22: Iterative particle tracking for TP-STB with and without predictor (discarded particles are shown in gray) [61].

1.6. Thesis Aim & Objectives

This section summarizes the motivations regarding the present research. Furthermore, the aims of this Thesis are presented. It is evident that wall interference can be mitigated by either correcting for the free stream velocity, or for the angle of attack, or both. Regarding rotor testing, the incidence angle of the wind tunnel velocity with respect to the rotor dictates the nature of the corrections. There are well established methods for each of those two different behaviors namely, lifting rotor (hover mode) or propeller, but the range of applicability of such methods remains within a narrow angle band ($90° \pm 10°$ and $0° \pm 10°$ approximately). Moreover, it is seen that agreement between different approaches is not satisfactory, even when comparing the same methods with results available in literature. Wall interference research is even more sporadic when it comes to rotor testing in test sections different than closed wall and for (IGE). Most of the research today in open-jet test sections is focused on aeroacoustics, or on the aerodynamics of non-lifting configurations such as automotive vehicles or wind turbines. Similar considerations apply for (IGE) testing due to the fact that the ground is a natural border in the forementioned tested objects. Additionally, proper correlation of aerodynamic measurements between different test sections is almost completely lacking from the available literature. Same notions apply for flow breakdown investigations, where the low speed-high thrust flow regime in which it occurs, is mainly avoided due to the strong effect of wall interference on the model. Considering the above, it is evident that wall interference is not properly understood, especially for powered-lifting configurations in open-jet test sections and in most of the cases, aerodynamic measurements are performed for small model sizes with respect to the wind tunnel cross-sectional area. The future need for more accurate wind tunnel measurements of V/STOL-like configurations, both in terms of fuel efficiency and due to the predicted high demand of such air-vehicles in the market, push the need for obtaining a more in-depth understanding of wall interference and wall correction methods for powered wind tunnel tests.

The research objectives of this Thesis are:

1. To compare a closed and a 3/4 open-jet test section in terms of powered wind tunnel testing and to determine the applicability and limitations of different wall correction methods in the low speed regime.
2. To identify the flow breakdown limits for both test sections.
3. To investigate the effect that the bottom wall of the test section (IGE testing) exhibits on wall corrections and flow breakdown.

This is made possible by performing tests for two different propellers at variable incidence angles in a closed and an 3/4 open-jet test section of the NLR-AWT wind tunnel. Wall interference is going to

be assessed by means of different wall correction methods. Additionally, 3D PTV is also going to be applied in order to quantitatively investigate the flow in the vicinity of the rotor, inside the wind tunnel. This can also serve as a more direct application of the boundary measurement methods. In other words, pressure measurements and its conversion to a velocity distribution at the boundaries, is not necessary, if PTV is used to obtain knowledge for the velocity field directly. Finally, interference-free data are necessary in order to asses the applied boundary corrections, therefore, the DNW-LST is employed.

1.7. Thesis Outline

In Chapter 2, the theoretical and practical formulations of the correction methods used in this Thesis are presented. Chapter 3 contains information with respect to the two test campaigns in the NLR-AWT and the DNW-LST. The general test-setup and the used measurement techniques are described. In Chapter 4, the global flow topology is presented by means of static pressure distribution at the boundaries and Particle Tracking Velocimetry in the vicinity of the propeller. Furthermore, the change in angle of attack and free-stream velocity (blockage) as predicted from different wall correction methods are discussed and compared with one another. Regarding flow breakdown, two established criteria available in literature are employed and compared with one derived purely from the static pressure signatures on the bottom wall of the two AWT test sections. Finally, the boundary-bounded performance results of the NLR-AWT are compared with the ones obtained in the DNW-LST under the assumption of zero boundary interference. In the last Chapter, an overview of this research is employed, along with some conclusions and recommendations for future work.

2

Wall Correction Methods

This chapter comprises an overview of the wall correction methods that are used for the current rotor tests. The basic background theory of those methods and the associated source codes are presented and the assumptions underlying those are highlighted. Furthermore, emphasis is given on the implementations and modifications of wall correction methods source codes that the author contributed during this study.

2.1. Introduction

In cases of extremely small models relative to the wind tunnel size, wall corrections should vanish and are not needed. Of course, that is the ideal situation for every wind tunnel test, but most of the times this is not satisfied. To present an order of magnitude of the scales mentioned, Rosenfeld et al. [71] has shown that for non-lifting bodies (frigate ships), tested in closed test sections, the model's solid blockage ratio should not exceed 5% and its length should be less than 67% of the tunnel's width for wall effects to be negligible. Thus, the necessity of wall corrections in wind tunnel testing is profound. This chapter comprises of a combination of theoretical background and applied implementations of the methods used in this research.

2.2. The Classical Correction Method

To begin with, the most basic and one of the oldest methods in determining wall interference on models in closed-wall and open-jet wind tunnels is the classical correction method as reported by H. Glauert and L. Prandtl [29], [65]. The assumptions underlying the classical wall interference theory include [16]:

- Flow in the wind tunnel is regarded as a linear potential flow.
- Flow at the tunnel boundaries is regarded as perturbation flow.
- Model with relatively small dimensions compared to the size of the test section and its wake extending straight downstream from the model.
- Tunnel of constant cross-sectional area extending far upstream and downstream of the model, while its boundaries are parallel to the direction of the flow. The boundary conditions prescribed are either no penetration for the velocity at the walls or a constant pressure in case of a free surface (open-jet test sections).

The velocity at any point inside the wind tunnel is the gradient of the the total potential function Φ, which is assumed to be expressible as a superposition of the wind tunnel's uniform free-stream velocity, the model representation potential and the wall potential as shown in equation (5). The wall interference velocity (perturbation velocity), which describes the induced flowfield due to the presence of the boundaries of the test section, is obtained as the gradient of the wall (perturbation) potential as shown in equation (6). Note that x, y, z denote the axial, lateral and normal to the model directions.

$$\Phi(x, y, z) = -u_\infty x + \phi_m(x, y, z) + \phi_w(x, y, z) \tag{5}$$

$$\underset{\sim}{u_w} = \frac{\partial \phi_w}{\partial x}\underset{\sim}{e_x} + \frac{\partial \phi_w}{\partial y}\underset{\sim}{e_y} + \frac{\partial \phi_w}{\partial z}\underset{\sim}{e_z} = u_w\underset{\sim}{e_x} + v_w\underset{\sim}{e_y} + w_w\underset{\sim}{e_z} \tag{6}$$

The perturbation potential satisfies the Laplace equation (A.18), under the linear potential flow assumption. Compressibility effects are taken into account by imposing the Prandtl-Glauert coordinate transformation as shown in Appendix A. As discussed above, the flow in the vicinity of the model that would occur in an unbounded stream is different from the wind tunnel flow. Therefore, the effect of the wind tunnel walls (wall interference) can be described by the wall induced perturbation velocities. The actual corrected, or free-air speed, can be estimated by superimposing the wind tunnel speed and the perturbation velocities induced by the walls.

$$\underset{\sim}{u_F} = u_\infty\underset{\sim}{e_x} + \underset{\sim}{u_w} = (u_\infty + u_w)\underset{\sim}{e_x} + (v_w)\underset{\sim}{e_y} + (w_w)\underset{\sim}{e_y} \tag{7}$$

The underlying assumptions of perturbation potential interference flow and a relative small size of the model with respect to the wind tunnel, implies that the interference velocities can be considered constant in the vicinity of the model, which is of interest. Thus, the determination of the wall interference velocity suffices for correcting the wind tunnel velocity to the actual unbounded conditions, as shown in equation (7). Most of the methods described below are based on calculating the interference velocities by means of non dimensional quantities as shown in equations (8) and (9), where ϵ is the non dimensional streamwise interference velocity or blockage interference velocity, $\Delta\alpha$ is the non dimensional upwash interference velocity or upwash interference and δ_w is the upwash or boundary interference parameter which is dependent on the test section geometry and type (boundary conditions) and on the model's geometry. The former can be interpreted as a change in the effective angle of attack, while the latter needs to be computed with the use of the method of images. Fortunately, it can be obtained from nomographs available in literature for different wind tunnel test sections for a given model [6],[16]. For a detailed derivation of the equations that lead to the estimation of the boundary interference factor δ_w with the use of the method of images the reader is referred to [25], [29] and [86]. Additionally, the streamwise gradients of δ_w and ϵ are of importance since they give an indication about the wall-induced forces which act on the vertical and horizontal directions on the model.

$$\epsilon = \frac{u_w}{u_\infty} \tag{8}$$

$$\Delta\alpha = \frac{w_w}{u_\infty} = \frac{\delta_w}{A_{WT}}\left(\frac{L}{q}\right) \tag{9}$$

Glauert's classical corrections are going to be applied and used as a baseline, since they are the most common and widely used wall interference correction methods. Classical corrections, differ depending on the tested configuration. In case of high lift configurations, the lifting line theory is employed in order to compute the flow angularity corrections, while in case of a non lifting system, blockage is estimated with

different kind of approaches depending on the tested model. In the present study, methods considering rotors and propellers are presented.

2.2.1. Lifting Rotors

Considering lifting rotors, the model is treated like a wing, and the method of images determines the flow angularity corrections. According to the test section configuration, the boundary conditions are satisfied via the mirror images leading into different boundary correction factors. The implementation for various rectangular tunnel types can be found in Theodorsen [86]. In general, the boundary correction factor δ_w can be retrieved from graphs available in literature [16], [6], [86], [25] and be applied to the respective formula (eqn. (9)) for the incidence angle correction $\Delta\alpha$. In practice, a small manipulation of the given formula is needed, when used for lifting rotors. Assuming that the rotor is set at 90 degrees incidence with the tunnel's wind speed, one can derive the following:

$$\Delta\alpha = \frac{w_w}{u_\infty} = \frac{\delta_w}{A_{WT}}(\frac{L}{q}) = \delta_w C_T(\frac{A_M}{A_{WT}}) = \frac{\delta_w c_T}{\mu^2}(\frac{A_M}{A_{WT}}) \tag{10}$$

Where the C_T and c_T are the thrust coefficients based on the wind tunnel free-stream velocity and tip speed respectively and μ is the advance ratio defined as the fraction between the wind tunnel velocity and the tip speed velocity. The forementioned parameters are defined in the Nomenclature section, while the tip speed is given by equation (11).

$$u_{tip} = \frac{2\pi n}{60} R \tag{11}$$

The assumptions of this correction method were presented in the begining of the chapter, while the results are expected to be in good agreement when small flow deflections are present and for infinitely small wings, or according to Theodorsen [86], for wing spans less than 75% of the tunnel width. According to H.Glauert [29], the 75% wing span will approximately introduce an additional 6% error in the upwash interference estimation which is significant.

Correction Procedure

DNW wind tunnel test engineers usually employ more advanced methods for applying wall corrections to the wind tunnel test data or, use the boundary interference parameter obtained directly from nomographs available therefore, the Glauert's correction method for lifting wings was not implemented in a form of a source code. Since a lifting rotor can be reliably compared with a wing only for low deflection angles (high advance ratios), while the focus of the current research is mainly at low advance ratios (low speed - high thrust conditions) it was decided not to implement a source code based on the above method. Therefore, the correction procedure was made possible by obtaining the boundary interference factors directly from nomographs and by using the equation (10), estimate the flow angularity corrections. Unfortunately, the absence of a source code led to the omission of the IGE flow angularity corrections assessment for that method, due to scarcity of available nomographs for In-Ground-Effect testing.

2.2.2. Blockage Corrections for Propellers

The theory underlying blockage corrections for propeller configurations was developed by Glauert and it is well documented in [23] and [29]. For the IGE correction procedure, a special treatment is developed based on the presented theory. The blockage estimation for propellers is based on the assumptions of

steady, incompressible, inviscid and irrotational flow (ideal flow) as described in Appendix A.1, while the propeller is treated as an actuator disk in which, a uniform distributed thrust force acts. Further research has been made by Mikkelsen and Sørrensen [57], [80] and by Werle [92] and [93]. The former method is directly compared with Glauert's method.

Propellers OGE

For an OGE correction procedure, consider a propeller centrally positioned inside a wind tunnel as depicted in Figure 2.1. The continuity equations are employed for the total and for a control volume enclosing the streamtube of the propeller.

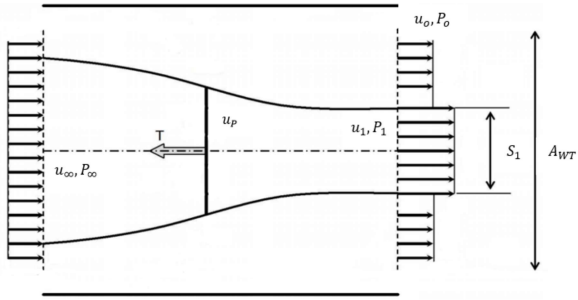


Figure 2.1: Flow-field formulation for a centrally positioned propeller inside a wind tunnel.

$$u_P A_P = u_1 S_1 \tag{12}$$

$$u_\infty A_{WT} = u_o(A_{WT} - S_1) + u_1 S_1 \tag{13}$$

The Bernoulli equation is used between the wind tunnel inflow region and the region outside the slipstream.

$$P_\infty + \frac{1}{2}\rho u_\infty^2 = P_o + \frac{1}{2}\rho u_o^2 \tag{14}$$

Similarly, the Bernoulli equation can be twice employed between wind tunnel inflow and before the disk, and between the region after the disk and the slipstream's end.

$$P_\infty + \frac{1}{2}\rho u_\infty^2 = P^- + \frac{1}{2}\rho u_{P^-}^2 \tag{15}$$

$$P^+ + \frac{1}{2}\rho u_{P^+}^2 = P_1 + \frac{1}{2}\rho u_1^2 \tag{16}$$

Velocity continuity through the disk implies that $u_{P^+} = u_{P^-}$ and thus, relation between the thrust of the disk and the outflow velocities may be obtained under the assumption that the pressures P_1 and

P_o are the same. In other words, that there is no vertical velocity component between slipstream and the outer region.

$$\frac{T}{A_P} = P^+ - P^- = (P_1 + \frac{1}{2}\rho u_1^2) - (P_\infty + \frac{1}{2}\rho u_\infty^2) = (P_1 + \frac{1}{2}\rho u_1^2) - (P_o + \frac{1}{2}\rho u_o^2) = \frac{1}{2}\rho(u_1^2 - u_o^2) \quad (17)$$

Additionally, the axial momentum conservation yields an additional equation for the thrust as a function of the three velocities inside the wind tunnel. This is made possible by using equation (14), in order to substitute the pressure term $(P_\infty - P_o)$.

$$T = -\rho u_\infty^2 A_{WT} + \rho u_o^2 (A_{WT} - S_1) + \rho u_1^2 S_1 + \frac{1}{2}\rho(u_\infty^2 - u_o^2) \quad (18)$$

By substituting equation $[(13)\times u_\infty^2]$ into the above relation one can show that:

$$T = \rho u_o (A_{WT} - S_1)(u_o - u_\infty) + \rho u_1 S_1 (u_1 - u_\infty) + \frac{1}{2}\rho(u_\infty^2 - u_o^2) \quad (19)$$

So far, the equations describing the flow are the two continuity equations (12), (13) and the two thrust equations (17), (19). In order to proceed any further, a relation connecting the thrust with the wind tunnel velocity and the free-air velocity needs to be derived. For that a new control volume needs to be used, describing the unbounded flow over the same propeller, shown in Figure 2.2. The equivalent free-air velocity u_F is defined such that it gives the same values to the propeller disk velocity u_P and thrust T.

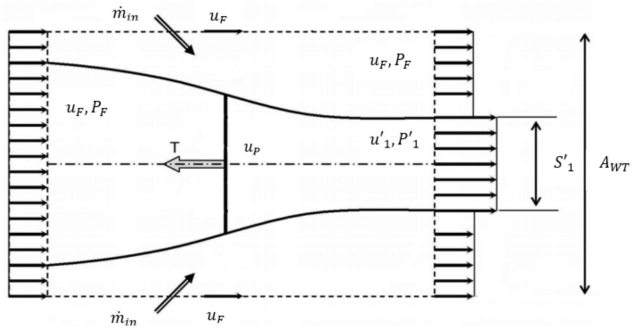


Figure 2.2: Flow-field formulation for an unbounded flow over a propeller.

From the conservation of mass one can compute the amount of mass exchange for the given control volume. Furthermore, the 1D momentum equation yields the thrust as a function of the free-air speed and the slipstream velocity u_F, u'_1.

$$\dot{m}_{in} = \rho u_F (A_{WT} - S'_1) + \rho u'_1 S'_1 - \rho u_F A_{WT} = \rho S'_1 (u'_1 - u_F) \quad (20)$$

$$T = \rho u'_1 S'_1 (u'_1 - u_F) \quad (21)$$

Following the same approach, by assuming velocity continuity through the disk and applying the Bernoulli equations (equations (15), (16) and (17)) before and after the disk region, a relation between the thrust, the slipstream and the free-air velocity is derived:

$$T = \frac{1}{2}\rho({u_1'}^2 - u_F^2) \tag{22}$$

By equating equations (21) and (22) and employing the continuity equation for the unbounded propeller (equation (12)), the following formula between the three velocities is derived:

$$u_1' = 2u_P - u_F \tag{23}$$

From relation (21) and by using the continuity for the propeller and equation (23) in order to eliminate the terms $u_1'S_1'$ and u_1' respectively, the following relation for the thrust is obtained:

$$T = 2\rho u_P A_P (u_P - u_F) \tag{24}$$

A further manipulation of the latter equation yields:

$$\begin{aligned} 4(u_P^2 - u_P u_F) &= \frac{2T}{\rho A_P} \\ (2u_P - u_F)^2 &= \frac{2T}{\rho A_P} + u_F^2 \end{aligned} \tag{25}$$

By introducing the following non-dimensional quantities $\lambda = u_\infty/u_F$, $x_P = (2u_P - u_F)/u_F$ and $\tau = T/(\rho u_\infty^2 A_P) = C_T/2$ and by dividing equation (25) with u_F^2 in order to form the appropriate analogies it is shown that:

$$x_P^2 = 2\tau\lambda^2 + 1 \tag{26}$$

Now that a relation is established between the non-dimensional thrust coefficient τ and the velocity ratio λ, the blockage ratio $a = A_P/A_{WT}$ and the slipstream ratio $\sigma = S_1/A_P$ are employed. One can use the continuity equations (12) and (13) in order to obtain the thrust as a function of $S_1, A_{WT}, u_P, u_\infty$ from equations (18) and (19). Additionally, the non-dimensionalization of the latter equations with σ, a, λ, τ and x_P and the expansion of the terms which contain second orders of a via Taylor series in order to ignore those (for $a << 1$), will yield the final two equations needed in order to obtain the thrust and the corrected velocity ratio.

$$x_P = (\Omega + 1)/(1 - \Omega) \tag{27}$$

$$\lambda = 1 + (x_P - 1)a\sigma^2 - \frac{(2\sigma - 1)x_P - 1}{2\sigma} \tag{28}$$

Where Ω is just an arbitrary constant for the sake of simplicity.

$$\Omega = \frac{(1 - \sigma)(1 - a\sigma)}{\sigma(1 - a\sigma^2)^2} \tag{29}$$

For a given propeller test inside a wind tunnel, the method first assumes a given value of the slipstream area σ and then, the equations (27), (28), (29) are successively solved. Finally, the thrust coefficient τ may be computed from the relation (26). In case the predicted thrust coefficient is different than the measured, or assumed one, the value of sigma is varied until those two values are in agreement. Since the slipstream area is unknown, the initial value of σ is chosen as the one which corresponds to free-air conditions ($\lambda = 1$).

$$\sigma_F = \frac{(x_P + 1)}{2x_P} \tag{30}$$

Propellers IGE

The Glauert's method described above is formulated for propellers positioned along the a wind tunnel's centerline. For an IGE correction procedure, consider a propeller positioned at a height ho above the wind tunnel bottom wall as depicted in Figure 2.3. It is feasible to correct for only the top wall interference by assuming that the propeller operates at the centerline of an equivalent (virtual) wind tunnel with cross-sectional area of $A^*_{W\cdot T} = 2W(H - ho)$. This is justified if one chooses a control volume along the propeller centerline, where the area of the control volume is $W(H - ho)$, while the surface area of the propeller is $A_P/2$. The analogy is directly discernible, since it results in a solid blockage ratio of $a = \frac{A_P/2}{W(H-ho)}$, in agreement with the above description.

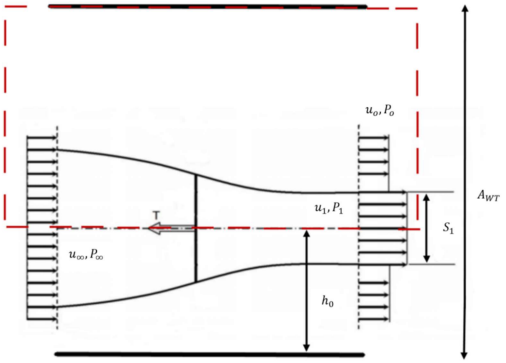


Figure 2.3: Flow-field formulation and control volume for an off-centered propeller wind tunnel test IGE.

Correction Procedure

A dedicated script was developed in which the described method was implemented. For the verification of the developed code a comparison with results provided by H.Glauert [29] is presented in Figure 2.4, where the velocity ratio is plotted as a function of the propeller thrust for different blockage ratios. It is important to mention here, that the convention for positive thrust, is on the direction shown in the above Figures. In general, the comparison is good and some slight deviations most probably originate from the digitization of the original plot which was made manually. As mentioned in the previous Chapter, there is an additional method developed by Mikkelsen and Sørrensen (M&S) [57], [80]. The mentioned authors managed to get rid of the singularity that the Glauert's method exhibited for the case of wind turbines at thrust coefficient values of $C_T = 1$. In this case the thrust convention is defined as opposite than described above, so that the positive thrust corresponds to a wind turbine and not a

propeller (see Figure 1.19b). The M&S method was implemented and the comparison between the two methods is shown in Figure 2.5. It is clear that for wind turbines (positive thrust coefficient) the two methods have significant differences, which is expected due to forementioned singularity exhibited by the Glauert's method. On the other hand, for propellers (negative thrust coefficient), the two methods are in very good agreement. The deviations between them, enlarge with the increase in blockage ratio and at higher thrust coefficients. This trend is expected, since in the Glauert's method, the second order terms of the blockage ratio are considered negligible and thus ignored ($a << 1$), which is usually the case for propeller wind tunnel tests. However, the error may surge when the blockage ratio is of the order of unity. The examined blockage ratios for the tests performed in this study were lower than 0.25 and even smaller for IGE cases, therefore, the use of Glauert's method was considered sufficient.

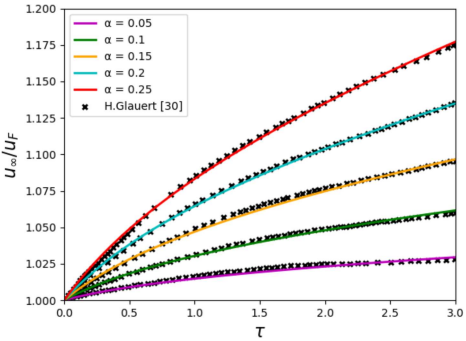


Figure 2.4: Velocity correction ratio versus thrust coefficient for propellers with different blockage ratios.

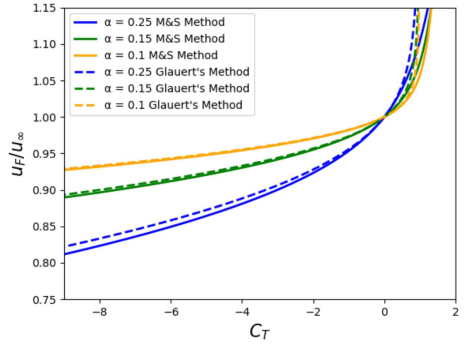


Figure 2.5: Comparison between the M&S and the Glauert methods.

2.3. The Heyson Method

In the previous subsection, the classical method for assessing lift interference, treats the lifting rotor like a wing. Furthermore, the assumption of small flow deflections may result in significant errors, for the usual conditions that helicopter rotors operate. Heyson realized that and created a method which takes into account the operating conditions of lifting rotors (large flow deflections). Assuming a single rotor, at a given angle of attack and force measurements, the determination of the horizontal U_0 and vertical W_0 induced velocities is possible. Propellers and rotors, typically exhibit two types of forces namely the thrust and the normal to the thrust force. For convenience, the latter will be called normal force. Figure 2.6 presents these forces and their associated velocity components for a wind tunnel test.

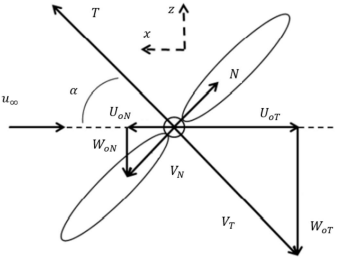


Figure 2.6: Propeller forces and their associated velocities [91].

From the above Figure, the total induced horizontal and vertical velocity components are given in equations (31) and (32), where the total velocity due to thrust V_T can be estimated from simple actuator disk theory considerations (equation (33)) and the total velocity due to the normal force V_N from equation (34) [91].

$$U_o = cos(\alpha)V_T - sin(\alpha)V_N \tag{31}$$

$$W_o = sin(\alpha)V_T + cos(\alpha)V_N \tag{32}$$

$$V_T = \frac{u_\infty}{2}(\sqrt{1 + C_T} - 1) \tag{33}$$

$$V_N = V_T \frac{C_N}{C_T} \tag{34}$$

Another method, based on momentum theory was used by Heyson [36] and a nomographic solution was provided. Voorst [91], was able to justify that the solution of equations ((31) - (34)) leads to the same results with that of Heyson. For given induced velocities, the wake skew angle can be determined from equation (35) as shown in Figure 2.7. The wake skew angle is a reference angle based on momentum theory, which represents the wake's direction in the vicinity of the rotor. The characterization reference angle lies in the fact that the wake of the rotor interacts with the wind tunnel's free-stream velocity making it difficult to approximate the final direction of the wake. Therefore, equation (35) works better for propeller wakes parallel to the wind tunnel velocity where this interaction is minimum in the vertical direction. Due to the above realization, Heyson [37] changed the geometrical solution for the skew angle as proposed in equation (35) and replaced it with an effective value given in (36). It is noted

here, that the effective skew angle given in equation (36) has been derived due to Heyson's experimental observations hence, it is purely empirical. Figure 2.8a shows different modelling approaches made by Heyson [37] in order to determine the effective value of the wake skew angle. The difference between the skew angle and the momentum angle θ used in some parts of this report is presented in Figure 2.8b.

$$\chi = tan^{-1}(\frac{u_\infty + U_0}{-W_0}) \tag{35}$$

$$\chi_{eff} = tan^{-1}(\frac{\pi^2}{4} tan(\chi)) \tag{36}$$

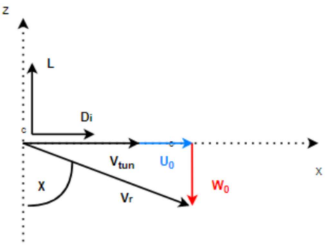
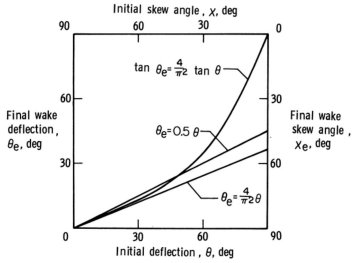
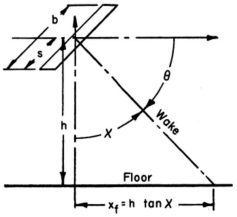


Figure 2.7: Induced velocities U_0, W_0 and skew angle definition [46].



(a) Different modelling approaches for the effective value of the momentum and skew angles.



(b) Difference between skew angle χ and momentum angle θ.

Figure 2.8: Heyson's theory for momentum, skew and effective skew angles [37].

For assessing lift interference, Heyson [34] made use of the method of images and he represented the wake of the rotor with horizontal and vertical oriented doublets along a semi-infinite line in the direction of the skew angle as shown in Figure 2.9. Vertical doublets shown in Figure 2.9a represent the lift interference, while horizontal doublets shown in Figure 2.9b represent the lift blockage due to the induced drag or horizontal induced velocity U_0. The circulation of the rotor is related with the strength of the doublet sheet and with the induced velocities. In a similar manner with the classical corrections and by using the method of images, Heyson [35] derived the vertical and longitudinal interference velocities due to lift interference (equations (37)) and the corresponding interference velocities due to induced drag or lift blockage (equations (38)). The above equations are characterized by their corresponding

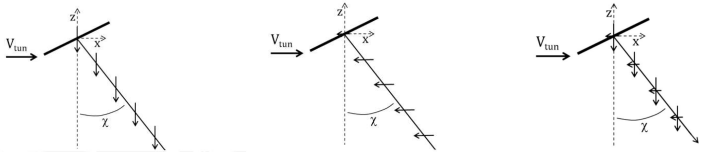
non-dimensional interference factors given in equations (39) and (40). Note that ζ is the ratio of wind tunnel semi-height $H/2$ to the remaining height of model $h/2$ above wind-tunnel floor $\zeta = H/h$, γ is the ratio of wind tunnel semi-width $W/2$ to wind tunnel semi-height, $\gamma = W/H$ and the coefficients $\bar{K}_{i,j}$ are derived by the method of images and depend on the test section configuration and the position of the model. The derivation by employing the method of images for different types of test sections and conditions is given in [34] and [35].

$$\Delta W_L = W_0 \frac{A_M}{A_{WT}} \delta_{w,L} \quad ; \quad \Delta U_L = W_0 \frac{A_M}{A_{WT}} \delta_{u,L} \tag{37}$$

$$\Delta W_D = U_0 \frac{A_M}{A_{WT}} \delta_{w,D} \quad ; \quad \Delta U_D = U_0 \frac{A_M}{A_{WT}} \delta_{u,D} \tag{38}$$

$$\delta_{w,L} = -\zeta^2 \frac{2\gamma}{\pi} \bar{K}_{w,L} \quad ; \quad \delta_{u,L} = -\zeta^2 \frac{2\gamma}{\pi} \bar{K}_{u,L} \tag{39}$$

$$\delta_{w,D} = -\zeta^2 \frac{2\gamma}{\pi} \bar{K}_{w,D} \quad ; \quad \delta_{u,D} = -\zeta^2 \frac{2\gamma}{\pi} \bar{K}_{u,D} \tag{40}$$



(a) Vertical doublets. **(b)** Horizontal doublets. **(c)** Combination of vertical and horizontal doublets.

Figure 2.9: Modelling of the wake of the rotor in a wind tunnel [9].

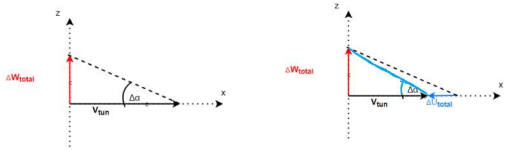
For a given component "i" its contribution to the interference velocities is expressed as a change in the vertical and the horizontal flow components as shown in equation (41). Finally, the contributions to the interference velocities are summed up for every model component according to (42). Finally, and the total upwash correction or change in the angle of attack is eventually calculated in equation (43). Figure 2.10 geometrically depicts equation (43) for the case of ignoring the induced lift blockage (only vertical doublets) and for the case of including the induced drag (both vertical and horizontal doublets). Similarly, a corrected tunnel velocity, or free-air speed V_{cor} can be estimated from equation (B.1). It is important to note that the corrected, or free-air velocity presented in equation (B.1), is based purely on lift blockage, since the Heyson method does not take into account solid and wake/slipstream blockage.

$$\Delta W_i = \Delta W_L + \Delta W_D \quad ; \quad \Delta U_i = \Delta U_L + \Delta U_D \tag{41}$$

$$\Delta W_{tot} = \sum_{i=1}^{N} \Delta W_i \quad ; \quad \Delta U_{tot} = \sum_{i=1}^{N} \Delta U_i \tag{42}$$

$$\Delta\alpha = tan^{-1}\left(\frac{\Delta W_{tot}}{\Delta U_{tot} + u_\infty}\right) \tag{43}$$

$$V_{cor} = \sqrt{(u_\infty + \Delta U_{tot})^2 + \Delta W_{tot}^2} \tag{44}$$



(a) Ignoring lift blockage correction $\Delta U_{tot} = 0$.

(b) With lift blockage correction $\Delta U_{tot} \neq 0$.

Figure 2.10: Angle of attack correction [46].

2.3.1. Correction Procedure

As already mentioned, the HWC had been verified for each new adaptation with results available in Heyson reports. The version which the author was given, was not reproducing feasible results, meaning that the skew angle was not varying for different rotor thrust - wind tunnel velocity conditions. After a careful inspection, it was found that the skew angle was held constant and varied only with respect to the angle of attack of the model. That of course should not be the case, since the skew angle is completely determined by the wind tunnel velocity and the measured forces on the rotor (equation (35)). Therefore, a slight adaptation on the HWC was implemented in order to make use of the forementioned equation. This adaptation is verified with results from R-302 [39] (Figure 28 of that report) for a uniformly loaded rotor centered at 90° incidence angle in a closed wind tunnel of $\gamma = 1.5$. Figure 2.11 presents the effect that the size of the rotor (D/W) exhibits on the wall interference field. More specifically, the averaged lift interference parameter due to the vertical induced velocity $\delta_{w,L}$ is presented as a function of the effective skew angle. As it is observed, the results are in complete agreement leading to a successful verification of the HWC. Finally, it should be noted that in the HWC, the loading distribution needs to be specified. For all the tests performed, a triangular loading distribution was chosen, since according to Heyson et al. [42] a non-uniform loading provides a more realistic and accurate model representation.

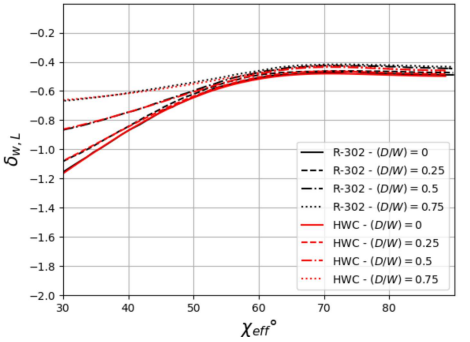


Figure 2.11: Average lift interference parameter for different sized rotors, a comparison between HWC and R-302 [39].

2.4. Boundary Measurement Methods

A small introduction with respect to boundary measurement methods was given in the previous chapter. The remaining part of this section focuses on the developed and applied methods. The reader is strongly referred to Appendix B, for obtaining a general knowledge of the classification and the general principles of such methods.

2.4.1. The 2D Two-Variable-Method

The theoretical background of this method is given by Maarsingh et al. [53] and it is similar with the approach of Ashill et al. [4]. It applies for 'correctable' flows under the small perturbation assumption, meaning that there must exist a free-flow, such that the disturbance velocities at S_M are approximately the same for both flow regimes. Additionally, this method assumes that both velocity components can be measured at any control (measurement) surface S_W of the wind tunnel. Further assumptions are that the flow in the vicinity of the measurement surface is considered irrotational and subsonic. Therefore, the boundary enclosing the wake of the model, does not need to be the same for the two flows considered. In accordance with the two variable methods, the tunnel flow is related with its corresponding free-air flow. Those two flows are presented in Figure 2.12, where D denotes for domain and S for surface. The flow in the wind tunnel U_{TT} is decomposed to the undisturbed (wind tunnel) free-stream flow U_∞ and to the model and wall induced disturbance velocities $U_T = U_M + U_w$. Similarly, the free-air flow is split between the undisturbed free flow and the model induced perturbation velocity $U_F = U_M$. For the domains shown in Figure 2.12, the Laplace equation should be satisfied for the following flows:

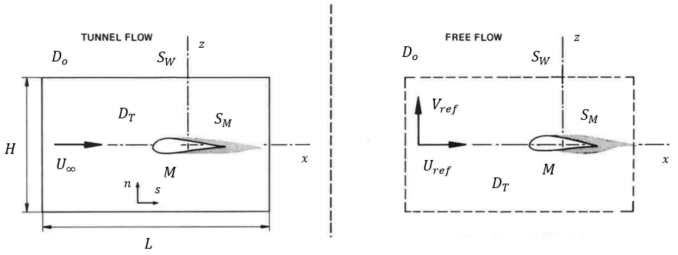


Figure 2.12: Flow domains for the wind tunnel and free-air flow [50].

$$U_{TT} = U_\infty + U_T \tag{45}$$

$$U_{TF} = U_{ref} + U_F \tag{46}$$

$$\nabla^2 \phi_T = 0, \qquad \text{in} \quad D_T \tag{47}$$

$$\nabla^2 \phi_w = 0, \qquad \text{in} \quad D_T \cup D_M \tag{48}$$

$$\nabla^2 \phi_M = 0, \qquad \text{in} \quad D_o \cup D_T \tag{49}$$

$$\nabla^2 \phi_\infty = 0, \qquad \text{in} \quad D_o \cup D_T \cup D_M \tag{50}$$

For any single-valued two dimensional function f satisfying the Laplace equation in a domain D bounded by two surfaces S_1 and S_2, as shown in Figure 2.13, equation (51) is applicable. The variable $r =$

$\sqrt{(x-\xi)^2+(z-\zeta)^2}$, denotes the distance from a point (ξ,ζ) inside the domain D to a fixed point $P(x,z)$.

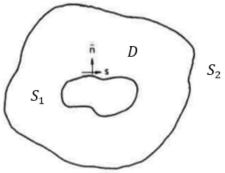


Figure 2.13: Domain for Green's Theorem application [50].

$$\iint_{S_1+S_2}(f\frac{\partial}{\partial n}(lnr)-\frac{\partial f}{\partial n}lnr)\,dS=\begin{cases}0, & \text{for P outside D}\\ -\pi f(P), & \text{for P on a boundary of D}\\ -2\pi f(P), & \text{for P inside D}\end{cases} \tag{51}$$

By applying the Green's formula for the 2D wind tunnel flow, directly for the velocity instead of the potential, any point P in the domain D_T, bounded by surfaces S_W and S_M, is determined by:

$$U_{TT}(P)=U_\infty-\frac{1}{2\pi}\iint_{S_W}(U_T\frac{\partial}{\partial n}(lnr)-\frac{\partial U_T}{\partial n}lnr)\,dS-\frac{1}{2\pi}\iint_{S_M}(U_T\frac{\partial}{\partial n}(lnr)-\frac{\partial U_T}{\partial n}lnr)\,dS \tag{52}$$

The irrotationality conditions for the perturbation velocity U_T is:

$$\frac{\partial U_T}{\partial n}=\frac{\partial W_T}{\partial s} \tag{53}$$

By substitution of equation (53) into equation (52) yields by partial integration:

$$U_{TT}(P)=U_\infty-\frac{1}{2\pi}\iint_{S_W}(U_T\frac{\partial}{\partial n}(lnr)-W_T\frac{\partial}{\partial s}(lnr))\,dS-\frac{1}{2\pi}\iint_{S_M}(U_T\frac{\partial}{\partial n}(lnr)-W_T\frac{\partial}{\partial s}(lnr))\,dS \tag{54}$$

The exact procedure is followed for the free-air flow (equation (46)). For any point P in the domain $D_o\cup D_T$, bounded by infinity and surface S_M, is determined by:

$$U_{TF}(P)=U_{ref}-\frac{1}{2\pi}\iint_{S_M}(U_F\frac{\partial}{\partial n}(lnr)-W_F\frac{\partial}{\partial s}(lnr))\,dS \tag{55}$$

The integral term containing the velocities at infinity is of course zero, due to the conditions that the disturbance velocities U_F and V_F are zero at infinity. By assuming that the disturbance velocities of the two flows at the vicinity of the model (at S_M) are approximately the same, ($U_F\approx U_T$, $V_F\approx V_T$), one can subtract equations (54) and (55) in order to get rid of the integral of the surface S_M. Moreover, it is assumed that $U_{TF}(P)=U_{TT}(P)$ at least in one point P in D_T in order to get:

$$\Delta U = U_{ref} - U_\infty = -\frac{1}{2\pi} \iint_{S_W} (U_T \frac{\partial}{\partial n}(lnr) - W_T \frac{\partial}{\partial s}(lnr))\, dS \tag{56}$$

Similar procedure is followed for the vertical velocity component leading to:

$$\Delta W = W_{ref} - W_\infty = -\frac{1}{2\pi} \iint_{S_W} (W_T \frac{\partial}{\partial n}(lnr) - U_T \frac{\partial}{\partial s}(lnr))\, dS \tag{57}$$

This derivation is very significant since it justifies the determination of wall corrections, by wind tunnel velocity measurements purely along the surface S_W. No model representation is needed and therefore, no knowledge and complex modeling with respect to the flow structures in the vicinity of the model. On the other hand, one would notice that the corrections are evaluated at an arbitrary point of choice $P(x, z)$ in D_T. This means that the corrections would be reliable only if there is a small and gradual variation of ΔU and ΔV. Finally, the corrections may be obtained from the classical formulations:

$$\epsilon = \frac{\Delta U}{U_\infty} = -\frac{1}{2\pi} \iint_{S_W} (u_T \frac{\partial}{\partial n}(lnr) - w_T \frac{\partial}{\partial s}(lnr))\, dS \tag{58}$$

$$\Delta\alpha = \frac{\Delta W}{U_\infty} = -\frac{1}{2\pi} \iint_{S_W} (w_T \frac{\partial}{\partial n}(lnr) - u_T \frac{\partial}{\partial s}(lnr))\, dS \tag{59}$$

Correction Procedure

A dedicated script was developed for the method described above. A closed wall test section is assumed, leading to zero vertical velocity $w_T = 0$ at the measurement surface S_W in accordance with the no-penetration boundary condition. Instead of correcting for the blockage effects (due to the test stand) by means of a correction to the wind tunnel free-stream velocity U_∞, it is decided to subtract the pressure coefficients measured only for the test stand and motor, from the propeller (total) measurements. Thus, the pressure coefficients are denoted as ΔCP. Typical pressure measurement locations can be seen in Figure 2.14, but the method is two dimensional, therefore, the average of the pressure coefficients is used in order to calculate the incremental (disturbance) velocities. After some research, it was found that the linearized version of the Bernoulli equation (see equation (A.22)) was not yielding sufficient results, therefore, equation (A.23) was employed. Consider the bottom wall as shown in Figure 2.14. Following the approach of Labrujère [49], it is hypothesized that the lateral velocity is zero at the first pressure readings right after the contraction ($v_{T,0} = 0$). Therefore, the axial disturbance velocity may be calculated from equation (60) for the first measurement point after the nozzle of the tunnel. For the rest point measurements, an estimation for the lateral component may be obtained from the irrotationality condition.

$$u_{T,0} = -0.5(\frac{\Delta C_{P3,0} + \Delta C_{P4,0}}{2}) \tag{60}$$

The derivative of the axial disturbance velocity with respect to the lateral direction may be approximated directly from the pressure readings:

$$(\frac{\partial v_T}{\partial x})_i = (\frac{\partial u_T}{\partial y})_i = -0.5 \frac{\Delta C_{P3,i} - \Delta C_{P4,i}}{\Delta y} \tag{61}$$

Then an integration of the lateral velocity component results to:

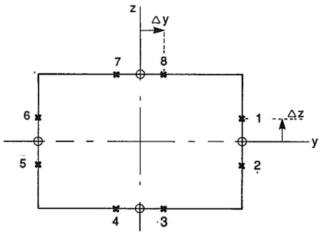


Figure 2.14: Typical pressure measurements on the wind tunnel boundaries (upstream/front view) [49].

$$v_{Ti} = \int_{x_{i-1}}^{x_i} \frac{\partial u_T}{\partial x} d\xi + v_{T,i-1} \tag{62}$$

Substituting equation (61) in the latter equation and by using the trapezoidal rule for the above integral the final relation for the lateral velocity at the measurement point 'i' is obtained.

$$\begin{aligned} v_{T,i} &= v_{T,i-1} + 0.5[(\frac{\partial u_T}{\partial y})_i + (\frac{\partial u_T}{\partial y})_{i-1}](x_i - x_{i-1}) \\ &= v_{T,i-1} + 0.5[\frac{\Delta C_{P3,_i} - \Delta C_{P4,_i}}{\Delta y} + \frac{\Delta C_{P3,_{i-1}} - \Delta C_{P4,_{i-1}}}{\Delta y}](x_i - x_{i-1}) \end{aligned} \tag{63}$$

Finally, the axial disturbance velocity at the measurement point 'i' is computed from:

$$u_{,T\ i} = -0.5(\frac{\Delta C_{P3,_i} + \Delta C_{P4,_i} - v_{T_i}^2}{2}) \tag{64}$$

Following the above method, an axial incremental velocity distribution can be estimated at every wall centerline and the wall corrections may be computed at a point $P(x, z)$ with the use of equations (58) and (59). The latter is made possible under the assumption that the front and back vertical surfaces of S_W are far enough such that the flow is undisturbed and their respective integrals are set to zero, or cancel with each other. Therefore, from equations (58) and (59) and assuming a solid-wall test section the final form of the corrections of this method are revealed, where z_{top} and z_{bot} are the fixed coordinates of the top and bottom wall with respect to the origin which is the tunnel centerline and x_{left} and x_{right} are the first and the last location of measured pressure.

$$\epsilon(x,z) = \frac{1}{2\pi}\int_{x_{left}}^{x_{right}} \frac{u_T(\xi, z_{top})}{(x-\xi)^2 + (z - z_{top})^2}(z - z_{top})d\xi + \frac{1}{2\pi}\int_{x_{left}}^{x_{right}} \frac{u_T(\xi, z_{bot})}{(x-\xi)^2 + (z - z_{bot})^2}(z - z_{bot})d\xi \tag{65}$$

$$\Delta\alpha(x,z) = -\frac{1}{2\pi}\int_{x_{left}}^{x_{right}} \frac{u_T(\xi, z_{top})}{(x-\xi)^2 + (z - z_{top})^2}(x - \xi)d\xi + \frac{1}{2\pi}\int_{x_{left}}^{x_{right}} \frac{u_T(\xi, z_{bot})}{(x-\xi)^2 + (z - z_{bot})^2}(x - \xi)d\xi \tag{66}$$

The above assumption implies a very long test section, which is not always the case for typical wind tunnels. An assessment of this method in 3D space is made by Labrujère [49], where an idealized wind tunnel flow over a wing is used in order to generate a pressure distribution at the walls. This method is found out to be insensitive to the number of the axial pressure taps that are employed and to the transverse location of the pressure bars at the side wall. However, the influence of the transverse location of the pressure bars at the top and the bottom walls and the length of test section, seem to be the parameters that mostly affect the results. The former leads to an overestimation of the wall induced upwash, while the latter will cause an underestimation. Their combined effect may effectively, cancel each error out. It should also be noted here that in the 2D Two-Variable-Method (2D-TVM), information from the side walls is not taken into account, although the perturbation velocities at all four walls can be estimated with the procedure described above.

2.4.2. The 3D Two-Variable-Method

The 3D Two-Variable-Method (3D-TVM) is an extension of the 2D-TVM described above. If pressure measurements are implemented in all four walls (see Figure 3.1.2), the axial disturbance velocity can be calculated for each wall in the same manner as in the 2D-TVM. By applying the Green's Theorem in a 3D domain D bounded by a surface Σ, it can be shown that for any single-valued function f, which satisfies the Laplace equation in that domain, there holds [50]:

$$\iint_{\Sigma}[f\frac{\partial}{\partial n}(\frac{1}{r})-\frac{\partial f}{\partial n}(\frac{1}{r})]\,dS=\begin{cases}0, & \text{for P outside D}\\ -2\pi f(P), & \text{for P on a boundary of D}\\ -4\pi f(P), & \text{for P inside D}\end{cases} \tag{67}$$

Where again, $r=\sqrt{(x-\xi)^2+(y-\eta)^2+(z-\zeta)^2}$ is the distance from any point (, η, ζ) inside the domain D to a fixed point P (x, y, z). As with the 2D-TVM, it is assumed that the influence of the front and the rear surfaces is negligible, an assumption reasonable for the upstream (inlet) surface of D_T but not that valid for the downstream surface, where the the model's wake, or slipstream influence may be significant. In any case this assumption is retained here. For including the contribution of the part of the wake of the model outside the control volume, in the wall interference assessment, the reader is referred to Labrujère [50]. By applying equation (67) for the disturbance velocities $f=u_M$, $f=u_w$, for a point P on the domain $D_T \cup D_M$ there yields:

$$0=\iint_{\Sigma}(u_M\frac{\partial}{\partial n}(\frac{1}{r})-\frac{\partial u_M}{\partial n}(\frac{1}{r}))\,d\Sigma \tag{68}$$

$$u_w(P)=\frac{1}{4\pi}\iint_{\Sigma}(u_w\frac{\partial}{\partial n}(\frac{1}{r})-\frac{\partial u_w}{\partial n}(\frac{1}{r}))\,d\Sigma \tag{69}$$

By addition of the latter two equations and by using the relation $u_T=u_M+u_w$ one can show relation (70) which can be further simplified to (71) by employing the irrotationality condition and partially integrating the derivative of u_T for a solid wall test section in accordance with the no-penetration boundary condition.

$$u_w(P)=\frac{1}{4\pi}\iint_{\Sigma}(u_T\frac{\partial}{\partial n}(\frac{1}{r})-\frac{\partial u_T}{\partial n}(\frac{1}{r}))\,d\Sigma \tag{70}$$

$$u_w(P)=\frac{1}{4\pi}\iint_{\Sigma}(u_T\frac{\partial}{\partial n}(\frac{1}{r}))\,d\Sigma \tag{71}$$

In a similar manner, the other two wall disturbance velocity components $v_w(P), w_w(P)$ may be derived. The difference lies on the terms containing the derivative of the disturbance velocities $\frac{\partial v_T}{\partial n}, \frac{\partial w_T}{\partial n}$, which are not zero for every closed wall surface. Therefore, the approach of Labrujère [49] is followed which takes advantage of the harmonic nature of the wall induced flow-field leading to the determination of the lateral and vertical wall induced velocity components from the irrotationality condition as shown below. In theory, for a very long test section where the upstream area (nozzle) is far away from the model, $x_{left} \approx -\infty$ and $v_w(x_{left}, y_P, z_P) = w_w(x_{left}, y_P, z_P) \approx 0$.

$$v_w(x_P, y_P, z_P) = \int_{x_{left}}^{x_P} \frac{\partial u_w}{\partial y} dx + v_w(x_{left}, y_P, z_P) \tag{72}$$

$$w_w(x_P, y_P, z_P) = \int_{x_{left}}^{x_P} \frac{\partial u_w}{\partial z} dx + w_w(x_{left}, y_P, z_P) \tag{73}$$

Correction Procedure

The 3D-TVM described here was implemented as an extension to the 2D-TVM thus, the same correction procedure applies. The lateral and axial disturbance velocity distributions per wall (node) are estimated with the use of relations (63) and (64). The wall-induced axial velocity is determined from equation (71) for the location of the propeller (x_P, y_P, z_P), but also at the locations of $(x_P, y_P \pm dy, z_P)$ and $(x_P, y_P, z_P \pm dz)$. Therefore, the gradients of u_w are directly available from the analytic expression and thus, they can be approximated by a central difference scheme. The choice of the spatial resolution dy and dz is arbitrary and an investigation showed the results are insensitive to that choice as long as it is sufficiently small (O(1 mm)). Given the gradients of u_w, the lateral and vertical wall-induced velocities are approximated iteratively with the trapezoidal rule as shown in (76 and 77).

$$\frac{\partial u_w(x_P, y_P, z_P)}{\partial y} = \frac{u_w(x_P, y_P + dy, z_P) - u_w(x_P, y_P - dy, z_P)}{2dy} \tag{74}$$

$$\frac{\partial u_w(x_P, y_P, z_P)}{\partial z} = \frac{u_w(x_P, y_P, z_P + dz) - u_w(x_P, y_P, z_P - dz)}{2dz} \tag{75}$$

$$v_w(x_i, y_P, z_P) = 0.5[(\frac{\partial u_w}{\partial y})_i + (\frac{\partial u_T}{\partial y})_{i-1}](x_i - x_{i-1}) + v_w(x_{i-1}, y_P, z_P) \tag{76}$$

$$w_w(x_i, y_P, z_P) = 0.5[(\frac{\partial u_w}{\partial z})_i + (\frac{\partial u_T}{\partial z})_{i-1}](x_i - x_{i-1}) + w_w(x_{i-1}, y_P, z_P) \tag{77}$$

Finally, the corrections for blockage and incidence (in degrees) are prescribed as:

$$\epsilon(x_P, y_P, z_P) = u_w(x_P, y_P, z_P) \tag{78}$$

$$\Delta\alpha(x_P, y_P, z_P) = (\frac{180}{\pi}) w_w(x_P, y_P, z_P) \tag{79}$$

3

Experimental Methods

In this chapter a description of the experimental facilities, the general test setup and the experimental methods used in each test campaign, is given. The measurements are split into three different types, namely, load and power, static pressure at the walls and PTV measurements. The latter two, are performed separately and only for the NLR-AWT campaign. The goal is to perform the tests at an environment of relatively high boundary induced conditions where wall corrections are of importance, while in order to obtain the interference-free performance curves for the propellers, the DNW-LST tunnel is employed. For each test campaign, some information regarding the testing facility is presented, followed by the general wind tunnel test setup and the associated measurement techniques.

3.1. The NLR-AWT Campaign

This campaign is planned such that the boundary induced interference field is of importance for both propellers tested. In order to compare different boundary conditions, two test sections are employed, namely a closed-wall and a 3/4 open-jet with an automotive floor set-up. During this campaign, all three measurement techniques mentioned before are used since the goal is to properly capture and assess wall-induced interference. The static pressures at the walls are measured for both propeller tests at both test sections, while the PTV measurements were performed only for the small propeller in the closed-wall test section.

3.1.1. The NLR-AWT Facility

The Aeroacoustic Wind Tunnel (NLR-AWT) is an atmospheric, closed circuit, water-cooled wind tunnel, powered by two 180 kW axial fans, with open-jet and closed test sections. It is comprised of a large anechoic room (9 x 8 x 6) m^3, completely covered with 0.5 m foam wedges [74]. For the purpose of this research campaign, the dimensions of both test sections are chosen such that they resemble the DNW-LLF facility at a $(1/10)^{th}$ scale.

Closed Test Section

For the closed test section configuration, a square (0.95×0.95) m^2 nozzle is used and the total length of the test section is 2.3 m. Additionally, the free stream turbulence intensity is within 0.01% to 0.06% for velocities ranging from 20 m/s to 120 m/s. This is due to the number of fine anti-turbulence screens

built into the settling chamber and the tunnel contraction ratio. For the PTV measurements, the turbulent intensity is expected to be slightly higher due to the presence of the seeding rake inside the settling chamber. The closed test section configuration is shown in Figure 3.1.

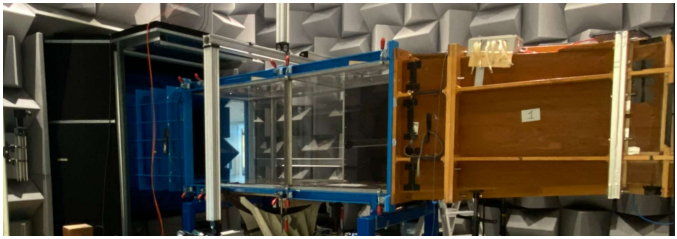


Figure 3.1: The AWT closed wall test section.

3/4 Open-Jet Test Section

For the 3/4 open-jet test section, the dimensions of the nozzle and the collector are (0.8 x 0.6) m^2 and (0.95 x 0.95) m^2 respectively. The test section is comprised with an automotive floor (ATF) that has a total length of 2.6 m, extending 0.3 m upstream and 0.3 m downstream inside the nozzle and the collector respectively. Moreover, its width is extended on both sides compared with the nozzle's width, resulting in a total width of 1.3 m. The 3/4 open-jet test section configuration is shown in Figure 3.2. The ATF is equipped with a suction pump, located below the floor, which effectively removes the boundary layer 0.3 m upstream of the nozzle and re-injects it below the floor, at the bottom part of the collector. A three dimensional view of the whole configuration is shown in Figure 3.3. The boundary layer suction pump settings had been optimized for a wind tunnel speed of 40 m/s in a previous research by Pernsteiner [62]. In the current tests, the tunnel is operated at speeds below 40 m/s. Additionally, the boundary layer suction pump is optimized for the wind tunnel velocities that are employed. More information regarding the suction pump optimization with respect to the employed tunnel velocities is given in section 3.1.2.

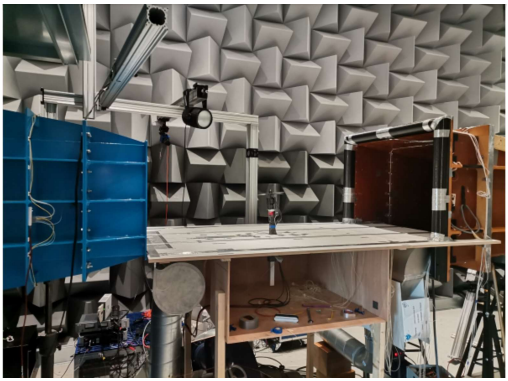


Figure 3.2: The AWT 3/4 open-jet test section with automotive floor.

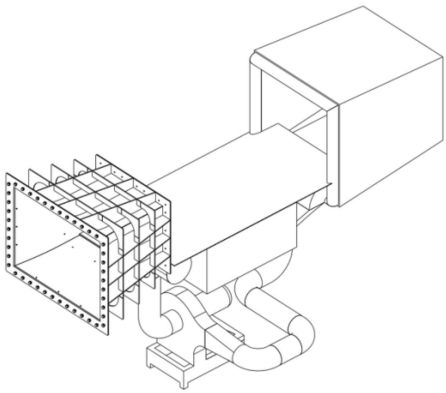


Figure 3.3: 3D drawing of the automotive setup in NLR-AWT [32].

3.1.2. General Test Setup

In order to investigate wall interference effects, wind tunnel tests for the two different propellers are performed, at three angles of attack 0°, 60° and 90°. The propellers and the angle of attack reference system are indicated in Figures 3.4 and 3.6a. For the sake of simplicity, the bigger propeller is going to be called propeller 1, while the smaller, propeller 2. The general characteristics for both propellers are shown in Table 3.1, where N_b is the number of blades and $\sigma_{0.7R} = (N_b c_{0.7R})/(\pi R)$ is the solidity based on the chord length of the propeller at $0.7R$.

Table 3.1: Propeller general characteristics.

	D [m]	$c_{0.7R}$ [cm]	N_b	$\sigma_{0.7R}$
Propeller 1	0.4069	3	6	0.28
Propeller 2	0.279	1.8	4	0.16

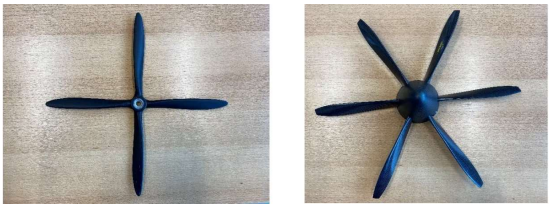


Figure 3.4: Propellers used in the tests (propeller 2 left and propeller 1 right).

For the mounting of the propellers, a two degree-of-freedom test stand is built as shown in Figure 3.6b. The ground plate is placed under the tunnel's test section floor to avoid any additional blockage effects and the strut can be easily adjusted over the vertical z-axis, whereas the angle of attack is adjusted manually. A load cell which can measure the force in the direction of the propeller axis (thrust) is installed in the junction between the strut and the electric motor of each propeller. The normal-to-the-thrust force is not measured in the current tests, since an additional external external balance will

be needed and its influence is assumed to be negligible ($T >> N$). Prior to the tests, the load cell was tested with the use of various known weights, in order to verify the load-voltage output calibration curve provided by the manufacturer. Furthermore, the voltage and current consumed by the the e-motor are measured directly from the power supply unit, thus the electric power consumed can be estimated from equation (80). Propellers 1 and 2 are rotating clockwise and counter-clockwise respectively, while two different electric motors are used. The motors are shown in Figure 3.5 and their main technical characteristics are specified in Table 3.2.

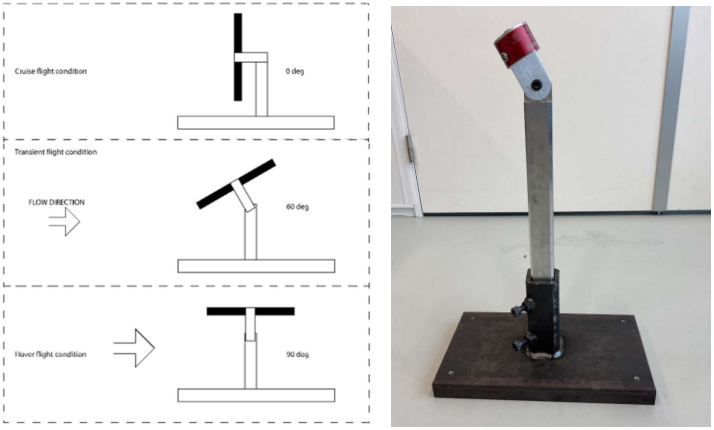
$$P_e = V_e \times A_e \tag{80}$$

Table 3.2: E-motor general characteristics.

	$\mathbf{P_{max}}$ [kW]	$\mathbf{rpm_{max}}$	$\boldsymbol{N_p}$ [poles]
E-Motor 1	15	7000	20
E-Motor 2	2	25000	10



Figure 3.5: Electric motors used for the propeller tests (e-motor 2 left and e-motor 1 right).



(a) Angle of attack definition. **(b)** Propeller test stand and load cell.

Figure 3.6: Angle of attack definition, test stand and load cell.

A. Wall Pressure Measurements

Static pressure distribution along the wind tunnel walls is measured with three electronic pressure scanning RAD modules. Each RAD module is comprised of 64 differential pressure transducers. Eight pressure bars of overall length of 2.2 m are employed, each comprising of 22 unevenly distributed pressure taps over a length of 2.1 m. The streamwise location of each pressure tap is given in Table 3.3, where the zero axial coordinate denotes the start of the test section. For the closed test section, two pressure bars are placed at a 0.23 m ($\Delta y = \Delta z = 0.242$W) distance from the centerline of each tunnel wall in accordance with Figure 2.14. This results to 2×22 pressure measurements per wall, or 176 measurements in total. Similarly, for the 3/4 open-jet test section the two pressure bars at the floor of the ATF are placed at about 0.2 m, in agreement with the same distance scaling ($\Delta y = \Delta z = 0.242$W) for that nozzle width. Additionally, static pressures inside the collector are measured by means of glued pressure taps. The pressure taps at the collector are placed from transition entry and up to a distance of 1.2 m with a step distance of 0.2 m as shown in Figure 3.7. A rectangular area with 1.2 m length and 0.15 m width located at the mid axis of the collector is equipped with those taps on the bottom and top surface. There are 14 (7 top and 7 bottom) pressure taps in total on a diagonal of about seven degrees over the whole surface shown. This arrangement is used to prevent boundary layer increase due to in-row glued taps and is in accordance with the measurements performed by Pernsteiner [62]. The number of pressure measurements for the 3/4 open-jet test section is $2 \times 22 + 14 = 58$ in total. The complete RAD assignment is given in Appendix C.1.2.

Table 3.3: Pressure taps distribution of a single bar (zero axial coordinate indicates the start of the test section).

Pressure Tap	1	2	3	4	5	6	7	8	9	10	11	12	13	14	15	16	17	18	19	20	21	22
x [mm]	2200	2022	1867	1732	1615	1513	1425	1348	1281	1223	1172	1128	1077	1039	952	875	787	685	568	433	278	100

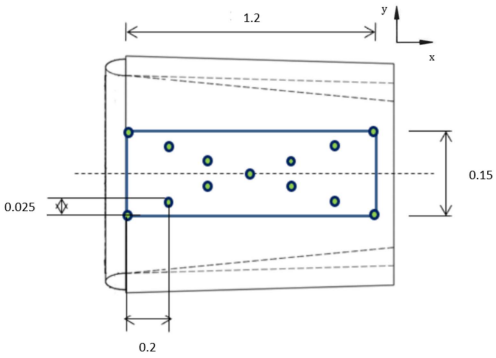


Figure 3.7: Top view of the static pressure measurements inside the collector (4th pressure tap corresponds to both top and bottom wall) [62].

Additionally, three rows with tufts are installed at the centerline of the bottom wall and at a $\Delta y \pm 0.15$ m distance from it. The centerline tufts initiated at an axial distance of 15 cm from the start of the test section for the centerline row, whereas, the other two parallel rows initiated at an axial distance of 40 cm. The tuft locations are the same for both test sections. Finally, considering the closed test section where the PTV measurements are also performed, a protective screen is installed at about 1.3 m inside the transition, in order to protect the wind tunnel circuit from soap contamination. The cloth screen, along with the glued pressure taps in the transition region, are shown in Figure 3.8. It should be noted here that the glued pressure taps (shown in the forementioned Figure) are also placed in the closed test section, but their measurements are useless, since they are placed after the breather gaps.

The forementioned pressure measurements are of interest only in the 3/4 open-jet test section, where the stagnation of the free-jet may be monitored. The protective screen installation initially resulted in a pressure rise along the test section, with the tunnel drawing ambient air from the circuit region close to the fan and discharging air throughout the test section region. By gradually reducing the thickness of the cloth screen, and taping-of several gaps where the wind tunnel was breathing from, the pressure distribution along the test section eventually matched with the one measured without the protective screen. Most of the main parts of the general set-up already described above are presented in Figure 3.9.

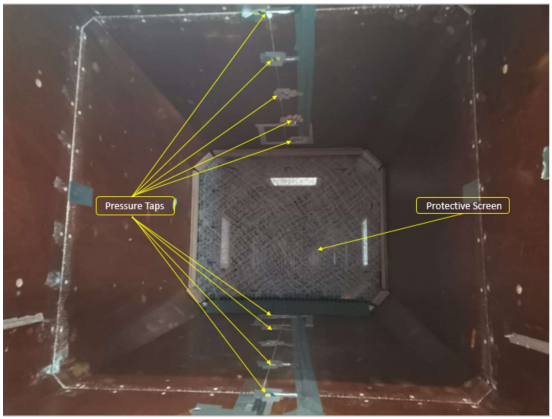


Figure 3.8: View inside the transition for the closed test section.

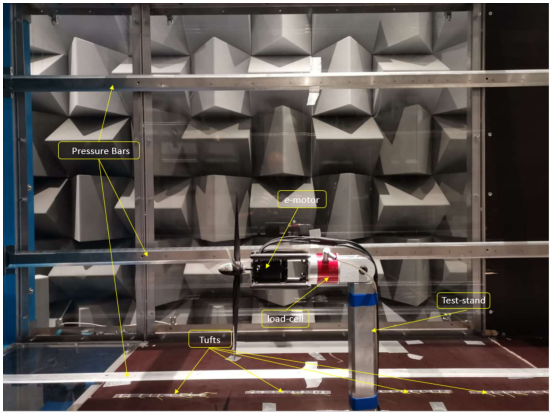
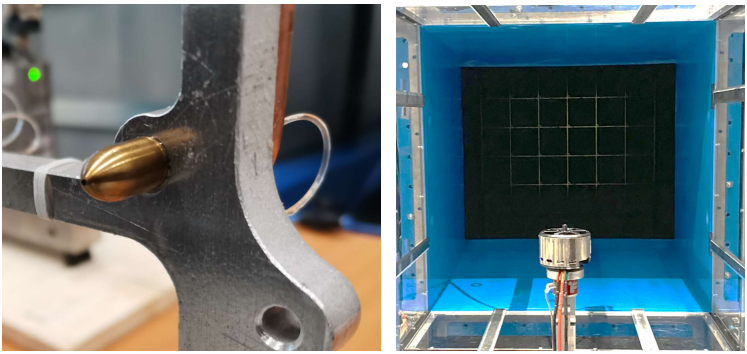


Figure 3.9: Wind tunnel setup for the closed test section (propeller 2).

B. PTV Setup

B.1 Seeding and Illumination

An orifice-type helium-filled soap bubbles (HFSB) rake of dimensions 1.2×1.4 m, is employed for seeding the wind tunnel flow. It is comprised of $7 \times 8 = 56$ generators of outer diameter of 1 mm (Figure 3.10a), spaced 20 cm apart with respect to one another. The seeding rake was placed upstream of the contraction (Figure 3.10b) in order to minimize the flow disturbance induced by its wake. It was positioned from the beginning of the closed wall test section measurements and not only for the PTV cases. The fluid supply unit operating conditions are adjusted such that they will produce a regular, periodically stable, bubble generation of monodisperse size distribution (bubbling regime, Faleiros et al. [18]). For more information regarding the generators, the control, production and the tracing fidelity of the HFSB, the reader is referred to Caridi [10] and Faleiros [19].



(a) HFSB Nozzle.

(b) Seeding rake inside the settling chamber of the AWT.

Figure 3.10: The AWT orifice-type helium-filled soap bubbles (HFSB) seeding rake.

The illumination source consists of a Quantel Evergreen 200 mJ double-pulse Nd:YAG laser (2×200 mJ at 15 Hz) which is placed along the sidewall of the tunnel opposite to the side-wall viewing camera 3. (see Figure 3.12). For minimizing the shadows that the propeller and the test stand would form, the laser beam is passed through a 50%-50% beam splitter. That results in the simultaneous shot of two beams from two different positions. In order to avoid damaging the beam splitter due to high laser intensity, the beam is expanded with the use of a set of concave and convex lenses. Additional mirrors are used to direct the laser beam at the desired positions. Finally, each beam is fired through an optical diffuser, which breaks the spatial coherence of the beam and is magnified by an additional concave lens. The former treatment is made in order to avoid any probable speckle patterns which will in turn bias the particle tracking [70]. The whole optical setup described above, along with the laser head is shown in Figure 3.11.

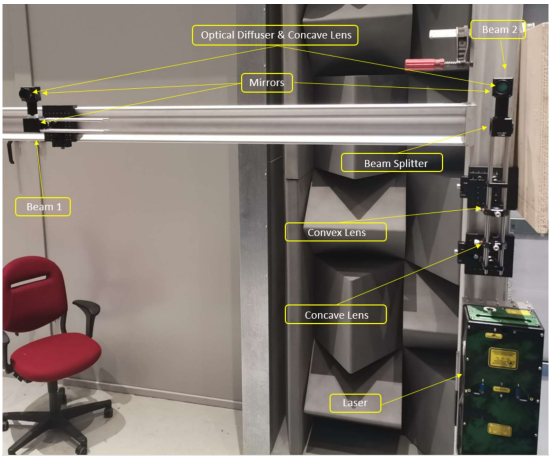


Figure 3.11: Optical setup and double illumination strategy.

B.2 Imaging and Recording

The recording system consists of three sCMOS high-speed cameras (35 mm lens, 2560 x 2160 pixels, 6.5 μm pixel pitch), set at aperture f# =11. Cameras 1 and 2 are arranged in an in-line configuration, from the top wall, while the third camera's (3) line of sight is from the side wall, opposite to the laser illumination. Figure 3.12 presents the image recording setup. The camera calibration was performed with a 2D calibration plate placed at three successive heights of constant increment Δh =23.6 cm, starting from the tunnel floor. Imaging view of the measurement volume is presented in Figure 3.13, for all three cameras for a propeller at 0° incidence angle, by means of raw camera images.

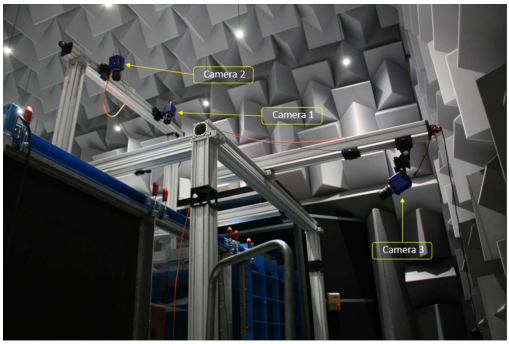


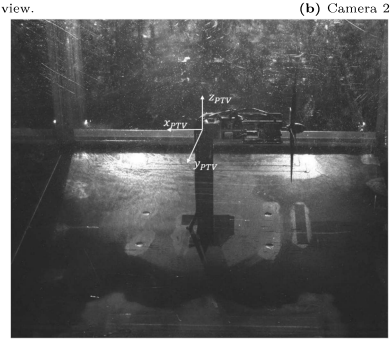
Figure 3.12: Imaging Setup.



(a) Camera 1 view.



(b) Camera 2 view.



(c) Camera 3 view.

Figure 3.13: Raw images of the measurement volume, PTV coordinate system and illumination directions.

B.3 Image and Data Processing

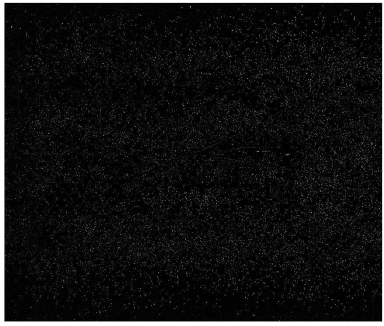
From the above figure, it is clear that the third camera's images have strong reflections (high background intensity), compared with the other two cameras. Moreover, unsteady background reflections are present in the recordings especially for camera 3 in the vicinity of the floor. In order to perform particle tracking the background intensity needs to be removed. This is achieved through image pre-processing. Initially, a time filter is employed which subtracts the minimum image intensity found within every 3 images, followed by a spatial filter which subtracts the local minimum over 5 pixels region, from each image pixel. Image background intensity is significantly minimized. In order to improve the inhomogeneous intensity between cameras 1,2 and 3, all images are normalized with the local average over a 10 pixel region. Finally, all intensities are normalized to the first frame. The third step involves the Gaussian smoothing and sharpening of the particle images and the multiplication of each pixel with a factor of 10. The result of image pre-processing is presented in Figure 3.14, where the images correspond to their raw counterparts shown above.

Despite of the measures taken in order to minimize the propeller, strut and wall reflections (spray painting), any reflection from the propeller blades and the motor might introduce errors, but since the flow surrounding the propeller is of interest, it is considered acceptable. LaVision DaVis 10.2.1 software was used for every PTV-related processing [52]. Furthermore, a Volume Self-Calibration (Wieneke [97]) is employed in order to reduce the geometric calibration errors to levels lower than 0.1 pixel for a volume of ($0.7\times0.5\times0.45$ m^3) in the vicinity of the propeller and to calculate the Optical Transfer Function (Schanz et al. [76]). The forementioned steps are essential for the double-pulse STB algorithm.

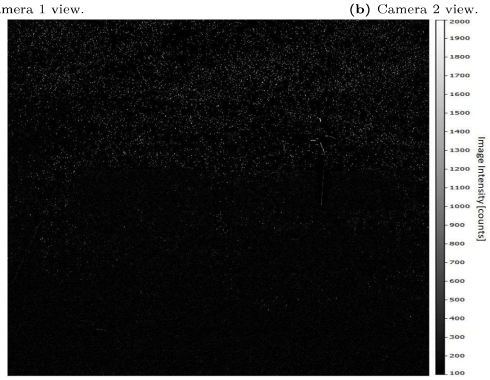
Instantaneous velocity is obtained for each identified track from the finite difference scheme. The velocity is transformed to a uniform Cartesian grid by a Gaussian weighted average based on the distance of the track from the grid point. The TP-STB cannot capture acceleration of the particles, thus, the velocities obtained at each measurement pulse are time-averaged. The subvolume (bin) size is 9 mm and corresponds to a vector pitch of 2.25 mm for a given 75% overlap. The dynamic spatial range (DSR) defined as the ratio of maximum to minimum captured lengthscale in the domain is approximately 80. An outline of the most relevant parameters with respect to the PTV setup is given in Tables 3.4 and 3.8.



(a) Camera 1 view.



(b) Camera 2 view.



(c) Camera 3 view.

Figure 3.14: Pre-processed images of the measurement volume (intensity scale is same for all three figures).

Table 3.4: Relevant parameters regarding the PTV setup and measurements.

Parameters	
Magnification	0.023
Object Focal Length [mm]	45
Aperture f#	11
Light-sheet Cross-section ($x \times z$) [m^2]	0.9×0.6
Measurement Volume ($x \times y \times z$) [m^3]	0.7×0.5×0.45
Number of Sub-volumes (Volume Self-Cal)	5×5×5
Image Acquisition Rate [Hz]	15
Number of Images	2000

C. ATF Optimization

The boundary layer scoop has a plate which can reduce the effective tube diameter upstream of the pump such that the suction rate is regulated. As mentioned before, the boundary layer suction pump had been optimized by Pernsteiner [62] for a velocity of 40 m/s at a fully open effective tube diameter. In order to achieve an effective boundary layer suction, the pump needs to be optimized for all the velocities tested (Table 3.5). The velocity of the sucked air, upstream of the pump, is estimated (equation (81)) with the use of two pressure taps measuring total and static pressure respectively. Given that the system was already optimized for the case of 40 m/s [62], the desired velocity $V_{pump,40}$ inside the pump was revealed. This velocity served as a target for testing at lower wind tunnel velocities. With the pump operating at zero tunnel speed, given a plate position, the optimized tunnel velocity can be estimated from equation (82). This procedure is repeated such that all the velocities of interest have a corresponding plate position (effective tube diameter). It is found that in order to effectively scoop the boundary layer, the following plate positions shown in Figure 3.15 in purple, are desired, where d denotes the plate's position with respect to the fully open (optimized at 40 m/s) diameter d_o and u_∞ is the wind tunnel velocity normalized with its previously optimized value (40 m/s). From that figure it is also clear that the reduction of the effective tube diameter (plate position) has a strong effect between the tunnel speeds corresponding for 40 m/s (fully open) to 25 m/s, while a further reduction of the tube's diameter has hardly any effect. Therefore, it was decided to switch the plate's position d/d_o from 1 at 40 m/s, to 0.8 and 0.4 for the speeds 35 and 30 m/s respectively. Further adjustment of that valve is neglected due to its small influence. This is shown in the red curve of Figure 3.15.

$$V_{pump,40} = \sqrt{\frac{P_{t,pump,40} - P_{s,pump,40}}{0.5\rho}} \tag{81}$$

$$u_\infty = V_{pump} \frac{40}{V_{pump,40}} \tag{82}$$

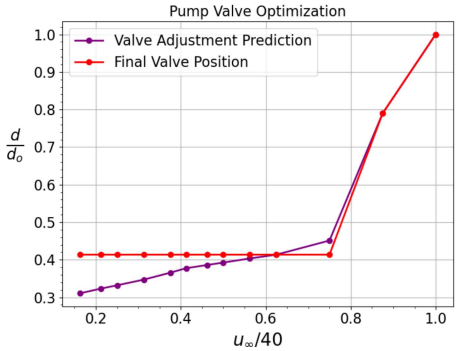


Figure 3.15: Normalized plate position based on estimated wind tunnel speed.

3.1.3. Simulation & Test Conditions

Both propellers are tested in the low-speed regime at incidence angles of 90°, 60° and 0°. The test stand is placed at a fixed streamwise position of 0.9 m and 0.95 m from the start of the nozzle along the tunnel centerline for the closed wall and 3/4 open-jet test section respectively. The propellers are tested in a variety of vertical positions according to the test matrix (Appendix C.1.1). The maximum wind tunnel speed is limited to 40 m/s, because that is the maximum speed for the optimized ATF. Additionally, higher speeds correspond to advance ratios which are not of interest for this research. Initially, the speed of the tunnel is held constant to 40 m/s while the rpm of the propeller are gradually increased until values close the maximum are reached. In order to reach a lower advance ratio, the propeller rpm sweep described before, is followed by a tunnel velocity sweep. For a given propeller, once the maximum rpm have been reached, the velocity is varied from 40 to 5 m/s in accordance with Table 3.5. For the 3/4 open-jet test section the minimum tunnel velocity is 6.5 m/s, due to the tunnel fan constraints. This testing strategy applies for both rotors. Further considerations for the choice of this strategy is that the pressure measurements become relatively more uncertain at lower speeds due to the fixed measuring range of RAD transducers. This is discussed further in Appendix D.2. The Mach number corresponding to the given wind tunnel speed range and the Reynolds number based on the hydraulic diameter of the nozzle are shown in Table 3.6. Moreover, the tip Mach number at maximum rpm and the Reynolds number based on the chord length of the propeller blade at 70% radius and wind tunnel speed are given in Table 3.7.

Table 3.5: Wind tunnel velocity sweep.

$\mathbf{u_\infty}$ **[m/s]**	40	35	30	25	22.5	20	18.5	16.5	15	12.5	10	8.5	6.5	5

Table 3.6: Range of the relevant dimensionless numbers based on the wind tunnel parameters.

	Ma_∞	$Re_{D_h} \times 10^6$
Closed TS	0.015 - 0.12	0.32 -2.6
3/4 Open-Jet TS	0.019 - 0.12	0.23 - 1.8

Table 3.7: Range of the relevant dimensionless numbers based on the propeller parameters.

	Ma_{tip}	$Re_{c_{0.7R}} \times 10^4$
Propeller 1	0.3	1.2 - 9.5
Propeller 2	0.6	0.6 - 4.9

Static pressure measurements are performed for both propellers and test sections. Initially, the empty test section wall pressures are measured for all the forementioned velocities, followed by measurements with only the strut and motor installed inside the test section. The former was made in order to capture the empty tunnel's boundary layer growth and wall divergence effects. Furthermore, the strut and motor pressure measurements are used in order to appropriately correct the propeller tests due to their associated blockage effects. This is made possible by subtracting the respective pressure coefficients for the test stand from the ones measured for the propeller at a given tunnel dynamic pressure q, under the assumption of small perturbation flow (Appendix A). Only the motor of propeller 1 is measured along with the strut, as shown in Figure 3.10b, due to limited time, but the effect of the size difference between the two electric motors is expected to be negligible. The above testing strategy is the same for both test sections employed. In the case of the ATF, the boundary layer suction pump's inlet effective diameter is adjusted for the three speed ranges in accordance with the optimization described before. The PTV measurements are performed separately from the wall pressure measurements due to probable clogging of the pressure transducers by soap. Only propeller 2 is tested, since the available seeding area is considered insufficient for the propeller 1 tests. The velocities corresponding to the PTV measurements are shown in Table 3.8. The seeding density for the higher tested velocity (40 m/s) was significantly lower than for the rest of the test points. Each measurement consisted of a sequence of 2000 recordings acquired at a rate of 15 Hz. The pulse separation time Δt was adjusted for every wind tunnel velocity in the test matrix such that the translation of a single particle in free-stream, would roughly correspond to 10 pixels. This is due to the fact that the main flow was also of interest and not only the propeller slipstream.The PTV test matrix is presented in Appendix C.1.1.

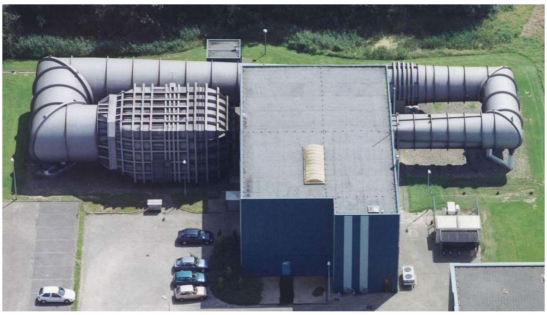
Table 3.8: Relevant PTV recording and data processing parameters based on the wind tunnel free-stream velocity.

$\mathbf{u_\infty}$ **[m/s]**	40	20	12.5	8.5
$\mathbf{\Delta t}$ **[**μ**s]**	88	176	280	414
Particle Shift (free-stream) [pix]	10	10	10	10
Seeding Density [bubbles/m^3]$\times$**10^5**	1	2	3.2	4.7
Bin Size [mm]	13	9	9	9
Vector Pitch [mm]	3.25	2.25	2.25	2.25
DSR	55	80	80	80

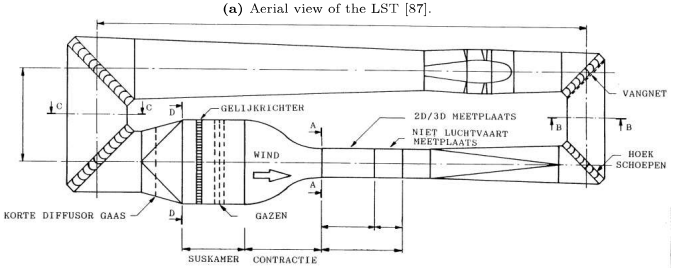
3.2. The DNW-LST Campaign

3.2.1. The DNW-LST Facility

The Low-Speed-Wind Tunnel (DNW-LST) is an industrial, atmospheric, closed circuit wind tunnel with exchangeable closed test sections powered by an electric motor of 700 kW. The closed-wall test section has a rectangular cross section of 3.0 m width, 2.25 m height and a total length of 8.75 m. Maximum speeds of up to 80 m/s can be achieved [12]. Free stream turbulence intensity ranges within 0.04% to 0.1% for the achievable velocity range 5 - 80 m/s respectively, due to its (9:1) contraction ratio, the honeycomb-type rectifier and three fine-mesh anti-turbulence screens installed at the settling chamber as shown in Figure 3.16b. The LST consists of an interchangeable Aeronautical and a fixed Industrial test section. An aerial and a circuit view of the LST are given in Figure 3.16.



(a) Aerial view of the LST [87].



(b) Circuit view of the LST [87].

Figure 3.16: The DNW Low-Speed-Wind Tunnel (DNW-LST).

3.2.2. General Test Setup

The Aeronautical Test Section

For the interference-free performance measurements, the Aeronautical test section is used along with a ground board of 4.1 m length, laterally spanning the whole test section and mounted 30 cm above the floor of the test section. The test stand's ground plate is fixed to the floor, and the strut protrudes the ground board at about 1.5 m downstream its leading edge. The test section velocity is monitored with a single pitot tube positioned 0.41 m below the ceiling, 0.7 m from the right side-wall of the tunnel and at the strut's streamwise position. The ground board, strut and pitot tube are shown in Figure 3.17. Since the boundary layer of the LST tunnel floor is significantly bigger than the ones of the previous test campaign, the purpose of this ground board is to form a new boundary layer such that the IGE testing conditions are considered comparable. Regarding the OGE conditions, a rectangular test section of an effective height of 1.9 m is considered due to the existence of the 5 cm thick board. For both propellers, the thrust and electric power are measured, as with the previous test campaign described in section 3.1.2. Propeller 2 was successfully tested at the tunnel centerline (OGE) and at the same (absolute) height (IGE) as in the closed test section of the NLR-AWT for the incidence angles of 90° and 0°. Similarly, propeller 1, was tested in-and-out-of-ground only for the incidence angle of 0°. For the lifting angles, when tested at the tunnel centerline, this propeller was inducing strong vibrations due to the strut's thin structure. Therefore, the baseline performance measurements are taken only for IGE at an angle of attack of 90°. All simulation conditions are given in Appendix C.2.1. Finally, the ratio between the test section (measured by the pitot) and the tunnel reference (measured inside the contraction) dynamic pressure q_m/q_{ref} is determined from two separate measurements. This was implemented because the empty tunnel calibration is not considered to be valid due to the presence of the ground board which introduces a substantial blockage effect. Measurements 1 and 2 shown in

Figure 3.18, correspond to the beginning and the end of the measurement campaign respectively, and are conducted without the presence of the propellers. In general, there is a good repeatability and most of the tested conditions exhibit a minor deviation mostly at lower wind tunnel speeds where the uncertainty of those measurements is higher. Figure 3.18 confirms the consideration of blockage introduced by the ground board and turned out to be around 6.5% of the flow reference system measured dynamic pressure.

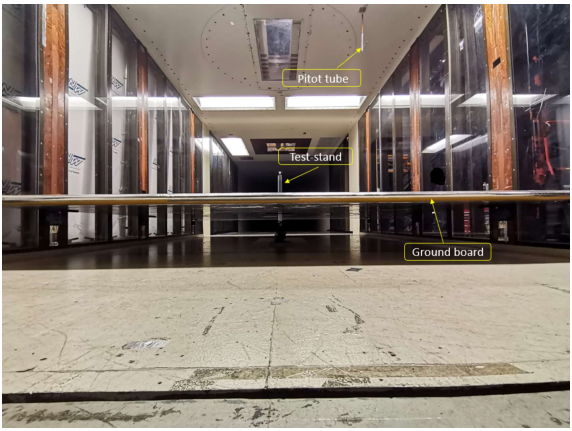


Figure 3.17: LST tunnel test setup during the test section calibration.

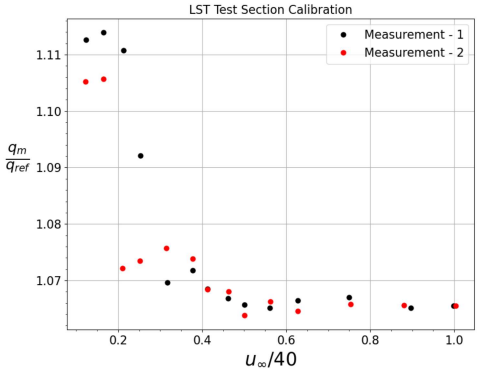


Figure 3.18: LST tunnel calibration factor for the tested free-stream velocities.

4

Results

This Chapter comprises of the results of the whole research. Initially, the global flow characterization based on the wall pressure measurements and the time-averaged PTV is given, followed by the applied wall correction methods for free-air and in-ground effect. The distinction is based on the angle of attack of the propeller, which corresponds to a different flow condition. Moreover, the flow breakdown limits for both tests sections and lifting angles are defined and compared with available criteria and with the measured static pressure distribution at the walls. Finally, the interference-free performance measurements are compared with the data from the NLR-AWT test campaign. In the end of each section, there is a discussion part which summarizes some important observations realized within this research.

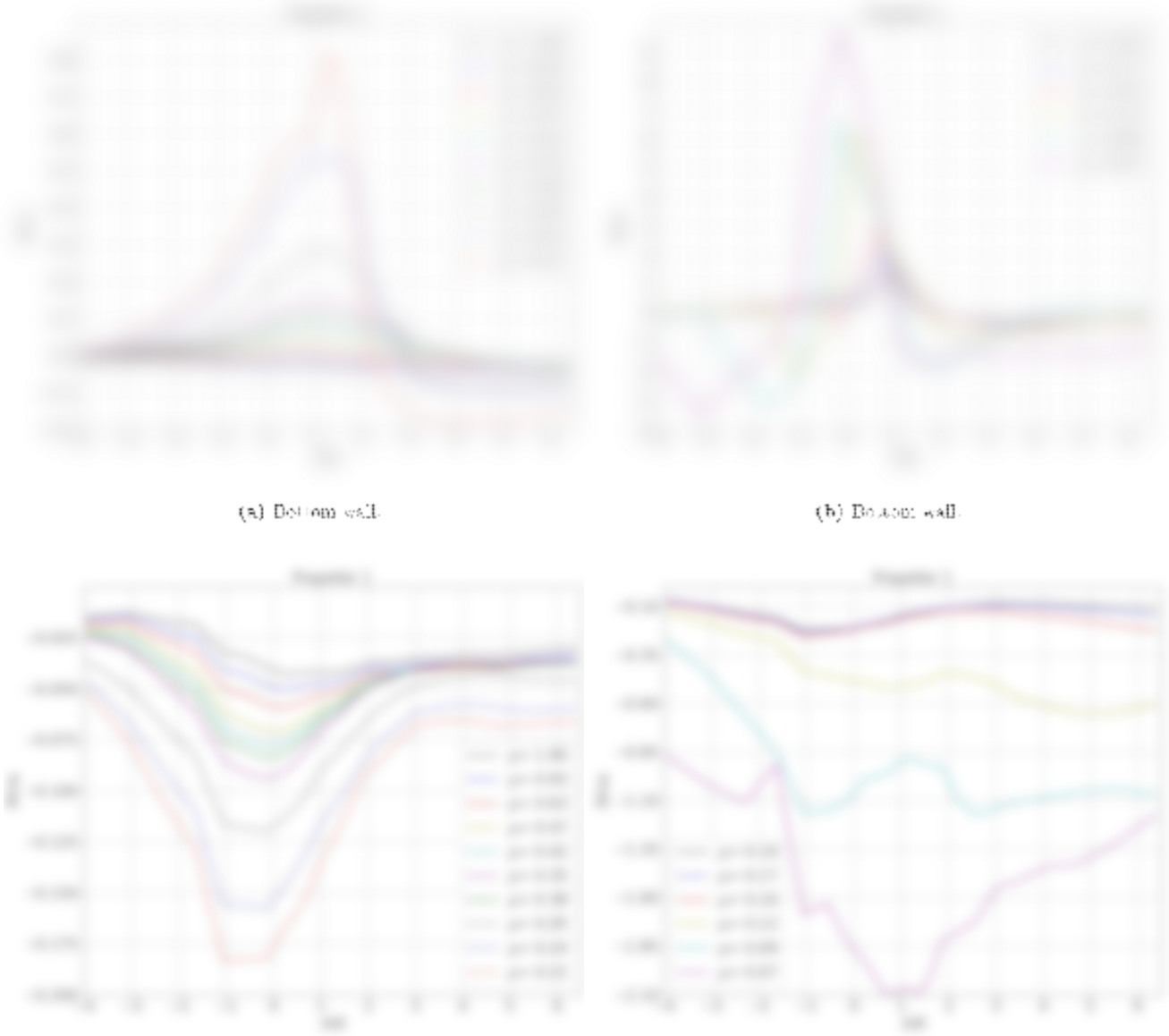
4.1. Global Flow Topology

Results from two different measurement techniques are presented in order to describe the time averaged flow field for the propeller tests at each angle of attack. As discussed before, the conditions vary with respect to the angle of attack since the propeller induced flow field changes in magnitude and direction.

4.1.1. Wall Static Pressure Signatures

The wall pressures are presented in the form of a difference in pressure coefficients ΔC_P between the propeller and the empty test section along with the test stand measurements. The wall pressures are differing strongly in sign and magnitude, therefore, the presented data are further split between higher tunnel velocities (high advance ratios) and lower ones (low advance ratios) corresponding to relatively low and high ΔC_P 's respectively. Moreover, selected data from certain measurement locations, which are considered the most indicative are presented here for conciseness. The numbering system of the shown pressures is in accordance with Figure 2.14, while the PTV coordinate system is used (see Figure 3.13) for the streamwise coordinate which is normalized with the propeller radius. The precise location of each pressure transducer can be also found in Appendix C.1.2. For clarity, it is highlighted that the two propellers have a different rotation direction, thus, for comparison reasons the wall pressures are presented with respect to the rotation of the blade (advancing, retreating side).

90° Incidence Angle



(a) Bottom wall

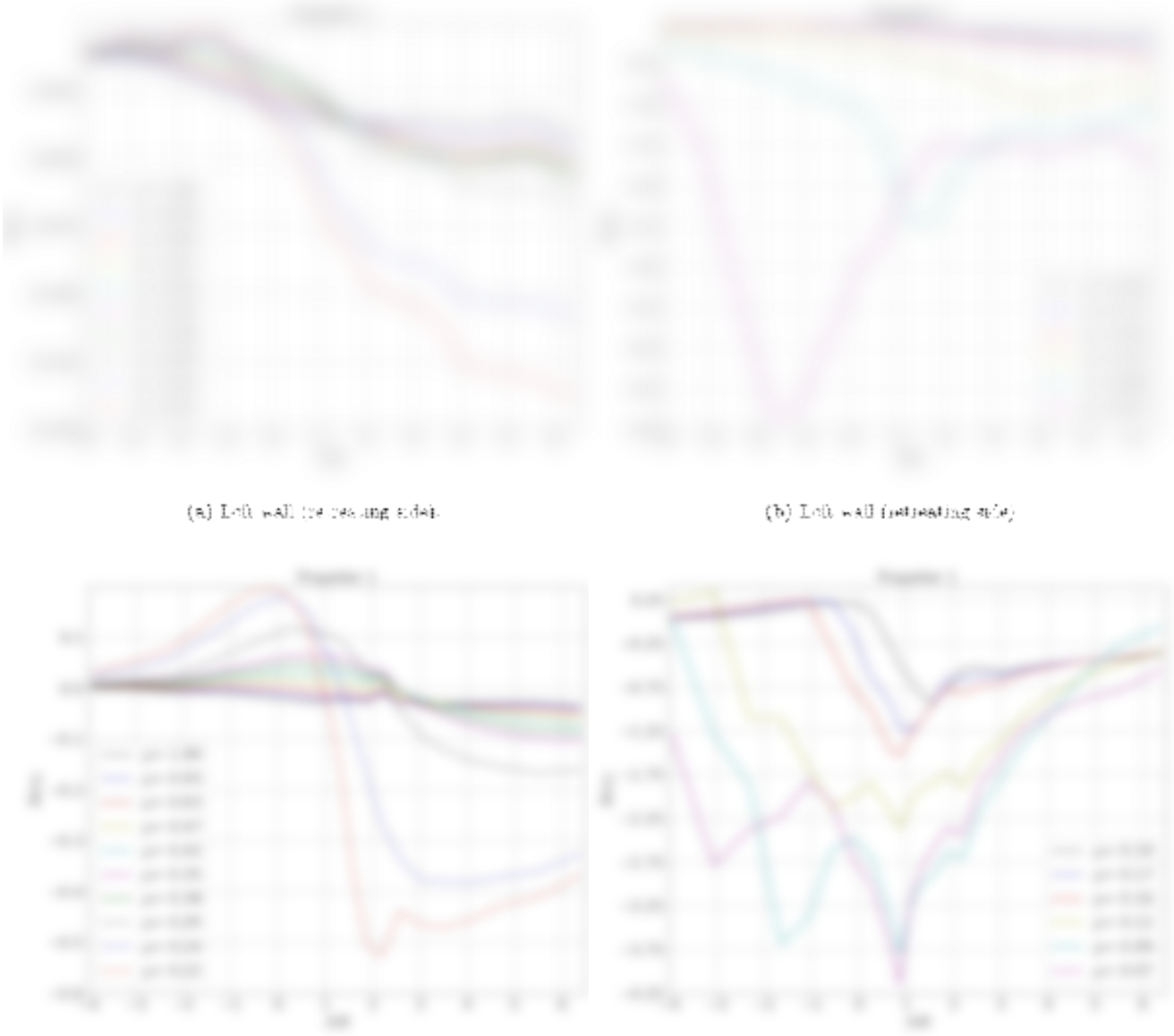
(b) Bottom wall

(c) Top wall

(d) Top wall

Figure 4.1: Pressure coefficient distributions at the following axial stations: [illegible] on the top wall (bottom figures) for different advance ratios (pressure becomes more negative as [illegible])

Regarding the pressure distribution on the bottom wall, the same trend is observed for both propellers. Figures 4.1a and 4.1b show that the bottom wall pressure experiences the most significant drop at the leading edge of the propeller. This behavior is physically realistic as the leading edge of the propeller is the first point of contact with the incoming flow, causing the fluid to accelerate and the pressure to decrease. As the flow progresses along the propeller surface, the pressure gradually recovers, indicating a deceleration of the fluid. This pressure recovery is a result of the conversion of the propeller's kinetic energy into pressure energy. The pressure gradient is also affected by the presence of the propeller blades, which create a region of low pressure on the suction side of the blades and a region of high pressure on the pressure side. This pressure difference is responsible for the generation of thrust by the propeller. The pressure distribution on the top wall is also affected by the presence of the propeller, but to a lesser extent than the bottom wall. This is because the top wall is further away from the propeller and the flow has already undergone some deceleration and pressure recovery by the time it reaches the top wall. However, the top wall still experiences a region of low pressure near the propeller, indicating that the propeller's influence is still felt at this location. Overall, the pressure distribution on the bottom and top walls is consistent with the expected behavior of a propeller in a flow field, and the differences between the two walls can be attributed to the different distances from the propeller and the different flow conditions at each location.



(a) Left wall (advancing side).

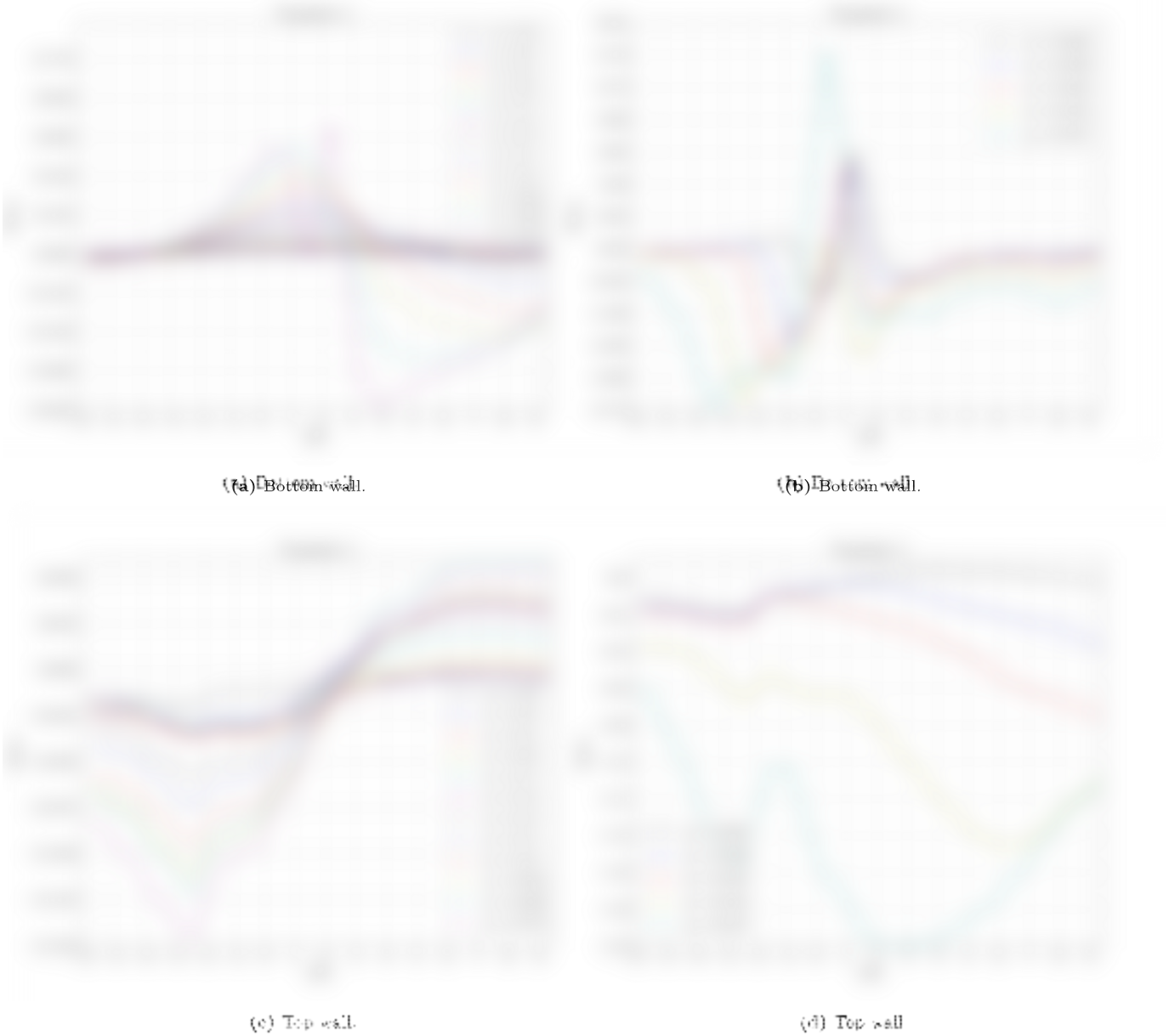
(b) Left wall (retreating side).

(c) Right wall (advancing side).

(d) Right wall (retreating side).

Figure 4.2: Pressure coefficient distribution of the lower side wall (left figures) and on the right wall (bottom figures) for different testing conditions between the anchoring system in accordance with Figure 3.14, right and left wall corresponds to [illegible] figure orientation.

Similar with Figure 4.1, Figure 4.2 presents the pressure distribution over the bottom and top wall for the smaller propeller (S). Again, the static pressure measurements close to the advancing blade (green = 0.6 and 0.8 for the propeller rotation) [illegible] Regarding the bottom wall pressure signature, there is a gradual pressure increase slightly behind the propeller above the figure (x/c = 0). Due to the presence of advance ratio, a pressure peak is formed along with an under-pressure propagating downstream (Figure 4.2b). The similarity of the bottom wall pressure signature is evident between the two of [illegible]. The overall [illegible] is magnified by the boundary layer [illegible] is not necessarily given as explained earlier for the case with propeller (Figure 4.1b). This is because the propeller is smaller than the aperture for the pressure taps to sense the same natural behavior for both closed wall cases. Therefore, the [illegible] probably happens closer to the [illegible] ($y = 0$, then to the wall location of the measurement ($y = 0.5$ m). This is the reason why accelerated [illegible] decelerated due to strong downwash and more unbalanced compared with the propeller I

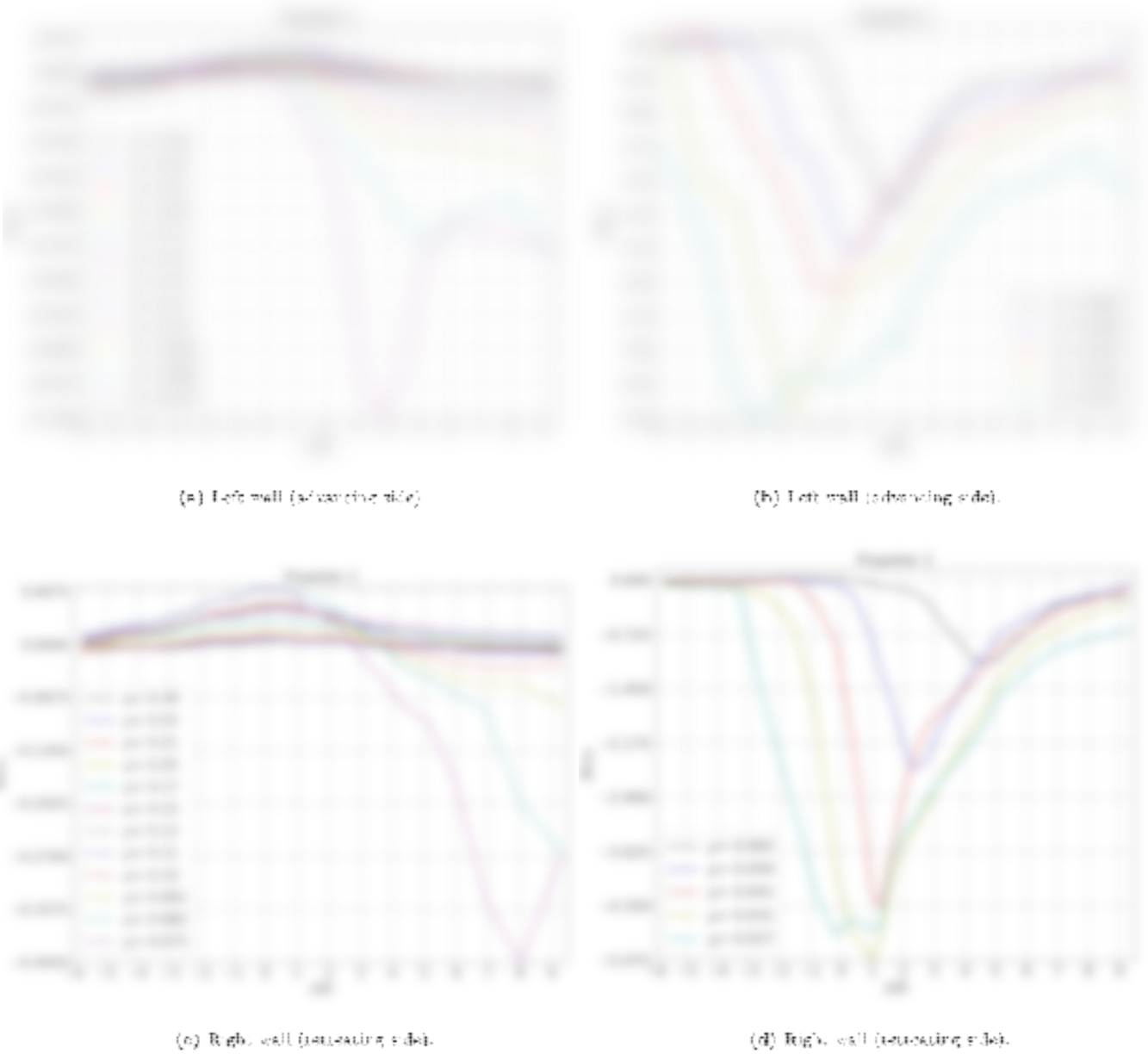


(a) Bottom wall. (b) Bottom wall.

(c) Top wall. (d) Top wall.

Figure 4.9: Pressure coefficient distributions of the side wall along axial coordinate location x_1/c on the top wall (bottom figures) for different advance ratios (pressure coefficient scale varies in accordance with Figure 4.4).

Figure 4.9a and 4.9b show the side wall pressure distribution on the advancing side of propeller 2. Over all truncated velocities the distributions is almost identical to that of propeller 1 (Figures 4.3a and 4.3b). This similarity between the two propellers can also be concluded for the side wall pressure distributions on the right wall of the wake tunnel (Figure 4.9c and 4.9d). Regarding the higher advance



(a) Left wall (advancing side).

(b) Left wall (retreating side).

(c) Right wall (retreating side).

(d) Right wall (advancing side).

(a) Bottom wall.

(b) Bottom wall.

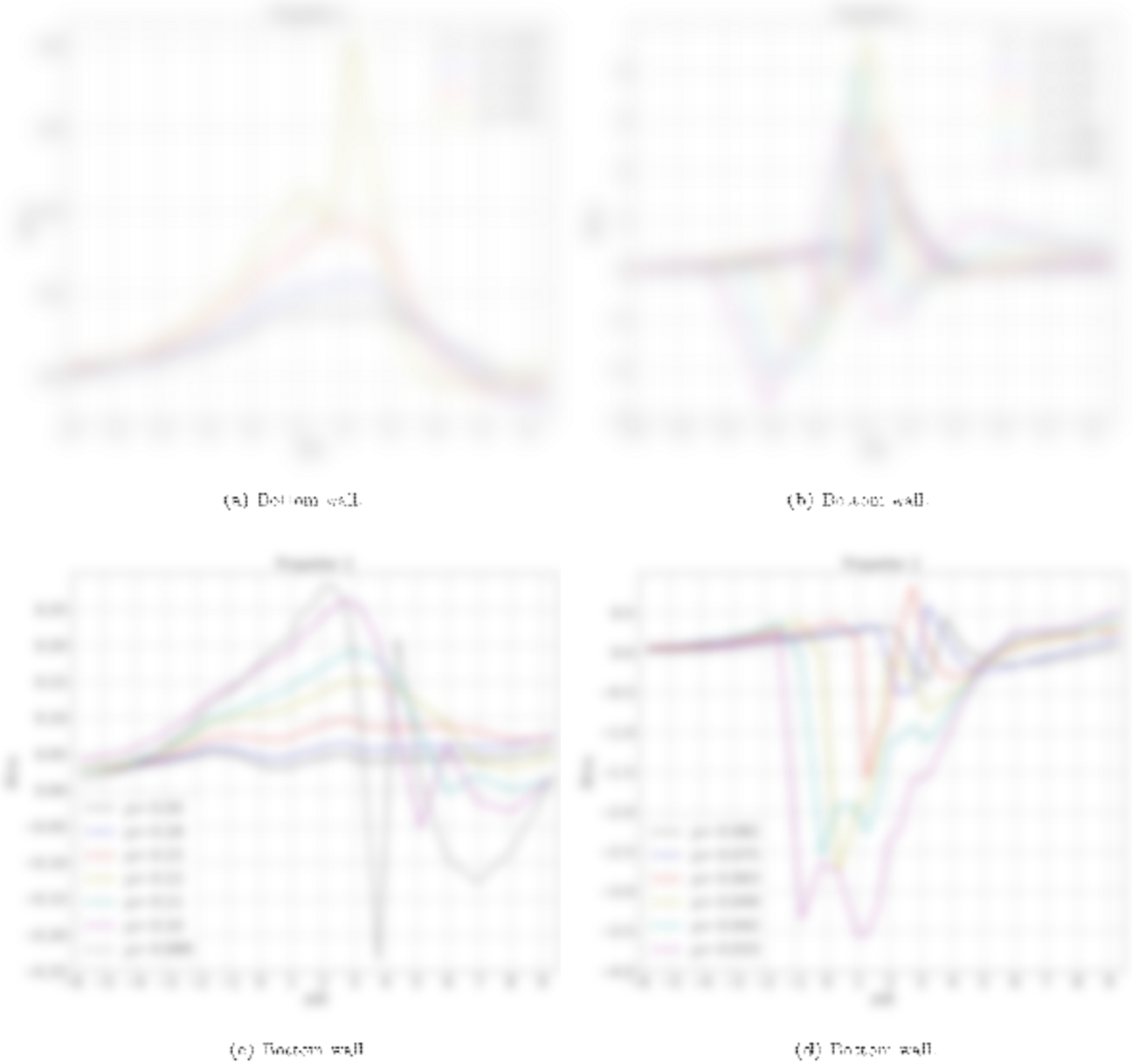
(c) Bottom wall.

(d) Bottom wall.

Figure 4.5: Mesh independence investigation results based on the local maximum pressure coefficient for the 0° incidence angle.

60° Incidence Angle

The wall pressure signature for the propeller tested at 60° incidence angle is not similar to those of the previous cases ($\alpha = 30°$). This is mainly due to the fact that there is a stronger vortical flow evident on this model. As the propeller rotates, it encounters the oncoming flow at a relatively high angle of attack. This results in the generation of a strong tip vortex that is ingested into the propeller disk. The vortex then interacts with the blade leading edge, inducing a localized suction peak that further amplifies the adverse pressure gradient. This results in the propeller being slightly less efficient than the axial case, but there is more blade area engaged in the flow. The propeller's power coefficient is $C_P = 0.0$ (Table 4.1) for the given case. Figure 4.7 shows the blade surface pressure distribution at the leading edge between the hub and the tip. The similarities between the current and the 30° incidence angle are profound. The blade's suction peak is also evident at the tip, which is the region where the highest velocities are encountered. The vortex is also evident in the contour plot. Another key feature that corresponds to a low work possible is the separation of boundary layer flow. It is higher for the current case compared to the 30° incidence angle. The vortex is observed to interact with the blade leading edge at 0.8R and then it is ingested into the propeller disk. The vortex is still evident in the wake, but its strength is reduced. Moreover, the vortex is also observed to be interacting with the blade at 0.6R, but it is not as strong as the one that is observed at higher radial locations. This is due to the fact that the local velocities are lower at lower radial locations, thus the propeller's loading is reduced.



(a) Bottom wall (b) Bottom wall

(c) Bottom wall (d) Bottom wall

Figure 4.6: Pressure coefficient distributions of the advancing side on the bottom wall of the closed-wall test section for properties 1 (left figures) and properties 2 (right figures) for different submersion ratios

Figure 4.6 presents the wall pressure coefficient distributions of the advancing side on the bottom wall of the VIT for the closed-wall test section. The results are similar with the closed test section, as mentioned earlier with the purely lifting case. The progression of the impinging jet with increasing submersion ratio can be tracked by following the location and magnitude of the wall pressure peak. Figure 4.6a shows that the impinging jet for very small submersion ratios still produces a wall pressure peak, albeit a very small one. The evolution that the pressure peak undergoes is quite similar to that of the free-surface case (Figure 4.4). The existence of a second peak, which was observed in the free-surface case (Figure 4.4 with $h/c = 0.6$), is also present in the closed-wall case. More discussion with respect to flow separation and stagnation points and their movements is given in section 4.3.

(a) Bottom wall.

(b) Bottom wall.

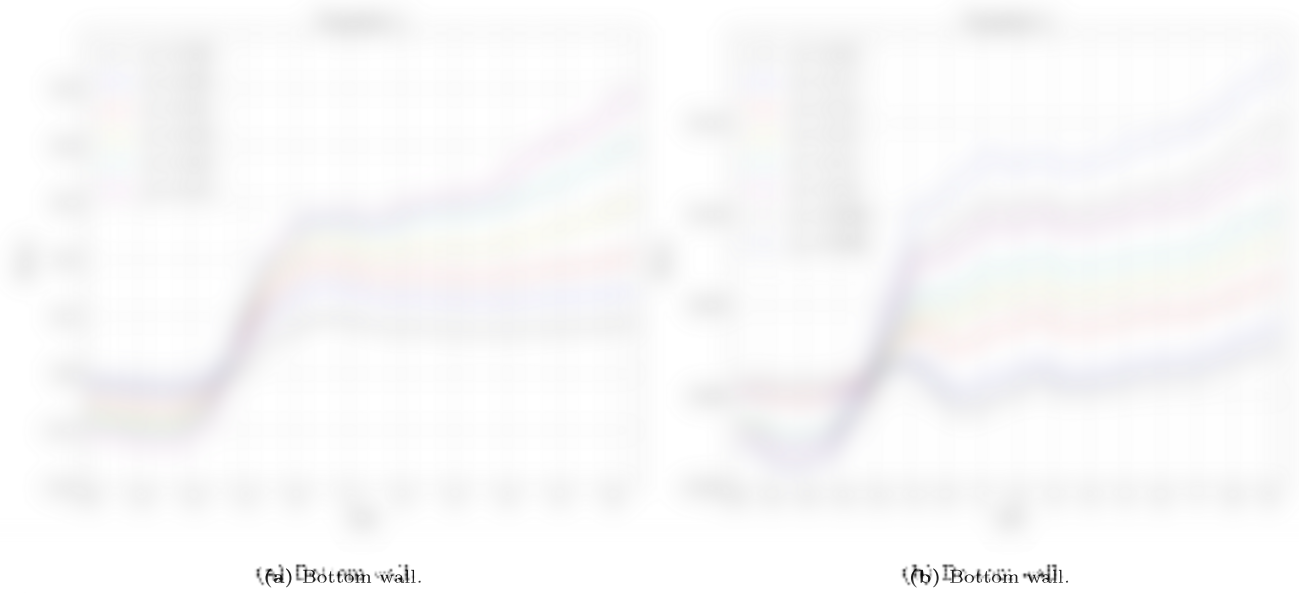
(c) Bottom wall.

(d) Bottom wall.

Figure 4.2: Rotational direction of propeller rotation based on the local reaction in pressure coefficient for the 0° incidence angle

0° Incidence Angle

As expected for the propeller rotating at an incidence ($\alpha = 0°$), the flow topology is different than the one presented above. In contrast to the propeller position in the previous section, both the standard and ground propeller need to account for the bottom wall. Thus, the bottom wall pressures are accounted for as significant areas of propeller wake mixing, or better, vortex shedding. Figure 4.1 shows the local pressure coefficient on the downwind surface for both propellers. As before, flow is from the root section ($\frac{r}{R} = 0$) and ends at the propeller tip ($\frac{r}{R} = 1$). For propeller 1 ($\omega = 2$ rad/sec), the tip vortex is evident at $\frac{r}{R} = 0.9$ and for propeller 2 ($\omega = 3$ rad/sec) at $\frac{r}{R} = 0.8$. Figures 4.1a and 4.1b also show that the ground propeller experiences a greater pressure coefficient. This is evident by the propeller's ability to achieve greater pressure gradients (pressure increase) in the vicinity of the propeller, which corresponds with a greater wake drop. Remember that the pressure gradient was used to calculate the higher thrust values, while it could also be the cause of the lower torque values. Since the top wall prevents the development of the flow velocity, which corresponds to the propeller's rotation, the development of the wake pressure field on the propeller surface can be attributed. The presence is clear from the static pressure field on the propeller hub.



(a) Bottom wall. (b) Bottom wall.

(c) Top wall. (d) Top wall.

4.1.2. Time-Averaged PTV Results

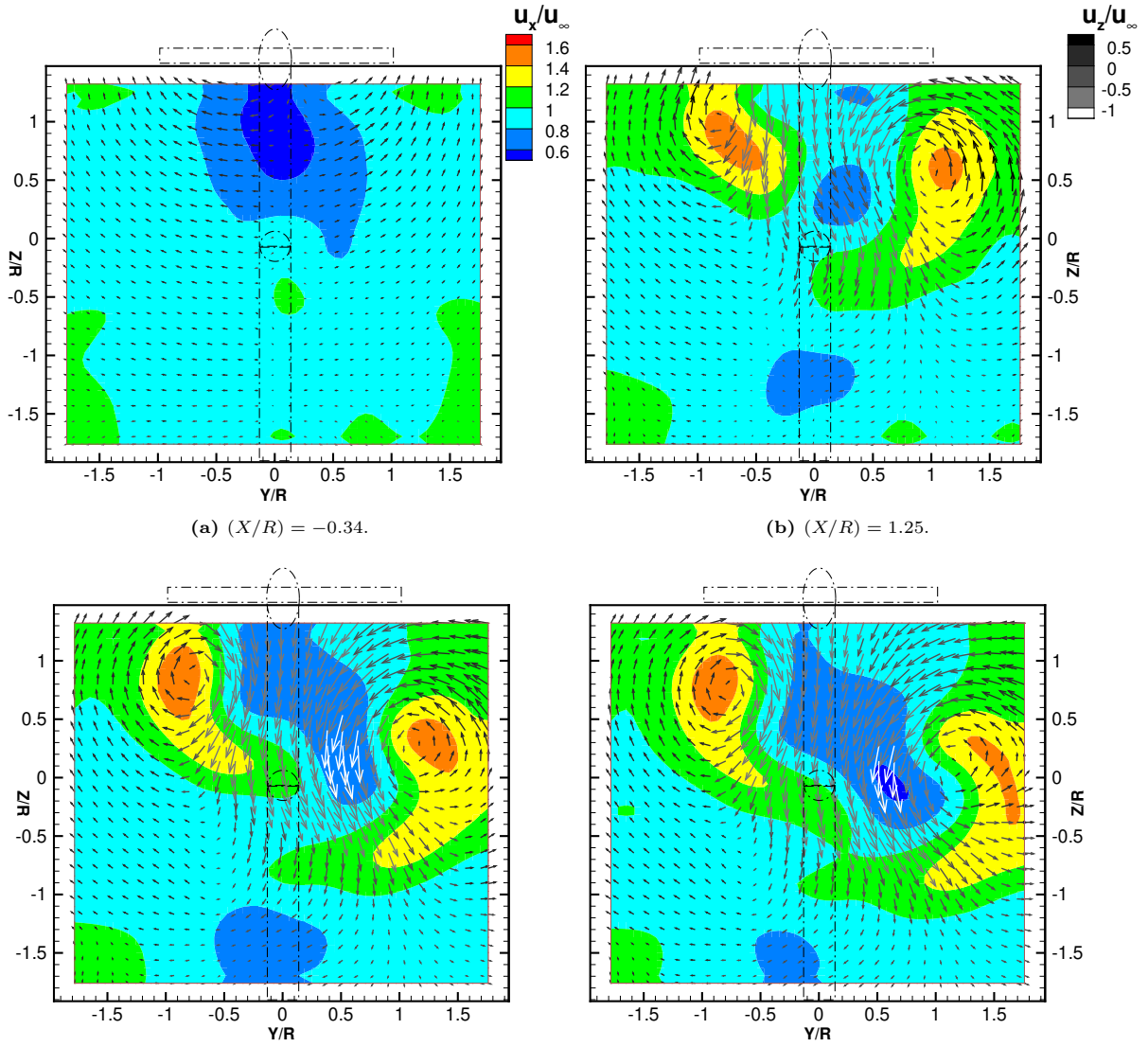
In this section the global flow topology is presented by means of the time-averaged PTV measurements. Two-dimensional contours of the 3D measurement volume are presented with the propeller and the test stand boundaries being depicted with a dash-dot line. The same coordinate system is used here, in which the origin is based on the position of the junction of the strut which is 27 cm above the bottom wall, 90 cm from contraction end and at the centerline with respect to the lateral direction y (see Figure 3.13c).

90° Incidence Angle

In order to characterize the flow regime for the 90° angle of attack, the intermediate case of $\mu = 0.1$ is chosen due to the observation of sufficient static pressure rise along the bottom wall, but not any signs of flow distortion as already shown in Figure 4.3a. Figure 4.11 shows 2D contours of the measurement volume at different streamwise positions in the vicinity of the rotor blades ($-1 \leq X/R \leq 1$) and further downstream ($X/R > 1$), where the rotor slipstream/wake advects due to the wind tunnel speed. In the majority of the blade region the flow is diverging from the centerline due to the rotor induced field (Figure 4.11a), however any significant downwash is not present in the measurement domain. Further downstream, at $X/R \approx 0.4$ a significant amount of downwash is observed, which eventually leads to the two counter-rotating vortices depicted in Figure 4.11b. Furthermore, it is observed that the vertical slipstream is not symmetric and that the advancing side vortex (right-hand-side (RHS), $Y/R > 1$) extends lower than the one on the retreating (left) side. This trend is also valid for the advection region ($X/R \approx 2$), where the wake is directed downwards. Additionally, the streamwise velocity on the left-hand-side (LHS) part of the slipstream is higher than that of the other side and thus, the strong flow entrainment from outside the slipstream area is directed towards the advancing side. This is also justified by the fact that the retreating side vortex core is not advected through the lateral direction ($Y/R \approx -1$), while the advancing side core translates slightly outwards ($Y/R > 1$) with increasing X/R. Figure 4.11d, explains the realization of probable flow wall impingement on the advancing side made by tuft observations and discussed in the previous sections, since there, the downwash is significantly stronger (see Figures 4.11c and 4.11d at $Y/R \approx 1$ and $Z/R \approx -0.5$), whereas on the other (retreating) side no downwash component is present. Still, the pressure rise on the advancing side of the bottom wall (Figure 4.3a) is not significant for the case of $\mu = 0.1$. That is because the rotor wake blocks the flow at a height of $Z/R \approx -0.2$ on the advancing side leading to streamwise velocity deficit (dark blue region) and side acceleration (red-yellow area on the RHS), however close to the bottom wall ($Z/R \approx -1.9$), the streamwise velocity is lower than the one measured by the wind tunnel reference system (u_∞), which justifies the static pressure rise measured at $Y/R = 1.6$. Likewise, at the advancing side side-wall, the measured ΔC_P at $Z/R = -0.2$ is negative as shown in Figure 4.4a for $X/R = 2.5$, which is due to the RHS acceleration described above and shown in Figure 4.11d.

Similar 2D contours are presented for the other two conditions tested at tunnel speeds of 40.56 and 12.5 m/s in Figure 4.12. For the higher tunnel velocity, most of the $x-$velocity in the volume exhibits a rise in the vicinity of the strut (Figure 4.12a) due to the strut blockage. As a result, the wake of the strut persists up to the end of the measurement domain as shown in Figure 4.12b. This strut blockage is present at every configuration tested on the tunnel velocity of 40 m/s and is further discussed in the 60° and 0° incidence angle flow topology. Moreover, no significant downwash is observed for that condition. The lower advance ratio depicted in Figures 4.12c - 4.12f, shows the propeller operating under an advance ratio of 0.062, where the measured pressure signature of the advancing side on the bottom wall at $Y/R = 1.6$ is significant and resembles flow impingement according to Figure 4.3b. Indeed, there is a significant downwash which persists all the way to the bottom right of the measurement volume (2 cm above the ground) as shown in Figures 4.12d and 4.12e. At those positions, the rotor wake persistently impinges on the floor of the tunnel but no significant $x-$velocity deficit is present such that an upstream propagating ground vortex is formed. However, there is a strong lateral recirculation which advects downstream. Advancing further downstream (see Figure 4.12f), the wake is forced to rotate in accordance with the RHS vortex rotation due to its ground proximity and the air-flow accelerates on the side in order to by-pass the streamwise velocity deficit region induced by the downwash. Nevertheless, the fluid in the bottom wall impingement region ($Y/R > 0.5$) advects downstream and no flow reversal is present as expected purely from the static pressure inspection. Thus, the impinging flow corresponding to a pronounced maximum in ΔC_P is considered valid, but the ground vortex and its propagation upstream hypothesis is not valid for the region of under-pressure measured in $-0.8 \leq X/R \leq 0.25$ (in Figure 4.3b). In any case, the flow is impaired and there seems to be some lateral recirculation in the proximity of the bottom wall of the tunnel at the advancing side ($Y/R > 0$). This condition is described by strong interactions between the bottom wall of the wind tunnel and the rotor wake and thus, it is possible that the data are non-correctable and flow breakdown has occurred. This is further discussed

in the next sections.



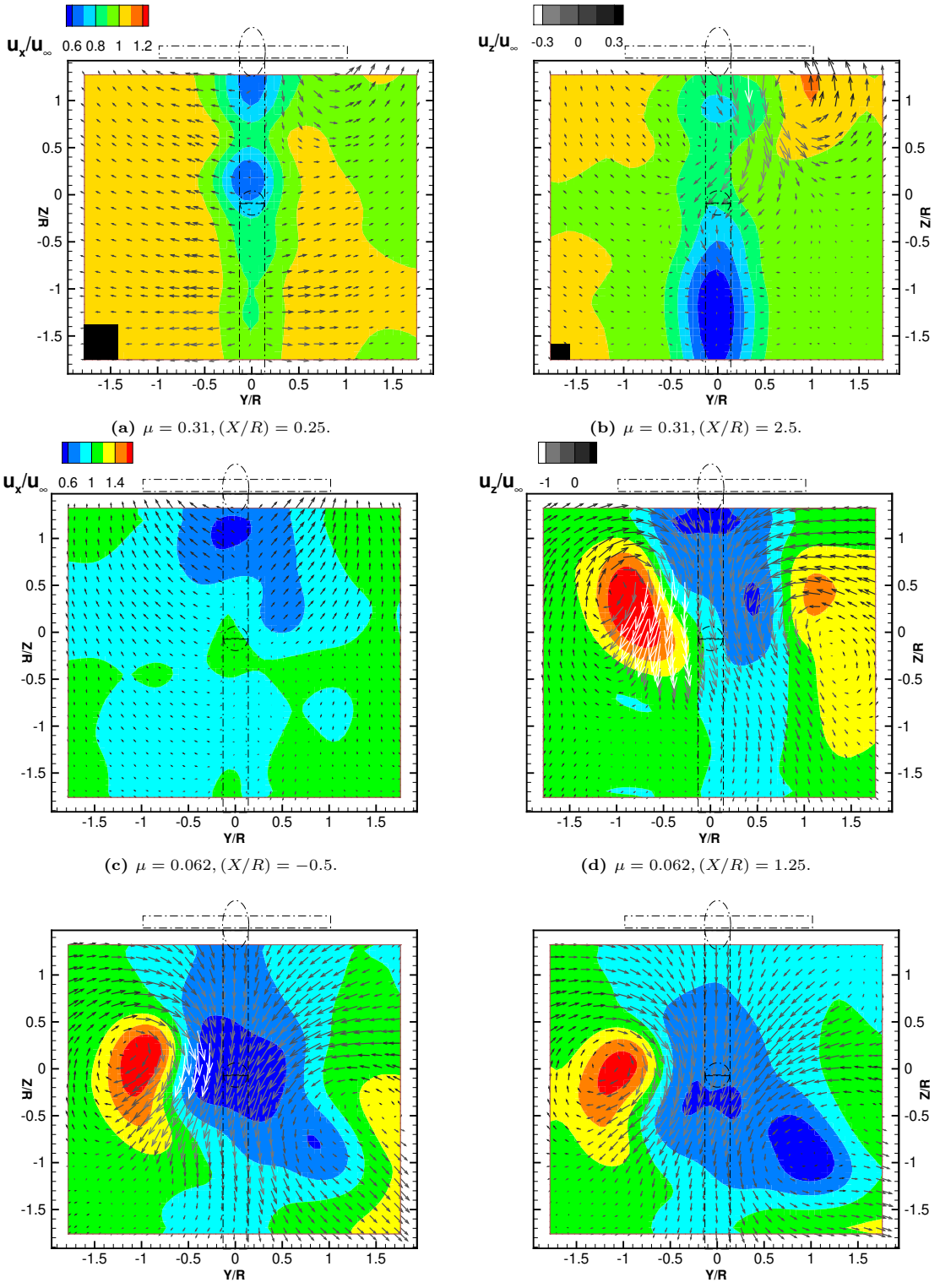
(a) $(X/R) = -0.34$.

(b) $(X/R) = 1.25$.

(c) $(X/R) = 2$.

(d) $(X/R) = 2.5$.

Figure 4.11: Axial and tangential velocity distribution within the measurement volume (x-slices) in the vicinity of the blades (a, b) and further downstream (c, d), for $\mu = 0.1$ (velocity vectors are flooded with the vertical velocity component).



(a) $\mu = 0.31, (X/R) = 0.25.$

(b) $\mu = 0.31, (X/R) = 2.5.$

(c) $\mu = 0.062, (X/R) = -0.5.$

(d) $\mu = 0.062, (X/R) = 1.25.$

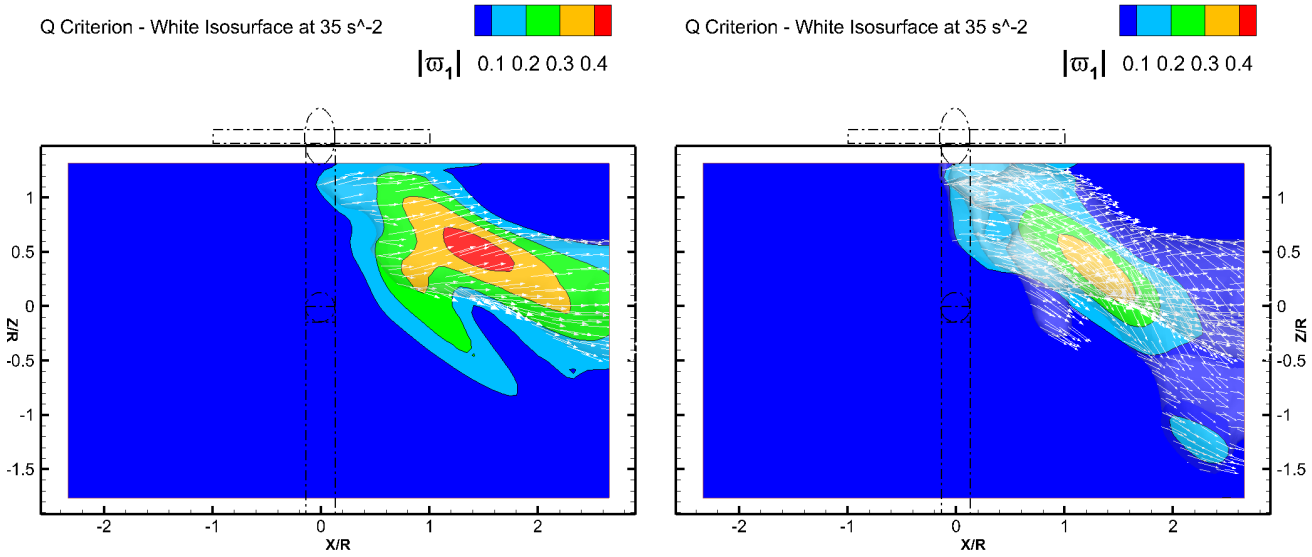
(e) $\mu = 0.062, (X/R) = 2.$

(f) $\mu = 0.062, (X/R) = 2.5.$

Figure 4.12: Axial and tangential velocity distribution within the measurement volume (x-slices) in the vicinity of the rotor blades (a, c, d) and further downstream (b, e, f), for two different thrust conditions at zero incidence angle (velocity vectors are magnified for $\mu = 0.31$, for $\mu = 0.062$ all scalings are the same with Figure 4.11), (areas with insufficient seeding are covered in black).

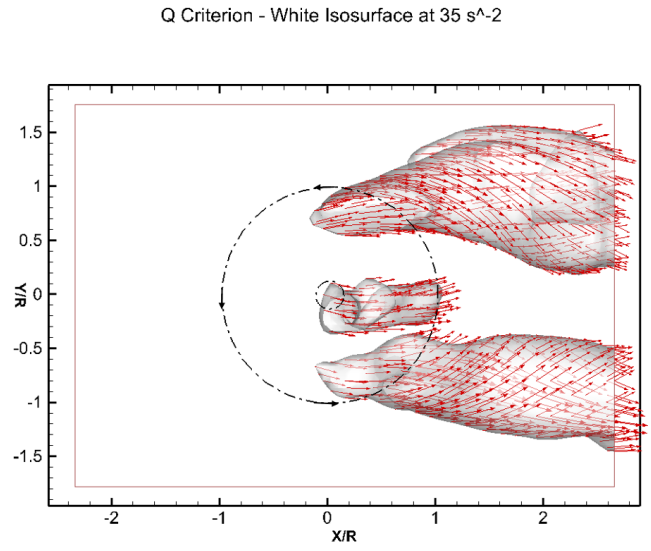
In a further attempt to investigate the difference in the measured in static pressure at $(Y/R = 1.60)$ for $\mu = 0.1$ and $\mu = 0.062$, the non dimensional vorticity magnitude along with the isosurface of the

Q criterion are presented in figures 4.13 and 4.14. From Figure 4.13d, it is seen that the isosurface corresponding to $Q_{crit} = 35\ s^{-2}$ identifies three dominant vortices. The two stronger are the ones already discussed in the previously. The third, is a weak vortex emerging from the blade root and the motor due to its hollow geometry (see Figure 3.9). The advancing side vortex is seen to extend almost all the way down to the ground thus, justifying the strong static pressure rise. On the contrary, for the case of $\mu = 0.1$ (Figure 4.14d), the advancing side vortex is not in ground proximity, thus the measured static pressure is not significantly high. The directions at which the wake is deflected on both sides is also clear and non-symmetric.

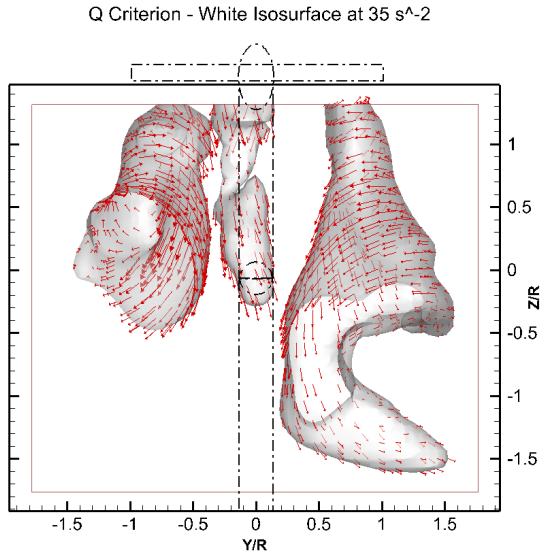


(a) $(Y/R) = -0.8$.

(b) $(Y/R) = 0.8$.

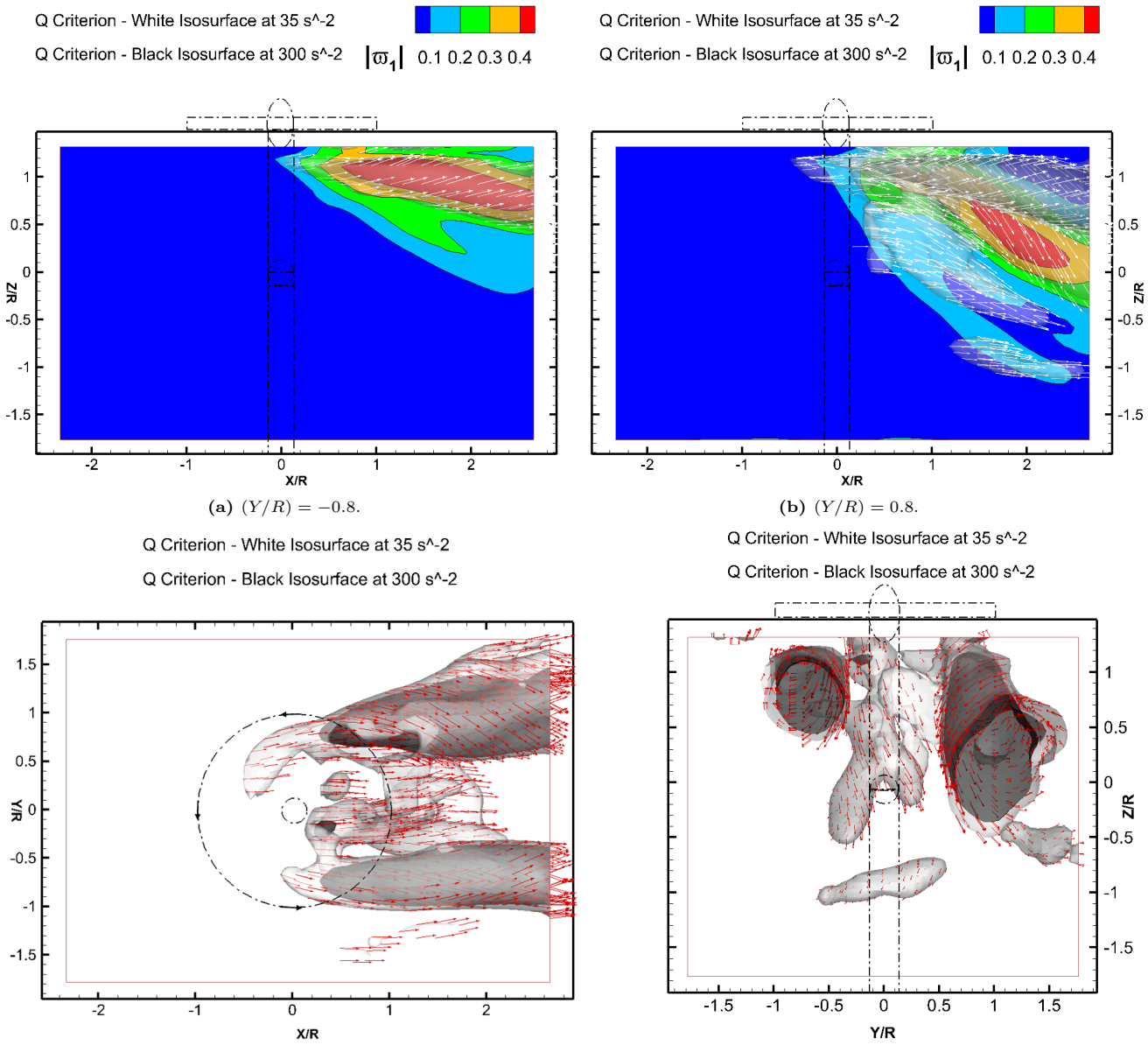


(c) Q-criterion isosurface on $x - y$ plane (top view).



(d) Q-criterion isosurface on $y - z$ plane (back view).

Figure 4.13: Non-dimensional vorticity magnitude 2D contours on the retreating (a) and advancing (b) side of the rotor blades along with the isosurface of the Q-criterion for $\mu = 0.062$ (velocity vectors are shown for even spacing and are coloured for visualization purposes).



(a) $(Y/R) = -0.8$.

(b) $(Y/R) = 0.8$.

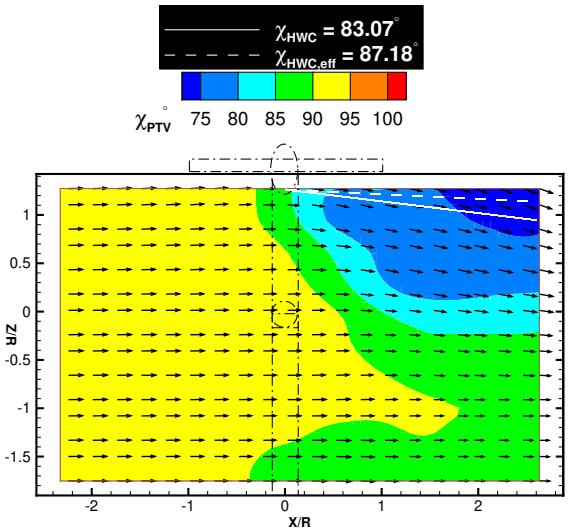
(c) Q-criterion isosurface on $x - y$ plane (top view).

(d) Q-criterion isosurface on $y - z$ plane (back view).

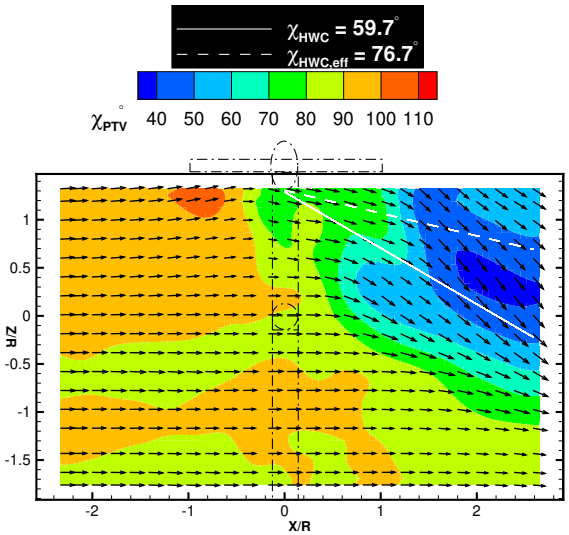
Figure 4.14: Non-dimensional vorticity magnitude 2D contours on the retreating (a) and advancing (b) side of the rotor blades along with the isosurfaces of the Q-criterion for $\mu = 0.1$ (velocity vectors are coloured for visualization purposes).

Finally, an investigation on the downwash itself and the skew angle is considered necessary in order to examine the validity and limitations of the modeling approaches that are used so far. The rotor induced downwash is contained between the 2 counter-rotating vortices shown above and its maximum occurs on the advancing side. Thus, Figure 4.15 shows a comparison of the local flow skew angle obtained from the measurements with the skew angles computed from the HWC, for a y-plane corresponding to $+0.25R$ from the centerline. As already shown, the HWC predicted skew angles are similar for low flow deflections, while their difference increases with decreasing advance ratio. However, in all three sub-figures, the HWC skew angles indicate the boundaries with the highest possible flow deflection for each condition. The momentum skew angle represents the lower boundary, while its effective value the upper boundary of the maximum downwash. A better comparison can be made when considering the isosurfaces depicted in the figures above. Regarding the condition at $\mu = 0.1$, from Figures 4.14a and 4.14b, it is obvious that the wake is distorted towards $Z/R \rightarrow 0.675$ and $Z/R \rightarrow -0.15$ respectively.

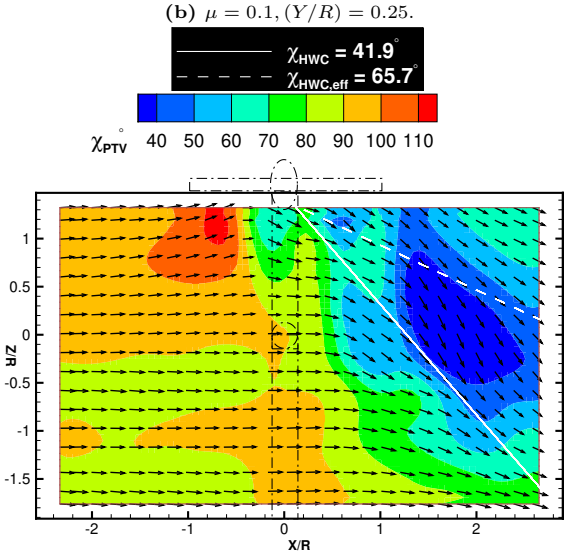
These directions fall very close to the calculations of the HWC for the effective and the momentum skew angles (see Figure 4.15b). Since it is shown that the rotor wake is not uniform, those 2 values represent the direction in which the wake is deflected for the retreating and advancing side respectively. The predictions are within good agreement also for the condition of $\mu = 0.062$, which corresponds to distortion towards $Z/R \rightarrow 0$ and $Z/R \rightarrow -1.5$ for the retreating and advancing side (Figures 4.13a and 4.13b). The same directions are predicted by the HWC angles as shown in Figure 4.15c. The HWC skew angle comparison with the local flow skew angle is less relevant for comparison since the HWC skew angle describes the global direction that the rotor wake is deflected. On the other hand, an additional and even more significant observation can be made from Figure 4.15. The existence of wall interference and flow angularity corrections is presented. One can clearly point out that upstream of the rotor there is an upwash ($\chi_{PTV} > 90°$) component which would not probably exist for for a non lifting model test. This upwash is a result of two contributions. The first is the rotor induced flow that may create such a disturbance which would also be present in a free-air case, or in a very big test section. This is because any lifting surface creates circulation which in turn is seen as flow curvature. This contribution, if it propagates that far upstream at all, is expected to be present in the vicinity of the rotor. But one can clearly observe that the upwash is present even in the left boundary of the measurement volume which is at about 0.2 m before the beginning of the blade area and for almost any height in the vicinity of the rotor. The second factor is the wall induced upwash, which is positive for a closed-wall test section. Any considerable sized lifting surface in a constraint environment would experience a flow angle which is different than what it would experience in free-air. That is what wall correction methods aim to correct when applied for lifting configurations. In principle one would be able to accurately obtain the wall-induced upwash distribution over the measurement volume, if a similar velocity field would be available for a very large test section (free-air) and such, the rotor's induced flow would had been quantified a-priori. Yet, far upstream, it is less possible that the rotor's circulation would be present. Thus, the flow angle (momentum) based on the angle of attack reference system (Figure 3.6a) is presented in Figure 4.16 for all the conditions described. Figures 4.16(a, c, e) present the whole flow angle range, while the figures on the RHS (b, d, f) show a limited range which is of interest for examining the average flow angle that the rotor experiences for each condition. Furthermore, the HWC wall induced upwash predictions are also included in terms of angle of attack corrections. As expected from the RHS figures, there is a gradual increase in flow angle from the inflow towards the start of the blades. Additionally, the HWC predictions are consistently lower than the local flow angle at the left boundary, however, the HWC angle of attack correction predicts an averaged wall-induced upwash in the vicinity of the disk (where the rotor induced flow is significant and has to be eliminated) and not upstream of it.



(a) $\mu = 0.31, (Y/R) = 0.25$.

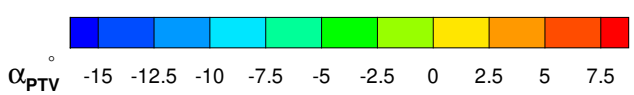


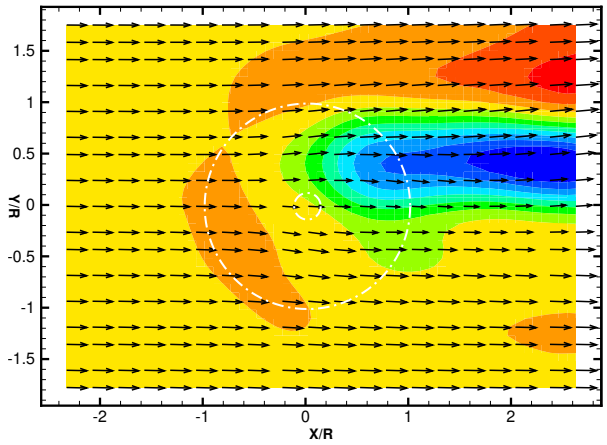
(b) $\mu = 0.1, (Y/R) = 0.25$.



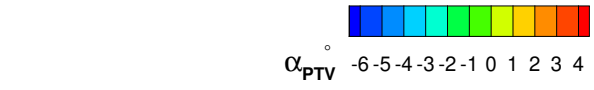
(c) $\mu = 0.062, (Y/R) = 0.25$.

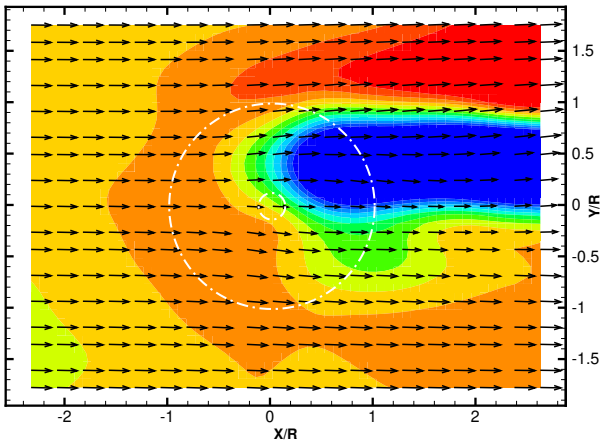
Figure 4.15: Local flow skew angle (direction) comparison with skew (solid white line) and effective (dashed white line) skew angles predicted by the HWC for the rotor wake modelling.



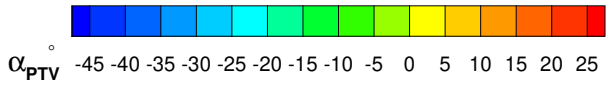


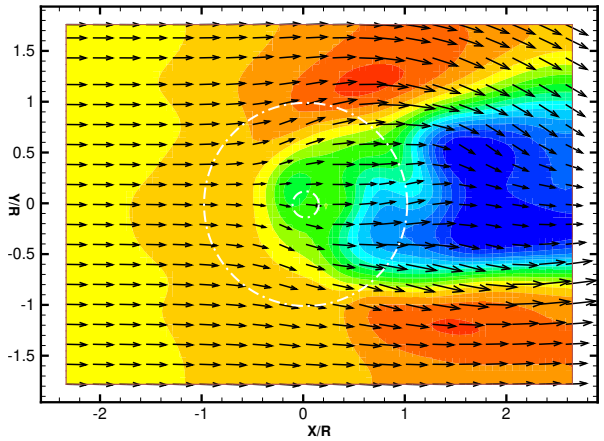
(a) $\mu = 0.31, (Z/R) = 0.85$.



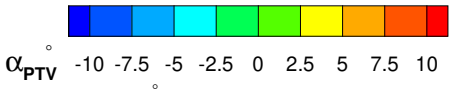


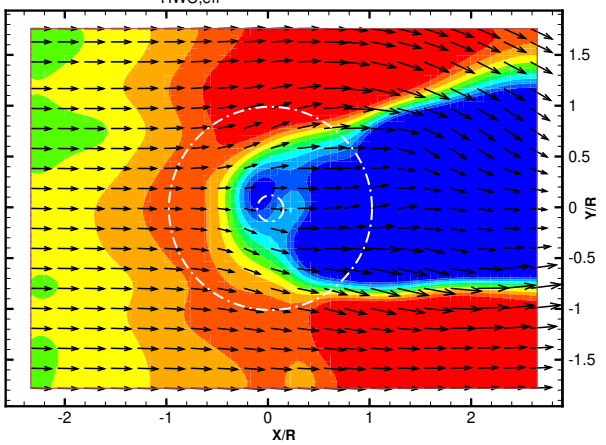
(b) $\mu = 0.31, (Z/R) = 0.85$.



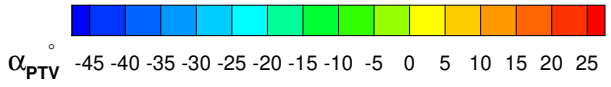


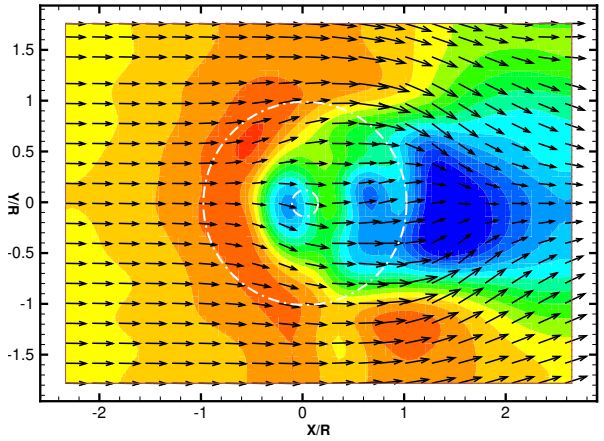
(c) $\mu = 0.1, (Z/R) = 0.85$.



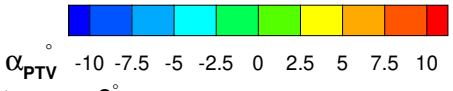


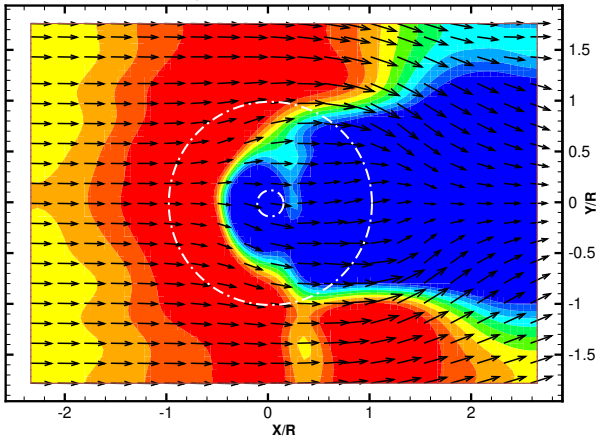
(d) $\mu = 0.1, (Z/R) = 0.85$.





(e) $\mu = 0.062, (Z/R) = 0.85$.



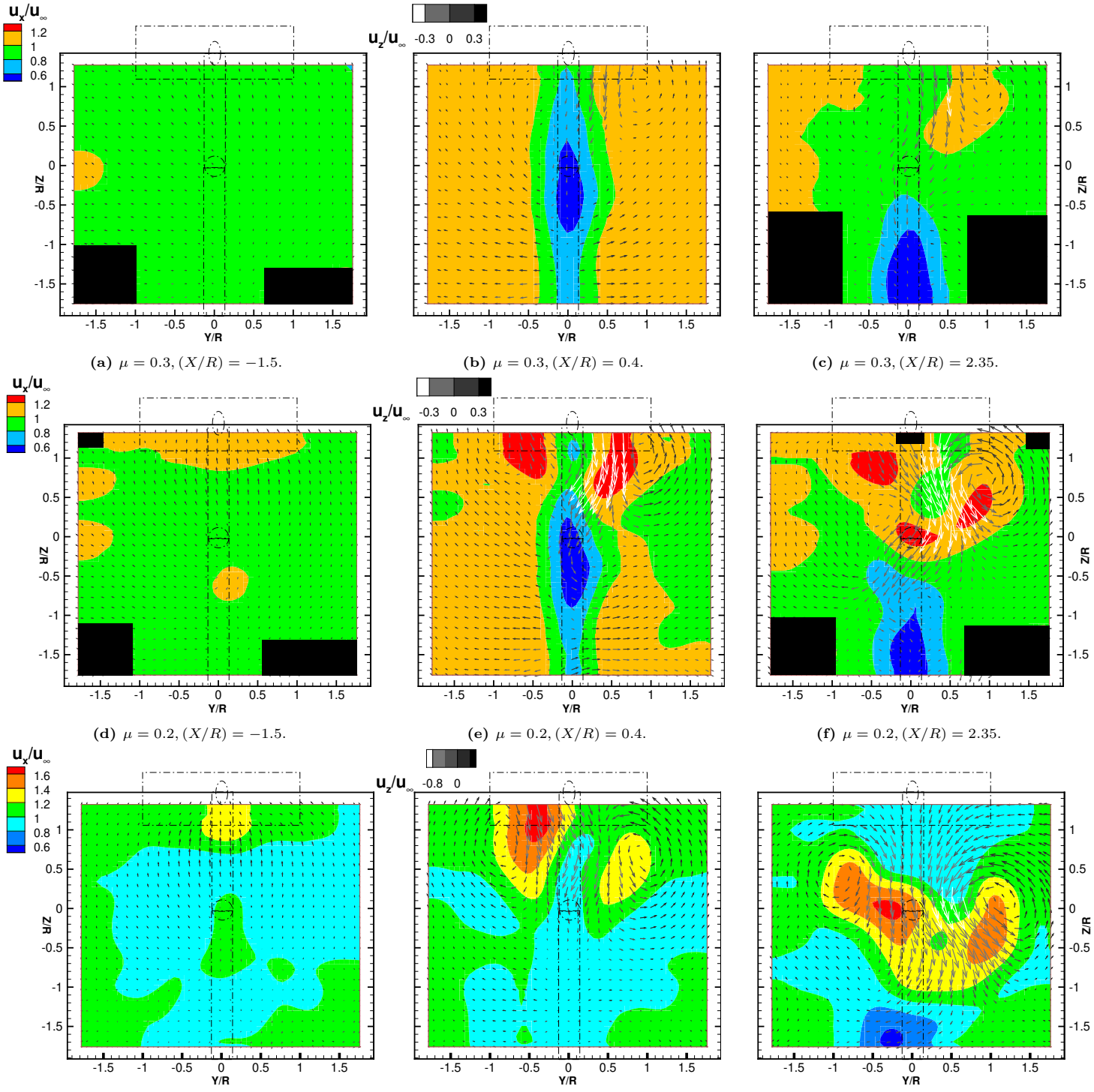


(f) $\mu = 0.062, (Z/R) = 0.85$.

Figure 4.16: Flow angle (upwash/downwash) $x - y$ contour at a height of 8.6 cm below the rotor disk for the 3 tested conditions (LHS figures full angle range / RHS figures limited range. Velocity vectors are same for the 2 lower advance ratios and magnified for the higher) and comparison with the HWC averaged upwash over the disk $\Delta\alpha$.

60° Incidence Angle

The propeller is inclined at 60° incidence angle resulting in a spinner position of $(X/R)_P \approx -0.72$. The three conditions measured are presented for the tunnel velocities of 40.55 (two conditions) and 20.15, corresponding to advance ratios of $\mu = 0.3, 0.2, 0.1$ respectively. The flow-field is depicted by means of the axial velocity, whereas tangential vectors show the other 2 velocity components. Furthermore, the vectors are coloured with the vertical velocity component. All velocities are non-dimensionalized with the free-stream velocity measured by the tunnel reference system. Two-dimensional slices of the measurement volume are shown in Figure 4.17 for the axial positions of X/R =-1.5, 0.4, 2.35. As with the wall pressures, the conditions at 60° angle of attack resemble the purely lifting case. Again, the slipstream composes of two dominant vortices, with the advancing side vortex ($Y/R > 0$) advecting further downwards than the other one. Additionally, there is a third vortex structure emerging from the slipstream-motor interaction in accordance with what is observed for the 90° conditions. For the higher tunnel velocity, this structure seems to play a more important role than the retreating side vortex which is hardly present within the measurement volume due to its smaller downward movement (see Figures 4.17c and 4.17f). This situation is also encountered for the 90° case (Figure 4.12b) and is attributed due to the strong wake induced by the strut at this free-stream speed, leading to favorable path for downwash. At lower advance ratios, this effect is less pronounced. The downwash is primarily determined by the two slipstream vortices as shown in Figure 4.17i and is directed towards the advancing side of the bottom wall. The advance ratios presented for this case do not correspond to any strong flow disturbance as measured by the wall pressures shown in Figure 4.7. Additionally, the local but consistent aerodynamic effect observed from the static pressure measurements for $\mu = 0.1$ at $X/R = 5 - 6$, is out-of-reach with respect to the PTV measurement volume and thus, its origin is not revealed. Despite the similarities encountered with the 90° incidence angle, this flow-field exhibits a significant difference. Far away from the strut and in the downwash region contained by the two counter-rotating vortices, it can be seen that the streamwise velocity component is higher than the tunnel free-stream speed (see Figure 4.17i). On the other hand for the purely lifting case, there is a strong axial velocity deficit at the same region (see Figures 4.11c and 4.11d). This is attributed to the fact that at 60° incidence the propeller produces significant amount of lift, but it also accelerates the flow in the streamwise direction, in contrast with the 90° incidence where the downwash is present at regions of strong streamwise velocity deficit. Due to that streamwise acceleration, a distinct peak of the pressure coefficient difference (ΔC_P) on the floor of the test section (e.g. see Figure 4.7d) is observed at a higher advance ratio ($\mu = 0.082$) than for the purely lifting case ($\mu = 0.062$, see Figure 4.3b). However, for the same reason, the forementioned peaks are lower in magnitude than in the 90° case, where the induced velocity vertically impinges on the floor. This observation applies for both test sections bottom wall pressure signatures and is further considered in section 4.3.



(a) $\mu = 0.3, (X/R) = -1.5$. **(b)** $\mu = 0.3, (X/R) = 0.4$. **(c)** $\mu = 0.3, (X/R) = 2.35$.

(d) $\mu = 0.2, (X/R) = -1.5$. **(e)** $\mu = 0.2, (X/R) = 0.4$. **(f)** $\mu = 0.2, (X/R) = 2.35$.

(g) $\mu = 0.1, (X/R) = -1.5$. **(h)** $\mu = 0.1, (X/R) = 0.4$. **(i)** $\mu = 0.1, (X/R) = 2.35$.

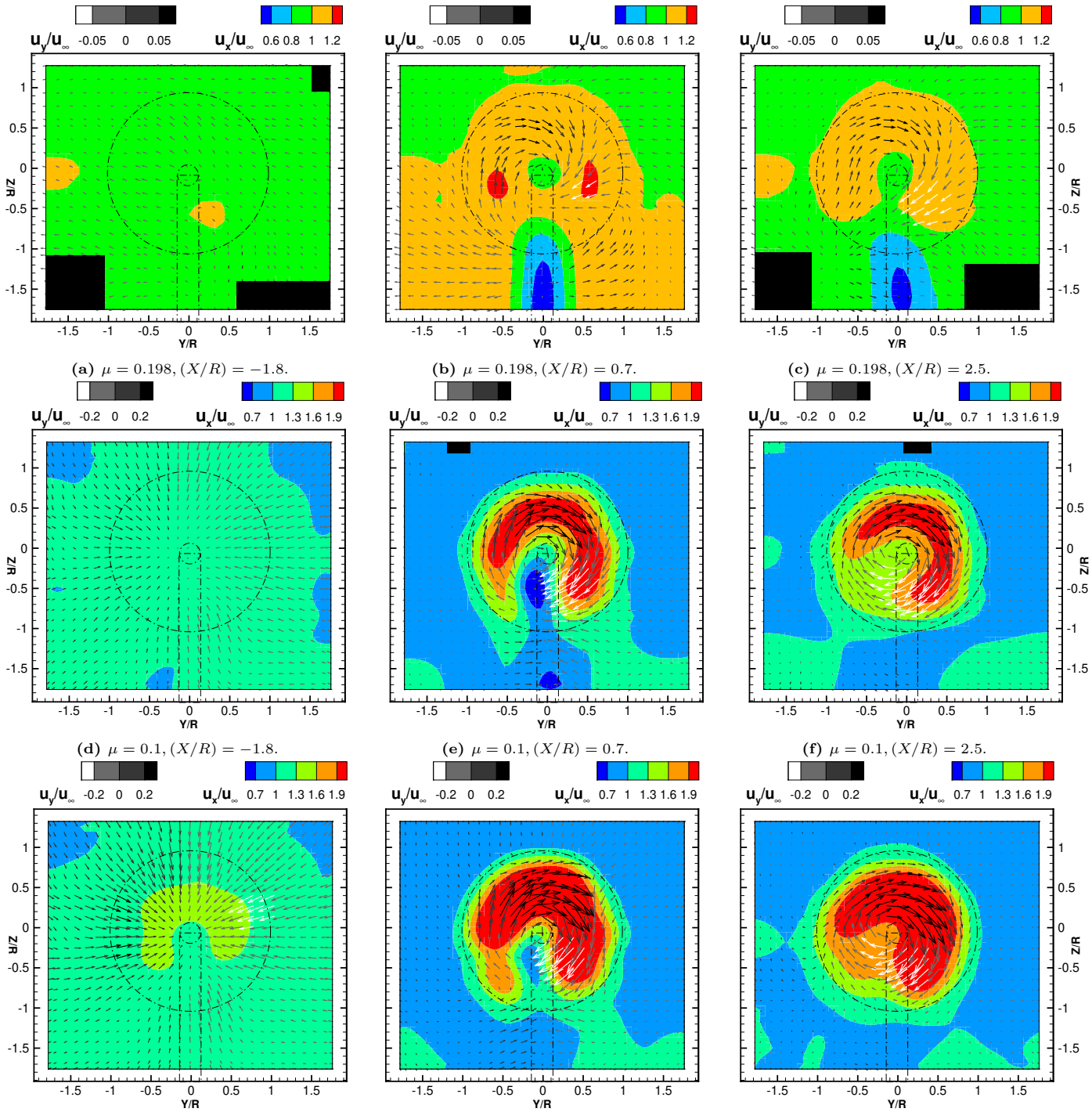
Figure 4.17: Axial and tangential velocity distribution within the measurement volume (x-slices) at the propeller inflow (a, d, g), after the strut (b, e, h) and further downstream (c, f, i), for three different thrust conditions at 60° incidence angle (velocity vectors scaling is the same for $\mu = 0.3$ and $\mu = 0.2$), (areas with insufficient seeding are covered in black).

0° Incidence Angle

Three testing conditions are presented, with the propeller operating at advance ratios of 0.198, 0.1 and 0.063 which correspond to measured wind tunnel velocities of about 40.56, 20.41 and 12.9 m/s respectively. Figure 4.18 shows the streamwise velocity distribution normalized by the measured wind

tunnel free-stream velocity on 2D slices within the measurement volume at the axial positions (X/R) of -1.8 (propeller streamtube, inflow), 0.7 (after the test stand) and 2.5 (slipstream, downstream). Furthermore, the tangential components are presented by means of a vector-field, where their colour describes the non-dimensional lateral velocity component distribution. The areas without or with extremely low seeding density (mainly for the higher wind tunnel speed), are blanked with black colour. It is seen that in the higher advance ratio, the fluid is hardly accelerated towards the streamwise direction and the slipstream's swirl is very low. Additionally, the wake of the test stand persists throughout the measurement domain (Figures 4.18b and 4.18c), while there is a velocity increase close to the bottom boundary at the test stand location (Figure 4.18b). This is attributed to the high wind tunnel speed which causes the acceleration of the flow in the vicinity of the test stand (see also discussion for Figure 4.19). In contrast to Figures 4.18e and 4.18h, where the flow has already re-attached (10 cm) behind the strut and with the velocity vectors converging towards its wake, the higher advance ratio configuration still exhibits a divergent behavior (Figure 4.18b). A converging behavior (re-attachment) was found at an axial position of $(X/R) \approx 1.05$ for the latter testing condition. For the lower advance ratios, the streamtube's contraction is more evident, while the propeller's induced velocity is of the order of the wind tunnel free stream velocity. Finally, it is evident that at $\mu = 0.1$ the velocity profile at the propeller inflow given in Figure 4.18d is more symmetric than the one for $\mu = 0.063$ (Figure 4.18g). That is attributed due to the propeller operating in the vicinity of the bottom wall, leading to an asymmetric inflow which becomes more pronounced closer to static thrust conditions. In general, the effect of the bottom wall is expected to be dominant for the zero incidence configuration, therefore, any correction with respect to free-air conditions should be cautiously interpreted. That is further discussed in the coming section. Regarding the wall pressure measurements, the measured bottom wall pressures shown in Figure 4.10b, are in consistence with the PTV results. For $\mu = 0.1$ and $\mu = 0.063$, the static pressure drop ahead of the propeller observed in Figure 4.10b corresponds to the velocity increase due to the propeller inflow (contraction) shown in Figures 4.18d and 4.18g. However, for $\mu = 0.198$, the velocity ahead of the propeller shown in Figure 4.18a is lower than the measured free-stream speed, which corresponds to a positive ΔC_P. Similar considerations apply for the slipstream region behind the propeller, where the velocity in the vicinity of the bottom wall is mainly lower than the measured wind tunnel speed and thus an increase in static pressure is observed. With respect to wall interference, wall-induced blockage (negative) cannot that clearly be distinguished for this flow since even at free air conditions, there is an expected velocity deficit outside of the slipstream due to its acceleration. The presence of the walls of the test section also contribute to that deficit depicted clearly in Figures 4.18 (c, e, f, h, i), but the combined effect of the actual free-stream deficit with the wall-induced blockage cannot be distinguished. As with the previous case, a similar velocity field of a free-air test (very large test section) would be needed in order to actually determine and quantify these wall effects.

The z-component of the vorticity non-dimensionalized by the propeller's rotational frequency is shown in Figure 4.19 for three different consecutive $z-$planes corresponding to the propeller mid-radius above the hub ($(Z/R) = 0.5$), the hub's vertical position ($(Z/R) = 0$) and at $(Z/R) = -1.35$ (about 8 cm above the floor of the test section). The high shear between the test stand's wake and the free-stream tunnel velocity is evident, for the higher advance ratio condition (Figure 4.19c). Its magnitude is strongly decreasing as the tunnel speed drops (Figures 4.19f and 4.19i). Another remarkable flow feature is the interaction between the hub and the motor configuration (Figures 4.19b, 4.19e, 4.19h). The depiction of the e-motor is available in Figure 3.9 and one can conclude that this hollow geometry may induce flow rotation and shear when subjected to a wind tunnel, or propeller slipstream flows. Those figures suggest that the strut and the hub-motor wakes interact with each other, in all cases. However, at the highest advance ratio this interaction is more pronounced due to the strong wake of both. Finally, the propeller slipstream is directly discernible both at $(Z/R) = 0$ and on the above plane ($(Z/R) = 0.5$).

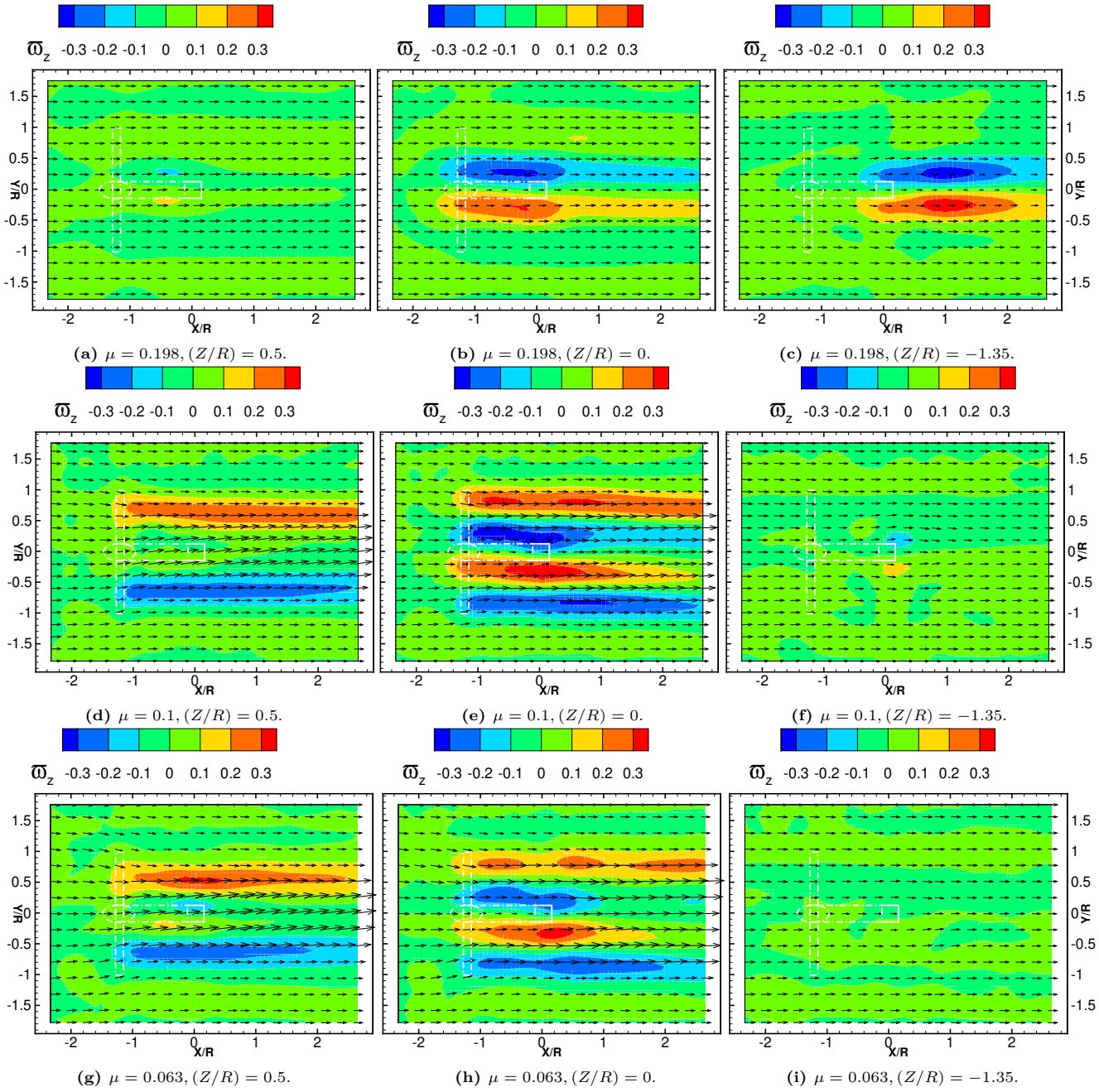


(a) $\mu = 0.198, (X/R) = -1.8$. **(b)** $\mu = 0.198, (X/R) = 0.7$. **(c)** $\mu = 0.198, (X/R) = 2.5$.

(d) $\mu = 0.1, (X/R) = -1.8$. **(e)** $\mu = 0.1, (X/R) = 0.7$. **(f)** $\mu = 0.1, (X/R) = 2.5$.

(g) $\mu = 0.063, (X/R) = -1.8$. **(h)** $\mu = 0.063, (X/R) = 0.7$. **(i)** $\mu = 0.063, (X/R) = 2.5$.

Figure 4.18: Axial and tangential velocity distribution within the measurement volume (x-slices) at the propeller inflow (a, d, g), after the strut (b, e, h) and further downstream (c, f, i), for three different thrust conditions at zero incidence angle (velocity vectors are magnified for $\mu = 0.198$, while the two lower advance ratios have the same scaling), (areas with insufficient seeding are covered in black).



(a) $\mu = 0.198, (Z/R) = 0.5.$ **(b)** $\mu = 0.198, (Z/R) = 0.$ **(c)** $\mu = 0.198, (Z/R) = -1.35.$

(d) $\mu = 0.1, (Z/R) = 0.5.$ **(e)** $\mu = 0.1, (Z/R) = 0.$ **(f)** $\mu = 0.1, (Z/R) = -1.35.$

(g) $\mu = 0.063, (Z/R) = 0.5.$ **(h)** $\mu = 0.063, (Z/R) = 0.$ **(i)** $\mu = 0.063, (Z/R) = -1.35.$

Figure 4.19: Normalized out-of-plane vorticity distribution within the measurement volume at three different heights (z-planes) corresponding to half radius above the hub, at the hub location and close to the bottom boundary, for the three configurations examined (velocity vectors are magnified for $= 0.198$, while the two lower advance ratios have the same scaling).

4.1.3. Summary & Discussion

In this chapter the global flow topology is presented by means of static pressure measurements at the boundaries and Particle Tracking Velocimetry. Overall, there is a good consistency between the measured static pressures and the PTV measurements, for all three configurations. It is shown that the two lifting angles of attack present similarities with each other in terms of both measurements. Additionally, the effect of the test stand is shown to influence all the measured flow conditions, especially at the higher advance ratio condition, where an increase in wind tunnel speed in the vicinity of the test stand is observed due to the strut's blockage. This behavior is not that pronounced for the lower

tested velocities. The subtraction procedure of the respective pressure coefficients is not affected by the forementioned effect, since the results are following the expected similar trends for all tunnel velocities. Comparably, the geometry of the electric motor is also influencing the flow field in the vicinity of the propeller. This is observed in every configuration, but its effect is more pronounced as the angle of attack decreases. It is shown that the blade root-motor generated shear is more dominant for the 60° and 0° configurations rather than for the purely lifting case.

For the lifting rotor conditions, the asymmetric nature of the rotor's wake is revealed. In both blade sides there are two distinct counter-rotating vortex structures which advect downstream at a higher velocity than the wind tunnel free-stream (for moderate advance ratios). It is shown that the downwash is contained between those two vortices and that it is directed towards the advancing side of the bottom wall. This is attributed to the fact that the advancing-side vortex is consistently deflected lower than its counterpart creating a favorable path for downwash towards that side due to its rotation. This behavior is also verified from the static pressure measurements. On the advancing side, the rapid increase and a maximum of the pressure coefficient corresponds to a high downwash and flow impingement at the bottom wall. However, the measured under-pressure upstream of the impingement region, does not correspond to a ground vortex propagating upstream, as it was firstly hypothesized, but it is rather a sign of acceleration of the flow when by-passing the impingement region. No PTV measurement has shown any signs of reversed flow, or ground vortex due to stagnation for the conditions presented here, nevertheless, it is expected that this flow condition eventually occurs at even lower advanced ratios. Additionally, due to the unsteady nature of such a phenomenon a time-resolved recording might be more appropriate for such an investigation. Regarding modelling, the HWC predictions are satisfying with respect to the direction of the wake. An investigation between the momentum and the effective skew angles employed by the HWC to model the wake's drift revealed that these values closely predict the deflections of the retreating and advancing side vortices respectively. Furthermore, an upwash at the most upstream part of the measurement volume is detected for all the conditions presented. This upwash may imply evidence of the wall effects exhibited by lifting surfaces, however an interference-free solution is needed to verify that, since the rotor's induced disturbance far upstream is unknown and thus, the wall-induced upwash cannot be revealed or quantified purely from the current measurements. Finally, there is a significant difference between the purely lifting and the 60° case. For both test sections, a distinct maximum in pressure coefficient difference is observed at higher tunnel velocities (advance ratios) for the latter condition. That is due to the higher velocity of the rotor's wake inclined towards the floor allowing it to influence the bottom wall pressure measurements at 60° incidence. However, the vertical component of the velocity is significantly lower as compared with the 90°, resulting in consistently lower pressure peak values.

For the thrusting propeller configuration, the time averaged slipstream is captured for the three presented conditions. The velocity decrease outside the slipstream region is evident for the lower tunnel speeds. For the higher advance ratio tested, the strut and slipstream-motor interaction is more noticeable than in the other cases resulting in shear comparable with the blades induced swirl.

4.2. Wall Corrections

This chapter presents the computed corrections in terms of blockage and change in angle of attack for each of the methods used. The results are presented for all measurement conditions irrespective to the validity of their predictions in terms of their magnitude and non-linearity and whether flow breakdown has occurred or not. Therefore, the corrections shown here are valid for a certain range of advance ratios and not for the whole span as presented in this section.

4.2.1. OGE Corrections

Lifting Rotor OGE Corrections

[illegible]

Table 4.1: [illegible]

	[illegible]	[illegible]	[illegible]
[illegible]	[illegible]	[illegible]	[illegible]
[illegible]	[illegible]	[illegible]	[illegible]

Table 4.2: [illegible]

	[illegible]	[illegible]	[illegible]
[illegible]	[illegible]	[illegible]	[illegible]
[illegible]	[illegible]	[illegible]	[illegible]

(a) Flow angularity corrections for the closed (left y-axis) and the 3/4 open jet test (right y-axis) working correctly across 30° to cruise.

(b) Flow angularity corrections for the closed (left y-axis) and the 3/4 open jet test (right y-axis) working correctly across 30° to cruise.

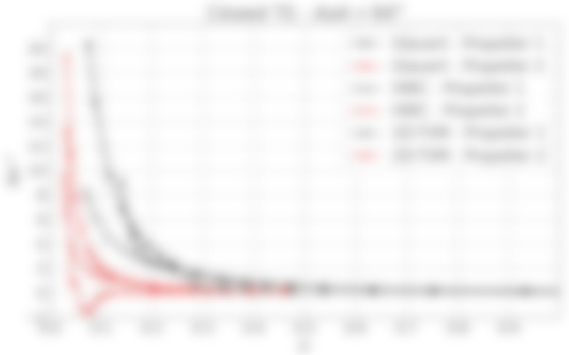
Figure 4.26: Flow angularity corrections for both propellers working correctly across 30° to cruise and 60° to hover.

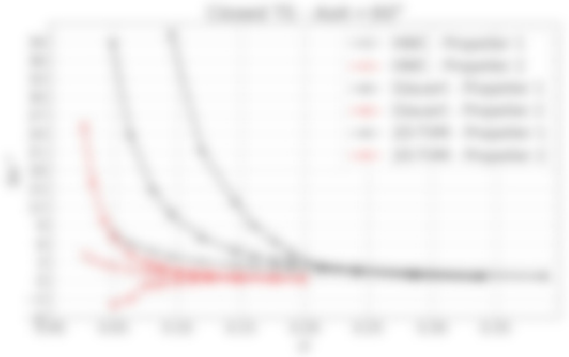
In addition, the corrections should be applied correctly to the right side. However, it is expected. Unfortunately, due to time constraints, the measurement of the vertical wing by another test is not available with the wing. The wing is mounted on the left side of the fuselage, so the wing is not in the wake of the propeller. The flow angularity corrections are applied to the RANS simulations as described in Figure 4.26. The results are shown in Figure 4.27. The results of the simulations are compared with the experimental data. The results are shown for the three different cases. The first case is the baseline case without any corrections. The second case is the case with the corrections applied. The third case is the case with the corrections applied and the propeller is removed

The HAWC wake model was tested against propeller test data, and the placement of the vertical and horizontal rotational drift factors that affect the wake diameter are shown in Figure 4.22. For the level advance ratio, the wall is similar to the rotational correction, and the corrections are presented here. For the 3/4 open-jet test section, a warning message is given. The correction and negative are exceeded, but there is a small discrepancy between the two. The position was: I am not very sure that we have a "flow" in the test section [34]. Note that the velocity correction factor $k_{x,y}$ is used to adjust the free-stream test section, since we can be sure that the wake is not affected by the walls. For the tunnel experiment, the wake model is used to predict the wall interference factors. The tunnel experiment is carried out in the open jet test section.

Figure 4.23: HAWC flow angle correction for the propeller in the open jet test section.

Figure 4.11: [illegible] for both propellers were [illegible] the [illegible] and the 3" quad-jet [illegible] at 30° inclination angle.





(a) Blockage correction for propeller 1 at 90° in the x-z, chord-wise section

(b) Blockage correction for propeller 2 at 90° in the x-z, chord-wise section

Figure 4.29: Comparison between HPC(MF) and 2D-TVH (overall) blockage predictions.

blockage at very low speeds and high thrust conditions.

(a) Blockage correction for propeller 1 at 0° inclination, chord sections

(b) Blockage correction for propeller 2 at 0° inclination, chord sections

Figure 4.26: Comparison between HAWC (FW) and ZONTAS (panel) blockage predictions.

Propeller OGE Corrections

For this configuration blockage corrections are also applied, the propeller is setting at zero inclination angle. Both propellers are tested at an advance ratio of 0.57 in front the fuselage and at the tail section. With an radius of 0.4572 m, a tip clearance of 0.04 m, the corrections over propeller diameter is around 8.8%, it would be of interest to try and implement for the former radius of influence of the boundary interference but due to the close proximity. Thus, the coefficients are only corrected for the tail and the above wall (see figure 3.24 in the next section). For the OGE configuration propeller 2 measurements are used to estimate the blockage effects. This is only possible by using the method described in section 3.4.2 for propeller 2 ground effect. The relationship is quite between top (0.01) and bottom wall (0.03) giving a real world mirror effect. Thrust coefficient values of 0.24, 0.14, and 0.04, respectively. Finally, the blockage control planes (each wall) are summed together to calculate the total blockage for both walls. This is shown in Figure 4.28, where ΔC_T corresponds to the overall wall effect consequently to the total correction of both walls.

Figure 4.28: Blockage correction for propeller 2 in the fuselage mounted configuration.

4.2.2. Summary & Discussion

Some relevant conclusions and observations with respect to the wall correction methods that are employed for an OGE representation are presented. For the closed-wall test section the most significant observations are:

- [illegible]
- [illegible]
- [illegible]
- [illegible]
- [illegible]
  - [illegible]
  - [illegible]
  - [illegible]
- [illegible]
- [illegible]
- [illegible]
- [illegible]

- [illegible]
- [illegible]

For the 3/4 open-jet test section some remarkable observations are:

- [illegible]
- [illegible]
- [illegible]
- [illegible]

[illegible]

4.2.3. IGE Corrections

This section presents the corrections for in-ground-effect. This is a common practice for reducing the magnitude of the boundary interference factors, since in high-lift configurations such as rotors, the bottom wall interference is dominant. Therefore, by excluding it from the image reflection system leads to significant reductions in wall corrections, but also their accuracy is better than those for OGE. However, for large skew angles, correcting for the IGE, does not provide any useful information, since such flows are not representing actual in-ground flight. On the other hand, at low advance ratios (low skew angles), the ground-effect may correspond to conditions resembling transition from hovering, to forward flight which are usually encountered for V/STOL aircrafts. Thus, the IGE corrections are of significance. It should be noted here, that for an accurate IGE simulation, the bottom wall boundary layer should be effectively eliminated with the use of boundary layer suction, ground blowing and moving belts. This is not the case for the current tests (only boundary layer suction for the 3/4 open-jet test section is applied), but still the effect of the bottom wall in the magnitude of the corrections is investigated. This section is again categorized according to the angle of attack, where for the lifting angles, the HWC is employed, due to its higher reliability than the classical method and the TVM. For the propeller configuration, the developed Glauert method for IGE along with the TVM are used.

Lifting Rotor IGE Corrections

(a) HWC flow angularity corrections

(b) HWC lift blockage corrections

Figure 4.30: HWC flow angularity and lift blockage corrections for both propellers and test conditions at 90° inflow angle.

(a) RWC flow angularity correction. (b) RWC lift blockage correction.

Figure 4.21 RWC flow angularity and lift blockage corrections for both propellers and test conditions at 90° incidence angle.

By evaluating both the boundary and the ground effect corrections it is possible to have an estimation for the reduction in flow angularity caused by the ground effect inclusion. This can be estimated as the percentage relative to the RWC correction: $\%GE = \Delta\alpha - \text{Ref.Correction}$ $\frac{\text{Ground Effect}}{\text{Boundary}}$ $\times 100$. However, this is possible for the closed test section where, the weight distribution between the ground and the boundary corrections are balanced by propeller. This is shown in Figure 4.22a and 4.22b for the configuration of 0° and 90°, respectively. It can be seen that at the propeller tip region the flow angularity reduction is significant (15%-18% for propeller 1 and 30%-70% for propeller 2), especially at the lower advance ratios where can potentially cause local loss of thrust due to leaving or turning flight. For the 90° angle of attack, the magnitude of the flow correction is significantly smaller due to the propeller axis, while the vertical RWC corrections are more notable. Like the flow deviation, it can also reach values from 10% to 30% for both propellers.

(a) Percentage reduction in flow angularity due to ground effect for incidence angle of 0°. (b) Percentage reduction in flow angularity due to ground effect for incidence angle of 90°.

Figure 4.22 Percentage reduction in flow angularity due to ground effect for the tilting angle of both propellers in the closed-wall test section.

Propeller IGE Corrections

The effective AC contribution angle is chosen for the IGE representation, due to both propellers being in ground proximity. The Glauert's method for propellers and the VLM are used in order to estimate the change in with the IGE, the Glauert's method relies into assuming only the 4 parameters (tip speed, blockage, wake deflection and axial induced velocity) while the VLM computes all possible blockage combinations with the same described by the previous cases for the tilting rotors analysis. From [37], the blockage which is of concern for ground effect simulation, that the Glauert's method described in section 2.2.1 is based with, for the IGE-VLM, only the axial induced velocity contribution is taken into account, in equation (2.6)

(a) Glauert's correction method versus the 2D-TVM for propeller 1

(b) Glauert's correction method versus the 2D-TVM for propeller 2

Figure 4.28: Glauert's method's induced velocity correction factor σ evaluated at the collocation points of the 2D-TVM for both propellers at the design condition. Correction factor σ evaluated at the collocation points of the 2D-TVM.

Considering the above results, the complete version of the TVM [2D-TVM] is also employed in order to be able to make comparisons. The actual 2D simulations only take into account the wall influences from the upper and the side walls as considered in equation (3.1). The respective comparison with the Glauert's method is shown in Figure 4.29, for both propellers. By utilizing propeller 2, the results are reasonable and qualitatively the same as the 2D-TVM presented above. However, by employing the equal distribution of blockage over varying complete cycles for the 2D-TVM, it is pointed out that this method is unsuitable for modeling that case, since a fundamental assumption that the simulations do not have a high spanwise variation. This is discussed in detail by Glauert [13]. Thus, in order to reflect the blockage positions from the TVM simulations suitable, especially for the lower advance ratios where the blockage seems to vary strongly with respect to the azimuthal coordinate, it is proposed to evaluate the integral of the blockage with respect to its spatial variation in the vertical direction, hence to obtain a single value representing the blockage inside the test section. That is of course only a blockage in varying manner inside the test section and thus, the TVM is deemed reliable for comparative cases.

(a) Gilbert's correction method versus the 3D TVM for propeller 1. (b) Gilbert's correction method versus the 3D TVM for propeller 2.

Figure 4.24: Gilbert's method's values for the wall correction factor ε_{wall} compared to the 3D TVM for both propellers at various advance ratios. Gilbert's method's values for the wall correction factor ε_{wall} compared to the 3D TVM for both propellers at various advance ratios.

The 3D Time-Variable-Doublet method applied to the FLIVV discretization of both propellers in the slipstream of the propeller planes (see Section 4.2.2) for the different boundary conditions of the velocity potential (see Section 4.2.1) was solved by computing the surface integrals over the frame cells' control volume surfaces. The results of the corresponding wall correction factors ε_{wall} for both propellers in the slipstream of the propeller planes (see Section 4.2.2) for the different boundary conditions of the velocity potential (see Section 4.2.1) were

- [illegible]

For the 0° configuration some relevant findings are:

- [illegible]
- [illegible]
- [illegible]
- [illegible]
- [illegible]
  - [illegible]
  - [illegible]
  - [illegible]

[illegible]

4.3. Flow Breakdown Limits

4.3.1. Established Criteria

(a) Flow breakdown limits for propeller 1 (b) Flow breakdown limits for propeller 2

Figure 4.23: Flow breakdown limits presented by Thorne [3] and the linear modified versions for both propellers

Table 4.3: Advance ratio and thrust coefficient corresponding to the breakdown limits presented by Thorne [3]

	Propeller 1	Propeller 2
J_{BD}	0.791	0.667
α_{BD}	62°	49°

Table 4.4: Advance ratio and thrust coefficient corresponding to the breakdown limits presented by Thorne [3]

	Propeller 1	Propeller 2
J_{BD}	0.79	0.665
α_{BD}	62°	49°

[illegible]

[illegible]

[illegible]

[illegible]

4.3.2. Criterion Based on Wall Pressures

[illegible]

Table 4.5: Minimum velocity flow breakdown limits in cross-wind direction and gradients (Δv_x / ΔP).

Table 4.6: Minimum velocity flow breakdown limits in cross-wind direction and gradients (Δv_x / ΔP).

[illegible] the above criterion, one can recognize that the slope angle similar to [illegible] is not a unique, but rather a range of values. This is because the slope angle γ_{sep} predicted by several numerical investigations [Hil+21; Ish+21; Ish+22; Ish+23], but also not the case for the considered test cases. Due to the [illegible] the [illegible] is not a unique value. The [illegible] is also not a unique value. The [illegible] is also not a unique value. The [illegible] is also

- No polarization is made to avoid the overlapping between the two curves for the LST campaign, solely for the small pressure.

4.4. Interference-Free Results

In this section the thrust measurements from the LST campaign are presented and compared with those of the AWT. The results are distinguished based on the angle of attack and the height of the model with respect to the ground board (IGE, OGE). The electric power measurements are not considered reliable, since the power settings of the power supply unit were not consistent throughout both campaigns. Additionally, the heating of the motor power cables was significant, resulting in non-uniform power losses even for a single measurement block. Therefore, the electric power consumption of the motors is not included in this report. Finally, focus is given on propeller 2 for the incidence angles of 90° and 0° due to the absence of a complete dataset for the other propeller and angle.

4.4.1. OGE Comparison

Figure 4.36: [illegible]

(a) High advance ratios.

(b) Low advance ratios.

4.4.2. IGE Comparison

Figure 4.49: Comparison of the fitted coefficients measured in the LSI and WFI control samples for proton-induced events.

For the 3° angle of attack, propeller 3 was located at the same height in both test sections of the WFT. Thus, the TOT interference-free results are obtained by positioning the propeller at the same height above the ground, which is $h/D = 1.541$. Figure 4.48 presents the data comparison at the two different tunnels and two methods. In a similar manner as with the CCT data, the WFT-based test section wall-induced velocities account for blockage in accordance with Figure 4.44 b. Since the 3-D WT blockage model has been averaged over planes to obtain a representative correction in the vicinity of the propeller, and the Glauert's added-mass is a similar correction magnitude, only the latter is used for the comparison with the LSI. As expected, the thrust coefficient based on the WFT for $M_\infty = 0.6$ is slightly higher than the one for CCT (presented in Figure 4.39) due to the propeller operating in ground vicinity. Furthermore, the corrections are smaller in magnitude and the WFT-derived test section data are in good agreement with the interference-free assessments. Uncertainties between the data sets might be associated with the slightly different measurement accuracies. As in the CCT, the 3/4-open-jet thrust coefficient is considerably lower than the others.

Figure 4.50: Thrust coefficient as a function of advance ratio for different wind speeds and test sections (open and solid symbols denote LSI and WFI data).

4.4.3. Summary & Discussion

[illegible]

Some factors which may be responsible for the above relationships are:

- [illegible]
- [illegible]
- [illegible]

[illegible]

- [illegible]

5

Conclusions & Recommendations

In the following, some important conclusions of the current research are summarized, and some recommendations for future research are shared. For individual findings and a more detailed overview, the reader is referred to the discussion parts at the end of each section.

5.1. Conclusions

First, the most important findings are shared, followed by the research goals and finally, some conclusions are discussed section by section. The most important outcomes of this research are:

- The time-resolved flow-field of a highly loaded propeller at 90° incidence angle is presented using large-scale Particle Tracking Velocimetry. The asymmetric nature of its wake is revealed and it is shown that the downwash is contained between the two counter-rotating vortices induced by the blades. Due to this asymmetry, the preferable path for downwash is on the advancing side which features a bigger and a greater deflected downwards vortex than the retreating side. Additionally, the notable increase in static pressure occurring during a slight decrease in advance ratio, indicates flow impingement on the bottom wall and the presence of the advancing side vortex that extends towards the floor of the test section.
- A flow breakdown criterion based on this sudden pressure rise described above is defined and is in good agreement with already established criteria for closed test sections. This criterion may be used for any test section with a solid bottom wall, provided that the static pressure distribution is measured.
- A procedure for compensating for blockage effects caused by off-center propellers at zero angle of attack is introduced. This makes use of the Glauert's method and the assumption that blockage is harmonic and thus, it can be split into separate contributions of each wall (top, bottom). Therefore, the propeller can be corrected for IGE (top wall) or for OGE by summing the separate blockage estimated for each wall. Its application to the AWT closed test section for both IGE and OGE is considered successful based on the LST data comparison.

[redacted]

- Different Data: There is a clear difference between the WVT data and the well corrected ones in the purple histograms. For both SGE, LCE and total emissions, the applied wall correction paths are shifted almost gradually towards lower values and histograms with the decrease of wall distance. This result is not observed when the WVT correction is applied. The LSE correction is an exception. In the inner wind speed region, the WVT data exhibit an overall correct flow angularity, whereas a rapid increase is predicted by the wall correction functions. For the WVT-Cyl speed test section, the HWA predicts a negative flow angularity for most of the tested distance range except for the lowest tested speeds. However, the raised emissions curve does not comply with the wall correction predictions. These discrepancies could also be a result of the local measurement errors.
- Jets Case: In contrast with the previous case, there is a very small spread between the WVT-Base, the modified and the LSE measurements for the 0° incidence angle. Furthermore, the correction performs satisfactorily both in terms and order-of-magnitude effect. For the WVT-Cyl speed test section, the HWA predicts a negative flow angularity for most of the tested distance range except for the lowest tested speeds. However, the raised emissions curve does not comply with the wall correction predictions. These discrepancies could also be a result of the local measurement errors.
- Conclusions: Based on the predictions of wall correction methods the two test sections are employed in terms of the correction magnitudes. However, the WVT-3 test section is also considered. For the closed one, this according to the small variation in energy, it is expected that it would yield too low emissions for the real-scale dimensions.

In summary, the results from the wind tunnel tests have been presented in the current section. According to the obtained results, it is clear that the wall correction methods have a significant impact on the emissions, particularly in the case of the WVT-Cyl test section. The results could be validated in order to be applied in real-scale dimensions. Additionally, the HWA measurements may exhibit some problems when the wall correction is applied, which are not considered in the current study. Some of these are:

- Surface roughness effects from the sheet flow caused by the low wind speeds in the wind tunnel facility.
- Simplifications of the calculations in the boundary layer equations by neglecting the flow's compressibility and the pressure gradient normal to the wall, which are not applicable in the case of the WVT-3 test section.

Many aspects for LSE measurements in wind tunnel facilities should be considered. In the WVT wind tunnel facility, it is the low speeds of the WVT-3 test section that are considered. For this and the other test sections, the boundary layer with a corresponding velocity range presents a challenge for measurements and calculations. This can imply that the assumed Reynolds number influences the WVT-3 measurements and that a higher wind speed is needed to obtain more realistic results. However, due to the small cross-sectional area, this is not possible.

Regarding the electric motor power fluctuations as well as the power consumption, it is necessary to ensure that the power supply is stable and the measurement is not affected by the fluctuations. For this purpose, the use of a battery is recommended. However, this is not always possible due to the high power consumption of the motor and the limited capacity of the battery. Therefore, it may be necessary to use a stabilized power supply that is not connected to the mains. Additionally, the motor should be placed in a way that it does not affect the flow in the test section. This could be achieved by placing the motor in a separate room and connecting it to the test section with a duct, as shown in Figure 5.1.

Finally, some challenges with the measurement of the Two-Track Tandem Main Landing Gear were encountered during the measurements. The WVT-3 test section has a relatively small



To conclude, boundary effects are present in any wind tunnel test and test section. Correcting the wind tunnel data to an a-priori unknown free-flight condition is necessary for accurate performance measurements and for a proper agreement of the data from different wind tunnels and test sections. Since that is desirable, a modelling approach is almost always inevitable. For accurate performance measurements, if relatively big models with respect to the wind tunnel dimensions are tested, the conditions need to be ideal. This means that no stall should be present and that the induced flow needs to abide by the small perturbation theory or any other modelling assumption needed for the applied wall corrections to perform appropriately. Alternatively, the test section needs to be exceedingly large with respect to the model's size. The need for new modelling approaches (wall corrections) that resolve the physics which are of importance and do not rely on such restrictive assumptions is substantial if such sizes and conditions are to be simulated with confidence.

5.2. Recommendations

Some recommendations have already been presented in the above section, however, they are also briefly mentioned here for completeness.

- A more complete measurement system might be necessary in order to measure the forces and moments on the model. Additionally, the forces of the test stand might also be necessary in order to estimate its contribution to wall effects and model support interference effects.
- Since stall is most probably taking place in the 90° incidence case (at high advance ratios), a more appropriate testing strategy might be helpful in order to separate and identify the stalling conditions. This would be to do a complete rpm sweep (increase) for every velocity tested and not only at 40 m/s, as done in this study. This will help identify stalling conditions and any other Reynolds effects associated with such tests.
- The intermediate angle of 60° needs to be measured in the LST in order to also obtain a comparison for this case.
- The AWT-3/4 open-jet test section along with the automotive floor may be calibrated for the velocity range and pump settings used in this study.
- The completion of the PTV measurements for the AWT-3/4 open-jet test section (this is a work in progress in the NLR-DNW research agenda).
- An interference-free PTV measurement at the same conditions and measurement volumes will reveal the wall interference field in terms of blockage and lift interference for the closed and the 3/4 open-jet test section.
- The verification of the 2D-TVM and 3D-TVM is lacking (all other methods are numerically verified). This can be easily done by using a potential flow script in order to compute the static pressure distribution at the boundaries of the test section and then use those as inputs to the TVM.

- The DNW - WaSiMe code may be employed in order to compare different boundary measurement methods. Nevertheless, under stalling conditions, it is expected that the results will be unsatisfactory.

References

[1] John Anderson. *EBOOK: Fundamentals of Aerodynamics (SI units)*. McGraw Hill, 2011.

[2] P. R. Ashill and R. F. A. Keating. "Calculation of tunnel wall interference from wall-pressure measurements". In: *The Aeronautical Journal (1968)* 92.911 (1988), pp. 36–53. DOI: 10.1017/S0001924000021813.

[3] PR Ashill. "Boundary-flow measurement methods for wall interference assessment and correction: Classification and review". In: *In AGARD* (1994).

[4] PR Ashill and DJ Weeks. "A method for determining wall-interference corrections in solid-wall tunnels from measurements of static pressure at the walls". In: *AGARD-CP-335 Wall Interference in Wind Tunnels 12 p(SEE N 83-20957 11-09)* (1982).

[5] M. Ballesteros, M. Kemp, R. Neiva, G. Horton, A. Pons, et al. "Investment Scenario and Roadmap for Achieving Aviation Green Deal Objectives by 2050". In: *European Parliament, Policy Department for Structural and Cohesion Policies, Brussels* (2022).

[6] Jewel B Barlow, William H Rae, and Alan Pope. *Low-speed wind tunnel testing*. John wiley & sons, 1999.

[7] Massimo Biava, M. Valentini, and Luigi Vigevano. "Wind tunnel corrections for isolated rotor tests". In: Sept. 2013.

[8] Massimo Biava and Luigi Vigevano. "Computational Assessment of Wind Tunnel Flow in Closed and Open Section Model Rotor Tests". In: *Journal of the American Helicopter Society* 59 (Jan. 2013). DOI: 10.4050/JAHS.59.012006.

[9] M. Broersma. *Heyson Wall Correction Code for the DNW LLF. Internship Report, DNW*. Tech. rep. 2014.

[10] Giuseppe Carlo Alp Caridi. "Development and application of helium-filled soap bubbles: For large-scale PIV experiments in aerodynamics". PhD dissertation. Delft University of Technology, 2018.

[11] Hugh W Coleman and W Glenn Steele. *Experimentation, validation, and uncertainty analysis for engineers*. John Wiley & Sons, 2018.

[12] German-Dutch Wind Tunnels - DNW. *LOW-SPEED TUNNEL (DNW-LST)*. URL: https://www.dnw.aero/wind-tunnels/lst/.

[13] V. Dossena, Giacomo Persico, Berardo Paradiso, Lorenzo Battisti, Sergio Dell'Anna, et al. "An Experimental Study of the Aerodynamics and Performance of a Vertical Axis Wind Turbine in a Confined and Unconfined Environment". In: *Journal of Energy Resources Technology* 137 (Sept. 2015), 051207 (1–12). DOI: 10.1115/1.4030448.

[14] Gerrit Elsinga, Fulvio Scarano, Bernhard Wieneke, and Bas Oudheusden. "Tomographic Particle Image Velocimetry". In: *Experiments in Fluids* 41 (Dec. 2006), pp. 933–947. DOI: 10.1007/s00348-006-0212-z.

[15] Gerrit Elsinga, Jerry Westerweel, Fulvio Scarano, and Matteo Novara. "On the velocity of ghost particles and the bias errors in Tomographic-PIV". In: *Experiments in Fluids* 50 (Apr. 2010), pp. 825–838. DOI: 10.1007/s00348-010-0930-0.

[16] BF Ewald. *AGARDograph 336 - Wind Tunnel Wall Corrections (la Correction des effets de paroi en soufflerie)*. Tech. rep. ADVISORY GROUP FOR AEROSPACE RESEARCH and DEVELOPMENT NEUILLY-SUR-SEINE (FRANCE), 1998.

[17] D Engler Faleiros, M Tuinstra, and HWM Hoeijmakers. "Drag, lift and effective angle of attack from analysis wake of an airfoil in open-jet wind tunnel". In: *54th AIAA Aerospace Sciences Meeting 2016*. American Institute of Aeronautics and Astronautics Inc.(AIAA). 2016.

[18] David Faleiros, Marthijn Tuinstra, Andrea Sciacchitano, and Fulvio Scarano. "Generation and control of helium-filled soap bubbles for PIV". In: *Experiments in Fluids* 60 (Feb. 2019). DOI: 10.1007/s00348-019-2687-4.

[19] David Engler Faleiros. "Soap bubbles for large-scale PIV: Generation, control and tracing accuracy". PhD dissertation. Royal Netherlands Aerospace Centre (NLR) - Delft University of Technology, 2021.

[20] Oliver Fischer. *Investigation of Correction Methods for Interference Effects in Open-Jet Wind Tunnels*. Jan. 2018. ISBN: 978-3-658-21378-7. DOI: 10.1007/978-3-658-21379-4.

[21] Arvind Gangoli Rao, Feijia Yin, and Henri Werij. "Energy Transition in Aviation: The Role of Cryogenic Fuels". In: *Aerospace* 7 (Dec. 2020), p. 181. DOI: 10.3390/aerospace7120181.

[22] HC Garner, EW Rogers, WE Acum, and EC Maskell. "Subsonic wind tunnel wall corrections (No. AGARD-OGRAPH-109)". In: *Advisory Group for Aerospace Research and Development, Neuilly-sur-Seine (FRANCE)* (1966).

[23] Hermann Glauert. "Airplane propellers". In: *Aerodynamic theory* (1935).

[24] Hermann Glauert. "The effect of compressibility on the lift of an aerofoil". In: *Proceedings of the Royal Society of London. Series A, Containing Papers of a Mathematical and Physical Character* 118.779 (1928), pp. 113–119.

[25] Hermann Glauert. *Wind tunnel interference on wings, bodies and airscrews*. Tech. rep. Aeronautical Research Council London (United Kingdom), 1933.

[26] Patrick Goulding, Lei Yang, and Norbert Ulbrich. "Developing a Robust Wall Interference Correction Methodology for Fixed-Wing Testing at the National Full-Scale Aerodynamics Complex". In: *50th AIAA Aerospace Sciences Meeting including the New Horizons Forum and Aerospace Exposition*. 2012, p. 1215.

[27] Patrick W Goulding, Christopher M Nykamp, and Billy B Bartow. "Assessing Wall Interference Effects on a Medium-Sized Rotor in the National Full-Scale Aerodynamics Complex". In: *55th AIAA Aerospace Sciences Meeting*. 2017, p. 0773.

[28] Kalman J Grunwald. *Experimental study of wind-tunnel wall effects and wall corrections for a general-research v/stol tilt-wing model with flap*. Tech. rep. NASA TN D-2887, 1965.

[29] H.Glauert. *The Elements of Aerofoil and Airscrew Theory*. Cambridge University Press, 1948.

[30] JE Hackett, DJ Wilsden, and DE Lilley. *Estimation of tunnel blockage from wall pressure signatures: a review and data correlation*. Tech. rep. NASA CR-15, 224, 1979.

[31] F.D. Harris. "Aerodynamic and dynamic rotary wing model testing in wind tunnels and other facilities". In: *Helicopter Aerodynamics and Dynamics, Advisory Group for Aerospace Research Development AGARD LS-63, Neuilly sur Seine, France, 1973, pp. 1018*. (1973).

[32] G.H. Hegen. *Cp Distribution Optimization of the LLF Automotive Test Section in the NLR-AWT*. Aug. 2021.

[33] Harry H Heyson. *FORTRAN programs for calculating wind-tunnel boundary interference*. Tech. rep. NASA TM X-1740, 1969.

[34] Harry H Heyson. *Jet-boundary corrections for lifting rotors centered in rectangular wind tunnels*. Vol. 71. US Government Printing Office, Tech. Rep. R-71, 1960.

[35] Harry H Heyson. *Linearized theory of wind-tunnel jet-boundary corrections and ground effect for vtol-stol aircraft*. US Government Printing Office, Tech. Rep. R-124, 1962.

[36] Harry H Heyson. *Nomographic Solution of the Mometum Equation for VTOL-STOL Aircraft*. National Aeronautics and Space Administration, Technical Note D-81, 1961.

[37] Harry H Heyson. *Rapid estimation of wind-tunnel corrections with application to wind-tunnel and model design*. National Aeronautics and Space Administration, NASA TN D - 6416, 1971.

[38] Harry H Heyson. *Theoretical study of conditions limiting v/stol testing in wind tunnels with solid floor*. National Aeronautics and Space Administration, Tech. Rep. NASA TN-D 5819, 1970.

[39] Harry H Heyson. *Use of superposition in digital computers to obtain wind-tunnel interference factors for arbitrary configurations, with particular reference to V/STOL models*. Tech. rep. NASA TR R-302, 1969.

[40] Harry H Heyson. *Wind Tunnel Wall Effects at Extreme Force Coefficients*. Tech. rep. NASA N 68-25433, 1967.

[41] Harry H Heyson and Kalman J Grunwald. "24. Wind-Tunnel Boundary Interference for V/STOL Testing". In: *Conference on V/STOL and STOL Aircraft, Ames Research Center, Moffett Field, California, April 4-5, 1966*. Vol. 116. Scientific and Technical Information Division, National Aeronautics and 1966, p. 409.

[42] Harry H Heyson and S Katzoff. *Induced velocities near a lifting rotor with nonuniform disk loading*. Tech. rep. NACA-TR-1319, 1957.

[43] B. J. Carolus Horsten. "Low-Speed Model Support Interference-Elements of an Expert System". PhD thesis. TU Delft, 2011.

[44] Venkit Iyer and Joel Everhart. "Application of pressure-based wall correction methods to two NASA Langley wind tunnels". In: *19th AIAA Applied Aerodynamics Conference*. 2001, p. 2472.

[45] Wayne Johnson. *Rotorcraft aeromechanics*. Vol. 36. Cambridge University Press, 2013.

[46] M. Jovetic. *Implementing Novel Model Aircraft Configurations into the Heysons Method for Lift Interference. Internship Report, DNW*. Tech. rep. 2021.

[47] Joseph Katz and Allen Plotkin. *Low-speed aerodynamics*. Vol. 13. Cambridge university press, 2001.

[48] Amir Kolaei, Devin Barcelos, and Götz Bramesfeld. "Experimental Analysis of a Small-Scale Rotor at Various Inflow Angles". In: *International Journal of Aerospace Engineering* 2018 (Oct. 2018), pp. 1–14. DOI: 10.1155/2018/2560370.

[49] Th E Labrujère. "Correction for wall interference in a solid-wall wind tunnel using sparse measured boundary conditions". In: *NLR Technical Publication TP 89004 U* (1989).

[50] Th E Labrujère. "Correction for wall-interference by means of a measured-boundary-condition method". In: *NLR-TR 84114 U* (1984).

[51] Hans-Juergen Langer, Randall L Peterson, and Thomas H Maier. *An experimental evaluation of wind tunnel wall correction methods for helicopter performance*. Tech. rep. Deutsche Forschungsanstalt für Luft- und Raumfahrt e.V. Institut für Flugmechanik, Braunschweig, Germany, 1996.

[52] Göttingen LaVision GmbH. *Product Manual FlowMaster Shake-the-Box (4D PTV)*. English. Version DaVis 10.2. LaVision GmbH. Nov. 19, 2021. 132 pp.

[53] RA Maarsingh, TE Labrujère, and J Smith. "Wind tunnel influence considering 2D high lift configurations". In: *NLR MP 84047 U* (1984).

[54] Hans-Gerd Maas, Armin Gruen, and Dimitrios Papantoniou. "Particle tracking velocimetry in three-dimensional flows Part 1. Photogrammetric determination of particle coordinates". In: *Experiments in Fluids* 15 (July 1993), pp. 133–146. DOI: 10.1007/BF00190953.

[55] Nadeem Malik, Th Dracos, and Dimitrios Papantoniou. "Particle tracking velocimetry in three-dimensional flows - Part II: Particle tracking". In: *Experiments in Fluids* 15 (Jan. 1993), pp. 279–294. DOI: 10.1007/BF00223406.

[56] Peter Manovski, Matteo Novara, Karthik Depuru-Mohan, Reinhard Geisler, Daniel Schanz, et al. "3D Lagrangian Particle Tracking of a High-Subsonic Jet Using four-Pulse Shake-The-Box". In: Apr. 2018.

[57] Robert Flemming Mikkelsen and Jens Nørkær Sørensen. “Modelling of Wind Tunnel Blockage”. English. In: *15th IEA Symposium on the Aerodynamics of Wind Turbines*. 15th IEA Symposium on the Aerodynamics of Wind Turbines ; Conference date: 26-11-2001 Through 27-11-2001. FOI Swedish Defence Research Agency, 2002.

[58] M Mokry, Yat-Yung Chan, and DJ Jones. *Two-dimensional wind tunnel wall interference*. Tech. rep. ADVISORY GROUP FOR AEROSPACE RESEARCH and DEVELOPMENT NEUILLY-SUR-SEINE (FRANCE), 1983.

[59] Matteo Novara, Daniel Schanz, Sebastian Gesemann, Kyle Lynch, and Andreas Schröder. “Lagrangian 3D particle tracking for multi-pulse systems: performance assessment and application of Shake-The-Box”. In: (2016).

[60] Matteo Novara, Daniel Schanz, Nico Reuther, Christian Kähler, and Andreas Schröder. “Lagrangian 3D particle tracking in high-speed flows: Shake-The-Box for multi-pulse systems”. In: *Experiments in Fluids* 57 (July 2016). DOI: 10.1007/s00348-016-2216-7.

[61] Matteo Novara, Daniel Schanz, and Andreas Schröder. “Two-pulse 3D particle tracking with Shake-The-Box”. In: *Proceedings of the 20th International Symposium on the Application of Laser and Imaging Techniques to Fluid Mechanics*. 221. 2022, pp. 2664–2678.

[62] P. Pernsteiner. *Re-entry of the sucked tunnel boundary layer*. June 2020.

[63] I. Philipsen. *Bepaling van wind tunnelwand correctiefactoren met behulp van de methode Heyson., TU Delft*. Tech. rep. LR 411, 1992.

[64] Iwan Philipsen. “Lift Interference Effects Evaluation for Powered Models in Closed-wall Low-speed Wind Tunnels”. In: *AIAA Scitech 2021 Forum*. 2021, p. 1105.

[65] Ludwig Prandtl and Albert Betz. *Vier Abhandlungen zur Hydrodynamik und Aerodynamik*. Vol. 3. Universitätsverlag Göttingen, 2010.

[66] William H Rae Jr. “An experimental investigation of the effect of test section geometryon the maximum size rotor that can be tested in a closed throat wind-tunnel”. In: *2nd Aerodynamic Testing Conference*. 1966, p. 736.

[67] William H Rae Jr. “Limits on minimum speed V/STOL wind-tunnel tests.” In: *Journal of Aircraft* 4.3 (1967), pp. 249–254.

[68] William H Rae Jr. and Shojiro Shindo. “Comments on V/STOL Wind Tunnel Data at Low Forward Speeds”. In: *Third CAL/AVLABS Symposium on Aerodynamics of Rotary Wing and V/STOL Aircraft, Buffalo, NY* 2 (June, 1969), pp. 18–20.

[69] William H Rae Jr. and Shojiro Shindo. *Limits on Low Speed Wind Tunnel Tests of Rotors.* Tech. rep. Washington University Seattle Department of Aeronautics and Astronautics, 1977.

[70] M. Raffel, Christian Willert, Fulvio Scarano, Christian Kähler, Steven Wereley, et al. *Particle Image Velocimetry A Practical Guide*. Jan. 2018. ISBN: 978-3-319-68852-7.

[71] Nicholas Rosenfeld, Kevin Kimmel, and Anish J Sydney. “Investigation of ship topside modeling practices for wind tunnel experiments”. In: *53rd AIAA Aerospace Sciences Meeting*. 2015, p. 0245.

[72] Rafael Rubin and Dan Zhao. “Identifying the Propeller Transition to Wing-Like Behavior at High Angles of Incidence”. In: *AIAA Journal* (Oct. 2021). DOI: 10.2514/1.J060932.

[73] Rafael Rubin and Dan Zhao. “New Development of Classical Actuator Disk Model for Propellers at Incidence”. In: *AIAA Journal* 59 (Dec. 2020), pp. 1–15. DOI: 10.2514/1.J059734.

[74] Koninklijk Nederlands Lucht- en Ruimtevaartcentrum - NLR. *Aeroacoustic Wind Tunnel (NLR-AWT)*. URL: https://www.nlr.org/research-infrastructure/aeroacoustic-wind-tunnel/.

[75] Daniel Schanz, Sebastian Gesemann, and Andreas Schröder. “Shake-The-Box: Lagrangian particle tracking at high particle image densities”. In: *Experiments in Fluids* 57 (Apr. 2016). DOI: 10.1007/s00348-016-2157-1.

[76] Daniel Schanz, Sebastian Gesemann, Andreas Schröder, Bernhard Wieneke, and Matteo Novara. "Non-uniform optical transfer functions in particle imaging: Calibration and application to Tomographic reconstruction". In: *Measurement Science and Technology* 24 (Dec. 2012), p. 024009. DOI: 10.1088/0957-0233/24/2/024009.

[77] Daniel Schanz, Andreas Schröder, Sebastian Gesemann, Dirk Michaelis, and Bernhard Wieneke. "Shake The Box: A highly efficient and accurate Tomographic Particle Tracking Velocimetry (TOMO-PTV) method using prediction of particle positions". In: Jan. 2013, pp. 1–13.

[78] Andrea Sciacchitano and Bernhard Wieneke. "PIV uncertainty propagation". In: *Measurement Science and Technology* 27 (Aug. 2016), p. 084006. DOI: 10.1088/0957-0233/27/8/084006.

[79] M Seidel and RA Maarsingh. "Test Capabilities of the German-Dutch Wind Tunnel DNW for Rotors, Helicopters, and V/STOL Aircraft". In: *5th European Rotorcraft and Powered Lift Aircraft Forum*. 1979.

[80] Wen Zhong Shen and Robert Mikkelsen. "Wall Correction Model for Wind Tunnels with Open Test Section". In: *Aiaa Journal - AIAA J* 44 (Aug. 2006), pp. 1890–1894. DOI: 10.2514/1.15656.

[81] Shojiro Shindo and William H Rae Jr. "Low-speed test limit of V/STOL model located vertically off-center". In: *Journal of Aircraft* 15.4 (1978), pp. 253–254.

[82] Patrick Shinoda and Wayne Johnson. "Performance results from a test of an S-76 rotor in the NASA Ames 80-by 120-foot wind tunnel". In: *11th Applied Aerodynamics Conference*. 1993, p. 3414.

[83] Patrick M Shinoda. "Wall interaction effects for a full-scale helicopter rotor in the NASA Ames 80-by 120-foot wind tunnel". In: *AGARD, Wall Interference, Support Interference and Flow Field Measurements* (1994).

[84] Tomas Sinnige. *Lecture notes in AE4115 Experimental Simulations, Wind-Tunnel Boundary Corrections*. Nov. 2021.

[85] Peter South. *Measurements of flow breakdown in rectangular wind tunnel working sections*. Tech. rep. National Aeronautical Establishment Ottawa (Ontario), 1968.

[86] Theodore Theodorsen. "The theory of wind-tunnel wall interference". In: *Annual Report of the National Advisory Committee for Aeronautics* 18 (1932), p. 219.

[87] DNW German-Dutch Wind Tunnels. *Internal Report*. DNW, 1991.

[88] RA Tyler and RG Williamson. "Wind tunnel testing of V/STOL engine models: Some observed flow interaction and tunnel effects(Thrust measurement interpretation for V/STOL models and transition performance of lift fan configurations)". In: *AGARD Inlets and Nozzles for Aerospace Eng. 12 p(SEE N 72-16685 07-28)* (1971).

[89] N Ulbrich and A Boone. "Real-time wall interference correction system of the 12 ft pressure wind tunnel". In: *36th AIAA Aerospace Sciences Meeting and Exhibit*. 1998, p. 707.

[90] Norbert Ulbrich. *The real-time wall interference correction system of the NASA Ames 12-foot pressure wind tunnel*. Tech. rep. NASA/CR-208537, 1998.

[91] S. Voorst. *Analysis of Lift Interference for Propeller Driven Aircraft in the Large Low-Speed Facility at DNW. Bachelor Thesis, DNW*. Tech. rep. 2017.

[92] M. J. Werle. "Propeller Wall Blockage Performance Corrections". In: *Journal of Propulsion and Power* 27.2 (2011), pp. 496–498. DOI: 10.2514/1.B34038. eprint: https://doi.org/10.2514/1.B34038. URL: https://doi.org/10.2514/1.B34038.

[93] M. J. Werle. "Wind Turbine Wall-Blockage Performance Corrections". In: *Journal of Propulsion and Power* 26.6 (2010), pp. 1317–1321. DOI: 10.2514/1.44602. eprint: https://doi.org/10.2514/1.44602. URL: https://doi.org/10.2514/1.4460.

[94] Jerry Westerweel and Fulvio Scarano. "Universal outlier detection for PIV data". In: *Experiments in fluids* 39 (2005), pp. 1096–1100.

[95] B. F. A. Wieneke. “PIV uncertainty quantification and beyond”. PhD thesis. Delft University of Technology, 2017.

[96] Bernhard Wieneke. “Iterative reconstruction of volumetric particle distribution”. In: *Measurement Science and Technology* 24.2 (2012), p. 024008.

[97] Bernhard Wieneke. “Volume self-calibration for 3D particle image velocimetry”. In: *Experiments in Fluids* 45 (Sept. 2008), pp. 549–556. DOI: 10.1007/s00348-008-0521-5.

A

Theoretical Background

In this Appendix the basic theoretical background used in this Thesis is presented. Most of the formulations used here can be found in the textbooks of Anderson [1] and Katz et al. [47].

A.1. Velocity Potential Equation for Incompressible Flows (Laplace Equation)

This analysis is valid for steady, incompressible, inviscid and irrotational flows. Since subsonic, low speed tests are employed, the Mach number is extremely small so the incompressibility is expected for most of the part of the flow and especially close to the walls and away from the propeller blades. Steady conditions are also in good correspondence with reality when keeping constant parameters like temperature, velocity, atmospheric pressure, etc. during the wind tunnel test. The target for a flow in a wind tunnel test section is to be uniform and unidirectional as much as possible. Under such circumstances, the irrotationality assumption is valid as long as the flow is far away from the walls and the slipstream. Similar considerations are used for the viscosity which only plays a role in the boundary layers developed close to the walls and in the wake behind the model. The irrotationality condition (eqn.(A.1)) yields that the velocity field is conservative and thus it can be described by a potential function Φ (eqn.(A.2)). This combined with the incompressible conservation of mass (eqn.(A.3)) are used to derive that the velocity potential obeys the Laplace equation as shown in equation (A.4). Furthermore, the Bernoulli equation (A.5) holds between any two points in the areas described above and not necessarily just on the same streamline due to irrotationality of the flow.

$$\underset{\sim}{\nabla} \times \underset{\sim}{u} = \underset{\sim}{0} \tag{A.1}$$

$$\underset{\sim}{u} = \nabla \cdot \underset{\sim}{\Phi} \tag{A.2}$$

$$\nabla \cdot \underset{\sim}{u} = 0 \tag{A.3}$$

$$\nabla^2 \underset{\sim}{\Phi} = 0 \tag{A.4}$$

$$P + \frac{1}{2}\rho u^2 = const \tag{A.5}$$

A.2. Linearization of the Bernoulli Equation

Assume a flow inside a solid-wall wind tunnel as shown in the left part of Figure 2.12 and characterized in section 2.4.1. One may use the Bernoulli equation in order to relate the perturbation velocity with the pressure coefficient at a certain point 'i' on the boundary S_W outside the wall boundary layer.

$$\begin{aligned} P_\infty + \frac{1}{2}\rho U_\infty^2 &= P_i + \frac{1}{2}\rho U_{TT,i}^2 + \frac{1}{2}\rho V_{TT,i}^2 \\ &= P_i + \frac{1}{2}\rho(U_\infty + U_{T,i})^2 + \frac{1}{2}\rho V_{T,i}^2 \\ &= P_i + \frac{1}{2}\rho U_\infty^2 + \rho U_\infty U_{T,i} + \frac{1}{2}\rho V_{T,i}^2 \end{aligned} \tag{A.6}$$

By reorganizing the above equation and dividing by $q = \frac{1}{2}\rho U_\infty^2$ the exact form of the Bernoulli relation connecting the measured pressure coefficient with the disturbance velocities at a point 'i' may be revealed:

$$u_{T,i}^2 + 2u_{T,i} + v_{T,i}^2 + C_{P,i} = 0 \tag{A.7}$$

The above equation, may be linearized, depending on the wind tunnel flow. By assuming that the axial disturbance velocity is greater than the other components $u_{T,i} >> v_{T,i}$, $w_{T,i}$ and that $u_{T,i} << 1$ one can derive to the linearized version of the Bernoulli equation:

$$2u_{T,i} + C_{P,i} = 0 \tag{A.8}$$

In case the lateral component of the disturbance velocity is of the order of $u_{T,i}$, but still both disturbance velocities are way lower than unity, one can use the following equation:

$$2u_{T,i} + v_{T,i}^2 + C_{P,i} = 0 \tag{A.9}$$

A.3. Velocity Potential Equation for Compressible Flows

It is known that an inviscid subsonic compressible flow over a body subject to uniform flow is irrotational [1]. Therefore, a velocity potential can be defined in accordance with the previous chapter derivation. The analysis below is given for 2D flows for the sake of simplicity. By employing the continuity equation for a steady compressible flow one can show that:

$$\frac{\partial(\rho u_x)}{\partial x} + \frac{\partial(\rho u_y)}{\partial y} = \rho[\frac{\partial^2\phi}{\partial x^2} + \frac{\partial^2\phi}{\partial y^2}] + \frac{\partial\phi}{\partial x}\frac{\partial\rho}{\partial x} + \frac{\partial\phi}{\partial y}\frac{\partial\rho}{\partial y} = 0 \tag{A.6}$$

Due to irrotationality of the flow the Euler's equations can be written in the form of:

$$\underset{\sim}{dP} = -\rho \underset{\sim}{u} d\underset{\sim}{u} = -\frac{\rho}{2} d[\frac{\partial^2\phi}{\partial x^2} + \frac{\partial^2\phi}{\partial y^2}] \tag{A.7}$$

Now by assuming the flow to be isentropic ($dP = \alpha^2 d\rho$), one can derive the two equations for the density gradient in the x and y directions through the above equation:

$$\frac{\partial \rho}{\partial x} = -\frac{\rho}{\alpha^2}\left(\frac{\partial \phi}{\partial x}\frac{\partial^2 \phi}{\partial x^2} + \frac{\partial \phi}{\partial y}\frac{\partial^2 \phi}{\partial x \partial y}\right) \qquad ; \qquad \frac{\partial \rho}{\partial y} = -\frac{\rho}{\alpha^2}\left(\frac{\partial \phi}{\partial y}\frac{\partial^2 \phi}{\partial y^2} + \frac{\partial \phi}{\partial x}\frac{\partial^2 \phi}{\partial x \partial y}\right) \tag{A.8}$$

Therefore, by substituting equations (A.8) into (A.6), one can derive to the velocity potential equation for compressible flows. The speed of sound α is also a function of constants of the flow and the velocity potential.

$$\left[1 - \frac{1}{\alpha^2}\left(\frac{\partial \phi}{\partial x}\right)^2\right]\frac{\partial^2 \phi}{\partial x^2} + \left[1 - \frac{1}{\alpha^2}\left(\frac{\partial \phi}{\partial y}\right)^2\right]\frac{\partial^2 \phi}{\partial y^2} - \frac{2}{\alpha^2}\frac{\partial \phi}{\partial x}\frac{\partial \phi}{\partial y}\frac{\partial^2 \phi}{\partial x \partial y} = 0 \tag{A.9}$$

In contrast with Appendix A.1, where the velocity potential equation for incompressible flows is given by a linear partial differential equation (Laplace equation (A.4)), the velocity potential equation is a non-linear partial differential equation which has no analytical solution and it needs to be solved numerically, or by linearizing it in order to reach an approximate solution. The latter will be discussed in the following section.

A.4. Linearized Velocity Potential Equation for Compressible Flows

For a 2D inviscid, irrotational, isentropic and compressible flow over a body subject to a uniform velocity u_∞, as described above, the horizontal and vertical velocity components can be defined as the sum of the uniform flow and the velocities induced by the geometry of the body. These velocity increments $U_{x,p}, U_{y,p}$ are called perturbation velocities.

$$U_x = u_\infty + U_{x,p} \qquad ; \qquad U_y = U_{y,p} \tag{A.10}$$

In a similar manner, one can define a perturbation velocity potential such that:

$$\phi = u_\infty x + \phi_p \tag{A.11}$$

$$\frac{\partial \phi}{\partial x} = u_\infty + \frac{\partial \phi_p}{\partial x} \qquad ; \qquad \frac{\partial \phi}{\partial y} = \frac{\partial \phi_{y,p}}{\partial y} \tag{A.12}$$

By substituting the above equations into equation (A.19), one can obtain the perturbation velocity potential equation:

$$\left[1 - \frac{1}{\alpha^2}\left(u_\infty + \frac{\partial \phi_p}{\partial x}\right)^2\right]\frac{\partial^2 \phi_p}{\partial x^2} + \left[1 - \frac{1}{\alpha^2}\left(\frac{\partial \phi_p}{\partial y}\right)^2\right] - \frac{2}{\alpha^2}\left(u_\infty + \frac{\partial \phi_p}{\partial x}\right)\frac{\partial \phi_p}{\partial y}\frac{\partial^2 \phi_p}{\partial x \partial y} = 0 \tag{A.13}$$

By using the energy equation (A.14) with respect to the free-stream parameters, and substitute it on the above equation, one gets the perturbation velocity equation as shown in (A.15).

$$\frac{\alpha_\infty^2}{\gamma - 1} + \frac{u_\infty^2}{2} = \frac{\alpha^2}{\gamma - 1} + \frac{(u_\infty + U_{x,p})^2 + U_{y,p}^2}{2} \tag{A.14}$$

$$(1-Ma_\infty^2)\frac{\partial U_{x,p}}{\partial x}+\frac{\partial U_{y,p}}{\partial y}=Ma_\infty^2[(\gamma+1)\frac{U_{x,p}}{u_\infty}+\frac{(\gamma+1)}{2}(\frac{U_{x,p}}{u_\infty})^2+\frac{(\gamma-1)}{2}(\frac{U_{y,p}}{u_\infty})^2]\frac{\partial U_{x,p}}{\partial x}$$
$$Ma_\infty^2[(\gamma-1)\frac{U_{x,p}}{u_\infty}+\frac{(\gamma+1)}{2}(\frac{U_{y,p}}{u_\infty})^2+\frac{(\gamma-1)}{2}(\frac{U_{x,p}}{u_\infty})^2]\frac{\partial U_{y,p}}{\partial y} \quad (A.15)$$
$$Ma_\infty^2[\frac{U_{y,p}}{u_\infty}(1+\frac{U_{x,p}}{u_\infty})(\frac{\partial U_{x,p}}{\partial y}+\frac{\partial U_{y,p}}{\partial x})]$$

By assuming subsonic or transonic flow $0 < Ma < 0.8$ and that the perturbation velocities are way smaller than the uniform velocity $U_{x,p}/u_\infty, U_{y,p}/u_\infty << 1$, one can perform an order of magnitude analysis in order to eliminate the right hand side terms of equation (A.15) which are smaller than the left. Thus, under these assumptions the non-linear differential equation has been replaced with a linear one as shown below:

$$(1-Ma_\infty^2)\frac{\partial U_{x,p}}{\partial x}+\frac{\partial U_{y,p}}{\partial y}=(1-Ma_\infty^2)\frac{\partial^2\phi_p}{\partial x^2}+\frac{\partial^2\phi_p}{\partial y^2}=0 \quad (A.16)$$

A.5. Prandtl-Glauert Transformation

The Prandtl-Glauert transformation is a coordinate change which relates the linearized velocity potential equation for a compressible flow to an equivalent incompressible flow state [24]. This transformation is applied for a 2D case, as follows, with $\beta=\sqrt{(1-Ma_\infty^2)}$ and

$$x_1=x \qquad ; \qquad y_1=\beta y \quad (A.17)$$

Then the Laplace equation can be written for the new stretched co-ordinate system which represents an equivalent incompressible regime:

$$\frac{\partial^2\phi_p}{\partial x_1^2}+\frac{\partial^2\phi_p}{\partial y_1^2}=0 \quad (A.18)$$

A.6. Greens Theorem for Incompressible Potential Flows

In this section, some fundamental considerations involving Green's theorem are derived due to their application in some parts of this Thesis.

A.6.1. The General Solution of the Laplace equation

In this section, a general solution for the velocity potential which satisfies the Laplace equation for an arbitrary body with boundary S_B enclosed in a volume V, with the outer boundary S_∞ as shown in Figure A.1. The velocity potential obeys the Laplace equation but also the boundary condition which indicates that the velocity component normal to the body's surface and to other solid boundaries must be zero or else, the well known no-penetration boundary condition (A.19). Most part of this derivation is based on [47] and [16].

$$\underset{\sim}{u}\cdot\underset{\sim}{n}=\nabla\underset{\sim}{\Phi}\cdot\underset{\sim}{n}=0 \quad (A.19)$$

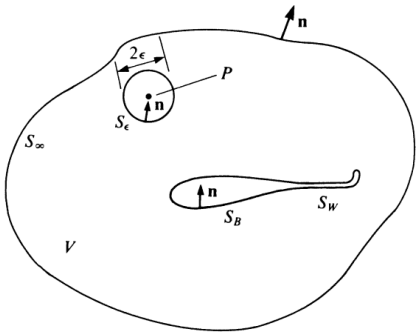


Figure A.1: Integration domain [47].

The divergence theorem states that for a vector $\underset{\sim}{q}$ the flux within a control surface is equal with the volume integral of the divergence of $\underset{\sim}{q}$ shown below:

$$\iint_S \underset{\sim}{q} \cdot \underset{\sim}{n}\, dS = -\iiint_V \nabla \cdot \underset{\sim}{q}\, dV \tag{A.20}$$

Now let vector field $\underset{\sim}{q}$ be replaced with $G\nabla\phi_I - \phi_I \nabla G$. According to equation A.20:

$$\iint_S (G\nabla\phi_I - \phi_I\nabla G) \cdot \underset{\sim}{n}\, dS = \iiint_V G\nabla^2\phi_I - \phi_I\nabla^2 G\, dV \tag{A.21}$$

As mentioned in Chapter 1, ϕ_I is the wall interference potential for a flow inside a wind tunnel which satisfies the Laplace equation, S is the total surface area and G is Green's function that is harmonic everywhere within the measurement region except at the point P. Near this point G behaves like $1/r$, where r is the distance between the point P and a variable point in the region. Since both ϕ_I and G are harmonic and if point P is outside the control volume then the volume integral of equation (A.21) is zero leading to:

$$\iint_S (G\nabla\phi_I - \phi_I\nabla G) \cdot \underset{\sim}{n}\, dS = 0 \tag{A.22}$$

In the case when the point P is inside volume V, it now needs to be excluded from the region of integration. Under the assumption that P is surrounded by a small spherical area of radius ϵ, outside of the sphere and in the remaining region V the potential ϕ_I satisfies the Laplaces equation while Green's function is $\nabla^2 G = \nabla^2(1/r) = 0$ leading to:

$$\iint_{S+S_{sph}} (G\nabla\phi_I - \phi_I\nabla G)\cdot \underset{\sim}{n}\, dS = \iint_{S_{sph}} (G\nabla\phi_I - \phi_I\nabla G)\cdot \underset{\sim}{n}\, dS + \iint_S (G\nabla\phi_I - \phi_I\nabla G)\cdot \underset{\sim}{n}\, dS = 0 \tag{A.23}$$

For the evaluation of the surface integral over the surface of the sphere a coordinate transformation to spherical system is necessary:

$$\underset{\sim}{n} = \underset{\sim}{e_r} \qquad ; \qquad \nabla\phi_I \cdot \underset{\sim}{n} = \frac{\partial \phi_I}{\partial r} \tag{A.24}$$

By letting the Green's function to take the form $G = 1/r$ the integral evaluated over the sphere's surface results to:

$$\iint_{S_{sph}} (G\nabla\phi_I - \phi_I\nabla G)\cdot \underset{\sim}{n}\, dS = \iint_{S_{sph}} (\frac{1}{r}\frac{\partial\phi_I}{\partial r})\, dS + \iint_{S_{sph}} (\frac{\phi_I}{r^2})\, dS \tag{A.25}$$

Finally, by replacing equation (A.25) into (A.23) it yields to:

$$[4\pi\epsilon^2 + 4\pi]\phi_I(P) + \iint_S (\frac{1}{r}\nabla\phi_I + \phi_I\nabla(\frac{1}{r}))\cdot \underset{\sim}{n}\, dS = 0 \tag{A.26}$$

Since the value of the wall interference potential ϕ_I at a point P is desired, the limit of $\epsilon \to 0$ is taken so as

$$\phi_I(P) = -\frac{1}{4\pi}\iint_S (\frac{1}{r}\nabla\phi_I - \phi_I\nabla(\frac{1}{r}))\cdot \underset{\sim}{n}\, dS = -\frac{1}{4\pi}\iint_S (G\nabla\phi_I - \phi_I\nabla G)\cdot \underset{\sim}{n}\, dS \tag{A.27}$$

This means that for any point within the region with volume V, the perturbation velocity potential can be calculated by obtaining the $\phi, G, \nabla\phi, \nabla G$ values at the boundary surfaces $S = S_B + S_\infty(+S_W)$.

B

Boundary Measurement Methods

In this appendix a brief overview of the boundary measurement methods is given. Most of the presented information is based on Ashill [3] and Ewald [16].

B.1. Overview

For a given test model and wind tunnel test section as shown in Figure B.1 the flow may be defined by a total velocity potential Φ_{TT} , which consists of the wind tunnel (uniform) speed and a perturbation velocity potential ϕ_T. As derived in Appendix A, the perturbation velocity potential satisfies the exact form of equation (A.15) as shown in (B.2), where the subscript "ref" i used to denote the already corrected for blockage to free-air value parameters. The Prandtl-Glauert transformation is then used to obtain equation (B.3).

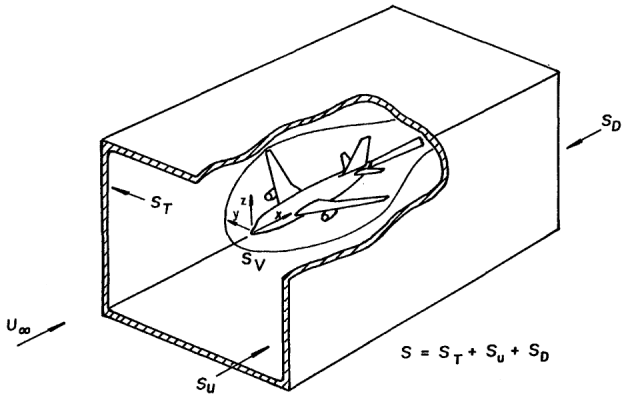


Figure B.1: Wind tunnel test section and model [3].

$$\phi_T = \Phi_{TT} - U_\infty x \tag{B.1}$$

$$\beta^2 \frac{\partial^2 \phi_T}{\partial x^2} + \frac{\partial^2 \phi_T}{\partial y^2} + \frac{\partial^2 \phi_T}{\partial z^2} = f(\frac{\partial \Phi_{TT}}{\partial x_i}, \frac{\partial^2 \Phi_{TT}}{\partial x_i \partial x_j}, (U_T/U_{ref}), Ma_F) \tag{B.2}$$

$$\nabla^2\phi_T = \frac{\partial^2\phi_T}{\partial x_1^2} + \frac{\partial^2\phi_T}{\partial y_1^2} + \frac{\partial^2\phi_T}{\partial z_1^2} = \frac{f(\frac{\partial\Phi_{TT}}{\partial x_i}, \frac{\partial^2\Phi_{TT}}{\partial x_i\partial x_j}, (U_T/U_{ref}), Ma_F)}{\beta^2} \tag{B.3}$$

In order to compare the flow in the wind tunnel with an actual free-air flow, one can assume an unbounded flow around the same model moving at the corresponding speed U_{ref} and at a negative angle of attack with respect to the vertical axis which differs by $\Delta\alpha$. This flow can also be characterized by the perturbation potential equation given in (B.4). Similarly with the above procedure, the unbounded flow also satisfies the exact form of equation (A.15).

$$\phi_F = \Phi_{TF} - U_{ref}x - \Delta\alpha z \tag{B.4}$$

$$\nabla^2\phi_F = \frac{\partial^2\phi_F}{\partial x_1^2} + \frac{\partial^2\phi_F}{\partial y_1^2} + \frac{\partial^2\phi_F}{\partial z_1^2} = \frac{f(\frac{\partial\Phi_{TF}}{\partial x_i}, \frac{\partial^2\Phi_{TF}}{\partial x_i\partial x_j}, (u_F/U_{ref}), Ma_F)}{\beta^2} \tag{B.5}$$

According to Ashill [3], in cases where either of the following conditions is valid,

- Those two flows can be considered identical ($\Phi_{TT} = \Phi_{TF}$) in the vicinity of the model such that the wind tunnel flow can be corrected to its corresponding free-air flow.
- The perturbations in the flow induced by the model are small everywhere.
- A subsonic low speed regime can be considered, resulting in a vanishingly small Mach number (incompressible flow).

by subtraction of equation (B.5) from (B.4), the Laplace equation for the difference in perturbation velocity potentials is satisfied as shown in (B.6). Thus, a variable ϕ_w is introduced which represents the difference between the perturbation potentials between bounded and unbounded flow states and which is harmonic throughout the whole flow domain. Considering equation (5) or (6), it is clear that ϕ_w is the wall interference potential for a flow inside a wind tunnel.

$$\nabla^2\phi_T - \nabla^2\phi_F = \nabla^2[\phi_T - \phi_F] = \nabla^2\phi_w = 0 \tag{B.6}$$

Since the wall interference potential is harmonic everywhere inside the flow domain according to the above equation, it is possible to use the Green's theorem for incompressible potential flows as shown in Appendix A.6.1. By making use of equation (A.27) one shows that:

$$\phi_w(P) = -\frac{1}{4\pi}\iint_S (G\nabla\phi_w - \phi_w\nabla G)\cdot \underset{\sim}{n}\, dS = -\frac{1}{4\pi}\iint_S (G[\frac{\partial\phi_T}{\partial n} - \frac{\partial\phi_F}{\partial n}] - (\phi_T - \phi_F)\frac{\partial G}{\partial n})\, dS \tag{B.7}$$

In Katz et al. [47], it is stated that for the wall interference potential to be harmonic everywhere within the volume bounded by S, the quantity $[\frac{\partial\phi_T}{\partial n} - \frac{\partial\phi_F}{\partial n}]$ must be single-valued, meaning that the circulations of the bounded and the unbounded flow around any closed loop should be mutually equal or else:

$$\iint_S [\frac{\partial\phi_T}{\partial n} - \frac{\partial\phi_F}{\partial n}]\, dS = \iint_S \frac{\partial\phi_w}{\partial n}\, dS = 0 \tag{B.8}$$

The above equation is the foundation of those methods which completely ignores the flow in the vicinity of the model (and its wake, S_V) and deducts information about the wall interference potential ϕ_w by

computing the necessary quantities on the boundaries of the test section S. By observing equation (B.7), it is obvious that three parameters need to be determined in order to obtain the wall interference potential. The perturbation potential of the wind-tunnel flow and its normal gradient have to be determined at the surface of the test section by means of measurements and the former variables have to be estimated for the free-air case. Therefore, the unbounded flow around the model needs also to be modelled and calculated. According to Ashill [3], the number of variables needed can be reduced to two by choosing an appropriate Green's function for the boundary-value problem. Those two variables can either be measured directly from the test section's surface (Two-Variable-Method), or one can be obtained by modelling the free-air case and the other from measurements on the boundaries (One-Variable-Method). So, depending on the amount of variables measured these methods are categorized. Finally, there is a hybrid method (Wall-Signature-Method) which combines two variable measurements (complete for one variable and for the other sparse measurements) but also uses a model representation and the method of images in order to connect the limited measurements with the modelling of the flow.

One Variable Methods

As mentioned earlier, with an appropriate choice of the Green's function such that it vanishes on the measurement surface, can lead to two conditions based on the variable to be measured. If the choice of the Green's function is such that the first term of the right hand side of equation (B.7) is zero ($G = 0$ at S), then the resulting form, usually referred as the Dirichlet Problem, is given by equation (B.9). Thus, the perturbation velocity potential of the wind tunnel flow needs to be measured at the boundaries. A model representation is needed for the free-air perturbation velocity potential at S.

$$\phi_w(P) = \frac{1}{4\pi} \iint_S (\phi_T - \phi_F) \frac{\partial G}{\partial n}) \, dS \tag{B.9}$$

The value of the perturbation velocity potential ϕ_T is usually determined by means of static pressure measurements on the wall boundaries of the test section S_T. According to [2], to an approximation consistent with that of the small perturbation equation, the streamwise perturbation non dimensional velocity, $u_T = U_T/U_\infty$, can be inferred from the corresponding increment in static pressure coefficient, C_P, by the linearized version of Bernoulli's equation. Equation (B.10) usually holds even in low speed flows however, in cases that the pressure coefficient C_P is not sufficiently small for the second order terms in Bernoulli's equation to be ignored, then the other components need to be taken into account. For more information the reader is refereed to Appendix A.2. For determining both the velocity components by integrating the above equation, the integration constant, corresponding to the vertical velocity component needs to be determined by measurements of the former upstream of the pressure measurement surface, or from measurements at the inlet and outlet surfaces, S_U and S_D respectively.

$$u_T = \frac{1}{U_\infty} \frac{\partial \phi_T}{\partial x_1} = -\frac{C_P}{2} \tag{B.10}$$

On the other hand, if the choice of the Green's function is such that the second term of the right hand side of equation (B.7) is zero ($\partial G/\partial n = 0$ at S), then the resulting form, usually referred as the Neumann Problem, is given by equation (B.11). Thus, the normal component of the velocity, or the flow angle needs to be specified at the boundaries. For solid wall test sections this is relatively easy since the no-penetration boundary condition is applicable, but for slotted wall or open jet configurations, defining the flow angle with the required accuracy is extremely difficult.

$$\phi_w(P) = -\frac{1}{4\pi} \iint_S G[\frac{\partial \phi_T}{\partial n} - \frac{\partial \phi_F}{\partial n}] \, dS \tag{B.11}$$

Finally, in cases where the normal component of velocity is well-defined (e.g. solid walls) on certain surfaces, while the velocity perturbation potential is easier to be defined on other (e.g. open jet), it is possible to split the boundary surface into two regions, say S_1 and S_2 respectively, in order to obtain a Mixed-Type Problem given by equation (B.12).

$$\phi_w(P) = \frac{1}{4\pi} \iint_{S_2} (\phi_T - \phi_F) \frac{\partial G}{\partial n}) \, dS - \frac{1}{4\pi} \iint_{S_1} G[\frac{\partial \phi_T}{\partial n} - \frac{\partial \phi_F}{\partial n}] \, dS \tag{B.12}$$

As mentioned above, these methods need a model representation in order to determine the forementioned values for the unbounded flow. Lastly, these methods are "auto-corrective" meaning that the errors resulting from either pressure or velocity measurements are cancelled out because of the integral form of their respective equations. The one variable method is not used in this study, but it is mentioned in the overview for completeness.

Two Variable Methods

Two variable methods rely purely on measurements and thus, they are not in need of any model representation. This is achieved by setting the contribution of the model representation terms, or better, the unbounded flow contribution to zero. Solving for the forementioned equation results in the free-air Green's function, which is shown to be $G_F \equiv 1/r$.

$$\frac{1}{4\pi} \iint_S (\frac{\partial \phi_F}{\partial n} G_F - \phi_F \frac{\partial G_F}{\partial n}) \, dS = 0 \tag{B.13}$$

Using equation (B.13) one can derive the required equation from (B.7) as shown below.

$$\phi_w(P) = -\frac{1}{4\pi} \iint_S (\frac{\partial \phi_T}{\partial n} G_F - \phi_T \frac{\partial G_F}{\partial n}) \, dS \tag{B.14}$$

Two variable methods offer the advantage of a global Green's function $G_F \equiv 1/r$, so wall interference can be performed relatively easily for complex flows by ignoring the flow around the model, on the expense though of measuring both velocity components at all respective surfaces comprised of S. This is straightforward for closed wall test sections because the no-penetration boundary condition offers a great advantage, however in other types of test sections, the velocity measurements could be very challenging. Another advantage of such methods is that they are also "auto-corrective" due to their conservation formulation as in one variable methods. A two variable method based on the work of Maarsingh et al. [53] has been developed in the context of the current study.

Wall Signature Methods

The Wall Signature Method is a hybrid form of the above two methods. It uses the advantage that the normal component of the velocity at the boundaries (walls) is known for closed test sections and by making use of sparse pressure measurements (signatures) at the walls, it gets an estimate of the axial component. This estimate is then either used to determine the strengths of the singularities of the model representation, or the values of a parameter linking the two flow variables. In the current Thesis, only the former variant is going to be discussed further. As mentioned above, this type of method is applied mostly to solid-wall wind tunnels where the no-penetration boundary condition applies for the velocity component normal to the walls. This leads to a Neumann Problem by choosing a Green function, such that it's normal gradient on the walls of the test section (measurement surface) vanishes. Therefore, by

applying the no-penetration boundary condition and differentiating over the axial direction on equation (B.11) it yields:

$$\frac{\partial \phi_w(P)}{\partial x} = -\frac{1}{4\pi} \iint_S \frac{\partial [G \frac{\partial \phi_F}{\partial n}]}{\partial x} \, dS \tag{B.15}$$

which results into the final equation shown below. The wind tunnel axial perturbation velocity at the measurement point P can be therefore estimated with a similar manner as described in the One Variable Method (see equation(B.11)). The difference lies upon the fact that those measurements are sparse and are used in order to determine the strengths of the singularities representing the model. That is made possible by connecting equation (B.16), whose left hand side can be directly determined by static pressure measurements on the points P.

$$U_T(P) = U_F(P) - \frac{1}{4\pi} \iint_S \frac{\partial \phi_F}{\partial n} \frac{\partial G}{\partial x} \, dS \tag{B.16}$$

Equation (B.16) can then be related with the singularities of the model representation by a linear system of equations as shown in Figure B.2. The vortex, source and doublet singularities at fixed locations, representing the model correspond to the matrix columns, whereas sensing locations on the tunnel walls (pressure orifices) correspond to the matrix rows. Various implementations of wall pressure signature

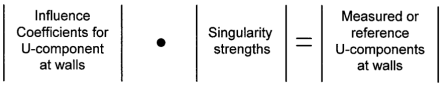


Figure B.2: Matrix of the wall pressure signature method [16].

methods exist. The most basic form of this method was reported by Hackett & Wilsden [30], whereas many other based on this method were evolved in the following years. A state-of-the-art version of a Wall Signature Method based on the Hackett & Wilsden method is presented in [90], while further implementations are given in [44]. DNW also has its own in-house wall signature method called WaSiMe. This code is similar to the implementations of [89] and [90].

C

Test Plans

This Appendix includes the test matrices for both test campaigns and the RAD assignment for the wall pressure measurements in the NLR-AWT.

C.1. NLR-AWT Test Campaign

C.1.1. NLR-AWT Test Matrices

The empty test section wall pressures are measured four successive times for the closed wall and two for the 3/4 open-jet test section, in order to check the repeatability of the measurements. A wind tunnel velocity sweep is performed two times. One single velocity sweep is presented in Table C.1. The protective (bubble) screen was not installed in those runs. Finally, the respective measurements are averaged in order to obtain an estimate for the empty test section wall pressures.

Table C.1: Wind tunnel velocity sweep (for the 3/4 open-jet test section the sweep was from 40 to 6.5 m/s).

$\mathbf{u_\infty}$ **[m/s]**	45	40	35	30	25	22.5	20	18.5	16.5	15	12.5	10	8.5	6.5	5

The above wind tunnel velocity sweep is also applied for the test stand and the motor of propeller 1. Double measurements are made for test stand configurations corresponding to angles of attack AoA= $[0°, 60°, 90°]$ for the closed and the 3/4 open-jet test sections respectively. The pressure coefficient measured at a location x, is given in equation (B.1), where P_{ref} is the nozzle and the plenum measured static pressure for the closed and the 3/4 open-jet test sections respectively. The dynamic pressure $q = 0.5\rho u_\infty^2$ is determined based on the tunnel reference system (calibration) with respect to the nozzle pressure and the plenum pressure for the closed-wall and the 3/4 open-jet test sections respectively.

$$C_{Px} = \frac{P_x - P_{ref}}{q} \tag{B.1}$$

The testing conditions for propeller 1 tested in both test sections are given in Table C.2. This table corresponds to 6 runs in total. The test stand junction height was held constant at 0.27 m (closed-wall test section) for all the runs (see Figure 3.6b). The extension (after the junction) along with the motor and the propeller is about 20 cm. Therefore, the heights corresponding to the forementioned angles of attack are h= $[0.27, 0.45, 0.47]$ m or approximately, $(h/H)_{closed} = [0.285, 0.475, 0.495]$. For

convenience, it is assumed that the propeller is on the centerline (h/H=0.5) for the cases of 60° and 90° incidence angles. Propeller 2 is tested by means of wall pressures and PTV. The pressure measurements correspond to the three incidence angles mentioned above at the same corresponding heights $(h/H)_{closed}$ (Table C.3). The PTV measurements are performed for the same forementioned conditions and for a propeller (spinner) total height of 0.27 m above the ground for each incidence angle (additional 2 runs for 90° and 60°). Therefore, the closed test section was comprised of 11 runs in total (3 for propeller 1 3 for propeller 2, at $(h/H)_{closed}$ and 5 for the PTV measurements).

Table C.2: Pressure measurements for propeller 1, for both test sections, for a given AoA, corresponding to a height above the ground $(h/H)_{closed}$ (3 AoA's, or 3 different runs per test section).

$\mathbf{u_\infty}$ **[m/s]**	40	35	30	25	22.5	20	18.5	16.5	15	12.5	10	8.5	6.5	5
n [rpm]	1000-5000	5000	5000	5000	5000	5000	5000	5000	5000	5000	5000	5000	5000	5000

Table C.3: Pressure measurements for propeller 2, for the closed-wall test section, for a given AoA, corresponding to a height above the ground $(h/H)_{closed}$ (3 AoA's, or 3 different runs).

$\mathbf{u_\infty}$ **[m/s]**	40	35	30	25	22.5	20	18.5	16.5	15	12.5	10	8.5	6.5	5
n [rpm]	6000-14000	14000	14000	14000	14000	14000	14000	14000	14000	14000	14000	14000	14000	14000

Table C.4: PTV measurements for propeller 2, for the closed-wall test section, for a given AoA, corresponding to a heights above the ground $(h/H)_{closed}$ (3 AoA's, or 3 different runs and 2 additional for a spinner height of 0.27, at 90° and 60°).

$\mathbf{u_\infty}$ **[m/s]**	40	20	12.5	8.5
n [rpm]	14000	14000	14000	14000

For the 3/4 open-jet test section, the final velocity is always up to 6.5 m/s due to tunnel's fan rpm constraints. Propeller 1 is tested in accordance with Table C.2. Propeller 2 is tested at the centerline of the tunnel $(h/H)_{3/4} = [0.5, 0.5, 0.5]$, for all the examined incidence angles, followed by an additional configuration corresponding to a 0° incidence, where the height was scaled according to the closed test section ($(h/H)_{3/4} = (h/H)_{closed} = 0.285$). The testing conditions for propeller 2 are given in Table C.5 for this test section. Additional measurements are also performed for the small propeller at angles 85° and 95 ° for the forementioned test section, resulting to $AoA_{3/4} = [0°, 60°, 85°, 90°, 95°]$. Two additional runs corresponding to the PTV runs of the closed-wall test section, at h/H = 0.285 at 60° and 90° incidence. The total wall pressure measurement runs for propeller 1 are six, while for propeller 2 are eleven. PTV measurements are performed only for propeller 2 in the closed-wall test section resulting into five total PTV runs.

Table C.5: Pressure measurements for propeller 2, for the 3/4 open-jet test section, for a given $AoA_{3/4}$, on the tunnel centerline and at $((h/H)_{AoA=0°} = 0.285$ (5 AoA's, or 5 different runs (centerline) and 3 additional, for h/H =0.285, at 0°).

$\mathbf{u_\infty}$ **[m/s]**	40	35	30	25	22.5	20	18.5	16.5	15	12.5	10	8.5	6.5
n [rpm]	5000-14000	14000	14000	14000	14000	14000	14000	14000	14000	14000	14000	14000	14000

C.1.2. NLR-AWT RAD Assignment

As mentioned in section 3.1.2, there are three electronic pressure scanning RAD modules, each comprised of 64 channels. The first two channels of each module are used for monitoring the ambient (barometric) and the nozzle pressure respectively. The RAD assignment for the closed test section consists of the eight pressure bars PB_i, each comprising of 22 pressure transducers, and 10 transition pressure stickers (5 for the top and 5 for the bottom). The latter pressure measurements are not of importance in the closed-wall test section since the measurements are conducted after the breather. The 3/4 open-jet RAD assignment consists of the two pressure bars installed in the bottom wall and the glued pressure taps

in the collector's upper and lower surface (7 at the top and 7 at the bottom). The RAD assignment for the closed and 3/4 open-jet test section is given in Tables B.6 and B.7, where each pressure transducer is characterized by its spatial position with respect to the start of the test section (nozzle exit) (X = 0) and the tunnel centerline ((Y,Z) = (0, 0)). The pressure bars are placed in the same manner as in Figure 2.14.

Table C.6: RAD assignment for the closed test section wall pressure measurements.

Channel #	**RAD Module**	**Module Channel**	**Function**	**Cable**	**X** [mm]	**Y** [mm]	**Z** [mm]
1	1	1	P_{amb}	-	-	-	-
2	1	2	$(P_t - q)_{nozzle}$	-	-	-	-
3	1	3	PB1−1	1-1	2200	475	230
4	1	4	PB1−2	1-2	2022	475	230
5	1	5	PB1−3	1-3	1867	475	230
6	1	6	PB1−4	1-4	1732	475	230
7	1	7	PB1−5	1-5	1615	475	230
8	1	8	PB1−6	1-6	1513	475	230
9	1	9	PB1−7	1-7	1425	475	230
10	1	10	PB1−8	1-8	1348	475	230
11	1	11	PB1−9	1-9	1281	475	230
12	1	12	PB1−10	1-10	1223	475	230
13	1	13	PB1−11	1-11	1172	475	230
14	1	14	PB1−12	1-12	1128	475	230
15	1	15	PB1−13	1-13	1077	475	230
16	1	16	PB1−14	1-14	1039	475	230
17	1	17	PB1−15	1-15	952	475	230
18	1	18	PB1−16	1-16	875	475	230
19	1	19	PB1−17	1-17	787	475	230
20	1	20	PB1−18	1-18	685	475	230
21	1	21	PB1−19	1-19	568	475	230
22	1	22	PB1−20	1-20	433	475	230
23	1	23	PB1−21	1-21	278	475	230
24	1	24	PB1−22	1-22	100	475	230
25	1	25	PB7−1	1-23	2200	-230	475
26	1	26	PB7−2	1-24	2022	-230	475
27	1	27	PB7−3	1-25	1867	-230	475
28	1	28	PB7−4	1-26	1732	-230	475
29	1	29	PB7−5	1-27	1615	-230	475
30	1	30	PB7−6	1-28	1513	-230	475
31	1	31	PB7−7	1-29	1425	-230	475
32	1	32	PB7−8	1-30	1348	-230	475
33	1	33	PB7−9	1-31	1281	-230	475
34	1	34	PB2−1	2-1	2200	475	-230
35	1	45	PB2−2	2-2	2022	475	-230
36	1	36	PB2−3	2-3	1867	475	-230
37	1	37	PB2−4	2-4	1732	475	-230
38	1	38	PB2−5	2-5	1615	475	-230
39	1	39	PB2−6	2-6	1513	475	-230
40	1	40	PB2−7	2-7	1425	475	-230
41	1	41	PB2−8	2-8	1348	475	-230
42	1	42	PB2−9	2-9	1281	475	-230
43	1	43	PB2−10	2-10	1223	475	-230
44	1	44	PB2−11	2-11	1172	475	-230
45	1	45	PB2−12	2-12	1128	475	-230
46	1	46	PB2−13	2-13	1077	475	-230
47	1	47	PB2−14	2-14	1039	475	-230
48	1	48	PB2−15	2-15	952	475	-230
49	1	49	PB2−16	2-16	875	475	-230
50	1	50	PB2−17	2-17	787	475	-230
51	1	51	PB2−18	2-18	685	475	-230
52	1	52	PB2−19	2-19	568	475	-230
53	1	53	PB2−20	2-20	433	475	-230
54	1	54	PB2−21	2-21	278	475	-230
55	1	55	PB2−22	2-22	100	475	-230
56	1	56	PB7−10	2-23	1223	-230	475
57	1	57	PB7−11	2-24	1172	-230	475

58	1	58	PB7−12	2-25	1128	-230	475
59	1	59	PB7−13	2-26	1077	-230	475
60	1	60	PB7−14	2-27	1039	-230	475
61	1	61	PB7−15	2-28	952	-230	475
62	1	62	PB7−16	2-29	875	-230	475
63	1	63	PB7−17	2-30	787	-230	475
64	1	64	PB7−18	2-31	685	-230	475
65	2	1	P_{amb}	-	-	-	-
66	2	2	$(P_t - q)_{nozzle}$	-	-	-	-
67	2	3	PB3−1	3-1	2200	230	-475
68	2	4	PB3−2	3-2	2022	230	-475
69	2	5	PB3−3	3-3	1867	230	-475
70	2	6	PB3−4	3-4	1732	230	-475
71	2	7	PB3−5	3-5	1615	230	-475
72	2	8	PB3−6	3-6	1513	230	-475
73	2	9	PB3−7	3-7	1425	230	-475
74	2	10	PB3−8	3-8	1348	230	-475
75	2	11	PB3−9	3-9	1281	230	-475
76	2	12	PB3−10	3-10	1223	230	-475
77	2	13	PB3−11	3-11	1172	230	-475
78	2	14	PB3−12	3-12	1128	230	-475
79	2	15	PB3−13	3-13	1077	230	-475
80	2	16	PB3−14	3-14	1039	230	-475
81	2	17	PB3−15	3-15	952	230	-475
82	2	18	PB3−16	3-16	875	230	-475
83	2	19	PB3−17	3-17	787	230	-475
84	2	20	PB3−18	3-18	685	230	-475
85	2	21	PB3−19	3-19	568	230	-475
86	2	22	PB3−20	3-20	433	230	-475
87	2	23	PB3−21	3-21	278	230	-475
88	2	24	PB3−22	3-22	100	230	-475
89	2	25	PB7−19	3-23	1513	-230	475
90	2	26	PB7−20	3-24	1425	-230	475
91	2	27	PB7−21	3-25	1348	-230	475
92	2	28	PB7−22	3-26	1281	-230	475
93	2	29	PB8−1	3-27	2200	230	475
94	2	30	PB8−2	3-28	2022	230	475
95	2	31	PB8−3	3-29	1867	230	475
96	2	32	PB8−4	3-30	1732	230	475
97	2	33	PB8−5	3-31	1615	230	475
98	2	34	PB4−1	4-1	2200	-230	-475
99	2	35	PB4−2	4-2	2022	-230	-475
100	2	36	PB4−3	4-3	1867	-230	-475
101	2	37	PB4−4	4-4	1732	-230	-475
102	2	38	PB4−5	4-5	1615	-230	-475
103	2	39	PB4−6	4-6	1513	-230	-475
104	2	40	PB4−7	4-7	1425	-230	-475
105	2	41	PB4−8	4-8	1348	-230	-475
106	2	42	PB4−9	4-9	1281	-230	-475
107	2	43	PB4−10	4-10	1223	-230	-475
108	2	44	PB4−11	4-11	1172	-230	-475
109	2	45	PB4−12	4-12	1128	-230	-475
110	2	46	PB4−13	4-13	1077	-230	-475
111	2	47	PB4−14	4-14	1039	-230	-475
112	2	48	PB4−15	4-15	952	-230	-475
113	2	49	PB4−16	4-16	875	-230	-475
114	2	50	PB4−17	4-17	787	-230	-475
115	2	51	PB4−18	4-18	685	-230	-475
116	2	52	PB4−19	4-19	568	-230	-475
117	2	53	PB4−20	4-20	433	-230	-475
118	2	54	PB4−21	4-21	278	-230	-475
119	2	55	PB4−22	4-22	100	-230	-475
120	2	56	PB8−6	4-23	1513	230	475
121	2	57	PB8−7	4-24	1425	230	475
122	2	58	PB8−8	4-25	1348	230	475
123	2	59	PB8−9	4-26	1281	230	475
124	2	60	PB8−10	4-27	1223	230	475

125	2	61	PB8−11	4-28	1172	230	475
126	2	62	PB8−12	4-29	1128	230	475
127	2	63	PB8−13	4-30	1077	230	475
128	2	64	PB8−14	4-31	1039	230	475
129	3	1	P_{amb}	-	-	-	-
130	3	2	$(P_t - q)_{nozzle}$	-	-	-	-
131	3	3	PB5−1	5-1	2200	-475	-230
132	3	4	PB5−2	5-2	2022	-475	-230
133	3	5	PB5−3	5-3	1867	-475	-230
134	3	6	PB5−4	5-4	1732	-475	-230
135	3	7	PB5−5	5-5	1615	-475	-230
136	3	8	PB5−6	5-6	1513	-475	-230
137	3	9	PB5−7	5-7	1425	-475	-230
138	3	10	PB5−8	5-8	1348	-475	-230
139	3	11	PB5−9	5-9	1281	-475	-230
140	3	12	PB5−10	5-10	1223	-475	-230
141	3	13	PB5−11	5-11	1172	-475	-230
142	3	14	PB5−12	5-12	1128	-475	-230
143	3	15	PB5−13	5-13	1077	-475	-230
144	3	16	PB5−14	5-14	1039	-475	-230
145	3	17	PB5−15	5-15	952	-475	-230
146	3	18	PB5−16	5-16	875	-475	-230
147	3	19	PB5−17	5-17	787	-475	-230
148	3	20	PB5−18	5-18	685	-475	-230
149	3	21	PB5−19	5-19	568	-475	-230
150	3	22	PB5−20	5-20	433	-475	-230
151	3	23	PB5−21	5-21	278	-475	-230
152	3	24	PB5−22	5-22	100	-475	-230
153	3	25	PB8−15	5-23	952	230	475
154	3	26	PB8−16	5-24	875	230	475
155	3	27	PB8−17	5-25	787	230	475
156	3	28	PB8−18	5-26	685	230	475
157	3	29	PB8−19	5-27	568	230	475
158	3	30	PB8−20	5-28	433	230	475
159	3	31	PB8−21	5-29	278	230	475
160	3	32	PB8−22	5-30	100	230	475
161	3	33	P_{bot}−3	5-31	2700	25	-
162	3	34	PB6−1	6-1	2200	-475	230
163	3	35	PB6−2	6-2	2022	-475	230
164	3	36	PB6−3	6-3	1867	-475	230
165	3	37	PB6−4	6-4	1732	-475	230
166	3	38	PB6−5	6-5	1615	-475	230
167	3	39	PB6−6	6-6	1513	-475	230
168	3	40	PB6−7	6-7	1425	-475	230
169	3	41	PB6−8	6-8	1348	-475	230
170	3	42	PB6−9	6-9	1281	-475	230
171	3	43	PB6−10	6-10	1223	-475	230
172	3	44	PB6−11	6-11	1172	-475	230
173	3	45	PB6−12	6-12	1128	-475	230
174	3	46	PB6−13	6-13	1077	-475	230
175	3	47	PB6−14	6-14	1039	-475	230
176	3	48	PB6−15	6-15	952	-475	230
177	3	49	PB6−16	6-16	875	-475	230
178	3	50	PB6−17	6-17	787	-475	230
179	3	51	PB6−18	6-18	685	-475	230
180	3	52	PB6−19	6-19	568	-475	230
181	3	53	PB6−20	6-20	433	-475	230
182	3	54	PB6−21	6-21	278	-475	230
183	3	55	PB6−22	6-22	100	-475	230
184	3	56	P_{bot}−4	6-23	2900	0.0	-
185	3	57	P_{bot}−5	6-24	3100	-25	-
186	3	58	P_{bot}−6	6-25	3300	-50	-
187	3	59	P_{bot}−7	6-26	3500	-75	-
188	3	60	P_{top}−3	6-27	2700	-25	-
189	3	61	P_{top}−4	6-28	2900	0.0	-
190	3	62	P_{top}−5	6-28	3100	25	-
191	3	63	P_{top}−6	6-30	3300	50	-

192	3	64	$P_{top}-7$	6-31	3500	75	-

Table C.7: RAD assignment for the closed test section wall pressure measurements.

Channel #	RAD Module	Module Channel	Function	Cable	X [mm]	Y [mm]	Z [mm]
1	1	1	P_{amb}	-	-	-	-
2	1	2	$(P_t - q)_{plenum}$	-	-	-	-
3	1	3	-	1-1	-	-	-
4	1	4	-	1-2	-	-	-
5	1	5	-	1-3	-	-	-
6	1	6	-	1-4	-	-	-
7	1	7	-	1-5	-	-	-
8	1	8	-	1-6	-	-	-
9	1	9	-	1-7	-	-	-
10	1	10	-	1-8	-	-	-
11	1	11	-	1-9	-	-	-
12	1	12	-	1-10	-	-	-
13	1	13	-	1-11	-	-	-
14	1	14	-	1-12	-	-	-
15	1	15	-	1-13	-	-	-
16	1	16	-	1-14	-	-	-
17	1	17	-	1-15	-	-	-
18	1	18	-	1-16	-	-	-
19	1	19	-	1-17	-	-	-
20	1	20	-	1-18	-	-	-
21	1	21	-	1-19	-	-	-
22	1	22	-	1-20	-	-	-
23	1	23	-	1-21	-	-	-
24	1	24	-	1-22	-	-	-
25	1	25	-	1-23	-	-	-
26	1	26	-	1-24	-	-	-
27	1	27	-	1-25	-	-	-
28	1	28	-	1-26	-	-	-
29	1	29	-	1-27	-	-	-
30	1	30	-	1-28	-	-	-
31	1	31	-	1-29	-	-	-
32	1	32	-	1-30	-	-	-
33	1	33	-	1-31	-	-	-
34	1	34	-	2-1	-	-	-
35	1	45	-	2-2	-	-	-
36	1	36	-	2-3	-	-	-
37	1	37	-	2-4	-	-	-
38	1	38	-	2-5	-	-	-
39	1	39	-	2-6	-	-	-
40	1	40	-	2-7	-	-	-
41	1	41	-	2-8	-	-	-
42	1	42	-	2-9	-	-	-
43	1	43	-	2-10	-	-	-
44	1	44	-	2-11	-	-	-
45	1	45	-	2-12	-	-	-
46	1	46	-	2-13	-	-	-
47	1	47	-	2-14	-	-	-
48	1	48	-	2-15	-	-	-
49	1	49	-	2-16	-	-	-
50	1	50	-	2-17	-	-	-
51	1	51	-	2-18	-	-	-
52	1	52	-	2-19	-	-	-
53	1	53	-	2-20	-	-	-
54	1	54	-	2-21	-	-	-
55	1	55	-	2-22	-	-	-
56	1	56	-	2-23	-	-	-
57	1	57	-	2-24	-	-	-
58	1	58	-	2-25	-	-	-
59	1	59	-	2-26	-	-	-
60	1	60	-	2-27	-	-	-
61	1	61	-	2-28	-	-	-

62	1	62	-	2-29	-	-	-
63	1	63	-	2-30	-	-	-
64	1	64	-	2-31	-	-	-
65	2	1	P_{amb}	-	-	-	-
66	2	2	$(P_t - q)_{plenum}$	-	-	-	-
67	2	3	PB3−1	3-1	2200	200	-475
68	2	4	PB3−2	3-2	2022	200	-475
69	2	5	PB3−3	3-3	1867	200	-475
70	2	6	PB3−4	3-4	1732	200	-475
71	2	7	PB3−5	3-5	1615	200	-475
72	2	8	PB3−6	3-6	1513	200	-475
73	2	9	PB3−7	3-7	1425	200	-475
74	2	10	PB3−8	3-8	1348	200	-475
75	2	11	PB3−9	3-9	1281	200	-475
76	2	12	PB3−10	3-10	1223	200	-475
77	2	13	PB3−11	3-11	1172	200	-475
78	2	14	PB3−12	3-12	1128	200	-475
79	2	15	PB3−13	3-13	1077	200	-475
80	2	16	PB3−14	3-14	1039	200	-475
81	2	17	PB3−15	3-15	952	200	-475
82	2	18	PB3−16	3-16	875	200	-475
83	2	19	PB3−17	3-17	787	200	-475
84	2	20	PB3−18	3-18	685	200	-475
85	2	21	PB3−19	3-19	568	200	-475
86	2	22	PB3−20	3-20	433	200	-475
87	2	23	PB3−21	3-21	278	200	-475
88	2	24	PB3−22	3-22	100	200	-475
89	2	25	-	3-23	-	-	-
90	2	26	-	3-24	-	-	-
91	2	27	-	3-25	-	-	-
92	2	28	-	3-26	-	-	-
93	2	29	-	3-27	-	-	-
94	2	30	-	3-28	-	-	-
95	2	31	-	3-29	-	-	-
96	2	32	-	3-30	-	-	-
97	2	33	-	3-31	-	-	-
98	2	34	PB4−1	4-1	2200	-200	-475
99	2	35	PB4−2	4-2	2022	-200	-475
100	2	36	PB4−3	4-3	1867	-200	-475
101	2	37	PB4−4	4-4	1732	-200	-475
102	2	38	PB4−5	4-5	1615	-200	-475
103	2	39	PB4−6	4-6	1513	-200	-475
104	2	40	PB4−7	4-7	1425	-200	-475
105	2	41	PB4−8	4-8	1348	-200	-475
106	2	42	PB4−9	4-9	1281	-200	-475
107	2	43	PB4−10	4-10	1223	-200	-475
108	2	44	PB4−11	4-11	1172	-200	-475
109	2	45	PB4−12	4-12	1128	-200	-475
110	2	46	PB4−13	4-13	1077	-200	-475
111	2	47	PB4−14	4-14	1039	-200	-475
112	2	48	PB4−15	4-15	952	-200	-475
113	2	49	PB4−16	4-16	875	-200	-475
114	2	50	PB4−17	4-17	787	-200	-475
115	2	51	PB4−18	4-18	685	-200	-475
116	2	52	PB4−19	4-19	568	-200	-475
117	2	53	PB4−20	4-20	433	-200	-475
118	2	54	PB4−21	4-21	278	-200	-475
119	2	55	PB4−22	4-22	100	-200	-475
120	2	56	-	4-23	-	-	-
121	2	57	-	4-24	-	-	-
122	2	58	-	4-25	-	-	-
123	2	59	-	4-26	-	-	-
124	2	60	-	4-27	-	-	-
125	2	61	-	4-28	-	-	-
126	2	62	-	4-29	-	-	-
127	2	63	-	4-30	-	-	-
128	2	64	-	4-31	-	-	-

129	3	1	P_{amb}	-	-	-	-
130	3	2	$(P_t - q)_{plenum}$	-	-	-	-
131	3	3	-	5-1	-	-	-
132	3	4	-	5-2	-	-	-
133	3	5	-	5-3	-	-	-
134	3	6	-	5-4	-	-	-
135	3	7	-	5-5	-	-	-
136	3	8	-	5-6	-	-	-
137	3	9	-	5-7	-	-	-
138	3	10	-	5-8	-	-	-
139	3	11	-	5-9	-	-	-
140	3	12	-	5-10	-	-	-
141	3	13	-	5-11	-	-	-
142	3	14	-	5-12	-	-	-
143	3	15	-	5-13	-	-	-
144	3	16	-	5-14	-	-	-
145	3	17	-	5-15	-	-	-
146	3	18	-	5-16	-	-	-
147	3	19	-	5-17	-	-	-
148	3	20	-	5-18	-	-	-
149	3	21	-	5-19	-	-	-
150	3	22	-	5-20	-	-	-
151	3	23	-	5-21	-	-	-
152	3	24	-	5-22	-	-	-
153	3	25	-	5-23	-	-	-
154	3	26	-	5-24	-	-	-
155	3	27	-	5-25	-	-	-
156	3	28	-	5-26	-	-	-
157	3	29	-	5-27	-	-	-
158	3	30	-	5-28	-	-	-
159	3	31	-	5-29	-	-	-
160	3	32	-	5-30	-	-	-
161	3	33	$P_{bot}-3$	5-31	2700	25	-
162	3	34	$P_{bot}-1$	6-1	2300	75	-
163	3	35	$P_{bot}-2$	6-2	2500	50	-
164	3	36	$P_{top}-1$	6-3	2300	-75	-
165	3	37	$P_{top}-2$	6-4	2500	-50	-
166	3	38	-	6-5	-	-	-
167	3	39	-	6-6	-	-	-
168	3	40	-	6-7	-	-	-
169	3	41	-	6-8	-	-	-
170	3	42	-	6-9	-	-	-
171	3	43	-	6-10	-	-	-
172	3	44	-	6-11	-	-	-
173	3	45	-	6-12	-	-	-
174	3	46	-	6-13	-	-	-
175	3	47	-	6-14	-	-	-
176	3	48	-	6-15	-	-	-
177	3	49	-	6-16	-	-	-
178	3	50	-	6-17	-	-	-
179	3	51	-	6-18	-	-	-
180	3	52	-	6-19	-	-	-
181	3	53	-	6-20	-	-	-
182	3	54	-	6-21	-	-	-
183	3	55	-	6-22	-	-	-
184	3	56	$P_{bot}-4$	6-23	2900	0.0	-
185	3	57	$P_{bot}-5$	6-24	3100	-25	-
186	3	58	$P_{bot}-6$	6-25	3300	-50	-
187	3	59	$P_{bot}-7$	6-26	3500	-75	-
188	3	60	$P_{top}-3$	6-27	2700	-25	-
189	3	61	$P_{top}-4$	6-28	2900	0.0	-
190	3	62	$P_{top}-5$	6-28	3100	25	-
191	3	63	$P_{top}-6$	6-30	3300	50	-
192	3	64	$P_{top}-7$	6-31	3500	75	-

C.2. DNW-LST Test Campaign

C.2.1. DNW-LST Test Matrices

During the DNW-LST test campaign, propeller 2 is tested for OGE and IGE for the angles of 90° and 0°. For the forementioned lifting angle, an angle of attack sweep is performed with a 3° step. During the tunnel centerline measurements (OGE), the angle sweep is ranging from 87°- 99°, while for the IGE the measured angles are from 87°- 93°. The simulation conditions are shown in Table C.8 for propeller 2 and in Table C.9 for propeller 1.

Table C.8: Simulation conditions for the performance measurements of propeller 2 at 90° (5 runs (AoA's) for OGE and 3 (AoA's) for IGE) and at 0° (1 run for OGE and 1 for IGE).

$\mathbf{u_\infty}$ **[m/s]**	40	35	30	25	22.5	20	18.5	16.5	15	12.5	10	8.5	6.5	5
n [rpm]	6000-14000	14000	14000	14000	14000	14000	14000	14000	14000	14000	14000	14000	14000	14000

Table C.9: Simulation conditions for the performance measurements of propeller 1 at 90° (1 run for IGE) and at 0° (1 run for OGE and 1 for IGE).

$\mathbf{u_\infty}$ **[m/s]**	40	35	30	25	22.5	20	18.5	16.5	15	12.5	10	8.5	6.5	5
n [rpm]	2000-5000	5000	5000	5000	5000	5000	5000	5000	5000	5000	5000	5000	5000	5000

D

Uncertainty Assessment

This Appendix presents a comprehensive uncertainty assessment with respect to the three measurements performed. The Taylor Series approach [11], is adopted for the error propagation and uncertainty assessment. The confidence level associated with the uncertainty of the measurements is always chosen as 95%. It is denoted here that this analysis takes into account only the random errors. Moreover, any temperature gradients are assumed to be negligible. (conclusion makes sense for tunnel-cooled but not for load, rpm)

D.1. Load & Power Measurements

D.1.1. Advance Ratio Estimation

The ESC samples the rpm over a frequency of 5 kHZ, but for data redundancy reasons, it averages over 12 intervals each consisting of $0.8192s \times 5kHz = 4096$ samples per interval. The average and the standard deviation of those 12 interval points is calculated directly and is given as an output. Assuming that the rpm measurement uncertainty follows the Student s distribution and for a 95% confidence level and $12-1$ degrees of freedom (t_{95}=2.201), it follows that:

$$U_n = \pm t_{95} \frac{\sigma_n}{\sqrt{12}} \tag{C.1}$$

Similarly, the tunnel's reference system is based on two total pressure measurements inside the contraction. These measurements are referenced to a position inside the test section according to the tunnel calibration. Assuming that this reference value is adequate, the tunnel velocity is determined based on 17 velocity measurements (t_{95}=2.120). The mean and the standard deviation are recorded. Therefore, the associated random uncertainty is:

$$U_{u_\infty} = \pm t_{95} \frac{\sigma_{u_\infty}}{\sqrt{17}} \tag{C.2}$$

As described above, the advance ratio is a function of the above two measured parameters (see equation (11)), therefore the error propagation can be assessed with the following relation:

$$U_\mu = \sqrt{(\frac{\partial \mu}{\partial u_\infty} U_{u_\infty})^2 + (\frac{\partial \mu}{\partial n} U_n)^2} \tag{C.3}$$

Table D.1, presents the uncertainty estimations for a typical measurement procedure for a propeller 1 test, in the closed-wall test section, at 90° incidence angle. Due to the high number of measurements only a few are presented for briefness. Additionally, the relative uncertainty percentage, defined as the uncertainty over the mean value ($R_\mu = U_\mu/\mu$) is given

Table D.1: Random uncertainty assessment for the advance ratio estimation.

($\mathbf{u_\infty}$, **n**, $\boldsymbol{\mu}$) **[m/s, rpm, -]**	$(\frac{\partial \mu}{\partial u_\infty} U_{u_\infty})^2 \times 10^{-9}$	$(\frac{\partial \mu}{\partial n} U_n)^2 \times 10^{-8}$	$U_\mu \times 10^{-4}$	R_μ [%]
(40.52, 1533, 1.24)	4.36	42	±6.51	0.05
(40.5, 3001, 0.63)	1.83	8.37	±2.92	0.046
(40.49, 4487, 0.42)	2.19	1.39	±1.27	0.03
(35.33, 4951, 0.33)	5.16	23.9	±4.9	0.14
(22.51, 4891, 0.22)	1.5	2.61	±1.67	0.077
(7.83, 4897, 0.075)	62.1	0.09	±2.51	0.33

Both contributions to the total uncertainty are extremely small. As expected the error over the propeller rpm measurements is contributing slightly more than that of the free-stream velocity measurements for the higher wind tunnel speeds. The opposite is observed for the lower speeds (low-speeds high rpm) where the rpm measurements are more precise than the wind tunnel velocity measurements. The forementioned effects are counteracting and the overall uncertainty of the advance ratio is of the order of 10^{-4} and more or less constant. The relative uncertainty increases at very low advance ratios, ($\mu < 0.1$), but still all values are way below 1 %. The same investigation was repeated for a similar run corresponding to propeller 2 with the overall advance ratio uncertainty ranging from orders 10^{-5} to 10^{-4}, while the relative uncertainty was lower than 1%. It is therefore concluded that the current setup is robust in terms of advance ratio estimation.

D.1.2. Thrust & Power Coefficients Estimation

Regarding the load measurements, the same acquisition is imposed as for the rpm. The mean and standard deviation of the measured force T_m is given for 12 already averaged intervals, each comprised of 4096 samples. Initially, the thrust is based on a 10 V excitation voltage. The corrected thrust T value is based on the actual excitation voltage V_{exc} measured. The random uncertainty estimation for the thrust and its corrected value is given in equations (C.4) and (C.5).

$$U_{T_m} = \pm t_{95} \frac{\sigma_{T_m}}{\sqrt{12}} \tag{C.4}$$

$$T = \frac{V_{exc}}{10} T_m \tag{C.5}$$

The measured excitation voltage has also an estimated uncertainty, while the above errors propagate in the corrected load estimation through the relation:

$$U_{V_{exc}} = \pm t_{95} \frac{\sigma_{V_{exc}}}{\sqrt{12}} \tag{C.7}$$

$$U_T = \sqrt{(\frac{\partial T}{\partial V_{exc}} U_{V_{exc}})^2 + (\frac{\partial T}{\partial T_m} U_{T_m})^2} \tag{C.8}$$

Table D.2 presents the uncertainty estimation for the propeller thrust measurements corresponding to the same test run presented above (Table D.1). It is clear that the most dominant error is the one of the load cell. The error contribution of the latter is 3 orders of magnitude higher than that of the excitation voltage. Therefore, the voltage error can be neglected in the analysis. The uncertainty lies within acceptable ranges and as anticipated, it is higher for lower thrust values. In general, in the low-speed high-thrust regime, the relative uncertainty is well below 1% for both propellers.

Table D.2: Random uncertainty assessment for the measured thrust.

($\mathbf{u_\infty}$, **n**, $\boldsymbol{\mu}$) [**m/s, rpm, -**]	$(\frac{\partial T}{\partial V_{exc}} U_{V_{exc}})^2 \times 10^{-6}$ [N^2]	$(\frac{\partial T}{\partial T_m} U_{T_m})^2 \times 10^{-3}$ [N^2]	U_T [N]	R_T [%]
(40.52, 1533, 1.24)	0.004	4.24	±0.06	1.5
(40.5, 3001, 0.63)	1.41	16.7	±0.13	0.61
(40.49, 4487, 0.42)	5.3	5.5	±0.07	0.11
(35.33, 4951, 0.33)	8.8	33.8	±0.18	0.23
(22.51, 4891, 0.22)	32.1	17.9	±0.13	0.16
(7.83, 4897, 0.075)	12.2	22.7	±0.15	0.24

Similarly, the error estimation of density variations can be estimated. This error is strongly dependent on the accuracy of the measured temperature. For the present study the effects of temperature variations and accuracy are not included. Therefore, only an estimate with respect to the standard deviation of the density is considered. Finally, the uncertainty associated with the two thrust coefficients used in the present study can be estimated from the relations (C.10) and (C.11). The total and relative uncertainty estimations for the thrust coefficient based on the free-stream wind tunnel speed and the respective contributions are presented in Table D.3.

$$U_\rho = \pm t_{95} \frac{\sigma_\rho}{\sqrt{17}} \tag{C.9}$$

$$U_{C_T} = \sqrt{(\frac{\partial C_T}{\partial T} U_T)^2 + (\frac{\partial C_T}{\partial \rho} U_\rho)^2 + (\frac{\partial C_T}{\partial u_\infty} U_{u_\infty})^2} \tag{C.10}$$

$$U_{c_T} = \sqrt{(\frac{\partial c_T}{\partial T} U_T)^2 + (\frac{\partial c_T}{\partial \rho} U_\rho)^2 + (\frac{\partial c_T}{\partial n} U_n)^2} \tag{C.11}$$

Table D.3: Random uncertainty assessment for the thrust coefficient based on the wind tunnel speed.

($\mathbf{u_\infty}$, **n**, $\boldsymbol{\mu}$) [**m/s, rpm, -**]	$(\frac{\partial C_T}{\partial T} U_T)^2 \times 10^{-7}$	$(\frac{\partial C_T}{\partial \rho} U_\rho)^2 \times 10^{-11}$	$(\frac{\partial C_T}{\partial u_\infty} U_{u_\infty})^2 \times 10^{-9}$	U_{C_T}	R_{C_T} [%]
(40.52, 1533, 1.24)	2.54	0.017	0.02	±0.0005	1.55
(40.5, 3001, 0.63)	10.2	1.6	0.5	±0.001	0.61
(40.49, 4487, 0.42)	3.36	0.8	1229	±0.0005	0.12
(35.33, 4951, 0.33)	35	47600	119	±0.0002	0.25
(22.51, 4891, 0.22)	111.5	3600	558	±0.0034	0.16
(7.83, 4897, 0.075)	9778	14065	7218000	±0.091	0.71

It is seen that in the low speed - high thrust conditions which are of interest the relative uncertainty is lower than 1%, even at conditions of, or close to flow breakdown. That is due to fact that the thrust

coefficient is very high at the forementioned regime. Furthermore, the contribution of the density to the error propagation is lower than the effects of measured load and wind tunnel velocity and may be neglected. Similarly, the random uncertainty assessment for the thrust coefficient based on the tip speed is given in Table D.4. As discussed before, the density error propagation is neglected. It is observed that the thrust coefficient based on the tip speed is slightly more accurate than the one based on wind tunnel speed, due to the higher accuracy of the rpm estimation compared with the wind tunnel free-stream speed.

Table D.4: Random uncertainty assessment for the thrust coefficient based on the blade tip speed.

($\mathbf{u_\infty}$, **n**, $\boldsymbol{\mu}$) **[m/s, rpm, -]**	$(\frac{\partial c_T}{\partial T}U_T)^2 \times 10^{-7}$	$(\frac{\partial c_T}{\partial n}U_n)^2 \times 10^{-9}$	U_{c_T}	R_{c_T} [%]
(40.52, 1533, 1.24)	6	2.73	±0.00078	1.5
(40.5, 3001, 0.63)	1.64	3.7	±0.00041	0.61
(40.49, 4487, 0.42)	0.109	2.5	±0.00011	0.13
(35.33, 4951, 0.33)	0.44	69.7	±0.00035	0.38
(22.51, 4891, 0.22)	0.24	21.15	±0.00021	0.22
(7.83, 4897, 0.075)	0.31	3.33	±0.00018	0.26

The voltage and current consumed by the electric motor are recorded directly from the power supply unit. There are 10 measurements for each of those. Thus, the voltage and current random uncertainties and their propagation to the power coefficient can be similarly estimated. Table D.6 presents the error propagation of the voltage and current to the power estimation. The electric current measurement is highly uncertain and its contribution is the dominant ($U_I >> U_{V_e}$) for the uncertainty estimation of the electric power. Finally, the power coefficient uncertainty assessment is presented in the following Table. Similarly, it can be concluded that the power coefficient is insensitive to random errors propagating due to the rpm, density and electric power measurements since the relative uncertainty is well below 1%.

$$U_{V_e} = \pm t_{95}\frac{\sigma_{V_e}}{\sqrt{10}} \tag{C.12}$$

$$U_I = \pm t_{95}\frac{\sigma_I}{\sqrt{10}} \tag{C.13}$$

$$U_{P_e} = \sqrt{(\frac{\partial P_e}{\partial V_e}U_{V_e})^2 + (\frac{\partial P_e}{\partial I}U_I)^2} \tag{C.14}$$

Table D.5: Random uncertainty assessment for the electric power estimation.

($\mathbf{u_\infty}$, **n**, $\boldsymbol{\mu}$) **[m/s, rpm, -]**	$(\frac{\partial P_e}{\partial V_e}U_{V_e})^2 \times 10^{-3}[\mathrm{W}^2]$	$(\frac{\partial P_e}{\partial I}U_I)^2[\mathrm{W}^2]$	$U_{P_e}[\mathrm{W}]$	R_{P_e} [%]
(40.52, 1533, 1.24)	0.000798	2	±1.42	0.37
(40.5, 3001, 0.63)	0.19	66.61	±8.16	0.45
(40.49, 4487, 0.42)	0.34	282.3	±16.8	0.3
(35.33, 4951, 0.33)	2	653.8	±25.57	0.33
(22.51, 4891, 0.22)	6	386.5	±19.66	0.25
(7.83, 4897, 0.075)	1.3	261.3	±16.16	0.26

$$U_{c_{P_e}} = \sqrt{(\frac{\partial c_{P_e}}{\partial P_e}U_{P_e})^2 + (\frac{\partial c_{P_e}}{\partial \rho}U_\rho)^2 + (\frac{\partial c_{P_e}}{\partial n}U_n)^2} \tag{C.15}$$

Table D.6: Random uncertainty assessment for the electric power coefficient estimation.

$(\mathbf{u_\infty}, \mathbf{n}, \boldsymbol{\mu})$ **[m/s, rpm, -]**	$(\frac{\partial c_{P_e}}{\partial P_e} U_{P_e})^2 \times 10^{-7}$	$(\frac{\partial c_{P_e}}{\partial n} U_n)^2 \times 10^{-9}$	$U_{c_{P_e}}$	$R_{c_{P_e}}$ [%]
(40.52, 1533, 1.24)	2.69	0.47	±0.0005	0.4
(40.5, 3001, 0.63)	1.6	0.14	±0.0004	0.48
(40.49, 4487, 0.42)	0.6	4.5	±0.00025	0.32
(35.33, 4951, 0.33)	0.77	125.7	±0.00045	0.56
(22.51, 4891, 0.22)	0.48	38.9	±0.0003	0.33
(7.83, 4897, 0.075)	0.327	7.06	±0.0002	0.28

D.2. Wall Pressure Measurements

The pressure bars used for the determination of the static pressure at the walls have a 7 kPa (1 psi) range and an accuracy of ±0.12% F.S. Thus, the uncertainty band is always constant (U_{P_x} = ±0.0012 × 7000 = 8.4 Pa). The rest of the parameters which contribute to the pressure coefficient determination are treated in the same manner as above, where the uncertainty is quantified based on the standard deviation, the number of measurements and a factor taken for 95% confidence level. The random uncertainty associated with the pressure coefficient at the walls is given by equation (C.17). Figure D.1, presents the pressure coefficient measured at the bottom wall, on the advancing side of propeller 1 (Pressure Bar 3) during an rpm sweep, at a constant wind tunnel velocity of 40 m/s. The uncertainty associated with the pressure coefficient estimation is included as an error bar. All the testing conditions are included in terms of advance ratio, with some of them corresponding to the forementioned conditions presented in the above tables. The velocity sweep is also presented in Figure D.2. The spatial variation of the pressure measurements makes it difficult to present such results in a tabulated manner as before, but an overall effect of those three terms is discussed. During the rpm sweep (Figure D.1), the contributions of the reference pressure and dynamic pressure (second and third term of equation (C.17)) into the total uncertainty for the pressure coefficient are extremely small (O(10^{-7} and O(10^{-11}) respectively) compared to the pressure coefficient itself (≥O(10^{-2})). As expected, the dominant contribution is due to the pressure transducer's accuracy (first term), which is constant for the given constant dynamic pressure. Same applies also for the velocity sweep, with the propagation uncertainties reaching to O(10^{-4}) for both the second and third term of equation (C.17). Thus, it is concluded that these contributions may be neglected, since the dominant limiting factor is the accuracy of the pressure transducers. Furthermore, during the velocity sweep, the wall static pressure increases due to the propeller impinging on the bottom wall. Thus, the highest relative uncertainty is encountered in the inlet and outlet pressure recovery regions. It should be highlighted, that when subtracting the wall pressures of the empty tunnel and the strut at the lowest wind tunnel velocities, the uncertainty can surge to values which can be prohibiting (up to 50% for an empty test section and a tunnel velocity of 5 m/s). A simple estimate for those errors can be made by computing the first term of equation (C.17), for a given dynamic pressure. The total uncertainty of this subtracting procedure, is the vector summation of the respective uncertainties in accordance with the Taylor Series Method.

$$U_{C_{P_x}} = \sqrt{(\frac{\partial C_{P_x}}{\partial P_x} U_{P_x})^2 + (\frac{\partial C_{P_x}}{\partial P_{ref}} U_{P_{ref}})^2 + (\frac{\partial C_{P_x}}{\partial q_n} U_{q_n})^2} \tag{C.17}$$

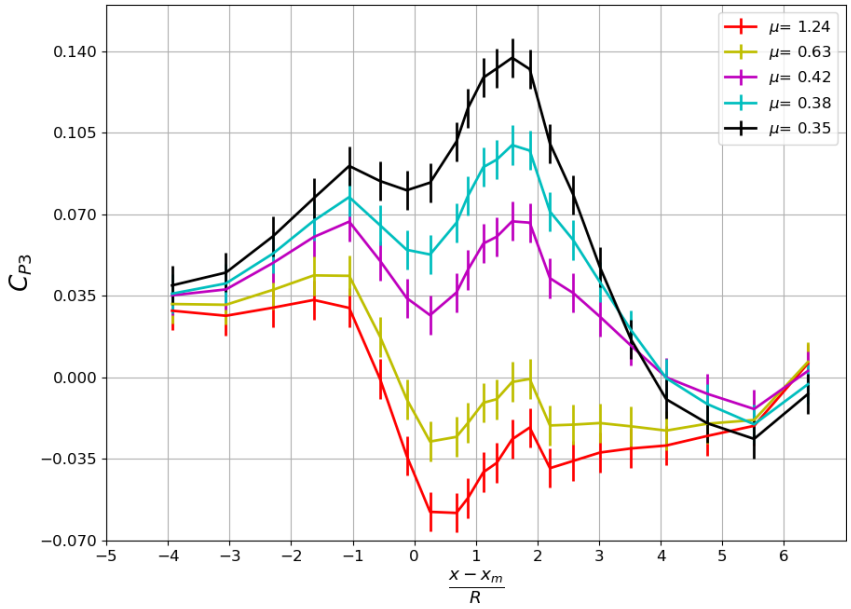


Figure D.1: Bottom wall pressure measurements and uncertainty bands at the advancing side of propeller 1 during an rpm sweep.

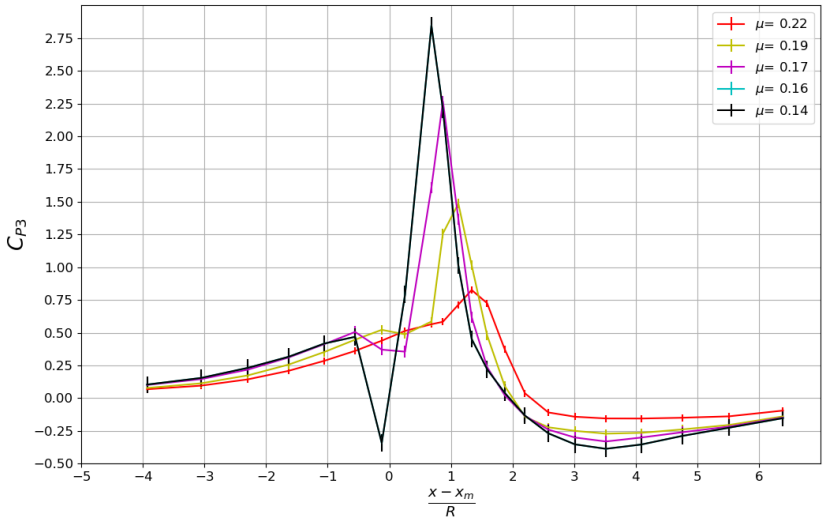


Figure D.2: Bottom wall pressure measurements and uncertainty bands at the advancing side of propeller 1 during a velocity sweep.

D.3. PTV Measurements

In this section, an approach is presented in order to quantify the measurement uncertainty associated with the velocity measurements based on physical laws. The uncertainty of the averaged velocity field can be estimated from equation (C.18), where $i = x, y, z$ and σ_u is the standard deviation of all the velocity vectors corresponding to N independent particles/samples contributing to the velocity estimation (within a bin). Equation (C.18) does not take into account systematic uncertainties due to

spatial modulation errors or peak locking [78]. The standard deviation σ_u contains both actual velocity fluctuations (turbulence) and fluctuations due to measurement errors (see equation (C.19)).

$$U_{\overline{u}} = \frac{\sigma_u}{\sqrt{N}} \tag{C.18}$$

$$\sigma_u^2 = \sigma_{u_{turb}}^2 + \sigma_{u_{err}}^2 \tag{C.19}$$

Due to the above realization, it was decided to utilize another method that makes use of the incompressible continuity equation whose real value is known a priori. In the current flow, compressibility effects are expected to be negligible far away from the propeller, due to the high tip Mach number which is about 0.6. That is the reason that the results presented here show the uncertainty quantification close to the boundaries of the illuminated volume, at regions further upstream and downstream of the propeller and away from the blades. The assessment presented here is based on the approach of Sciacchitano et al. [78] and uses the TSM (Taylor-Series-Method) in order to propagate the velocity uncertainty on the continuity equation. In practice, the inverse is used due to the "true" value of the latter. For the time-averaged velocity which is of interest here, the standard uncertainty (68% confidence level) associated with the time-averaged continuity equation is given below, where N_{eff} corresponds to the effective number of statistically uncorrelated contributing vectors (samples) for a given bin. The effective number for the continuity equation is chosen such that it adheres to equation (C.21), where T is the total observation time for a given measurement and $T_{int,xyz}$ is the integral time scale of the flow. Finally, equation (C.20) holds for only random errors present [78].

$$U_{(\nabla\overline{u})} = \frac{\sigma_{(\nabla u)}}{\sqrt{N_{eff}}} \tag{C.20}$$

$$N_{eff} = \frac{T}{2T_{int,xyz}} \tag{C.21}$$

Once the uncertainty of the time averaged continuity equation ($U_{(\nabla\overline{u})}$) is determined, the uncertainty associated with the averaged velocity measurements can be estimated by establishing a relation which describes how the velocity error propagates into the continuity equation with the use of the Taylor Series Method (TSM). The continuity equation may be discretized by a finite difference scheme and a uniform grid spacing in all directions is employed ($h_x = h_y = h_z = h$). Furthermore, it is assumed that the errors of $\overline{u}$, $\overline{v}$, $\overline{w}$, are spatially uncorrelated ($\rho(\delta\overline{u}_{\pm h},\delta\overline{v}_{\pm h})= \rho(\delta\overline{u}_{\pm h},\delta\overline{w}_{\pm h})= \rho(\delta\overline{v}_{\pm h},\delta\overline{w}_{\pm h})= 0$) and the correlated errors of each velocity component at ±h has an equal cross-correlation coefficient of ($\rho(\delta\overline{u}_{+h},\delta\overline{u}_{-h}) = \rho(\delta\overline{v}_{+h},\delta\overline{v}_{-h}) = \rho(\delta\overline{w}_{+h},\delta\overline{w}_{-h}) = \rho(2h)$). Additionally, the uncertainty of each component at $\pm h$ is considered the same. Under the above assumptions, one can derive relation (C.23), which can be further simplified by assuming that $U_{\overline{u}} = U_{\overline{v}} = U_{\overline{w}} = U_{\overline{U}}$, as shown below.

$$\begin{aligned}\nabla\overline{u} = \frac{\partial\overline{u}}{\partial x} + \frac{\partial\overline{v}}{\partial y} + \frac{\partial\overline{w}}{\partial z} = \frac{1}{2h}[&\overline{u}(x+h,y,z) - \overline{u}(x-h,y,z) + \overline{v}(x,y+h,z) - \overline{v}(x,y-h,z) \\ &+\overline{w}(x,y,z+h) - \overline{w}(x,y,z-h)]\end{aligned} \tag{C.22}$$

$$U^2_{(\nabla\overline{u})} = (\frac{1}{2h})^2[2U^2_{\overline{u}} + 2U^2_{\overline{u}} + 2U^2_{\overline{w}} - 2\rho(2h)(U^2_{\overline{u}} + U^2_{\overline{v}} + U^2_{\overline{w}})] = \frac{3}{2h^2}([1-\rho(2h)]U^2_{\overline{U}}) \tag{C.23}$$

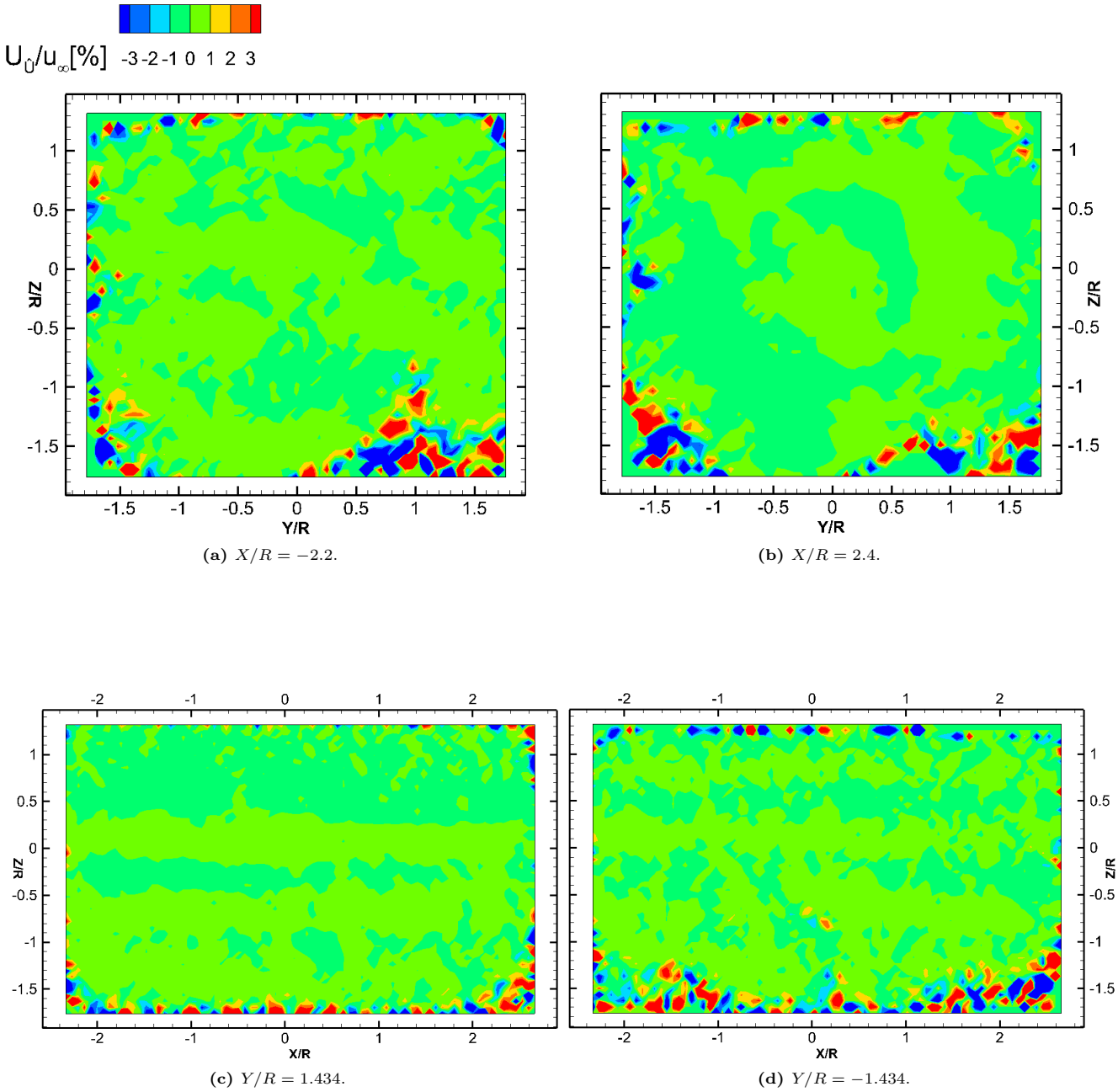
Finally, for a given divergence uncertainty (relation (C.20)), an estimate for the velocity uncertainty is possible for a spatial auto correlation of the measurement error at separation distance $2h$ of approximately 0.45, for the given 75% overlap and a 31×31 voxel bin size, as reported by Wieneke [95] for a 2D

PIV Monte Carlo simulation of a null displacement field. It should be noted here that this approach is valid for a 2D PIV where the errors of u and v are spatially uncorrelated. That is not the case for the current data therefore the actual uncertainty is expected to be slightly higher since the spatial cross correlation of the rest of the velocity components will contribute to a further increase of the time-averaged velocity uncertainty. Still, the outcome of this assessment is considered indicative of the magnitude of the errors associated with the estimated mean velocity.

$$U_{\overline{U}} = hU_{(\nabla\overline{u})}\sqrt{\frac{2}{3[1-\rho(2h)]}} \tag{C.24}$$

The time-averaged velocity uncertainty normalized by the wind tunnel free-stream velocity is presented in Figure D.3, for the propeller 2 test in 0° incidence angle, at 0.1 advance ratio. Figure D.3a presents a 2D contour 0.11 m upstream of the propeller, while Figure D.3b shows the same contour for 535 m downstream of the propeller position. Additionally, Figures D.3c and D.3d present the normalized uncertainty at a position $y = \pm 0.2$ m from the tunnel centerline (y=0). The vertical and lateral coordinates Z, Y presented in the Figures are centered on the propeller location. The axial coordinate is centered on the test stand location in accordance with the PTV coordinate system (see Figure 3.13) with the propeller extending about 0.2 m upstream ($(x/R)_{prop,0^\circ} = -1.433$). The data presented in Figure D.3 are unprocessed, meaning there is no filter applied for denoising and vector validation. In order to reduce outliers, a vector validation procedure was followed. This included the application of a spatial median filter Westerweel et al. [94], a polynomial fitting filter based on the local uncertainty value and finally, a local smoothing of the velocity vectors. The normalized velocity uncertainty after the vector validation procedure is presented in the same manner in Figure D.4.

Overall, it is observed that the data quality in the vicinity of the boundaries of the measurement volume is degraded, while, on the remaining most part, the uncertainty lies below ±1% of the wind tunnel free-stream speed ($u_\infty \approx 20.41$ m/s). Additionally, the velocities on the lower part of the domain are more uncertain than the ones on the top boundary. That is expected since the two cameras (1 and 2) are viewing the measurement volume from top and due to the fact that the wind tunnel floor exhibited high background noise. The same can be concluded for the advancing side of the propeller 2 ($y > 0$) which is less erroneous than the retreating side ($y < 0$), due to the viewing position of camera 3. Moreover, the vector post-processing scheme has considerably decreased the random uncertainty in most of the parts of the volume, thus it is considered desirable and necessary. Figures D.5 and D.6 show the uncertainty assessment for the conditions corresponding to advance ratios of 0.197 and 0.063 respectively. It should be kept in mind that in the higher advance ratio the seeding density is considerably smaller than in the other two cases due to the high wind tunnel velocity. Thus, the velocity vectors traced are significantly smaller if none, especially at the boundaries. That of course, cannot be observed in Figure D.5, where the region closer to the boundaries of the volume has an uncertainty value of zero, due to the absence of velocity vectors. The actual resolved boundaries for that case may be distinguished by the higher uncertainty regions on the top and on the bottom (more discernible) boundaries. In the core flow, the relative uncertainty is somewhat higher than in the previous case due to the lower number of detected tracks as discussed before. On the contrary, for the lowest velocity presented here ($u_\infty \approx 12.91$ m/s), where the seeding density was the highest, the random relative uncertainty value lies almost everywhere within ±1%.



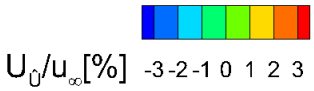
(a) $X/R = -2.2$.

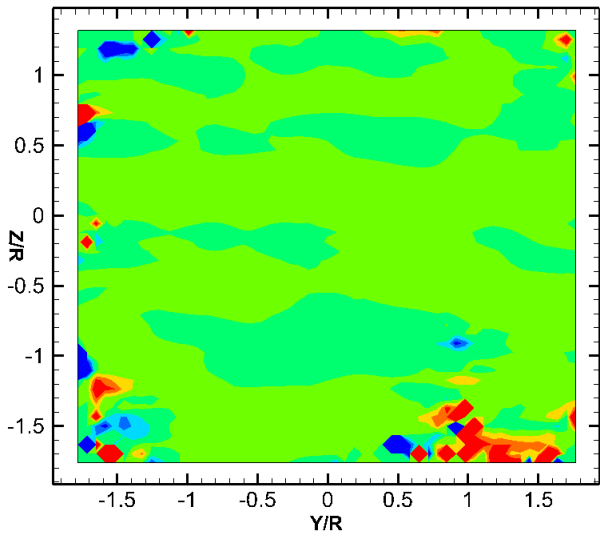
(b) $X/R = 2.4$.

(c) $Y/R = 1.434$.

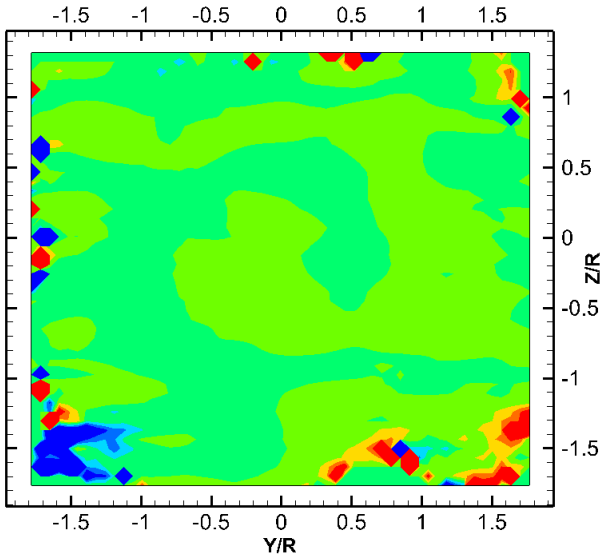
(d) $Y/R = -1.434$.

Figure D.3: Normalized velocity uncertainty for a propeller 2 test at $\mu = 0.1$, 0° incidence angle (unprocessed data, colour bar same for all sub-figures).

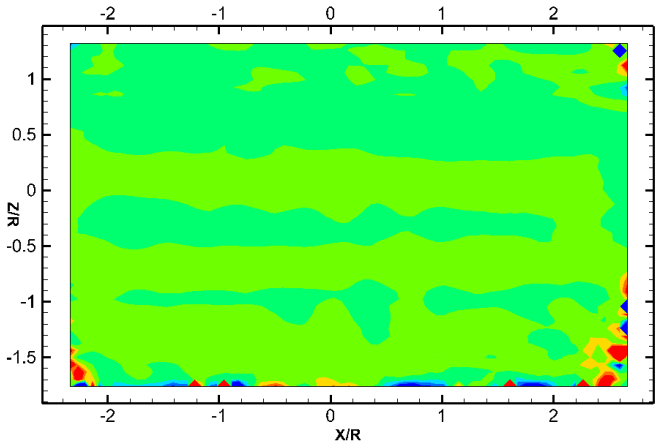




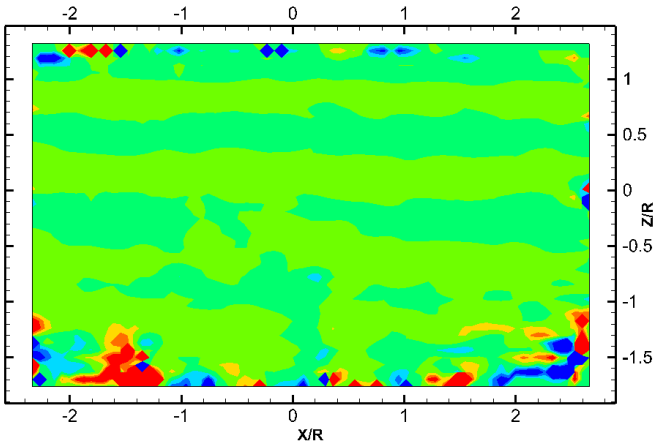
(a) $X/R = -2.2$.



(b) $X/R = 2.4$.

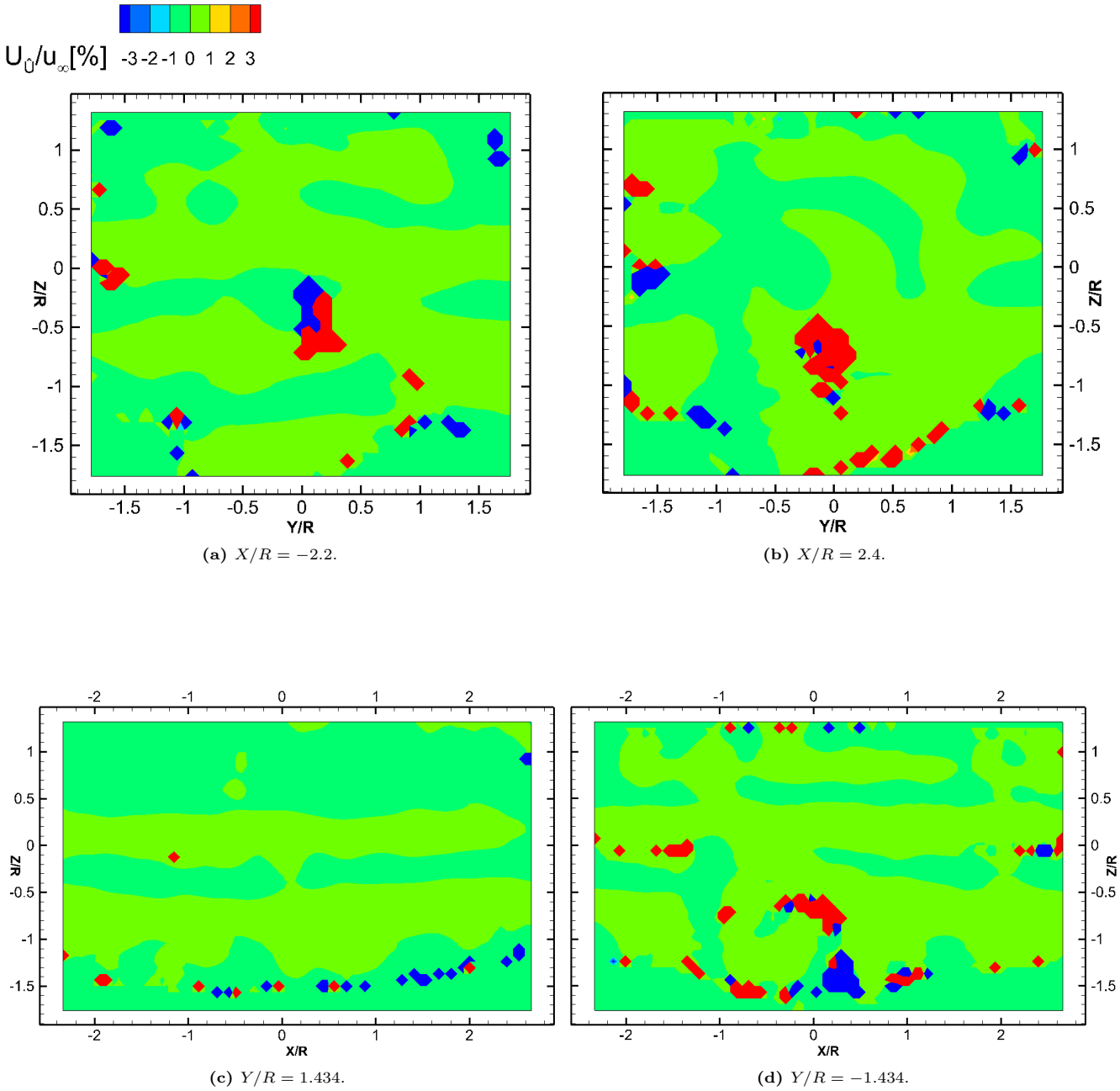


(c) $Y/R = 1.434$.



(d) $Y/R = -1.434$.

Figure D.4: Normalized velocity uncertainty for a propeller 2 test at $\mu = 0.1$, 0° incidence angle (post-processed data, colour bar same for all sub-figures).



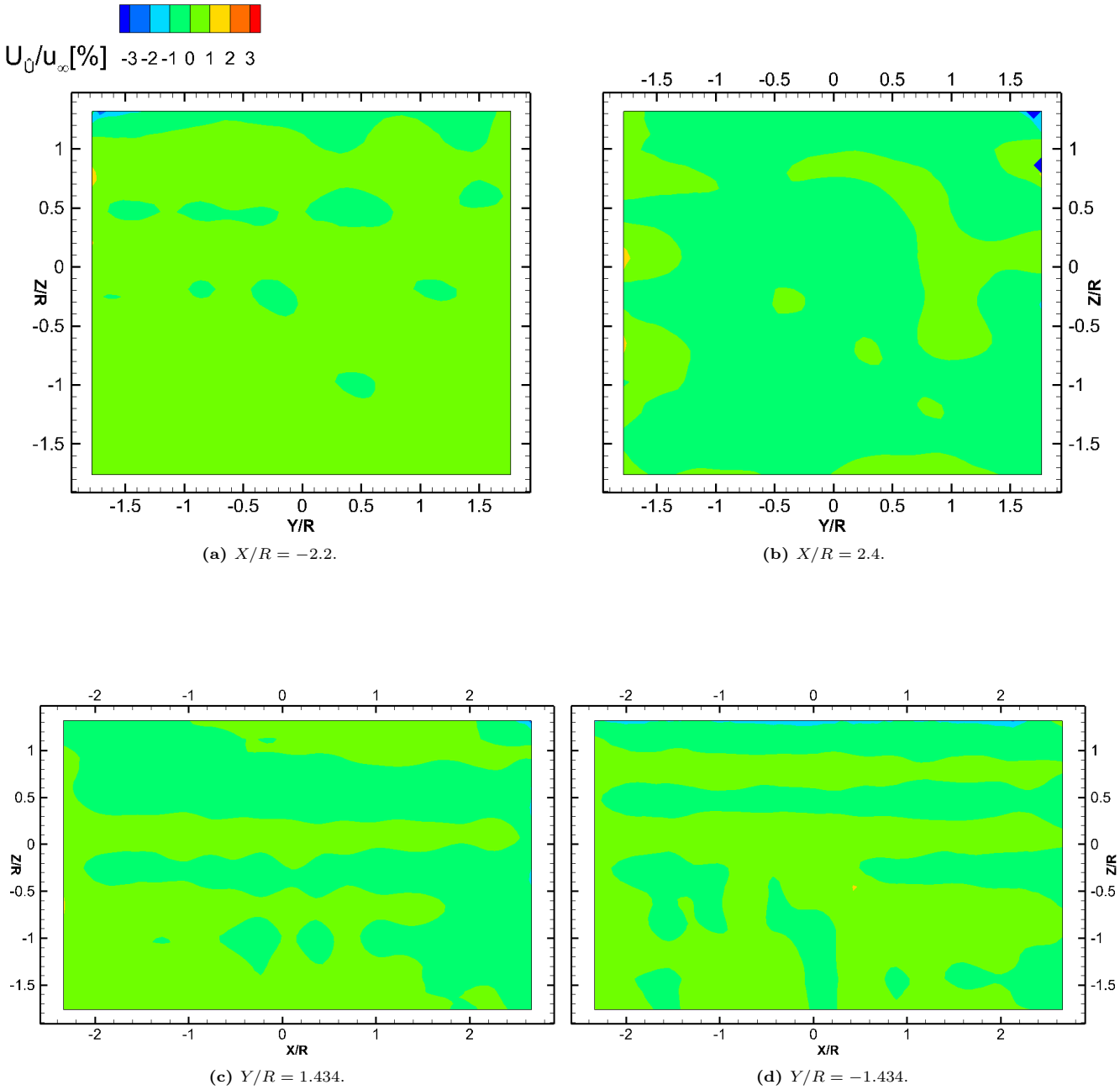
(a) $X/R = -2.2$.

(b) $X/R = 2.4$.

(c) $Y/R = 1.434$.

(d) $Y/R = -1.434$.

Figure D.5: Normalized velocity uncertainty for a propeller 2 test at $\mu = 0.197$, 0° incidence angle (post-processed data, colour bar same for all sub-figures).



(a) $X/R = -2.2$.

(b) $X/R = 2.4$.

(c) $Y/R = 1.434$.

(d) $Y/R = -1.434$.

Figure D.6: Normalized velocity uncertainty for a propeller 2 test at $\mu = 0.063$, 0° incidence angle (post-processed data, colour bar same for all sub-figures).

D.4. Conclusions

This section presents a comprehensive uncertainty assessment of the wind tunnel test setup and measurement procedures. The setup is evaluated based on the random errors that may propagate and influence the quality and accuracy of the results. It is concluded that the set up is robust in the advance ratio determination, since the rpm and the free-stream velocity measurements have very low contribution to the final uncertainty. The same considerations apply for the thrust and power coefficients with the relative uncertainty being lower than ±1%. Regarding the pressure measurements, the accuracy of the pressure transducers is the dominant parameter affecting the pressure coefficient estimation. At low wind tunnel speeds, the uncertainty may reach to values up to 50% for the empty test section. On the other hand, the propeller high thrust testing conditions results into a strong pressure rise inside the

test section as shown in Figure D.2, which cause a decrease in the uncertainty of the measurements. Still, the error of the empty test section measurements may propagate and influence the results when subtracting the pressure coefficients at a given dynamic pressure corresponding to low wind tunnel speeds, but the induced pressure rise by the propeller, is still dominant compared with the uncertainty values of the empty test section measurements. Regarding the PTV measurements, it is shown that for the core region of the measurement volume the relative uncertainty is within $\pm 1\%$ of the wind tunnel free-stream velocity. On the other hand, in the vicinity of the boundaries of the measurement volume (especially on the bottom and on the retreating side ($y < 0$)), the most uncertain measurements were identified. That is attributed to optical blockage by the test stand, the propeller and the other tracer particles present in the flow and is a limitation of the current setup. The seeding density is also a significant factor affecting the quality of the results, since it is adequately connected with the number of identified tracks per pulse which governs the velocity field spatial and temporal statistics.